Structural and spectroscopic studies on the porin-cytochrome complex from *Shewanella oneidensis* MR-1

Matthew Lawes

Ph.D Thesis

School of Biological Sciences

University of East Anglia

Norwich

April 2015

Acknowledgments

Thanks must go to Dr Tom Clarke my supervisor as well as both Dr Andrew Hemmings and Prof. David Richardson, for all their patience, knowledge and leadership.

Additionally thanks must go to Prof. Julea Butt, Dr Marcus Edwards, Dr Gaye White, Dr Andrew Gates, Dr Nick Watmough, and Dr Richard Bowater who as part of the CMSB were a greatly appreciated source of guidance.

Thanks must also go to all the past and present members of lab 2.30. Invariably I owe you all one (in someway or another).

Lastly, thanks must go to my family. You know why.

Abstract

The outer membrane, hetero-trimeric multi-heme cytochrome complex MtrCAB, enables the process of dissimilatory metal reduction (DMR) in *Shewanella oneidensis.*

The properties of the decaheme protein MtrA as well as a truncated version of this protein were investigated using analytical ultracentrifugation (AUC), small angle X-ray scattering (SAXS) and spectropotentiometric techniques. MtrA and a truncated N-terminal MtrA construct containing the five N-terminal hemes (MtrA N) were both observed to be prolate and highly extended along one axis. Through aligning MtrA N with MtrA, the N terminus of the MtrA structure was identified. Redox titration experiments were performed on MtrA as well as N and C terminal truncations. From these titrations three distinct groups of hemes were identified; a high, a middle potential and a low potential group of hemes. The five N terminal hemes contained the high and middle potential groups of hemes; whereas the five C terminal hemes contained the middle and low potential groups of hemes.

The MtrCAB complex was inserted into liposomes containing either methyl viologen, small tetra heme cytochrome (STC) or cytochrome c. Using these proteoliposomes the rate of electron transfer across MtrCAB was investigated. MtrCAB was seen to enable the reduction and oxidation of methyl viologen and STC, but only the reduction of cytochrome c. STC was reduced during the experiments, implying an electron storage role in the periplasm during respiration.

Finally, the structure of MtrCAB was investigated through small angle neutron scattering (SANS). Structures of MtrCAB were highly elongated with a globular head region and a tail region. Through density matching buffers, scattering produced from detergents was removed and a prediction of the relative location of MtrB within the model made. The model produced was found to be long enough to span the periplasm enabling direct contact of MtrA with proteins on the inner membrane.

Abbreviations

ALA	5-aminolevulinic acid
ATP	Adenonsine triphosphate
AUC	Analytical ultracentrifugation
Ccm	Cytochrome c maturation
DEAE	(Diethylaminoethyl) cellulose
DMSO	Dimethylsulfoxide
DNA	Deoxyribonucleic acid
EDTA	Ethylenediaminetetraacetic acid
$FADH_2$	Flavin adenine dinucleotide
HEPES	4-(2-hydroxyethyl)-1-piperazineethanesulfonic acid
IMAC	Immobilized metal-ion affinity column
Mtr	Metal reductase
NADH	Nicotinamide adenine dinucleotide
Nrf	Nitrite reductase with formate
NTA	Nitriloacetic acid
Omc	Outer membrane cytochrome
Ottel	Optically transparent tin electrode
PAGE	Polyacrylamide gel electrophoresis
PFV	Protein film voltammetry
SDS	Sodium dodecyl sulfate
SE	Sedimentation equilibrium
SHE	Standard hydrogen electrode
STC	Small tetraheme cytochrome
SRP	Signal recognition particle
TMAO	Trimethylamine *N*-oxide
Tris/HCl	Tris-(hydroxylmethyl)-aminomethanehydrochloride
UV-vis	Ultraviolet-visible

1 | Introduction

1.01 Eukaryotic Respiration

Respiration is a catabolic process fundamental to all of the kingdoms of life (Nicholls & Ferguson, 2002). In eukaryotic organisms such as higher animals and plants, cellular respiratory processes occur in the mitochondria, resulting in the production of adenosine 5´triphosphate (ATP). ATP is exported from the mitochondria, where the exogenic hydrolysis of phosphate groups is used to drive unfavorable chemical reactions essential for life. The respiratory process that forms ATP proceeds through the catabolism of carbon, via glycolysis and the tricarboxylic acid (TCA) cycle. Liberated electrons are transferred from freely diffusible low redox potential donors, such as NADH, or protein-associated carriers, such as $FADH_2$, into a multi-protein electron transfer pathway located in the inner mitochondrial membrane. Electrons are transferred through the pathway via a series of free or protein-associated redox co-factors. These include flavins, iron-sulfur clusters, copper centers and hemes. The mitochondrial electron transfer process terminates with the reduction of the high potential terminal electron acceptor, which in aerobic conditions is oxygen.

Electron transport processes proceed due to an overall shift from low to high electrochemical potential of the redox couples comprising the chain. The midpoint redox potential is the potential at which half the chemical species is reduced and half is oxidised (at pH 7 this is termed $E^{o\prime}$), this is indicative of the electrochemical potential of the species in question. The initial redox couples of species in the electron transport pathway have a low electrochemical potential. For example, the redox couple of NAD^+/NADH is ~−320 mV (versus the standard hydrogen electrode, SHE). This is in contrast to the terminal $½O_2/H_2O$ redox couple which has a $E^{o\prime}$ of ~+820 mV. Thus electrons flowing though a chain beginning and then terminating with these two couples will change potential by +1140 mV. This change in potential is energetically 'downhill' (Nicholls & Ferguson, 2002), and thus energy is liberated by the reaction. This free-energy (ΔG) that is made available drives the translocation of protons across the inner mitochondrial membrane. This results in the generation of a trans-membrane proton electrochemical gradient or proton-motive force (Δp). The proton-motive force can be subsequently coupled to the synthesis of ATP, or cellular functions such as solute transport and motility.

1.02 Bacterial Respiration

The basic description of respiration described above for eukaryotes is also fundamental to the Bacterial kingdom of life. However the relative respiratory flexibility displayed by prokaryotes is vastly different; with bacteria and archaea containing respiratory flexibility that is comparatively diverse and extreme.

In higher eukaryotes cytochrome aa_3 oxidase provides the main mechanism of electron output, achieved through oxygen reduction (Richardson, 2000). There is some respiratory flexibility in the mitochondria of yeast, filamentous fungi and ancient protozoa (Richardson 2000), however this is relatively minor when compared to bacteria. In bacteria, a diverse range of terminal electron acceptors are utilized, including elemental sulphur, (Hamilton, 1998), sulphur oxyanions, organic sulphoxides, (Lie *et al.,* 1999), nitrogen oxy-anions and nitrogen oxides (Berks *et al.,* 1995), organic N-oxides, (Czjzek *et al.,* 1998), halogenated organics, metalloid oxy-anions, transition metal minerals, (Lovley *et al.*, 1991a; Lovley, 1994; Loveley *et al.,* 1995; Lovley & Coates, 1997), and radionuclides, (Lovley *et al.,* 1993; Marshall *et al.,* 2006). This diversity in bacterial respiration has evolved due to the broad range of environments that bacteria have successfully inhabited. The ability of bacteria to endure in these oxic and micro-oxic to anoxic environments is key for the transitioning of essential biogeochemical cycles, such as the carbon, nitrogen, sulphur and iron cycles (Lovely *et al.,* 1991b).

The redox midpoint potentials of some common electron acceptors terminating respiratory electron chains are given in Table 1.1. Although not a truly comprehensive list, the table illustrates the diversity of electron donors and acceptors that can be coupled by bacteria to derive cellular energy, compared to eukaryotic cells. Eukaryotes have evolved to use the most abundant, easily accessible compound with a high redox midpoint. This enables large amounts of energy to be obtained from electron transport chains terminating with oxygen. Bacteria that subsist using more diverse, less common and lower potential terminal redox acceptors are able to derive less energy from the electron transport chains, as a smaller amount of Gibbs free energy is liberated.

Redox half reaction	E^{o}' (mV)
CO_2/glucose	-430
$2H^+/H_2$	-420
NAD^+/NADH	-320
S^0/H_2S	-280
SO_4^{2-}/H_2S	-260
Fumarate/succinate	+30
Amorphous $Fe(OH)_3/Fe^{2+}$ **	+59
TMAO/TMA***	+130
DMSO/DMS***	+160
Fe^{3+}-citrate/ Fe^{2+}-citrate****	+374
NO_3^-/NO_2^-	+430
MnO_2/Mn^{2+}	+600
Fe^{3+}/Fe^{2+}	+770
$½O_2/H_2O$	+820
N_2O/N_2*****	+1350

Table 1.1 Biological standard reduction potentials of selected electron donors and acceptors. E^{o}' refers to the standard redox potential against standard hydrogen electrode, measured at pH 7. All values taken from Thauer *et al.,* (1998), except; **Hernandez & Newman, (2001); *** Madigan *et al.,* (2000); **** Thamdrup, (2000). *****Richardson *et al.,* (2009). Abbreviations; TMAO (trimethylamine N-oxide), DMSO (dimethylsulfoxide), DMS (dimethylsulfide).

1.03 Bacterial dissimilatory respiration

Some of the most interesting examples of bacterial respiratory adaptations are those that use substances, such as heavy metals, to deposit electrons after they have passed through the respiratory electron transport chain. When these substances are not incorporated into the cell then the process is dissimilatory and the externally reduced substance acts as an electron sink. The focus of this thesis will be dissimilatory metal reduction (DMR). Lovely (1987) has described that a great diversity of microorganisms can couple the oxidation of sugars or amino acids with the reduction of Fe(III). However, in all the cases examined, Fe(III) reduction is a trivial side reaction in the metabolism of these organisms (Lovley *et al* 1991b). The primary products of the metabolism of the fermentative Fe(III)-reducing microorganisms are typical fermentation acids, alcohols, and H_2.

In DMR metals such as iron, manganese, technetium, chromium and uranium (as well as dissimilarity reduction of non metals such as fumarate, thiosulphate trimethylamine N-

oxide (Venkateswaran *et al.,* 1999; Gao *et al.,* 2004; Gralnick, Vali, Lies, & Newman, 2006; Ross *et al.,* 2007; Richter, Schicklberger, & Gescher, 2012) are used as substrates for the final redox couple in the respiratory oxidative process. These metals will often be external to the cell, present as ions or particulate solids, and can be part of metal-containing minerals that are insoluble at circumneutral pH and thus are unable to diffuse across the cell membrane. The mode by which electrons are transported from the cell surface to extracellular compounds is currently a controversial topic of debate within the scientific community. There are a number of proposed methodologies as to how the electron transport chain is completed. These include theories about direct cellular contact with heavy metal particles, cellular extrusion of nano wires and flavin electron shuttling (Lower *et al.,* 2001; Marsili *et al.,* 2008; Jensen *et al.,* 2010; El-Naggar *et al.,* 2010; Coursolle, *et al.,* 2010).

Dissimilatory metal and sulphur respiration have applications in municipal solid waste recycling (Muyzer & Stams 2008; Smith 2009) and the bioremediation of heavy metal contaminants (Macaskie *et al.,* 1987; Macaskie & Dean 1989; Nealson *et al.,* 1991; Nealson & Myers 1992; Finneran *et al.,* 2002; Orellana *et al.,* 2013; Orellana *et al.,* 2014). Applications for dissimilatory metal reducers to become part of electrical circuits and fuel cells are also under investigation (Lovley *et al.,* 2011; Nevin *et al.,* 2011). The use of alternative terminal electron acceptors to oxygen allow DMR bacteria to survive in anoxic and micro-oxic environments. The evolution of DMR bacteria often depends on the abundance of oxygen alternatives, which are varied and which produce specialized DMR adaptations. A striking feature of DMR proteins is their modular character, which has been described as being based on a ‘‘redox protein construction kit’’ (Baymann *et al.,* 2003). Using a modular approach to create protein complexes, different combinations of a limited number of protein modules can allow DMR bacteria to respire in relatively diverse environments. The modular character by which DMR seems to have arisen, which has been observed in many other protein families, probably reflects the high level of gene exchange that was presumably present in the pool of organisms that occupied niches requiring DMR (Woese 2000).

The focus of this thesis is the iron reducing *Shewanella oneidensis*. This bacterium uses a heterotrimeric complex located in its outer membrane to pass respiratory electrons from its periplasm to extra-cellular minerals. In order to place the DMR system employed by *S. oneidensis* in a wider context, examples of other bacterial adaptations to metal reduction, metal oxidation and sulphur reduction are described below.

Dissimilatory metal reduction in *Shewanella oneidensis* MR-1

The dissimilatory metal reduction pathway of *Shewanella oneidensis,* strain MR-1 (metal reducer 1) has been well studied. The principal components of the *S. oneidensis* DMR pathway are the outer membrane associated MtrA MtrB and MtrC and the inner membrane CymA. Periplasmic STC is also thought to be involved as well as various other outer membrane cytochromes such as OmcA and UndA, which presumably provide specificity of DMR though connecting in a modular fashion with the base MtrCAB complex.

Unlike *Desulfovibrio desulfuricans, S. oneidensis* cannot perform dissimilatory sulphur reduction, and unlike *Sideroxydans lithotrophicus* it is not known to oxidize extra cellular iron oxides for respiration, although the protein components that *Sideroxydans lithotrophicus* use for this process do share homology with those used by *S. oneidensis*. In Arnold, Dichristina, & Hoffmann, (1986) the authors used various electron transport chain inhibitors in heavy metal reduction studies. They showed that *S. putrefaciens* sp. 200 (a DMR bacterial related strain to *S. oneidenis* MR-1) has adapted to respire anaerobically on various organic and inorganic substrates and that these substrates were being used to start the process that ended in DMR of iron oxides. These extracellular minerals range from the iron-containing goethite, lepidocrocite and hematite (White *et al.,* 2013), to more exotic Mn technetium and uranium containing ores (Macaskie & Dean, 1989; Nealson *et al.,* 1991; Nealson & Myers, 1992; Raton *et al.,* 1997; Finneran *et al.,* 2002). Non-standard metal electron acceptors, such as uranium [U(VI)] (Caccavo *et al.,* 1992), chromium [Cr(VI)] (Wielinga *et al.,* 2001), iodate (Farrenkopf *et al.,* 1997), technetium (Wildung *et al.,* 2000), neptunium (Lloyd *et al.,* 2000), plutonium (Boukhalfa *et al.,* 2007), selenite, tellurite (Klonowska *et al.,* 2005) and vanadate (Carpentier *et al.,* 2003) have been shown to be accessible as terminal electron acceptors of *S. oneidensis*. In addition to the reduction of extracellular minerals containing metals such as Fe(III) or Mn(III/IV), MtrAB homologues have also been shown to be involved in the extracellular reduction of DMSO. Therefore the MtrAB of MR-1 can be cast as the prototype of a model system for electron transfer across the bacterial outer membrane (Gralnick *et al.,* 2006; Jiao & Newman, 2007; Hartshorne *et al.,* 2009).

Analysis of the genomes of metal-reducing *Shewanella* strains revealed that the *mtrC-mtrA-mtrB* genes were well conserved amongst all the analysed genomes (Fredrickson *et*

al., 2008). The gene for deca-heme cytochrome OmcA, also commonly associated with this cluster, was occasionally found. In some genomes, this gene was replaced by *undA* or *undA1*, genes which both encode 11-heme cytochrome C proteins. Both *undA* and *undA1* are believed to be similarly participating in DMR. In some genomes the mtr cluster varied from containing four genes (*omcA-mtrC-mtrA-mtrB* such as in *S. oneidensis and S. frigidmarina*) through to nine genes with duplications (such as in *S. halifaxensis* which has a *mtrD-mtrE-mtrF-omcA- undA-omcA-mtrC-mtrA-mtrB* cluster).

The MtrA, MtrB and MtrC components make up the core of what could be described as a canonical DMR system for bacteria. In *S. oneidensis,* CymA sits in the periplasmic face of the inner membrane accepting electrons from respiratory processes (Myers & Myers, 2000). It is unclear whether STC or another redox protein is then used to transport electrons across the periplasm to MtrCAB, or whether the MtrA can span the periplasm and make contact directly with CymA. MtrA is a decaheme c-type cytochrome and it is tightly associated with MtrB. MtrB has high levels of sequence similarity to β barrel pores, and it localizes with outer-membrane fractions during purification. In-silico modeling programs predict that 24 – 28 β strands compose the pore of MtrB, as well as long loop regions on the extra cellular face of MtrB. Expression of MtrB without MtrA has been reported to be unviable (Hartshorne *et al.,* 2009). This may suggest that MtrA is a permanent interacting partner of MtrB, effectively plugging a pore that would otherwise enable unregulated exchange or solutes and ions between the periplasm and extracellular space.

Similar to MtrA, MtrC is also a deca-heme c-type cytochrome. MtrC is associated with the outer face of *S. oneidensis's* outer membrane. It has been shown to be tightly bound to MtrAB and susceptible to protease degradation when MtrCAB is inserted in to proteoliposomes (White *et al.,* 2013); in contrast to MtrA and the majority of MtrB. The presence of MtrC greatly speeds up the electron transfer rate of MtrCAB compared to MtrAB, indicating that it helps make the electrical contact to the metal oxide minerals undergoing dissimilatory reduction (White *et al.,* 2013). Coursolle & Gralnick (2010) report that the MtrCAB complex is modular and the individual components are somewhat interchangeable between homologous protein. This could be a method that *S. oneidensis* uses to adapt to niche conditions.

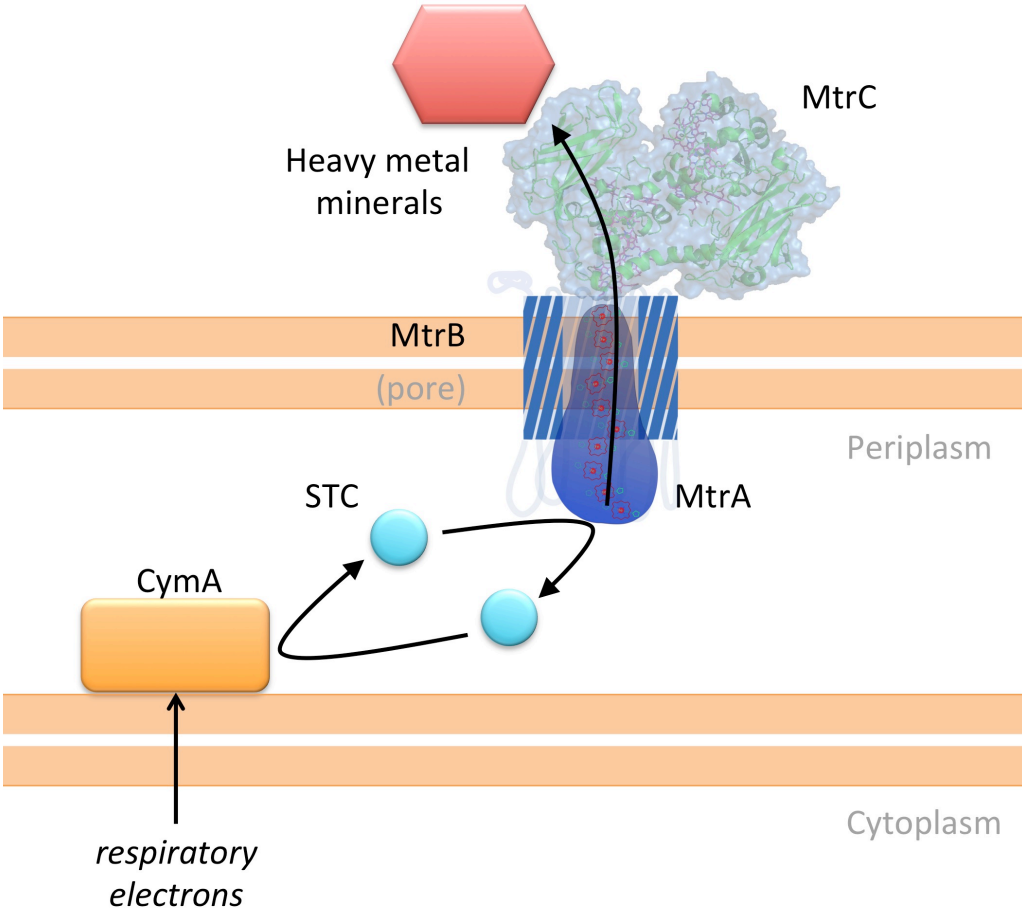

Figure 1. 1 A cartoon schematic of the proposed *S. oneidensis* dissimilarly metal reduction pathway.

Dissimilatory metal reduction by *Geobacter*

Geobacter sulfurreducens is a DMR bacterium. In anoxic environments *G. sulfurreducens* has been shown to use a range of heavy metals including iron and manganese as terminal electron acceptors (D R Lovley 1991a; Lovley *et al.,* 2011; Nevin *et al.,* 2011). Dissimilatory metal reduction was first investigated in *Geobacter sulfurreducens,* as this was the organism in which molecular biological and genetic tools were first developed (Coppi *et al.,* 2001). Another strain of *Geobacter*, called *Geobacter metalreducens*, has since been shown to be comparatively better adapted for dissimilatory metal reduction than *Geobacter sulfurreducens.* It has also been shown to be able to locate extracellular heavy metals through chemotaxis (Childers *et al.,* 2002). When using extracellular iron as the terminal electron acceptor for respiratory processes, *G. sulfurreducens* uses an outer

membrane complex of multi-heme cytochromes (abbreviated to OmC's) (Smith *et al.,* 2013).

Using electrons donated from complexes on the inner membrane (Butler *et al.,* 2004) or periplasm (Lloyd *et al.,* 2003), such as MacA or PpcA (Lovley, 2006; Smith *et al.,* 2013), the outer membrane c-type cytochrome, OmcB, (Leang *et al.,* 2003; Leang & Lovley 2005; Kim *et al.,* 2006), is used to transfer respiratory electrons across the outer membrane and onto pili made conductive by being coated with the cytochrome protein OmcS, (Mehta *et al.,* 2005; Leang *et al.,* 2010; Malvankar & Lovley, 2012; Malvankar *et al.,* 2012) OmcE (Mehta *et al.,* 2005). *G. sulfurreducens* needs the multicopper protein, OmpB (Mehta *et al.,* 2006) to utilize ferric oxide deposits (but not ferric citrate) (Smith *et al.,* 2013). No OmcB homologues are found in *G. metalreducens* but another multiheme cytochrome is found in a similar location (Aklujkar *et al.,* 2009; Smith *et al.,* 2013).

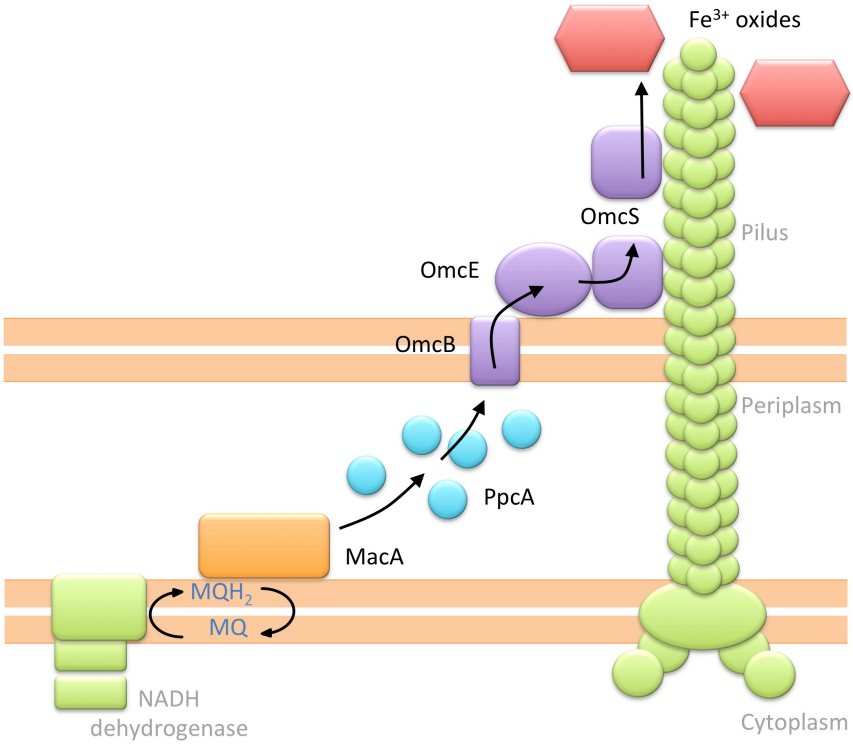

Figure 1. 2 The dissimilatory metal reducing pathway of *Geobacter sulfurreducans*, adapted from (Lovley, 2006).

A recent study, Smith *et al.,* (2014) details how a *ΔpilA* mutant of *G. sulfurreducens* KN400, was still able to dissimilatory respire using iron oxides. The strain was found to be up-regulating the extracellular c-type cytochrome PgcA, which they proposed was acting as an electron shuttle from the outer membrane to the iron deposits.

Analyses by Liang Shi (Shi *et al.,* 2007; Shi *et al.,* 2009) showed that the *Geobacter* strain M21 contained MtrAB homologues (GM21_0397 and GM21_0398). Unlike in *S. oneidensis* an MtrC homologue was not identified next to these genes. Liang Shi suggests that this indicates that the identified MtrAB homologues may not be involved in metal reduction. The lack of Mtr type proteins in *Geobacter* suggests that its own DMR systems were evolved independently from *S. oneidensis* and did not come about due to a gene transfer event.

Iron oxidation by *Sideroxydans lithotrophicus*

Sideroxydans lithotrophicus is a bacterium found in freshwater, groundwater and marine environments as well as in most soils and sediments (Emerson *et al.,* 2007; Emerson *et al.,* 2010). It has been recognized to oxidize Fe(II) deposits in circumneutral micro-oxic environments in order to gain electrons to feed its respiratory electron chains (Emerson & Moyer 1997; Liu *et al.,* 2012; Emerson *et al.,* 2013). In DMR bacteria, the reverse redox reaction takes place, whereby oxidised metals are reduced as the terminal electron acceptors of respiratory chains. This is only possible in environments where there is a sufficient quantity of substrate Fe(II) minerals that are not being readily oxidised by the presence of excess oxygen.

It has been shown that the ES-1 stain of *S. lithotrophicus* is unable to grow on Mn(II) oxides or sulphide. Similarly, it is unable to grow on typical organic carbon respiratory substrates, such as acetate, pyruvate and glucose. Unlike the DMR bacteria, such as *G. sulfurreducens* and *S. oneidensis, S. lithotrophicus* cannot reduce Fe(III) oxides (Emerson & Moyer, 1997). The protein complex MtoAB is employed by *S. lithotrophicus* to conduct electrons across the outer membrane. The periplasmic cytochrome shuttle MtoD transports electrons to MtoAB after receiving them from the inner membrane associated MtoC. The MtoA protein is 332 kDa and has homology with the MtrA protein described in *S. oneidensis* (Liu *et al.,* 2012; Shi *et al.,* 2012). It has ten C-XX-CH motifs that are the binding locations of c-type heme cofactors. MtoB is homologous to the outer membrane β

barrel pore MtrB. It is thought that MtoA fits inside MtoB and allows electron transport across the outer membrane to external metal oxides (Liu *et al.,* 2012). MtoA was found to partially restore the early phase dissimilatory metal (ferrihydrite) reductive capacity of *S. oneidensis* strains that were knockouts for MtrA (Liu *et al.,* 2012). This meant MtoA must have formed a functioning complex with MtrB. Like MtrA, MtoA was found to have bi-directional electron transport abilities (Liu *et al.,* 2012). MtoA is believed to take electrons from extracellular Fe^{2+} minerals and tunnel them through the outer membrane via the ten heme cofactors whilst as a complex with MtoB. It then passes the electrons onto the periplasmic MtoD. This mono-heme cytochrome has only recently been described (Beckwith *et al* 2015 in production) and could fulfill a similar role to the *S. oneidensis* protein small tetraheme cytochrome (STC). STC is a periplasmic protein that is pervasive in the periplasm of *S. oneidensis* and is believed to provide charge transfer between static membrane components through its own diffusion (Harada *et al.,* 2002; Tsapin *et al.,* 2001; Leys *et al.,* 2002). MtoD is thought to act in a similar fashion by passing electrons from MtoA to MtoC. MtoC is a CymA homologue (Shi *et al.,* 2012). MtoC could then feed these electrons into the electron transport chains of *S. lithotrophicus*.

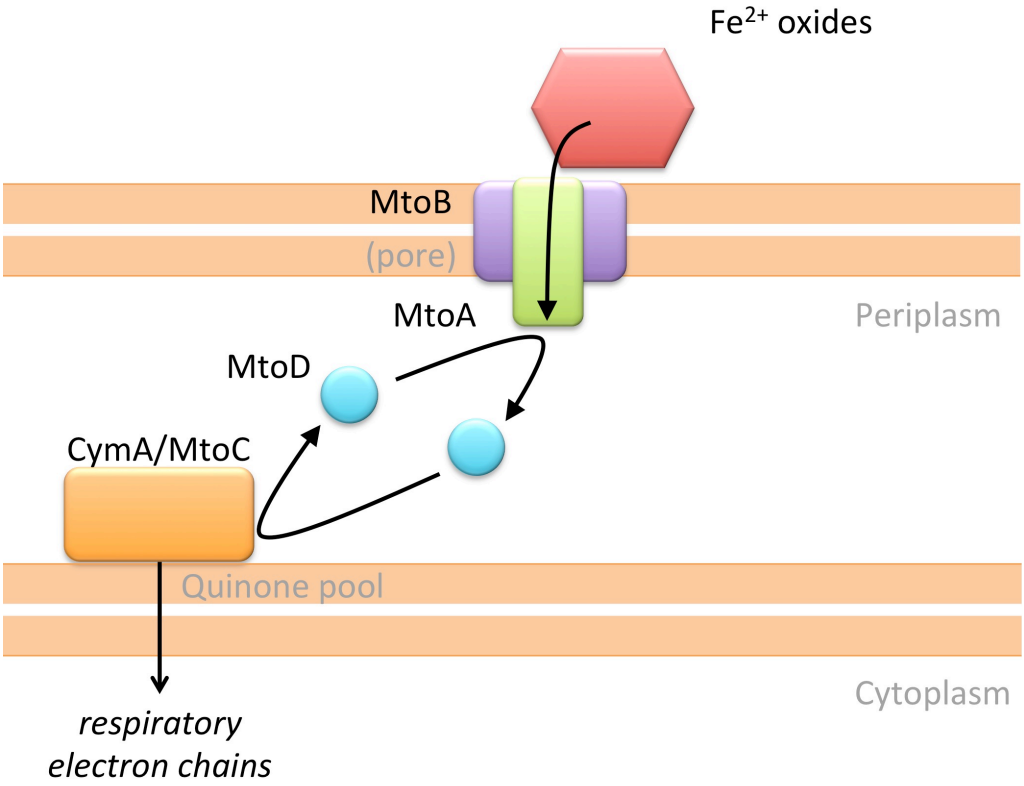

Figure 1. 3 A cartoon schematic of the proposed iron-oxidative electron chain for *S. lithotrophicus.*

The specific mechanisms about how cells conserve energy from oxidation Fe(II) at circumneutral pH are still in the process of being understood (Emerson *et al.,* 2010; Ilbert & Bonnefoy 2013; Emerson *et al.,* 2013)

Sulphur respiration by *Desulfovibrio desulfuricans*

Desulfovibrio desulfuricans is commonly found in aquatic environments with high levels of organic material, as well as in water-logged soils (Lovley & Phillips 1992). The bacteria may also act as opportunistic pathogens when carried in the human gut causing primary bacteremia and abdominal infections, such as abscesses and cholecystitis (Goldstein *et al.,* 2003). They are mainly considered micro-oxic, but have been shown to be able to survive in relatively oxic environments (Lobo *et al.,* 2007). In anoxic and micro-oxic environments they have the ability to reduce sulphurous compounds as their terminal electron acceptor in both assimilatory and dissimilatory manners. Dissimilatory sulphate-reducing bacteria (DSR bacteria) play a key role in the coupling of the carbon and sulphur biogeochemical cycles (Wagner *et al.,* 1998) when they use sulphate as the terminal electron acceptor for the oxidation of organic matter (Amrani *et al.,* 2014). Like DMR bacteria, DSR bacteria have a modular complex that catalyse electron movement. In *S. desulfuricans* the group of protein complexes that facilitate DSR are an ATP sulfurylase, AprBA and DsrAB. Unlike DMR bacteria, sulphate needs chemical modification (or activation) before it can be used as a terminal electron acceptor. The ATP sulfurylase (an trimeric sulphate adenylyl transferase) activates free sulphate by reaction with two units of ATP to form adenosine-5′-phosphosulphate (APS) (Ullrich *et al.,* 2001). Following activation of sulphate an APS reductase (AprBA) reduces APS is reduced to sulphite (Fritz *et al.,* 2002). Sulfite is reduced by the dissimilatory sulfite reductase DsrAB, a siroheme containing protein reputedly regulated by DsrC (Truper 1993; Moura *et al.,* 1988). The presence of a heme protein is common between DMR and DSR bacteria.

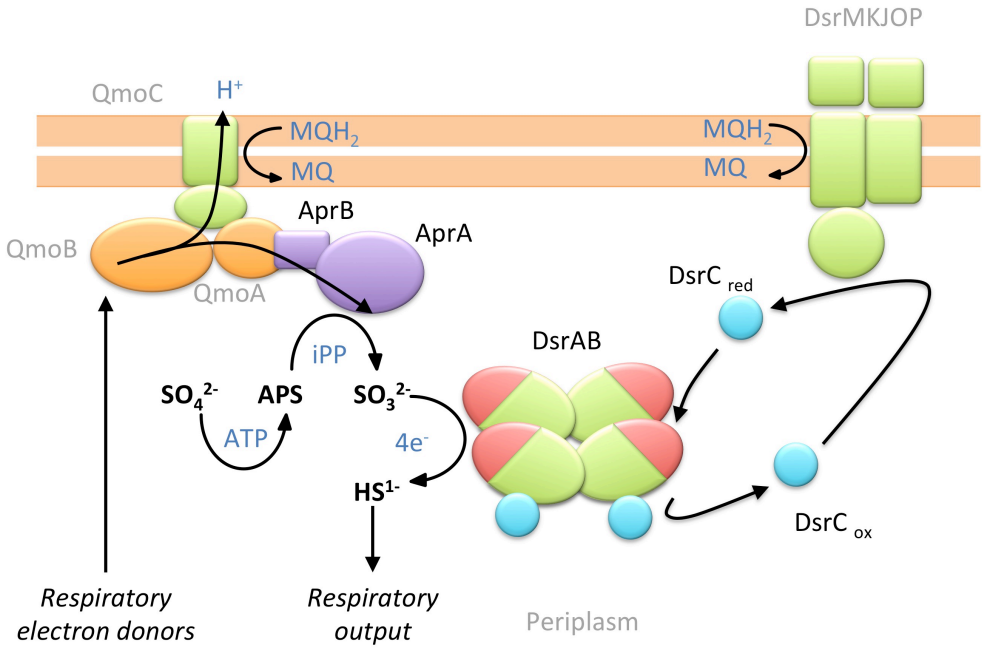

Figure 1. 4 A cartoon schematic of the terminal respiratory step of *S. Sulfuricans.* Based on figure from Grein *et al.,* (2013).

1.05 Cytochrome proteins

Nearly all of the components that facilitate electron transfer for DMR are cytochrome c proteins. These cytochromes contain a heme cofactor bound to the amino acid sequence. This heme cofactor is composed of a protoporphyrin ring with a central iron atom that can change oxidation state usually between 3^+ and 2^+. Proteins containing heme c have diverse structures, however most cytochromes act as electron carriers, cycling between reduced and oxidised (ferrous and ferric) states, thus allowing cytochromes to perform single electron transfers (Scott & Mauk, 1996; Pettigrew & Moore, 1987; Bowman & Bren, 2009).

Functions of c-type cytochromes

The functions of heme c containing proteins are far less varied than that of proteins containing heme b (Bowman & Bren, 2009). Heme b containing proteins have a similar protoporphyrin IX ring and iron structure to heme c, however heme b is not covalently bound to the protein but is joined only as a prosthetic group in b type cytochromes. Heme c is synthesized from heme b and the use of heme c requires a greater investment from the organism (Bowman & Bren, 2009). Understanding how these important proteins are made allows for a greater understanding of the DMR process they are involved in.

Although cytochromes c most often function as electron carriers through redox cycling, it is important to note examples of the other functions of cytochrome c proteins. In eukaryotes, mitochondrial cytochrome c has been found to play a key role in apoptosis (Liu *et al.,* 1996). While it is not clear that the heme plays a direct role in the triggering of apoptosis, the redox state of mitochondrial cytochrome c has been linked to pro-apoptotic activity and a conformational change of the heme crevice (Pan *et al.,* 1999; Brown & Borutaite, 2008; Jemmerson *et al.,* 1999). In addition, it has been proposed that mitochondrial cytochrome c detoxifies reactive oxygen species (Zhao *et al.,* 2003). Some heme c containing proteins have been identified as acting as gas or redox sensors through binding exogenous ligands at an open coordination site. A bacterial example from *Paracoccus denitrificans* is cytochrome c'. This is a cytochrome that binds NO leading to the suppression of NO when it reaches toxic levels (Moir, 1999; Cross *et al.,* 2000). Another gas sensing (high-spin) cytochrome c, found in *Rhodobacter sphaeroides*, is SHP, It binds oxygen as a ligand however its function is unknown (Klarskov *et al.,* 1998). Multiple c-heme-containing sensor proteins have been identified in *G. sulfurreducens*, two of which have been found to contain a PAS-type fold. This motif usually binds heme b, however in

this instance it binds heme c. These cytochromes were found to be involved in chemotaxis (Pokkuluri *et al.,* 2008). Redox changes in the heme groups were found to cause a change in cofactor coordination, from low to high spin upon reduction. Although the actual physiological effector molecule for these high-spin hemes c is not known Klarskov *et al* suggest CO and NO are candidates.

Another cytochrome c was found to be acting as a sensor through redox-driven switching. DcrA from *Desulfovibrio vulgaris,* is a c type cytochrome that is thought to induce signals instigating chemotaxis (Yoshioka *et al.,* 2005). DcrA has two endogenous axial ligands in its reduced state but has an open coordination site when oxidised. CO can bind to the reduced protein and replace one of the distal ligands, which induces a signal. These diverse functions, which are similar to the electron carrying function that most cytochromes have, require the variable oxidation state of the Fe ion within heme to function. C type cytochromes such as MtrA, MtrC, STC and CymA all act as electron carriers, as do the majority of known cytochromes. All of these cytochromes have specific adaptations that allow them to bind c-heme. Heme c is characterized by the presence of two covalent thioether bonds formed between cysteine side chains and the heme vinyl groups Fig 1.5. (at positions 2 and 4 on the porphyrin ring).

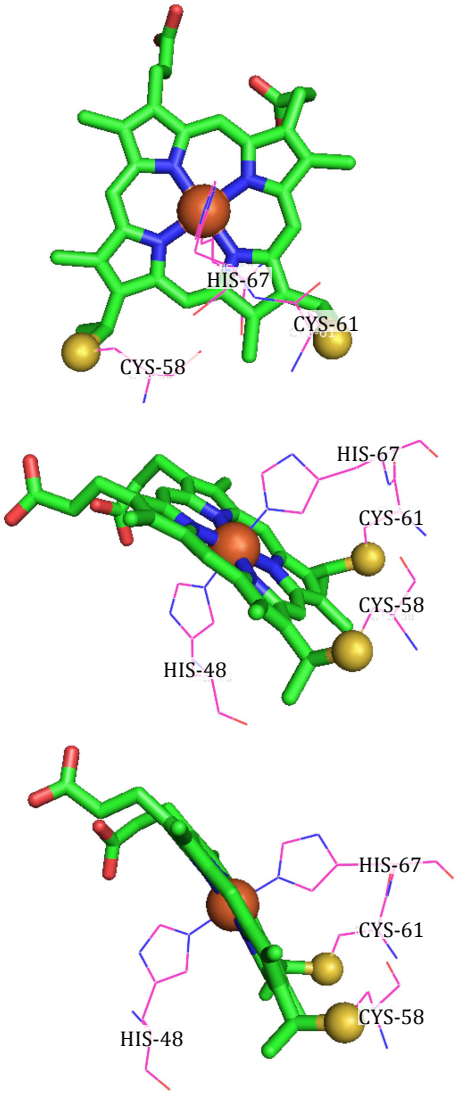

Figure 1. 5 Structure of heme C in various orientations represented in PYMOL. [thick green lines] porphyrin ring. [orange sphere] Iron atom. [yellow spheres] sulphur atoms [thin purple lines] selected sections of amino acid chain from protein bonded to heme cofactor, demonstrating two histidine side groups bonding to the iron center and two cysteine side chains forming vinyl bonds with the porphyrin ring.

This bonding to the amino acid chain is coordinated by a specific sequence. Canonically, the vinyl groups at positions 2 and 4 of the c heme are attached to the N- and C-terminal cysteines of a pentapeptide C-XX-CH motif. Usually, the C-XX-CH pentapeptide segment provides the cysteine residues which are needed for the formation of the thioether bonds to the porphyrin and a histidine to serve as axial ligand to iron. Usually, a second distal

histidine (or methionine) from elsewhere in the amino acid code also ligates to the iron, which forms a stable low spin heme cofactor. XX represents variable residues. In nature, all amino acids have been found in the XX segment, including glyciene, proline, and histidine, with the exception of cysteine (Bowman & Bren, 2009).

Non standard c-type hemes

Although identification of the highly conserved C-XX-CH motif within an amino acid sequence will usually positively identify the sequence as a c type cytochrome, there are a small number of cytochromes c with heme attachment sites that do not follow the normal C-XX-CH pattern. It is important for the understanding of c type cytochromes to investigate these examples.

The b_6f plant photosynthetic protein-complex contains a c heme referred to as heme ci' (ci' also denoted x). Heme ci' is unusual as it is covalently attached, through a single thioether bond, to the cytochrome b component of the complex. Heme ci' is unusual as it lacks protein-donated ligands to heme iron, instead, it is usually only axially ligated by a water or a hydroxyl group (Stroebel *et al.,* 2003; Kurisu *et al.,* 2003; Vitry *et al.,* 2004; Alric *et al.,* 2005). Covalent binding of heme cofactors to a single cysteine is observed for cytochromes c and c1 in the mitochondria of *Euglena, Trypanosoma*, and *Leishmania* species. These c type cytochromes bind to AXXCH or FXXCH motifs with histidine as an iron ligand (Ikegami *et al.,* 1968; Pettigrew *et al.,* 1974).

Another unconventional heme c binding motif is found at the active site of pentaheme nitrite reductase NrfA from *Wolinella succinogenes*. This consists of a CXXCK pentapeptide motif where the c type heme cofactor attaches to the two cysteines. The lysine serves as the proximal axial ligand to iron with a distal histidine completing the cofactor (Einsle *et al.,* 1999; Lukat *et al.,* 2008). Longer forms of the heme attachment motif also have been identified where there are greater numbers of amino acids between the two cysteines that form thioether bonds to the protoporphyrin ring. A C-XXX-CH motif has been found in a diheme cytochrome c_3 as well as a diheme cytochrome $c_{552.}$ Additionally a C-XXXX-CH motif is found in the tetraheme cytochrome $c_{3.}$ All three proteins originate from *Pseudomonas stutzeri* (Jungst *et al.,* 1991). Most impressively, a C-{X_{15}}-CH c type heme attachment motif has been found in the *Wolinella succinogenes* MccA protein (Hartshorne *et al.,* 2007). All these c type cytochromes incorporate heme cofactors in order to gain the ability to undergo redox reactions. This is because the function of heme c is to stably

accept and donate electrons, which determines the thermodynamics of the electron transfer reaction and plays a role in determining electron transfer kinetics (Marcus & Amos, 1985).

C type heme cofactors are useful because their redox potentials are extremely dependent on the redox Bohr effect. Consequently, they have a malleable redox midpoint potential dependent on the environment surrounding the cofactor, which is itself largely determined by amino acid tertiary structure. The range of c type heme reduction potentials found in nature is broad, spanning well over 1 V. This is a significantly larger range of reduction potentials than achieved by heme b containing cytochromes, when proteins with the same heme axial ligation are compared, as the identity of the axial ligands is an important determinant of potential. This goes some way to show why organisms invest more energy into making c type cytochromes (Raphael & Gray, 1991).

Cytochrome export via the Sec Pathway

There are three main systems by which organisms make c type cytochromes. System I, also known as the cytochrome c maturation (Ccm) process,is employed in some protozoan mitochondria, α and γ proteobacteria (Thöny-Meyer, 1997; Thöny-Meyer, 2000). The Ccm system is employed by *S. oneidensis* to produce the Mtr proteins for DMR. System II, also known as the cytochrome c synthesis (Ccs) process, is found in Gram-positive bacteria, cyanobacteria, chloroplasts of plants and algae, and some β-, δ- and ε type proteobacteria (Kranz *et al.,* 1998). System III, also called the cytochrome c heme lyase (CCHL) process, occurs in the mitochondria of fungi, invertebrates, and vertebrates.

System I for cytochrome c maturation consists of nine main proteins CcmABCDEFGHI; as well as a number of accessory proteins. This Ccm operon has been well studied (Mori & Ito 2001). When expressing γ proteobacteria cytochromes in an exogenous system for purification the standard laboratory *E coli* is often used (as in this study). The expression host is transformed with two plasmids: one with the cytochrome sequence and another (under separate control) with the CcmABCDEFGHI genes. The expression of these genes allows the production of fully functioning cytochromes, such as the Mtr proteins from *S. oneidensis.*

In general, the cytochrome c gene is first expressed as a pre-apoprotein. This means that the amino acid sequence has a N-terminal signal peptide that is recognized by the

secretory (Sec) pathway. This causes it to be transported across the inner cytoplasmic membrane and into the periplasm (Thöny-Meyer & Kunzler, 1997). Leader peptidases cleave the signal peptide to leave the apoprotein. The Sec pathway is therefore essential to the maturation of cytochromes as the pathway relies on a set of proteins termed SecABYEGDF, (Mori & Ito, 2001).

Using *Escherichia coli* as an example, the signal recognition particle (SRP), which is a protein RNA complex, binds to the signal sequence of exported pre-apoprotein cytochromes and targets them to the membrane. In *E. coli* the SRP is composed of the Ffh protein and 4.5S RNA. The protein FtsY is thought to be the SRP receptor on the inside of the inner membrane, and it is the specificity of the SRP for FtsY that enables accurate cytochrome Sec export (Dalbey & Kuhn, 2000). A hydrophobic core of ten or more residues generally characterizes signal sequences in Sec precursor proteins, such as cytochrome c proteins. A positively charged region at the amino terminus and a hydrophilic region at the carboxy-terminus flank this hydrophobic core. The hydrophilic region contains a consensus sequence for cleavage by the leader peptidase in the Sec apparatus (Dalbey & Kuhn 2000). Although these export sequences are required for the initiation of translocation, their cleavage is not essential for this process. An inner membrane associated cytochrome (such as, but not specifically including, CymA) can have a lipid anchor. This anchor can be formed from a signal-sequence element missing the peptidase cleavage site. Once the C terminus of the protein is exported, the N terminal signal sequence is released from the Sec machinery and becomes embedded in the inner membrane. The exported protein still assumes an N terminus in and C terminus out transmembrane orientation (Kihara & Ito, 1998). Additionally, the Sec accessory protein YidC has been shown to be involved in this process (Urbanus *et al.,* 2001; Van der Laan *et al.,* 2001). SecB is a dedicated chaperone to proteins that have a signal export sequence.

The Sec pathway, unlike the Tat pathway (which can export fully folded proteins), is unable to handle tightly folded proteins, so the chaperone prevents the pre-apo-cytochrome from forming secondary structures that would stop its export. SecA is an ATPase that uses ATP hydrolysis to energetically drive protein movement into and across the inner membrane. SecY, SecE and SecG form a hetero-trimeric complex in the inner membrane, which they span with alpha helices ten, three and two times respectively (Mori & Ito, 2001). SecYEG forms a channel or pore for the exported polypeptide to move through when passing out of the cytoplasm. In combination SecA (the ATPase) and SecYEG

(the pore) are known as the translocase and are the primary components of the translocation machinery. SecD and SecF are also required for efficient protein export when in vivo. SecA, in combination with SecYEG and an ATP source, has been shown to enable protein export from liposomes (Mori & Ito, 2001).

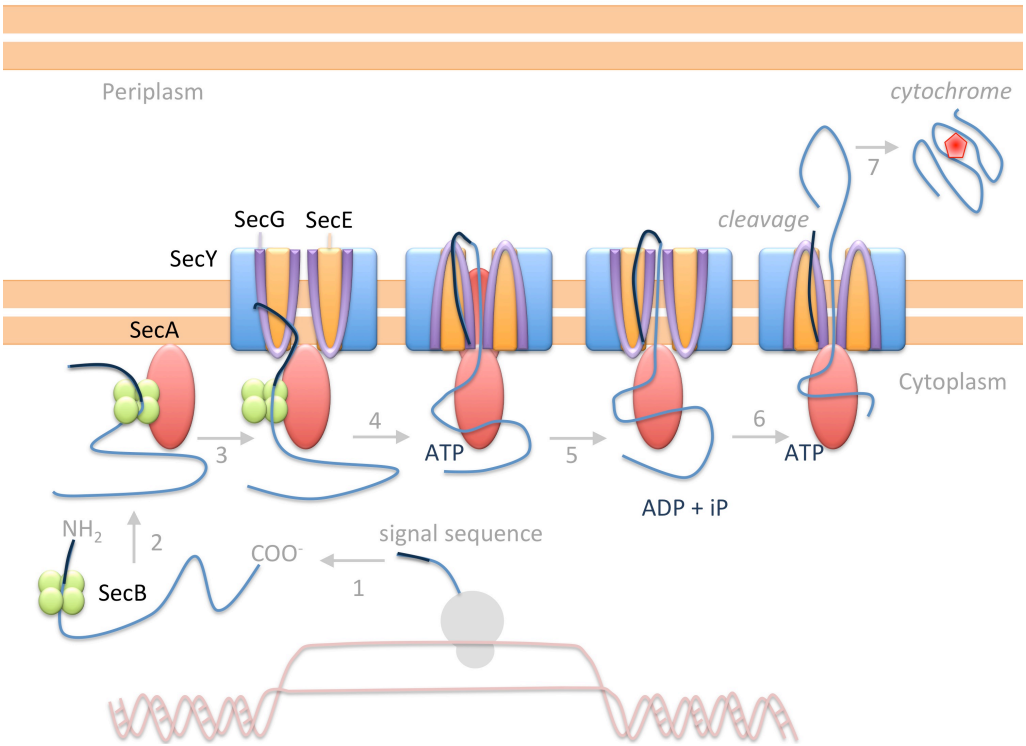

Figure 1. 6 A cartoon schematic of the Sec dependant export of proteins into the periplasm.

Heme cofactor synthesis

Once the cytochromes are exported through the inner membrane by the Sec apparatus, they need to have the c type heme cofactors incorporated to become functional. Heme is synthesized in the cytoplasm and can be divided into three parts: the formation of the precursor molecule 5-aminolevulinic acid (ALA), the formation of the cyclic tetrapyrrole uroporphyrinogen III, and the conversion of uroporphyrinogen III into heme. The canonical pathway is briefly described below, however variations occur in some bacteria and the archaea (Ishida *et al.,* 1998; Buchenau *et al.,* 2006; Lobo *et al.,* 2009).

The formation of (ALA) is important for the cell, as it is the common precursor for all naturally occurring tetrapyrroles. This can occur through ALA synthase combining succinyl CoA and glycine or through glutamyl-tRNA reduction (by glutamyl-tRNA reductase) to glutamate-1-semialdehyde, and then the swapping of the amine and aldehyde groups (by glutamate-1-semialdehyde mutase) (Layer *et al.,* 2010). Two ALA molecules are condensed to the pyrrole porphobilinogen (PBG) through the action of PGB synthase. Four PBG molecules are then oligomerised (by PGB deaminase) to form a linear tetrapyrrole intermediate called pre-uroporphyrinogen (1-hydroxymethylbilane). This linear molecule is then circularised (by uroporphyrinogen III synthase) to form a cyclic tetra-pyrrole intermediate called uroporphyrinogen III (UROGEN). The side chains of the macrocycular UROGEN is then modified (by UROGEN decarboxylase and then a COPPROGEN oxidase or hydrogenase), resulting in the intermediates coproporphyrinogen III (COPROGEN) and protoporphyrinogen IX (PROTOGEN). The PROTGEN ring system is then aromatized (PROTOGEN oxidases) forming protoporphyrin IX (PROTO). Finally, iron is inserted to yield heme through a ferrochelatase. (Heinemann *et al.,* 2008; Layer *et al.,* 2010). Heme created by this biochemical process is then transferred out of the cytoplasm and into the periplasm, joining the translocated apo-cytochrome. This is completed though an, as of yet, unknown mechanism (Bowman & Bren 2009).

To form functioning c type cytochromes, the heme cofactors need to be localized and then ligated to the apo-cytochrome polypeptide. This needs to be completed in a way that results in the correct orientation of the heme within the tertiary structure of the protein and with the correct stereochemistry of the thioether sulphurs.

Heme cofactor insertion into apo-cytochromes

The previously mentioned CcmABCDEFGH cassette produced proteins that enabled the accurate insertion of heme cofactors into cytochromes. The functions of some, but not all, of the Ccm gene products have been characterized.

CcmAB is similar to an ATP-dependent ABC-type transporter, with CcmA known to hydrolyze ATP (Keightley *et al.,* 1998) The specific substrate transported by CcmAB has not yet been identified, and it is not thought to be heme (Bowman & Bren 2009). CcmE has been identified as a heme chaperone requiring the ATP hydrolysis activity of CcmAB (Christensen *et al.,* 2007; Schulz *et al.,* 1998). CcmC is required for delivery of heme to

CcmE (Schulz *et al.,* 1999), and together they are involved in heme delivery to the cytochrome c heme lyase complex consisting of CcmFH. CcmE forms transient covalent bonds to the heme cofactor, however the precise details of the heme transfer mechanism remain unclear (Schulz *et al.,* 1998; Uchida *et al.,* 2004; García-Rubio *et al.,* 2007) Holo-CcmE is thought to be the substrate for CcmF in the CcmFH complex. CcmF is thought to transfer heme to apocytochrome and CcmH is proposed to facilitate thioether bond formation (Ren *et al.,* 2002). CcmD is a small polypeptide that forms a complex with CcmABC. It was found to be required for the release of holo-CcmE from CcmABCD (Richard-Fogal *et al.,* 2008). CcmG is a thioredoxin-like protein (Edeling *et al.,* 2002). As such, its function is likely to be involved in disulphide bond reduction as well as isomerization reactions in the formation of the cytochrome. In addition to the heme maturation specific CcmABCDEFGH proteins, DsbABD proteins are also thought to play a role. DsbA catalyzes the formation of disulphide bonds in the periplasm, and DsbB then releases electrons obtained from DsbA through this process to the respiratory system via the quinol pool. Both these proteins have been reported to be important for the formation of a disulphide bond in the apo-cytochrome prior to cytochrome c attachment.

The integral membrane protein DsbD supplies CcmGH with the necessary electrons for apo-cytochrome reduction. It does this through taking electrons from cytoplasmic thioredoxins and transferring them into the periplasm. This pathway is represented in cartoon form in Figure 1.7.

The Ccm cytochrome maturation system is not compatible with substitutions for the histidine ligand in the C-XX-CH motif (Allen *et al.,* 2005). Therefore, alternative systems are required for unusual cytochromes c, which include the previously mentioned B6f, NrfA and MccA proteins. A set of proteins called CCB proteins have been identified in plants that perform the biogenesis of the (heme b axially coordinated and singling cysteine bound) high-spin ci' heme of cytochrome b6f (Kuras *et al.,* 2007). Likewise, unique maturation proteins are found in *W succinogenes* for the attachment of the heme group to the CXXCK motif in NrfA (Eaves *et al.,* 1998) as well as the CcsA1 protein that is proposed to be dedicated to attachment of heme to the two cysteine residues in the C-{X_{15}}-CH motif in MccA (Hartshorne *et al.,* 2007).

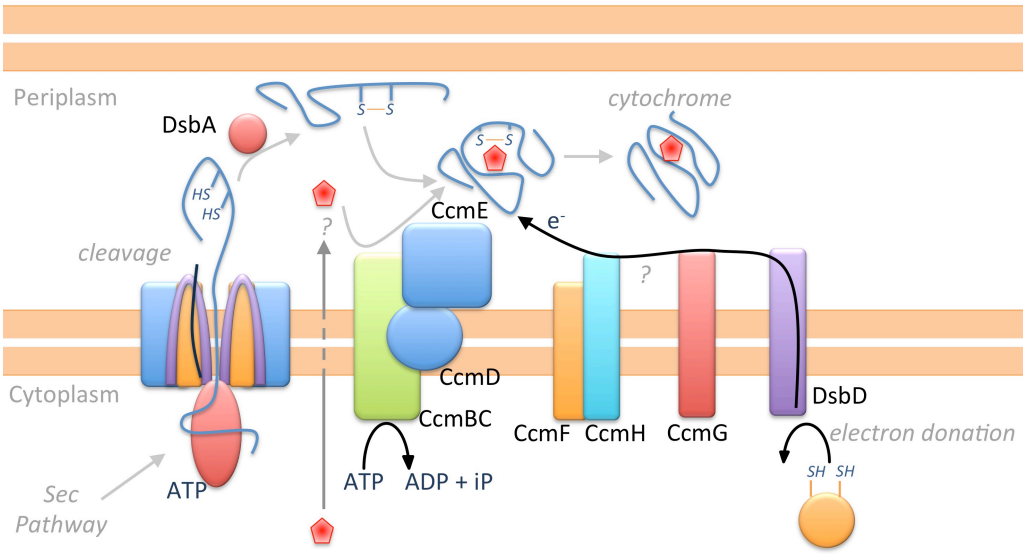

Figure 1. 7 Cartoon schematic of the insertion of heme into apo-cytochrome exported intot the periplasm from Sec dependant pathways. Adapted and based on Figures from the website of Prof Nick Le Brun.

The specific cytochromes that enable *S. oneidensis* to respire via DMR are MtrA and MtrC. These work in combination with the transmembrane β barrel MtrB. These three proteins form a hetrotrimeric complex and cooperatively facilitate DMR by transporting electrons across the outer membrane.

1.06 MtrCAB

The MtrCAB complex was purified as a single unit in (Ross *et al.,* 2007). During the purification process, they found OmcA was easily purified however MtrC was very difficult to stably purify and separate from MtrB. Using antibodies raised against MtrC, MtrA, and MtrB, the authors discovered that these three proteins co-purified as a complex. The authors then completed analytical ultracentrifugation on the solubilized MtrCAB complex. These results yielded molecular masses of 198 and 197 kDa for the 2.5 μM and 0.25 μM MtrCAB samples tested. These results indicate that MtrCAB is very tightly bound together. In (Hartshorne *et al.,* 2009) it was found that MtrB was not successfully expressed in *ΔmtrA* strains.

In Ross *et al.,* (2007) the reactivity of the MtrCAB complex was demonstrated by spectroscopic studies. Purified MtrCAB was reduced with incremental addition of the strong reductant sodium dithionite. These additions were conducted until the MtrCAB complex was fully reduced, which was detected by monitoring the heme UV-vis absorbance peak at 550 nm. Reduced MtrCAB was found to be stable for over 40 min in an anaerobic glovebox. The authors then added different iron minerals to different aliquots of the reduced MtrCAB and observed that it was rapidly oxidised by aqueous ferric citrate in 15 seconds. Solid phase six-line ferrihydrite (a semi-crystalline nano-particle of ferrihydrite molecules that produce six x-ray diffraction lines) took a much slower 4 minutes, and the minerals goethite and birnessite took 10 and 35 minutes respectively. The rates of reduction for the iron oxide minerals were probably too slow to support effective DMR and it suggests that MtrCAB is not fully oxidised whilst functioning as an electron transporter. In Ross *et al.,* (2011) the authors attached *S. oneidensis* to an electrode and used electron transport through MtrCAB to catalyze the two-electron reduction of fumarate to succinate via MtrCAB, driving a fumarate reductase through passing it electrons. This showed how MtrCAB could be used for electron movement in the opposite direction to DMR.

Work by Hartshorne *et al.,* (2009) and White *et al.,* (2013) showed that MtrCAB could be incorporated into liposome structures, together making proteoliposomes. The MtrCAB proteins were uniformly inserted with MtrC on the outside of proteoliposome. The proteoliposomes were filled with the redox indicator methyl viologen. The reduction status of this encapsulated methyl viologen could be measured through the magnitude of

the UV-vis absorbance band at 603 nm, which is indicative of reduced methyl viologen. White *et al* were able to show the reduction of methyl viologen, over time, through MtrCAB complexes in proteoliposomes, as well as the re-oxidation of this reduced encapsulated methyl viologen through the addition of chemical iron oxidants and iron minerals used by *S. onedensis* for DMR. The biochemistry of MtrCAB depends on the functioning of the individual components.

1.07 MtrA

MtrA is a 333 amino acid protein that contains ten C-XX-CH motifs, which are the canonical binding sequences for c-type heme cofactors. MtrA has been noted to bear some sequence similarity to the penta-heme NrfB, with suggestions that it evolved from a duplication event (Pitts *et al.,* 2003; Clarke *et al.,* 2007; Ross *et al.,* 2007).

Phylogenetic analysis of the amino acid sequence of MtrA shows homologues in the 19 sequenced *Shewanella* strains (Fredrickson *et al.,* 2008). There are also examples of paralogues in the following strains: MtrD in the *S. oneidensis* MR-1 genome, MtoA from *S. lithotrophicus* as well as PioA of *R. palustris* TIE-1. Like the MtoAB system for iron oxidation, the *pioABC* complex is also specifically required for phototrophic Fe(II) oxidation (Jiao & Newman 2007) and thus bears functional similarities with both MtrCAB and MtoAB.

Jiao and Newman, (2007) demonstrated that MtrA from *S. oneidensis* MR-1 was 42–44% identical to MtoA from *Sideroxydans lithrophicus*, with PioA from *R. palustris* having 40% identity and 55% similarity over 285 amino acids to MtrA. MtoA was found to be 39% identical to PioA. They noted that MtoA lacked an N-terminal extension compared to the MtrA sequences analysed. They suggested that this similarity was mostly due to the highly conserved nature of the C-XX-CH heme binding sites that are essential for the correct functioning of the proteins. These proteins are clearly evolved to contain multiple hemes that are maintained through evolution.

Other multiheme cytochromes thought to produce nanowires like MtrA and MtrC include the *Geobacter* GSU1996, GSU0592, GSU2210 and supposed evolutionary ancestor of these *Geobacter* proteins PpcA C7, (Londer *et al.,* 2006; Pokkuluri *et al.,* 2008; Pokkuluri *et al.,* 2010; Pokkuluri *et al.,* 2011). GSU1996 and GSU0592 are dodecaheme proteins, whereas

GSU 2210 contains twenty-seven hemes. The PpcA protein contains a C7 motif that is duplicated within the GSU1996, GSU0592, GSU2210 proteins. Using CLUSTAL_OMEGA a phylogenetic tree can be constructed showing how related these proteins are to each other Figure 1.8. Due to the highly conserved C-XX-CH motif, the proteins all bear resemblance to each other. By compiling a multiple sequence alignment, we can demonstrate how these c-heme binding regions are conserved within these proteins, Figure 1.9. Thus the evolutionary ancestor of MtrA could alternatively be a protein such as STC, which has high degrees of similarity to NfrB.

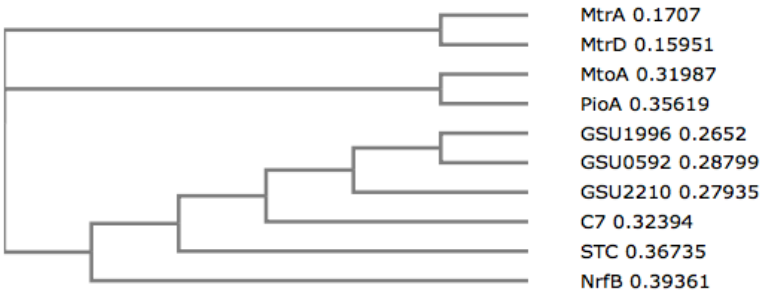

Figure 1. 8 A Phylogram comparing the amino acid sequences of MtrA, MtrD MtoD PioA, GSU1996 GSU0592 GSU2210 PpcA NrfB and STC.

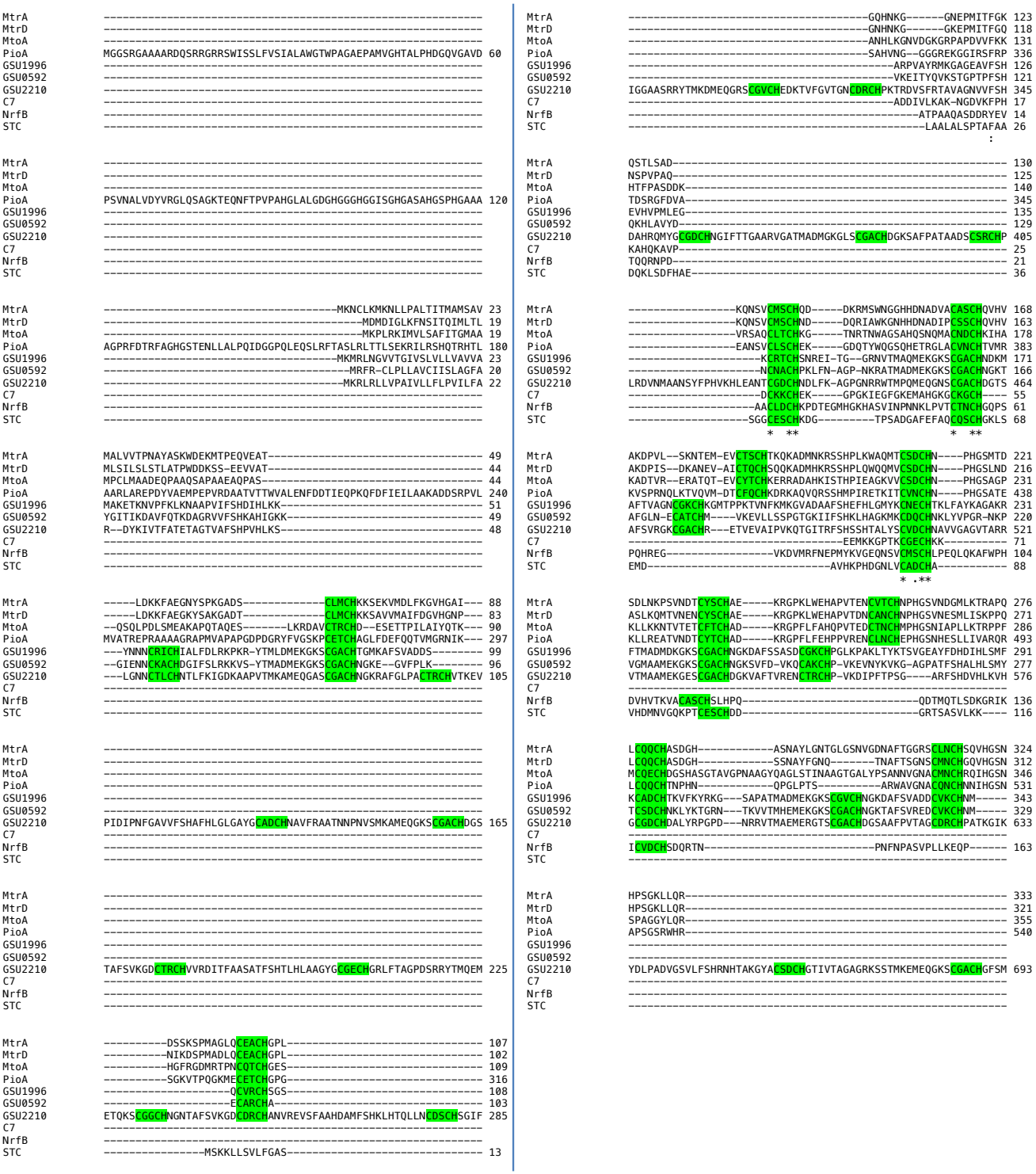

Figure 1. 9 Multiple amino acid sequence alignment of MtrA, MtrD, MtoD, PioA, GSU1996 GSU0592, GSU2210, PpcA (C7), NrfB and STC.

When attempting to produce crystals of GSU1996, the authors also produced two truncations of the N and C terminal halves, each containing six heme cofactors (Pokkuluri *et al.,* 2011). This enhanced the possibility of producing X-ray crystal structures of GSU1996, as each half may have differing properties and thus crystalize in different conditions – enhancing the likelihood of successful experiments. Producing N and C terminal truncations is useful for examining the biochemical characteristics of different parts of multi-heme cytochromes, and was used in this thesis to examining MtrA.

As has been shown there are large numbers of multiheame cytochromes in most DMR bacteria. A hypothesis proposed for the presence of large numbers of multiheme cytochromes in *Geobacter sulphurreducens* is that these molecules may serve as electron-storage sinks or capacitors (Esteve-Núñez *et al.,* 2008). As each heme can carry a single electron, multiheme proteins could therefore store many electrons. For example, STC could store up to four electrons and MtrA or MtrC up to ten. This ability to store electrons would allow the organism to survive in the absence of immediately available external electron acceptors, as well as possibly provide signals for responses to alleviate the situation. This would allow the organism to continuously generate energy and provide time for the organism to adapt or find new environments.

MtrA Biochemistry

The properties of isolated MtrA were first described by Pitts *et al.,* (2003). Purified MtrA was predicted to be around 30 kDa based on SDS PAGE. MALDI-TOF mass spectrometry confirmed the mass to be 38,584 kDa. Using the bioinformatics program SignalP the signal sequence of MtrA was predicted start after the 34th amino acid. The authors also performed optical redox titrations, measuring the absorbance at 552 nm over a range of potentials. Because the height of the 552 nm peak was proportional to the reduction state of the MtrA solution, the midpoint potential could be calculated using a Nernst derived line of best fit. The midpoint potentials of the distinct groups of hemes were calculated to be-375 mV and -200 mV, with a 30:70 ratio of absorbance change for each respective group. These redox potentials overlap with the more negative end of the potential range of MtrCAB published by Hartshorne *et al*., 2009 which was -400 mV to 0 mV determined by protein film voltammetry (PFV) methods. Magnetic circular dichroism of MtrA showed results consistent with ferric low spin hemes, typical of bis-his-coordinated cytochromes. Electron paramagnetic resonance (EPR) experiments on MtrA revealed g-values consistent with bis-histidine ligated hemes, in which the histidine imidazole ring planes

are approximately parallel to each other. Spin integration of the signals revealed that two major low spin species each account for 40% of the heme population. Approximately 20% of the heme population is unaccounted for by the integrations of the low spin features. The authors theorise that this population of heme may account for a pair of spin-coupled hemes, which could be EPR silent. Finally the authors performed experiments to investigate the catalytic properties of MtrA. They added different oxidised iron compounds to reduced MtrA and measured the changes in the UV-vis absorbance spectra of the solution. All of the ferrous hemes in MtrA were found to be rapidly oxidised upon addition of Fe(III) NTA (Ferric nitrilotriacetate), Fe(III) EDTA (Ferric Ethylenediaminetetraacetic acid) or Fe(III) Maltol compounds. The addition of fumarate did not result in re-oxidation, whereas the addition of nitrite and nitrate resulted in a slow re-oxidation that was 1–2 orders of magnitude slower than that of Fe(III) EDTA (for which a rate of approximately 5 nmol of electrons/s was reported). They also report that the CymA homologue NapC from *E. coli* can reduce exogenously expressed MtrA from *S. oneidensis* using electrons from the *E. coli* respiratory system.

The work by Pitts *et al.,* (2003) was extended by Firer-Sherwood *et al.,* (2008). In this publication the authors conduct PFV on MtrA as well as MtrC, OmcA STC and CymA. During PFV a protein film is attached to a working electrode. When the working electrode is incorporated into an electrochemical cell with counter and reference electrodes, the current through the working electrode can be measured at different specific voltages. The authors produced an apparent midpoint potential for MtrA, composed of the contributions from all of the ten hemes. This was found to be -100 mV. Pitts' work was then extended even further by Hartshorne *et al.,* (2009), who again conducted PFV on MtrA. In this publication, the authors repeated the PFV experiments in different buffer conditions. They then compared the redox window of MtrA calculated from PFV with two optical redox titration data sets (like those published in (Pitts *et al.,* 2003). Hartshorne *et al.,* (2009) found very similar apparent midpoint potentials to Firer-Sherwood *et al.,* (2008) and concluded that the active redox window of MtrA was from 0 through to approximately -400 mV, the same as the potential range they calculated for the entire MtrCAB window. They noted that because the spectroscopic changes for a mono-heme cytochrome undergoing a single electron transformation typically span approximately 200 mV, which is the potential range spanned by redox transitions for multiheme cytochromes, the active redox range for these cytochromes will contain contributions from multiple hemes with overlapping potentials (Hartshorne *et al.,* 2009).

Biophysics of MtrA

As well as biochemical investigations into MtrA, biophysical techniques such as AUC and small angle X-ray scattering have been used to gain some insight into the shape of MtrA. In Firer-Sherwood *et al.,* (2011) the authors use both analytical ultracentrifugation (AUC) and small angle X-ray scattering (SAXS) to produce a shape reconstruction of MtrA in free solution. Attempts at crystallization of MtrA have not, at the time of writing, yielded any results, thus alternative solution based techniques were employed for model building. The authors show through AUC experiments that the sample of MtrA they were using was sedimenting with an apparent molecular mass of 42.8 kDa in monomeric fashion, with DCDT+ c(s) analysis which giving a single dominant S_{w20} peak of 3 S. The DCDT+ method (or time derivative method) calculates g(S) differential sedimentation profiles by subtracting consecutive scan pairs from each other and mapping the resulting difference curves to the S domain thereby obtaining a DCDT curve. The advantages of this method are in its ability to negate and remove time invariant noise in absorbance or scattering caused by such factors as scratches or dirt in the windows of the AUC cuvettes, as well as refractive index hetereogeneities. For SAXS experiments to yield useful results samples must be non-aggregating and mono-disperse whilst at high concentration (typically 1- 10 mg/mL) and in the x-ray beam-line. These AUC results suggested that at 0.5 mg/mL MtrA was soluble and non-aggregating whilst being ultra centrifuged. DCDT+ analysis of the data reported similar findings with an apparent molecular weight of 35.6 to 36.9 kDa and a sedimentation coefficient of 3.4 S. AUC results of this type usually allow for the prediction of an axial ratio (through the use of a program such as ULTRASCAN). The data suggests that MtrA is extended in one axis when it is modeled as a cylinder or prolate spheroid, although the authors do not publish their results for this. The authors then go on to examine MtrA in solution using SAXS. They state that samples over a concentration range of 0.5 – 4 mg/mL produced non-aggregating (well behaved) scattering profiles. Using these scattering profiles the authors conducted shape reconstructions (using the 3 mg/mL scattering profile). These reconstructions produced a ~100 x 40 x 30 Å prolate shape. The reconstruction had one end of its major axis thicker than the other and in this thicker end there was a concave indent giving the reconstruction a spoon or paddle like shape.

1.08 Outer membrane cytochromes such as MtrC

MtrC is situated on the outer face of the outer-membrane of *S. oneidensis.* Like MtrA, MtrC is a decaheme cytochrome. It has many homologous proteins including MtrF, OmcA and UndA that are also outer-membrane cytochromes. It is thought that these homologues provide modularity in DMR, with each protein being interchangeable and specially adapted to specific environments. Additionally it is theorized that the numerous outer-membrane proteins of this type could act as an umbrella network of cytochromes making contact with extracellular minerals.

Conserved crystal structures of outer-membrane cytochromes

Crystal structures of soluble versions (truncations without lipid anchor sections) of MtrF have been published as well as structures of UndA, OmcA (Clarke *et al.,* 2011; Edwards *et al.,* 2012; Edwards *et al.,* 2014). The structure of MtrC is in the process of being published, Figure 1.10. In all of these structures, the proteins are globular and reasonably oblate with approximate dimensions of 85 × 70 × 30 Å. Four domains have been recognized. Domains I and III both contain seven antiparallel β-strands folded in an extended Greek key topology that gives the domains a split-barrel tertiary structure. Domains II and IV contain five heme cofactors each packed between alpha helical coils. These four domains come together, with domains II and IV forming a central core where all heme cofactors are in the correct orientation and close enough to enable rapid electron transfer. The hemes form a line from one end to the other of the protein in what has been termed a staggered decaheme cross (Edwards *et al.,* 2012). Domains I and III flank either side of this central heme-containing core. The undecaheme cytochrome UndA follows the same domain pattern and staggered cross heme formation with an additional heme located in the sequence. This additional heme is located between hemes 6 and 8 in UndA's sequence which correspond to hemes 6 and 7 in MtrF. This sequence location places the heme structurally on the outer edge of one of the peripheral 'staggers' of the staggered cross formation (Edwards *et al.,* 2012). Suggestions have been made that these staggered hemes are not necessary for direct electron transport through the central core of MtrF, MtrC OmcA or UndA but instead could be used for transporting electrons to small soluble substrates that bind into the split β barrel domains (Edwards *et al.,* 2012). This could indicate that proteins like MtrC have dual mechanisms of electron transport and add to the complexity of DMR via the MtrCAB system.

Figure 1. 10 The crystal structure of MtrC, adapted from Edwards *et al*, 2015; (publication in press) with the amino acid sequence as a cartoon, with heme cofactors highlighted.

MtrC Biochemistry

Potentiometric titrations of MtrC in (Hartshorne *et al.,* 2009) show that the potentials of the hemes within MtrC cover a wider range than MtrA. This creates a gradient from negative to positive potential up which electrons would have to overcome to get out of the cell and onto extracellular heavy metals during DMR. These potentials were 0 to −0.260 V for solvated MtrC and between −0.044 V and −0.312 V from protein film voltammetry (Hartshorne *et al.,* 2009).

Molecular dynamic simulations have been used to compute heme microscopic redox potentials for MtrF through the construction of a free energy landscape for electron transport (Breuer, Zarzycki, Blumberger, *et al.,* 2012; Breuer, Zarzycki, Shi, *et al.,* 2012). The authors initially found an almost symmetric and flat free-energy profile of heme potentials, with only small differences in the redox potentials of the terminal hemes (which were of slightly higher potential than the inner hemes). However, revisions to the model included some changes that introduced energetically uphill electron transfer during heme to heme electron transport in MtrF DMR function. These results imply that electron transport across MtrF is nearly reversible.

Both Wang *et al.,* (2008) and Ross *et al.,* (2009) characterize the kinetic constants for electron transfer between various forms of soluble iron and OmcA or MtrC. In (Ross *et al.,* 2009) these were measured with a stopped-flow kinetic apparatus. Reaction rates were

obtained by monitoring the change in absorbance of protein at either wavelengths corresponding to the Soret band at 419 nm or the α/β region at 550 nm. The increase in absorbance of both of these regions is associated with the reduction of ferriheme to ferroheme. Rate constants were fitted with a single exponential. The results found that both MtrC and OmcA reacted quicker with some form of soluble iron than others with a preference of EDTA-Fe^{3+} >NTA-Fe^{3+} >Citrate-Fe^{3+} >Goethite. MtrC and OmcA seemed to be able to pass electrons to these different forms of soluble iron at roughly the same rates, with a maximal rate for MtrC being 9.2 x10^5 $M^{-1}s^{-1}$ for EDTA-Fe^{3+} and a slowest rate of 0.0099 $M^{-1}s^{-1}$ for Goethite. OmcA's maximal rate was 3.0 x10^5 $M^{-1}s^{-1}$ for EDTA-Fe^{3+} and it had a slowest rate of 0.019 $M^{-1}s^{-1}$ for Goethite (both for purified MtrC and OmcA). These rates indicate how fast electrons can transition across the free energy landscape described in (Breuer, Zarzycki, Shi, *et al.,* 2012) and indicate that the rate of electron transport for EDTA-Fe^{3+} would likely be able to support DMR respiration. However, an organism would struggle to respire with a rate of reduction found, in this case, for minerals such as Goethite. As Goethite is likely to be used by *S. oneidensis* for DMR in its natural environment, additional factors must intervene to allow it to be used.

1.09 MtrB and outer-membrane pore proteins

Although MtrB is not a cytochrome, it plays an essential role in enabling DMR. Through spanning the impermeable outer membrane, MtrB allows the cytochromes MtrA and MtrC to tunnel electrons to places they would otherwise be shielded from. Unlike the inner membrane of *S. oneidensis,* the outer membrane does not contain within it a quinone pool as an energetic intermediate (or any a α-helical membrane proteins (Wimley, 2003)). Therefore, a pore acting as a bridge across impermeable membranes for soluble proteins is important for efficient DMR. In *Shewanella* strains that have had *mtrB* deleted, DMR ceases (Myers & Myers, 2002). This indicates that it is essential for the observed DMR processes.

The sequence of MtrB has been identified as belonging to the β barrel transmembrane pore super family. In the *S. oneidensis* genome *mtrE* has been identified as a homologue to *mtrB*. MtrE is thought to perform the same function as MtrB, as through forming a complex with MtrD and MtrF, it enables DMR. From the PioABC gene cluster responsible for dissimilatory metal oxidation in *Rhodopseudomonas palustris,* PioB is predicted to be a transmembrane pore. PioB has 21% identity to MtrB and 38% similarity over the 536 amino acids close to the C-terminus of MtrB (Jiao & Newman, 2007). MtoB is also homolgous to MtrB (Liu *et al.,* 2012) as it performs the same function as other pores by creating a gap in the outer membrane in which cytochromes can sit, facilitating electron transfer to externally located heavy metals. These pores are therefore a common feature in DMR.

Structural information of MtrB like outer membrane pores

Approximately 2–3% of the genes in Gram-negative bacteria, such as *S. oneidensis,* encode β-barrels (Wimley, 2003). Despite this, currently there are 91 β barrel outer membrane pore structures published in the protein data bank. This small number of structures is due to the difficulty in forming crystals of membrane proteins.

From the structural data available it can be seen that trans-membrane proteins fold into structures that are roughly cylindrical across the bilayer and only expose predominantly nonpolar side-chains to the membrane (Wimley, 2003). Sequences of 9 -13 non-polar or hydrophobic residues are used for the in-silico recognition of potential trans-membrane proteins. The polar groups of trans-membrane buried sections of amino acid sequence

must form hydrogen bonds (White & Wimley, 1999; Wimley, 2003). Only those that form a trans-membrane β barrel satisfy this. They do this through β strands laterally hydrogen bonding in a circular pattern. These hydrogen bonds between β strands of a β-barrel membrane protein are the dominant structure stabilizing interaction (Bishop *et al.,* 2001). This is because they occur in the nonpolar bilayer milieu. The extensive nonlocal backbone hydrogen bonds between strands also rigidify the core of the barrel structure (Arora *et al.,* 2001). Estimates have calculated the contribution of each hydrogen bond to stabilization to be as high as 0.5 kcal/mol/residue (Wimley *et al.,* 1998; White & Wimley, 1999; Ladokhin & White, 1999). In (Wimley, 2003) the author asserts that due to the scale of amino acids involved in hydrogen bonding where even the smallest β-barrels have at least 80 amino acids in the membrane, the effects are very significant. Therefore, as a result of hydrogen-bonding interactions, β-barrels make very stable structures that do not readily unfold in membranes (Haltia & Freire, 1995; Rosenbusch, 2001).

The formation of outer membrane β barrel pores

Outer membrane β-barrel pores, such as OmpA and PulD, can be formed from spontaneous and cooperative insertion after the amino acid sequence is exported to the periplasm by the Sec machinery. However, this is unlikely to be the major route of outer membrane β barrel pore insertion (Kleinschmidt & Tamm, 2002; Collin *et al.,* 2007).

Most Gram negative bacteria use the β-barrel assembly machinery (BAM) protein complex to achieve bacterial pore insertion (Knowles *et al.,* 2009; Wenz *et al.,* 2014). This is similar, and likely evolutionarily related, to the mitochondrial TOM/SAM proteins. These dedicated molecular machines are the more likely routes for MtrB outer membrane insertion.

To create an outer membrane β barrel pore such as MtrB, a transmembrane polypeptide is first secreted from the cytoplasm, in an unfolded manner, using the Sec apparatus. Following the polypeptide's release into the periplasm, it associates with many periplasmic chaperones, most notably SurA, Skp and DegP. Literature searches have not revealed any findings for a specific signal sequence to target these systems. They presumably bind due to the hydrophobic or non-polar regions that will be inserted into the outer-membrane. These chaperones are thought to form two pathways, the SurA pathway and the Skp–DegP pathway, which transport nascent OMPs across the periplasmic space to the outer membrane and the BAM complex (Rizzitello *et al.,* 2001; Onufryk *et al.,* 2005; Ruiz *et al.,* 2006; Sklar *et al.,* 2007). Through double knock-out

experiments, functional redundancy among the chaperones was revealed. SurA acts in one manner that Sklar *et al.,* (2007) suggest is the pathway responsible for the assembly of most β-barrel outer-membrane pores. Skp and DegP function in a separate pathway, rescuing those outer membrane proteins that have fallen off the normal assembly route for some reason (Rizzitello *et al.,* 2001; Onufryk *et al.,* 2005; Sklar *et al.,* 2007). Interestingly, DegP has also been identified to have protease activity. It was also found to be regulated in a temperature-dependent manner, indicating that the pathway could also be used to limit outer membrane β barrel pore insertion (lipinska *et al.,* 1990; Spiess *et al.,* 1999). These chaperones allow the exported polypeptide to make contact with the BAM machinery, although the fine details of how this is completed have yet to be fully elucidated.

The BAM complex is composed of BamA, BamB, BamC, BamD and BamE (formerly called Omp85/YaeT, YfgL, NlpB, YfiO and SmpA respectively). BamA is the major component of the BAM complex with BamBCDE termed accessory proteins. BamA is reportedly found in all Gram-negative bacteria. Its functioning is reported to be based around a set of five polypeptide transport-associated (POTRA) domains oriented towards the periplasm, as well as a carboxy-terminal β-barrel inserted into the outer membrane (Sanchez-Pulido *et al.,* 2003). When BamA is depleted in *N. meningitides*, unfolded outer membrane proteins were observed to accumulate as aggregates in the periplasm (Voulhoux *et al.,* 2003). The exact role of BamA in outer membrane pore formation at the time of writing remains unclear. However, there is evidence that the POTRA domains might have a role in binding outer membrane polypeptide chains prior to folding. BamA is thought to recognise a specific recognition motif encoded in the C-terminal β-strand of exported pores (Sanchez-Pulido *et al.,* 2003; Robert *et al.,* 2006).

The BAM accessory proteins BamBCDE associate with BamA. The roles of these proteins also currently remain unknown. However there are theories that they could have chaperone functionality or could act as docking sites for periplasmic chaperones that carry nascent outer membrane pore polypeptides. Both of these putative functions help to transfer the exported polypeptide to the BAM complex (Onufryk *et al.,* 2005).

The BAM accessory proteins, BamBCDE, have been shown to form a tight complex with *E. coli* BamA based on their co-purification (Wu *et al.,* 2005; Sklar *et al.,* 2007). The proteins BamABCD are reported to exist in equal stoichiometry (Stenberg *et al.,* 2005), however the

relative numbers of BamE in the BAM complex are still unclear. Once the unfolded polypeptide destined to be a β barrel outer membrane pore has reached the BAM complex, it undergoes a process that allows it to fold correctly and then insert into the lipid bilayer. Several mechanisms have been suggested as to how the BAM complex achieves this (Knowles *et al.,* 2009).

Firstly, there is a pore-folding model. In this, the BAM complex could function as a single monomeric complex. The β-barrel pore formed by BamA incorporates the nascent exported polypeptide, which is guided to it through periplasmic components of the BAM complex acting as targets for the reciprocal chaperones. These periplasmic parts of the BAM complex then thread the nascent polypeptide into the BamA barrel core, where it is folded and then released. The β barrel section of BamA has some homologous proteins that collectively exhibit pore activity that is responsive to substrate binding (Ertel *et al.,* 2005; Robert *et al.,* 2006; Méli *et al.,* 2006). The hydrogen bonding that completes the tertiary structure of BamA's β barrel pore is very dense, so it would be difficult to break. Consequently, releasing the then folded β-barrel membrane protein into the lipid bilayer would be energetically difficult.

Secondly, instead of the nascent exported polypeptide inserting into the pore of a monomeric BamA protein, a central pore is formed by the BAM complex that is lined by BamA β-barrels, this is the space where nascent exported polypeptides are transported to, to allow folding into β barrel proteins, Figure 1.11. This BAM-complex based model overcomes the issue in the first model where potentially high energies are required to "open" the β barrel section of a monomeric BamA, as release of the folded β barrel protein into the membrane could occur due to the opening of the BAM oligomeric assembly. In the complex pore-folding model, the periplasmic components of the BAM complex would help fold and deposit the protein directly into the membrane.

In the third proposed model, the BamA structure provides a surface onto which the exported polypeptide interacts and then folds into the membrane. This barrel-folding model does not require nascent polypeptide to be exported inside a pore. Together with the complex pore-folding model, this model is supported by conductance studies that detected a closed, low-conductance BAM channel that is not widened by substrate binding (Schleiff & Soll, 2005).

Finally a model where DegP acts as a chaperone of fully folded B-barrel membrane proteins rather than nascent polypeptides is being developed. Homo-trimeric and homo-hexameric DegP structures have been modelled by both electron microscopy and X-ray crystallography (Krojer, Pangerl, *et al.,* 2008; Krojer, Sawa, *et al.,* 2008; Jiang *et al.,* 2008). This was the first indication that DegP monomers have the ability to form larger complex structures. Further to this, DegP has been shown to form large cage-like complexes from 12 or 24 DegP units. These large DegP complexes have been shown to co-purify with known β barrel outer membrane proteins (Krojer, Pangerl, *et al.,* 2008). Electron microscopy of the dodecameric DegP complex showed a folded β barrel outer membrane protein in the core of the DegP cage. Thus, in this model, the nascent polypeptide chain binds to DegP, which oligomerises around it forming a cage in which it can fold. This complex then interacts with the BAM complex, leading to its insertion into the outer membrane lipid bilayer.

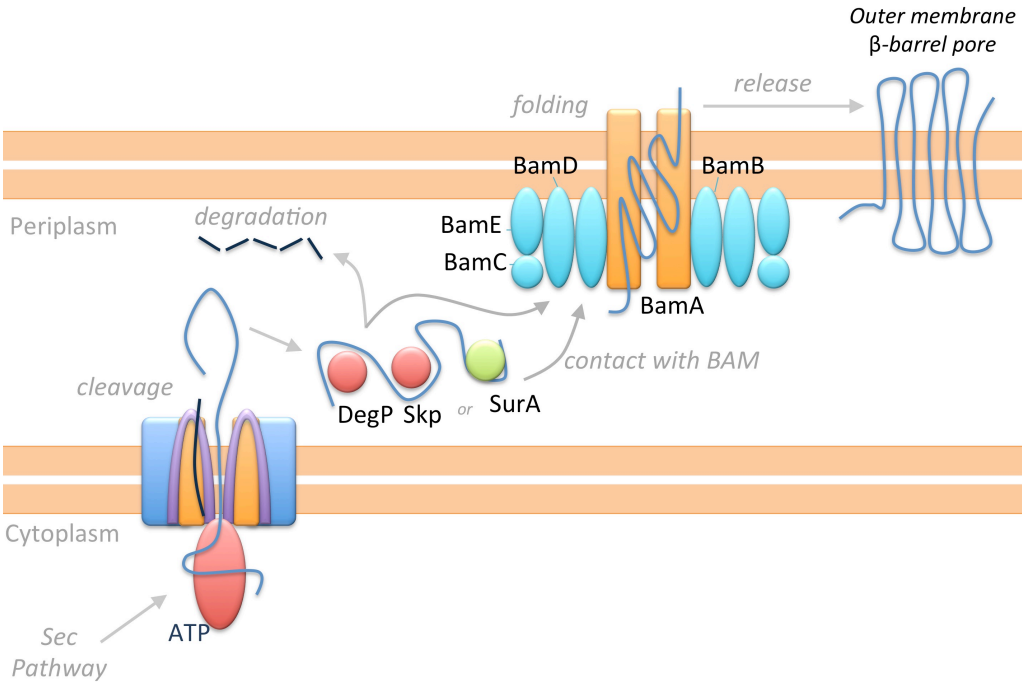

Figure 1.11 a cartoon representation of the BAM pathway based on the cartoon from Knowles *et al* 2009.

Through the action of the BAM complex and periplasmic chaperones, outer-membrane complexes such as MtrB are formed, which enables proteins such as MtrA and MtrC to function as electron transporters.

1.10 Thesis aims

This thesis aims to increase the understanding of the form and functioning of deca-heme cytochrome MtrA and the MtrCAB outer membrane complex, which are important in the dissimilatory metal respiration process of *Shewanella oneidensis*.

Chapter 3 investigates the shape of MtrA and the midpoint potentials of its ten heme co-factors. Small angle x-ray scattering and analytical ultracentrifugation were used to study its structure and to simulate 3D bead models of MtrA, the N-terminal truncated half of MtrA and the evolutionarily related small tetraheme cytochrome (STC). The mid point potentials (E_m) of the full-length MtrA protein, as well as the N and C terminal truncated halves of MtrA were investigated by soluble redox titrations and optically transparent tin electrode experiments. This characterization of MtrA gave insight into the role it plays within the MtrCAB complex.

Chapter 4 investigates the kinetics of electron transport through MtrCAB. MtrCAB was incorporated into proteoliposomes containing different redox indicators. The redox indicator methyl viologen and both the periplasmic cytochrome shuttles cytochrome c and STC were used to create artificial periplasmic analogues. The reduction and oxidation of proteoliposomes were described and a model developed for the electron transfer between periplasmic cytochromes and the outer membrane MtrCAB complex.

Chapter 5 investigates the shape of the MtrCAB complex using small angle neutron techniques (SANS). The shape of MtrB was modeled *in silico* and the shape of MtrC was described through the use of SANS. Building on this, the shape of the MtrCAB complex, both with and without scattering contributions from lipids bound to MtrB, was investigated through both SANS and AUC techniques. A theory of how MtrCAB functions within a periplasm environment was then developed through these models.

Chapter 6 goes on to briefly discuss the results from Chapters 3, 4 and 5 and gives a broader perspective of their impact. Chapter 6 investigates how this study contributes to the knowledge of the structure and function of MtrA and MtrCAB within the dissimilatory bacterial respiratory processes.

1.11 Bibilography

Aklujkar, M. *et al.,* 2009. The genome sequence of Geobacter metallireducens: features of metabolism, physiology and regulation common and dissimilar to Geobacter sulfurreducens. *BMC microbiology*, 9, pp.109.

Arnold & Hoffmann,1986. Inhibitor Studies of Dissimilative Fe (III) Reduction by Pseudomonas sp . Strain 200 (“ Pseudomonas ferrireductans ”). *Applied and Environmental Microbiology*, 52: 2, Pp. 281-289

Allen, J.W.A., Leach, N. & Ferguson, S.J., 2005. The histidine of the c -type cytochrome CXXCH heme-binding motif is essential for heme attachment by the Escherichia coli cytochrome c maturation (Ccm) apparatus. *Biochemical Journal*, 592, pp.587–592.

Alric, J. et al., 2005. Spectral and redox characterization of the heme ci of the cytochrome b6f complex. *Proceedings of the National Academy of Sciences of the United States of America*, 102, pp.15860–15865.

Amrani, A. *et al.,* 2014. Transcriptomics reveal several gene expression patterns in the piezophile Desulfovibrio hydrothermalis in response to hydrostatic pressure. *PloS one*, 9(9), p.e106831.

Arora, A. *et al.,* 2001. Structure of outer membrane protein A transmembrane domain by NMR spectroscopy. *Nature Structural Biology*, 8(4), pp.334–8.

Baymann, F. *et al.,* 2003. The redox protein construction kit: pre-last universal common ancestor evolution of energy-conserving enzymes. *Philosophical transactions of the Royal Society of London. Series B, Biological sciences*, 358(1429), pp.267–74.

Berks, B. C., Richardson, D. J., Reilly, A., Willis, A. C. & Ferguson, S. J., 1995. The napEDABC gene cluster encoding the peri- plasmic nitrate reductase system of Thiosphaera pantotropha. *Biochemistry Journal*, 309, 983–992.

Bishop, C.M., Walkenhorst, W.F. & Wimley, W.C., 2001. Folding of β-sheets in membranes: specificity and promiscuity in peptide model systems. *Journal of molecular biology*, 309, pp.975–988.

Boukhalfa, H. *et al.,* 2007. Plutonium(IV) reduction by the metal-reducing bacteria Geobacter metallireducens GS15 and Shewanella oneidensis MR1. *Applied and Environmental Microbiology*, 73(18), pp.5897–903.

Bowman, S.E.J. & Bren, K.L., 2009. The Chemistry and Biochemistry of Heme c: Functional Bases for Covalent Attachment. *Natural Product Report*, 25(6), pp.1118–1130.

Breuer, M., Zarzycki, P., Shi, L., *et al.,* 2012. Molecular structure and free energy landscape for electron transport in the decaheme cytochrome MtrF. *Biochemical Society Transactions*, 40, pp.1198–203.

Breuer, M., Zarzycki, P., Blumberger, J., *et al.,* 2012. Thermodynamics of electron flow in the bacterial deca-heme cytochrome MtrF. *Journal of the American Chemical Society*, 134, pp.9868–9871.

Brown, G.C. & Borutaite, V., 2008. Regulation of apoptosis by the redox state of cytochrome c. *Biochimica et Biophysica Acta*, 1777(7-8), pp.877–81.

Buchenau, B. *et al.,* 2006. Heme biosynthesis in Methanosarcina barkeri via a pathway involving two methylation reactions. *Journal of Bacteriology*, 188(24), pp.8666–8.

Butler, J.E. *et al.,* 2004. MacA , a Diheme c -Type Cytochrome Involved in Fe (III) Reduction by Geobacter sulfurreducens. *Journal of Bacteriology*, 186(12), pp.4042–4045.

Caccavo, F., Blakemore, R.P. & Lovleyl, D.R., 1992. A Hydrogen-Oxidizing , Fe (III) -Reducing Microorganism from the Great Bay Estuary New Hampshire. *Applied and Environmental Microbiology*, 58(10), pp.3211–3216.

Carpentier, W. *et al.,* 2003. Microbial Reduction and Precipitation of Vanadium by Shewanella oneidensis. *Applied and Environmental Microbiology*, 69(6), pp.3636–3639.

Childers, S.E., Ciufo, S. & Lovley, D.R., 2002. Geobacter metallireducens accesses insoluble Fe(iii) oxide by chemotaxis. *Nature*, 416(6882), pp.767–769.

Christensen, O. *et al.,* 2007. Loss of ATP hydrolysis activity by CcmAB results in loss of c-type cytochrome synthesis and incomplete processing of CcmE. *The FEBS Journal*, 274(9), pp.2322–32.

Clarke, T. a *et al.,* 2007. The crystal structure of the pentaheme c-type cytochrome NrfB and characterization of its solution-state interaction with the pentaheme nitrite reductase NrfA. *The Biochemical Journal*, 406(1), pp.19–30.

Clarke, T.A. *et al.,* 2011. Structure of a bacterial cell surface decaheme electron conduit. *Proceedings of the National Academy of Sciences*, 108(23), pp.9384–9389.

Collin, S. *et al.,* 2007. YaeT-independent multimerization and outer membrane association of secretin PulD. *Molecular Microbiology*, 64, pp.1350–1357.

Czjzek, M., Dos Santos, J. P., Pommier, J., Giordano, G., Mejean, V.&Haser, R. 1998. Crystal structure of oxidised trimethylamine N-oxide reductase from Shewanella massilia at 2.5A resolution. *Journal of Molecular Biology*, 284, 435–447.

Coppi, M. V *et al.,* 2001. Development of a genetic system for Geobacter sulfurreducens. *Applied and Environmental Microbiology*, 67(7), pp.3180–7.

Coursolle, D. & Gralnick, J. A, 2010. Modularity of the Mtr respiratory pathway of Shewanella oneidensis strain MR-1. *Molecular microbiology*, 77(July), pp.995–1008.

Coursolle, D. *et al.,* 2010. The Mtr respiratory pathway is essential for reducing flavins and electrodes in Shewanella oneidensis. *Journal of bacteriology*, 192(2), pp.467–74.

Cross, R. *et al.,* 2000. Cytochrome c J from Rhodobacter capsulatus Confers Increased Resistance to Nitric Oxide. *Journal of Bacteriology*, 182(5), pp.1442–1447.

Dalbey, R.E. & Kuhn, A., 2000. E volutionarily related insertion pathways of bacterial mitochondrial, and thylakoidmembrane proteins. *Annual Review of Cell Developemental Biology*, pp.51–87.

Eaves, D.J. *et al.,* 1998. Involvement of products of the nrfEFG genes in the covalent attachment of heme c to a novel cysteine – lysine motif in the cytochrome c 552 nitrite reductase from Escherichia coli. *Molecular Microbiology*, 28, pp.205–216.

Edeling, M.A. *et al.,* 2002. Structure of CcmG/DsbE at 1.14 A resolution: high-fidelity reducing activity in an indiscriminately oxidizing environment. *Structure (London, England : 1993)*, 10(7), pp.973–979.

Edwards, M.J. *et al.,* 2012. The crystal structure of the extracellular 11-heme cytochrome UndA reveals a conserved 10-heme motif and defined binding site for soluble iron chelates. *Structure (London, England : 1993)*, 20(7), pp.1275–84.

Edwards, M.J. *et al.,* 2014. The X-ray crystal structure of Shewanella oneidensis OmcA reveals new insight at the microbe-mineral interface. *FEBS letters*, 588(10), pp.1886–90.

Einsle, O. *et al.,* 1999. Structure of cytochrome c nitrite reductase. *Letters to Nature*, 400(July), pp.476–480.

El-Naggar, M.Y. *et al.,* 2010. Electrical transport along bacterial nanowires from Shewanella oneidensis MR-1. *Proceedings of the National Academy of Sciences of the United States of America*, 107(42), pp.18127–31.

Emerson, D. *et al.,* 2007. A novel lineage of proteobacteria involved in formation of marine Fe-oxidizing microbial mat communities. *PloS one*, 2(7), p.e667.

Emerson, D. *et al.,* 2013. Comparative genomics of freshwater Fe-oxidizing bacteria: implications for physiology, ecology, and systematics. *Frontiers in Microbiology*, 4(September), pp.254.

Emerson, D., Fleming, E.J. & McBeth, J.M., 2010. Iron-oxidizing bacteria: an environmental and genomic perspective. *Annual Review of Microbiology*, 64, pp.561–583.

Emerson, D. & Moyer, C., 1997. Isolation and Characterization of Novel Iron-Oxidizing Bacteria That Grow at Circumneutral pH. *Applied and Environmental Microbiology*, 63(12), pp.4784–4792.

Ertel, F. *et al.,* 2005. The evolutionarily related B-barrel polypeptide transporters from Pisum sativum and Nostoc PCC7120 contain two distinct functional domains. *Journal of Biological Chemistry*, 280(31), pp.28281–28289.

Esteve-Núñez, A. et al., 2008. Fluorescent properties of c-type cytochromes reveal their potential role as an extracytoplasmic electron sink in Geobacter sulfurreducens. *Environmental microbiology*, 10(2), pp.497–505.

Farrenkopf, A.M. *et al.,* 1997. Reduction of iodate in seawater during Arabian Sea shipboard incubations and in laboratory cultures of the marine bacterium Shewanella putrefaciens strain MR-4. *Marine Chemistry*, 57(3-4), pp.347–354.

Finneran, K.T., Housewright, M.E. & Lovley, D.R., 2002. Multiple influences of nitrate on uranium solubility during bioremediation of uranium-contaminated subsurface sediments. *Environmental Microbiology*, 4(9), pp.510–516.

Firer-Sherwood, M., Pulcu, G.S. & Elliott, S.J., 2008. Electrochemical interrogations of the Mtr cytochromes from Shewanella: Opening a potential window. *Journal of Biological Inorganic Chemistry*, 13, pp.849–854.

Firer-Sherwood, M.A. *et al.,* 2011. Solution-based structural analysis of the decaheme cytochrome, MtrA, by small-angle X-ray scattering and analytical ultracentrifugation. *Journal of Physical Chemistry B*, 115(38), pp.11208–11214.

Fredrickson, J.K. *et al.,* 2008. Towards environmental systems biology of Shewanella. *Nature reviews Microbiology*, 6(8), pp.592–603.

Fritz, G., Büchert, T. & Kroneck, P.M.H., 2002. The function of the [4Fe-4S] clusters and FAD in bacterial and archaeal adenylylsulfate reductases. Evidence for flavin-catalyzed reduction of adenosine 5'-phosphosulfate. *The Journal of Biological Chemistry*, 277(29), pp.26066–73.

Gao, H. et al., 2004. Global Transcriptome Analysis of the Heat Shock Response of Shewanella oneidensis Global Transcriptome Analysis of the Heat Shock Response of Shewanella oneidensis. *Journal of bacteriology*, 186(22), pp.7796–7803.

Gao, H. et al., 2010. Impacts of Shewanella oneidensis c-type cytochromes on aerobic and anaerobic respiration. *Microbial biotechnology*, 3(4), pp.455–66.

García-Rubio, I. *et al.,* 2007. Axial coordination of heme in ferric CcmE chaperone characterized by EPR spectroscopy. *Biophysical Journal*, 92(4), pp.1361–73.

Goldstein, E.J.C. *et al.,* 2003. Desulfovibrio desulfuricans Bacteremia and Review of Human Desulfovibrio Infections. *Journal of Clinical Microbiology*, 41(6), pp.2752–2754.

Gralnick, J. a *et al.,* 2006. Extracellular respiration of dimethyl sulfoxide by Shewanella oneidensis strain MR-1. *Proceedings of the National Academy of Sciences of the United States of America*, 103(12), pp.4669–74.

Grein, F. *et al.,* 2013. Unifying concepts in anaerobic respiration: insights from dissimilatory sulfur metabolism. *Biochimica et Biophysica Acta*, 1827(2), pp.145–60.

Haltia, T. & Freire, E., 1995. Forces and factors that contribute to the structural stability of membrane proteins. *Biochimica et Biophysica Acta*, 1228, pp.1–2.

Hamilton, W. A. (1998). Bioenergetics of sulphate-reducing bacteria in relation to their environmental impact. *Biodegradation,* 9, pp.201–212.

Hernandez , M. E. & Newman, D. K. (2001) Extracellular electron transfer, *Cellular and Molecular Life Sciences*, 58:1562-1571.

Harada, E. *et al.,* 2002. A directional electron transfer regulator based on heme-chain architecture in the small tetraheme cytochrome c from Shewanella oneidensis. *FEBS letters*, 532(3), pp.333–337.

Hartshorne, R.S. *et al.,* 2007. A dedicated heme lyase is required for the maturation of a novel bacterial cytochrome c with unconventional covalent heme binding. *Molecular Microbiology*, 64(4), pp.1049–60.

Hartshorne, R.S. *et al.,* 2009. Characterization of an electron conduit between bacteria and the extracellular environment. *Proceedings of the National Academy of Sciences*, 106(52), pp.22169–22174.

Heinemann, I.U., Jahn, M. & Jahn, D., 2008. The biochemistry of heme biosynthesis. *Archives of Biochemistry and Biophysics*, 474(2), pp.238–51.

Ikegami, I., Katoh, S. & Takamiya, A., 1968. Nature of heme moiety and oxidation-reduction potential of cytochrome 558 in Euglena chloroplasts. *Biochimica et Biophysica Acta*, 162, pp.604–606.

Ilbert, M. & Bonnefoy, V., 2013. Insight into the evolution of the iron oxidation pathways. *Biochimica et Biophysica Acta*, 1827(2), pp.161–75.

Ishida, T. *et al.,* 1998. A primitive pathway of porphyrin biosynthesis and enzymology in Desulfovibrio vulgaris. *Proceedings of the National Academy of Sciences of the United States of America*, 95(April), pp.4853–4858.

Jemmerson, R. *et al.,* 1999. A Conformational Change in Cytochrome c of Apoptotic and Necrotic Cells Is Detected by Monoclonal Antibody Binding and Mimicked by Association of the Native Antigen with Synthetic Phospholipid Vesicles . *Biochemistry*, pp.3599–3609.

Jensen, H.M. *et al.,* 2010. Engineering of a synthetic electron conduit in living cells. *Proceedings of the National Academy of Sciences of the United States of America*, 107(45), pp.19213–8.

Jiang, J. *et al.,* 2008. Activation of DegP chaperone-protease via formation of large cage-like oligomers upon binding to substrate proteins. *Proceedings of the National Academy of Sciences of the United States of America*, 105(12), pp.11939–11944.

Jiao, Y. & Newman, D.K., 2007. The pio operon is essential for phototrophic Fe(II) oxidation in Rhodopseudomonas palustris TIE-1. *Journal of Bacteriology*, 189(5), pp.1765–73.

Jungst, A. *et al.,* 1991. The nirSTBM region coding for cytochrome cd1-dependent nitrite respiration of Pseudomonas stutzeri consists of a cluster of mono-, di-, and tetraheme proteins. *FEBS letters*, 279(2), pp.205–209.

Keightley, J.A. *et al.,* 1998. Cloning and Expression in Escherichia coli of the Cytochrome c 552 Gene from Thermus thermophilus HB8. *The Journal of Biological Chemistry*, 273(20), pp.12006–12016.

Kihara, A. & Ito, K., 1998. Translocation , Folding , and Stability of the HflKC Complex with Signal Anchor Topogenic Sequences. *Journal of Biological Chemistry*, 273(45), pp.29770–29775.

Kim, B. *et al.,* 2006. Two Putative c -Type Multiheme Cytochromes Required for the Expression of OmcB , an Outer Membrane Protein Essential for Optimal Fe (III) Reduction in Geobacter sulfurreducens. *Journal of Bacteriology*, 188(8), pp.3138–3142.

Klarskov, K. *et al.,* 1998. Ligand Binding and Covalent Structure of an Oxygen-Binding Heme Protein from Rhodobacter sphaeroides , a Representative of a New Structural Family of c -Type. *Biochemistry*, 2960(97), pp.5995–6002.

Kleinschmidt, J.H. & Tamm, L.K., 2002. Secondary and tertiary structure formation of the β-barrel membrane protein OmpA is synchronized and depends on membrane thickness. *Journal of Molecular Biology*, 324(02), pp.319–330.

Klonowska, A., Heulin, T. & Vermeglio, A., 2005. Selenite and tellurite reduction by Shewanella oneidensis. *Applied and environmental microbiology*, 71(9), pp.5607–9.

Knowles, T.J. *et al.,* 2009. Membrane protein architects: the role of the BAM complex in outer membrane protein assembly. *Nature Reviews Microbiology*, 7(March), pp.206–214.

Kranz, R., Lill, R. & Goldman, B., 1998. MicroReview Molecular mechanisms of cytochrome c biogenesis : three distinct systems. *Molecular Microbiology*, 29, pp.383–396.

Krojer, T., Pangerl, K., *et al.,* 2008. Interplay of PDZ and protease domain of DegP ensures efficient elimination of misfolded proteins. *Proceedings of the National Academy of Sciences of the United States of America*, 105, pp.7702–7707.

Krojer, T., Sawa, J., *et al.,* 2008. Structural basis for the regulated protease and chaperone function of DegP. *Nature*, 453(7197), pp.885–890.

Kuras, R. *et al.,* 2007. A specific c-type cytochrome maturation system is required for oxygenic photosynthesis. *Proceedings of the National Academy of Sciences of the United States of America*, 104(23), pp.9906–10.

Kurisu, G. *et al.,* 2003. Structure of the Cytochrome b 6 f Complex of Oxygenic Photosynthesis : Tuning the Cavity. *Science*, 302, pp.1009–1014.

Ladokhin, a S. & White, S.H., 1999. Folding of amphipathic alpha-helices on membranes: energetics of helix formation by melittin. *Journal of Molecular Biology*, 285, pp.1363–1369.

Layer, G. *et al.,* 2010. Structure and function of enzymes in heme biosynthesis. *Protein science : a publication of the Protein Society*, 19(6), pp.1137–61.

Leang, C. *et al.,* 2010. Alignment of the c-type cytochrome OmcS along pili of Geobacter sulfurreducens. *Applied and Environmental Microbiology*, 76(12), pp.4080–4.

Leang, C., Coppi, M. V & Lovley, D.R., 2003. OmcB , a c -Type Polyheme Cytochrome , Involved in Fe (III) Reduction in Geobacter sulfurreducens. *Journal of bacteriology*, 185(7), pp.2096–2103.

Leang, C. & Lovley, D.R., 2005. Regulation of two highly similar genes, omcB and omcC, in a 10 kb chromosomal duplication in Geobacter sulfurreducens. *Microbiology (Reading, England)*, 151(Pt 6), pp.1761–7.

Lie, T. J., Godchaux, W. & Leadbetter, E. R. (1999). Sulfonates as terminal electron acceptors for growth of sulfite-reducing bacteria (Desulfitobacterium spp.) and sulfate-reducing bacteria: effects of inhibitors of sulfidogenesis. *Applied Environmental Microbiology,* 65, pp.4611–4617.

Leys, D. *et al.,* 2002. Crystal structures at atomic resolution reveal the novel concept of "electron-harvesting" as a role for the small tetraheme cytochrome c. *The Journal of Biological Chemistry*, 277(38), pp.35703–11.

Lipinska, B., Zylicz, M. & Georgopoulos, C., 1990. HtrA (DegP) Protein, Essential for Escherichia coli Survival at High Temperatures, Is an Endopeptidase. *Journal of Bacteriology*, 172(4), pp.1791–1797.

Liu, J. *et al.,* 2012. Identification and Characterization of MtoA: A Decaheme c-Type Cytochrome of the Neutrophilic Fe(II)-Oxidizing Bacterium Sideroxydans lithotrophicus ES-1. *Frontiers in Microbiology*, 3, p.37.

Liu, X. *et al.,* 1996. Induction of Apoptotic Program in Cell-Free Extracts: Requirement for dATP and Cytochrome c. *Cell*, 86(1), pp.147–157.

Lloyd, J.R. *et al.,* 2003. Biochemical and genetic characterization of PpcA, a periplasmic c-type cytochrome in Geobacter sulfurreducens. *Biochemistry*, 161, pp.153–161.

Lloyd, J.R., Yong, P. & Macaskie, L.E., 2000. Biological Reduction and Removal of Np(V) by Two Microorganisms. *Environmental Science & Technology*, 34(7), pp.1297–1301.

Lobo, S. a L. *et al.,* 2009. Functional characterization of the early steps of tetrapyrrole biosynthesis and modification in Desulfovibrio vulgaris Hildenborough. *The Biochemical Journal*, 420(2), pp.317–25.

Lobo, S. a L. *et al.,* 2007. The anaerobe Desulfovibrio desulfuricans ATCC 27774 grows at nearly atmospheric oxygen levels. *FEBS letters*, 581(3), pp.433–6.

Londer, Y.Y. *et al.,* 2006. Heterologous expression of dodecaheme "nanowire" cytochromes c from Geobacter sulfurreducens. *Protein Expression and Purification*, 47(1), pp.241–8.

Lovley, D.R., 1987. Organic matter mineralization with the reduction of ferric iron: a review. *Geomicrobiology*, 5(3), pp.375–399.

Lovely, D.R. *et al.,* 1991a. Nature Publishing Group. *Nature*, 350, pp.413–416.

Lovley, D.R., 1991b. Dissimilatory Fe (III) and Mn (IV) Reduction. *Microbiological Reviews*, 55(2), pp.259–287.

Lovley, *et al*. 1995. Bioremediation of organic and metal contaminants with dissimilatory metal reduction. *Journal Ind Microbiology*, 14, 85–93.

Lovley, D. R. 1997. Microbial Fe(III) reduction in subsurface environments. *FEMS Microbiology Reviews,* 20, 305–313.

Lovley, D.R., 2006. Bug juice: harvesting electricity with microorganisms. *Nature Reviews Microbiology*, 4(7), pp.497–508.

Lovley, D.R. *et al.,* 2011. Geobacter: the microbe electric's physiology, ecology, and practical applications. *1st ed., Elsevier Ltd*.

Lovley, D. R. & Coates, J. D. 1997. Bioremediation of metal contamination. *Current Opinion in Biotechnology*, 8, 285–289.

Lovley, D.R. & Phillips, E.J.P., 1992. Reduction of Uranium by Desulfovibrio desulfuricans. *Applied and Environmental Microbiology*, pp.850–856.

Lovley, D. R., Widman, P. K., Woodward, J. C. & Phillips, E. J. (1993). Reduction of uranium by cytochrome c3 of Desulfovibrio vulgaris. *Applied Environmental Microbiology*, 59, 3572–3576.

Lovley, D. R., Woodward, J. C. & Chapelle, F. H. (1994). Stimulated anoxic biodegradation of aromatic hydrocarbons using Fe(III) ligands. *Nature,* 370, 128–131.

Lower, S.K., Hochella, M.F. & Beveridge, T.J., 2001. Bacterial recognition of mineral surfaces: nanoscale interactions between Shewanella and alpha-FeOOH. *Science (New York, N.Y.)*, 292(5520), pp.1360–3.

Lukat, P. *et al.,* 2008. Binding and Reduction of Sulfite by Cytochrome c Nitrite Reductase. *Biochemistry*, pp.2080–2086.

Macaskie, L. & Dean, A., 1989. Microbial metabolism, desolubilization, and deposition of heavy metals: metal uptake by immobilized cells and application to the detoxification of liquid wastes. *Advances in Biotechnology Processes*, 12, pp.159–201.

Macaskie, L.E., Wates, J.M. & Dean, A.C.R., 1987. Cadmium accumulation by a Citrobacter sp. immobilized on gel and solid supports: Applicability to the treatment of liquid wastes containing heavy metal cations. *Biotechnology and Bioengineering*, 30(1), pp.66–73.

Madigan, M. T., Jung, D. O., Woese, C. R., Achenbach, L. A. (2000). *Rhodoferax antarcticus sp. nov*., a moderately psychrophilic purple nonsulfur bacterium isolated from an antarctic microbial mat. *Archives of Microbiology, 173*(4), 269-277.

Malvankar, N.S. *et al.,* 2012. Supercapacitors based on c-type cytochromes using conductive nanostructured networks of living bacteria. *Chemphyschem : a European journal of Chemical Physics and Physical Chemistry*, 13(2), pp.463–8.

Malvankar, N.S. & Lovley, D.R., 2012. Microbial nanowires: a new paradigm for biological electron transfer and bioelectronics. *ChemSusChem*, 5(6), pp.1039–46.

Marcus, R.A. & Amos, A., 1985. Electron transfers in chemistry and biology and Norman Sutin b. *Biochimica et Biophysica Acta*, 811, pp.265–322.

Marshall, M.J. *et al.,* 2006. c-Type cytochrome-dependent formation of U(IV) nanoparticles by Shewanella oneidensis. *PLoS biology*, 4(9), p.e268.

Marsili, E. *et al.,* 2008. Shewanella secretes flavins that mediate extracellular electron transfer. *Proceedings of the National Academy of Sciences*, 105(10), pp.3968–3973.

Mehta, T. *et al.,* 2006. A putative multicopper protein secreted by an atypical type II secretion system involved in the reduction of insoluble electron acceptors in Geobacter sulfurreducens. *Microbiology (Reading, England)*, 152(Pt 8), pp.2257–64.

Mehta, T. *et al.,* 2005. Outer Membrane c -Type Cytochromes Required for Fe (III) and Mn (IV) Oxide Reduction in Geobacter sulfurreducens. , 71(12), pp.8634–8641.

Méli, A.C. *et al.,* 2006. Channel properties of TpsB transporter FhaC point to two functional domains with a C-terminal protein-conducting pore. *Journal of Biological Chemistry*, 281(1), pp.158–166.

Moir, J.W.B., 1999. Cytochrome c' P from Paracoccus denitrificans : spectroscopic studies consistent with a role for the protein in nitric oxide metabolism. *Biochimica et Biophysica Acta*, 1430, pp.65–72.

Mori, H. & Ito, K., 2001. The Sec protein-translocation pathway. *Trends in Microbiology*, 9(10), pp.494–500.

Moura, I., Peck, H.D. & Dervartanian, D. V, 1988. Characterization of Two Dissimilatory Sulfite Reductases (Desulforubidin and Desulfoviridin) from the Sulfate-Reducing Bacteria. Mossbauer and EPR Studies. *Journal of the American Chemical Society*, (9), pp.1075–1082.

Muyzer, G. & Stams, A.J.M., 2008. The ecology and biotechnology of sulphate-reducing bacteria. *Nature reviews. Microbiology*, 6(6), pp.441–54.

Myers, C.R. & Myers, J.M., 2002. MtrB Is Required for Proper Incorporation of the Cytochromes OmcA and OmcB into the Outer Membrane of Shewanella MtrB Is Required for Proper Incorporation of the Cytochromes OmcA and OmcB into the Outer Membrane of Shewanella putrefaciens MR-1. *Applied and Environmental Microbiology*.

Myers, J.M. & Myers, C.R., 2000. Role of the Tetraheme Cytochrome CymA in Anaerobic Electron Transport in Cells of Shewanella putrefaciens MR-1 with Normal Levels of Menaquinone Role of the Tetraheme Cytochrome CymA in Anaerobic Electron

Transport in Cells of Shewanella putrefaciens MR-1. *Journal of Bacteriology*, 182(1), pp.67–75.

Nealson, K.H. & Myers, C.R., 1992. MINIREVIEW: Microbial Reduction of Manganese and Iron : New Approaches to Carbon Cycling. *Applied and Environmental Microbiology*, 58(2), pp.439–443.

Nealson, K.H., Myers, C.R. & Wimpee, B.B., 1991. Isolation and identification of manganese-reducing bacteria and estimates of microbial Mn(IV)-reducing potential in the Black Sea. *Deep Sea Research Part A. Oceanographic Research Papers*, 38(ll), pp.S907–S920.

Nevin, K.P. *et al.,* 2011. Anaerobes unleashed: Aerobic fuel cells of Geobacter sulfurreducens. *Journal of Power Sources*, 196(18), pp.7514–7518.

Nicholls & Ferguson, 2002. *Bioenergetics* (Third Edition) ISBN: 978-0-12-518121-1

Onufryk, C. *et al.,* 2005. Characterization of six lipoproteins in the sigmaE regulon. *Journal of Bacteriology*, 187(13), pp.4552–4561.

Orellana, R. *et al.,* 2014. Proteome of Geobacter sulfurreducens in the presence of U(VI). *Microbiology (Reading, England)*, 160(Pt 12), pp.2607–2617.

Orellana, R. *et al.,* 2013. U(VI) reduction by diverse outer surface c-type cytochromes of Geobacter sulfurreducens. *Applied and Environmental Microbiology*, 79(20), pp.6369–74.

Pan, Z., Voehringer, D.W. & Meyn, R.E., 1999. Analysis of redox regulation of cytochrome c-induced apoptosis in a cell-free system. *Cell Death and Differentiation*, 6, pp.683–688.

Pettigrew, G. & Moore, G., 1987. *Cytochromes c: Biological Aspects.*, Berlin: Springer-Verlag.

Pettligrew, B.G.W. *et al.,* 1974. Purification , Properties and Amino Acid Sequence of Atypical Cytochromne c from Two Protozoa , Euglena gracilis and Crithidia oncopelti. *Biochemical Journal*, 147(1915), pp.291–302.

Pitts, K.E. *et al.,* 2003. Characterization of the Shewanella oneidensis MR-1 decaheme cytochrome MtrA: expression in Escherichia coli confers the ability to reduce soluble Fe(III) chelates. *The Journal of Biological Chemistry*, 278(30), pp.27758–65.

Pokkuluri, P.R. *et al.,* 2010. Structural characterization of a family of cytochromes c(7) involved in Fe(III) respiration by Geobacter sulfurreducens. *Biochimica et Biophysica Acta*, 1797(2), pp.222–32.

Pokkuluri, P.R. *et al.,* 2011. Structure of a novel dodecaheme cytochrome c from Geobacter sulfurreducens reveals an extended 12 nm protein with interacting hemes. *Journal of Structural Biology*, 174(1), pp.223–33.

Pokkuluri, P.R. *et al.,* 2008. Structures and solution properties of two novel periplasmic sensor domains with c-type heme from chemotaxis proteins of Geobacter sulfurreducens: implications for signal transduction. *Journal of Molecular Biology*, 377(5), pp.1498–517.

Raphael, A.L. & Gray, H.B., 1991. Semisynthesis of Axial-Ligand (Position 80) Mutants of Cytochrome c. *Journal of the American Chemical Society*, 113(14), pp.1038–1040.

Raton, B. *et al.,* 1997. Microbially-mediated reduction and removal of technetium from solution. *Research in Microbiology*, 148(Vi), pp.530–532.

Ren, Q., Ahuja, U. & Thöny-Meyer, L., 2002. A bacterial cytochrome c heme lyase. CcmF forms a complex with the heme chaperone CcmE and CcmH but not with apocytochrome c. *The Journal of Biological Chemistry*, 277(10), pp.7657–63.

Richardson, D. *et al.,* 2009. Mitigating release of the potent greenhouse gas N2O from the nitrogen cycle - could enzymic regulation hold the key? Trends in Biotechnology, 27(7), pp.388–397.

Richardson, D.J., 2000. Bacterial respiration: a flexible process for a changing environment. Microbiology (Reading, England), 146, pp.551–571.

Richter, K., Schicklberger, M. & Gescher, J., 2012. Dissimilatory reduction of extracellular electron acceptors in anaerobic respiration. *Applied and environmental microbiology*, 78(4), pp.913–21.

Richard-Fogal, C.L., Frawley, E.R. & Kranz, R.G., 2008. Topology and function of CcmD in cytochrome c maturation. *Journal of Bacteriology*, 190(10), pp.3489–93.

Rizzitello, A.E.M.Y.E., Harper, J.R. & Silhavy, T.J., 2001. Genetic Evidence for Parallel Pathways of Chaperone Activity in the Periplasm of Escherichia coli Genetic Evidence for Parallel Pathways of Chaperone Activity in the Periplasm of Escherichia coli. *Journal Of Bacteriology*, 183(23), pp.6794–6800.

Robert, V. *et al.,* 2006. Assembly factor Omp85 recognizes its outer membrane protein substrates by a species-specific C-terminal motif. *PLoS Biology*, 4(11), pp.1984–1995.

Rosenbusch, J.P., 2001. Stability of membrane proteins: relevance for the selection of appropriate methods for high-resolution structure determinations. *Journal of Structural Biology*, 136(2001), pp.144–157.

Ross, D.E. *et al.,* 2007. Characterization of protein-protein interactions involved in iron reduction by Shewanella oneidensis MR-1. *Applied and Environmental Microbiology*, 73(18), pp.5797–808.

Ross, D.E. *et al.,* 2011. Towards electrosynthesis in Shewanella: Energetics of reversing the Mtr pathway for reductive metabolism. *PLoS ONE*, 6(2). pe.16649

Ross, D.E., Brantley, S.L. & Tien, M., 2009. Kinetic characterization of OmcA and MtrC, terminal reductases involved in respiratory electron transfer for dissimilatory iron reduction in Shewanella oneidensis MR-1. *Applied and Environmental Microbiology*, 75(16), pp.5218–26.

Ruiz, N., Kahne, D. & Silhavy, T.J., 2006. Advances in understanding bacterial outer-membrane biogenesis. *Nature Reviews Microbiology*, 4(1), pp.57–66.

Sanchez-Pulido, L. *et al.,* 2003. POTRA: a conserved domain in the FtsQ family and a class of β-barrel outer membrane proteins. *Trends in Biochemical Sciences*, 28(10), pp.523–526.

Schleiff, E. & Soll, J., 2005. Membrane protein insertion: mixing eukaryotic and prokaryotic concepts. *EMBO reports*, 6(11), pp.1023–1027.

Schulz, H. *et al.,* 1999. Heme transfer to the heme chaperone CcmE during cytochrome c maturation requires the CcmC protein , which may function independently of the ABC-transporter CcmAB. *Proceedings of the National Academy of Sciences of the United States of America*, 96(May), pp.6462–6467.

Schulz, H., Hennecke, H. & Thony-Meyer, L., 1998. Prototype of a Heme Chaperone Essential for Cytochrome c Maturation. *Science* , 281(August), pp.1197–1201.

Scott, R. & Mauk, A., 1996. Cytochrome c: A Multidisciplinary Approach., *Sausalito, CA: University Science Books;*

Shi, L. *et al.,* 2012. Mtr extracellular electron-transfer pathways in Fe(III)-reducing or Fe(II)-oxidizing bacteria: a genomic perspective. *Biochemical Society Transactions*, 40(6), pp.1261–7.

Shi, L. *et al.,* 2007. Respiration of metal (hydr)oxides by Shewanella and Geobacter: a key role for multiheme c-type cytochromes. *Molecular Microbiology*, 65(1), pp.12–20.

Shi, L. *et al.,* 2009. The roles of outer membrane cytochromes of Shewanella and Geobacter in extracellular electron transfer. *Environmental Microbiology Reports*, 1(4), pp.220–7.

Sklar, J.G. *et al.,* 2007. Defining the roles of the periplasmic chaperones SurA, Skp, and DegP in Escherichia coli. *Genes and Development*, 21, pp.2473–2484.

Smith, J. a *et al.,* 2014. Going wireless: Fe(III) oxide reduction without pili by Geobacter sulfurreducens strain JS-1. *Applied and Environmental Microbiology*, 80(14), pp.4331–40.

Smith, J. a, Lovley, D.R. & Tremblay, P.-L., 2013. Outer cell surface components essential for Fe(III) oxide reduction by Geobacter metallireducens. *Applied and Environmental Microbiology*, 79(3), pp.901–7.

Smith, S.R., 2009. A critical review of the bioavailability and impacts of heavy metals in municipal solid waste composts compared to sewage sludge. *Environment International*, 35(1), pp.142–56.

Spiess, C., Beil, A. & Ehrmann, M., 1999. A temperature-dependent switch from chaperone to protease in a widely conserved heat shock protein. *Cell*, 97, pp.339–347.

Stenberg, F. *et al.,* 2005. Protein complexes of the Escherichia coli cell envelope. *Journal of Biological Chemistry*, 280(41), pp.34409–34419.

Stroebel, D. *et al.,* 2003. An atypical heme in the cytochrome b(6)f complex. *Nature*, 426(6965), pp.413–8.

Thauer, R. K. (1998). 140th ordinary meeting of the society for general microbiology, 31 march 1998: Biochemistry of methanogenesis: A tribute to Marjory Stephenson. *Microbiology, 144*(9), 2377-2406.

Thamdrup, B. (2000). Bacterial manganese and iron reduction in aquatic sediments. *Advances in Microbial Ecology, 16*(1), 41-84

Thöny-Meyer, L., 1997. Biogenesis of Respiratory Cytochromes in Bacteria. *Microbiology and Molecular Biology Reviews*, 61(3), pp.337–376.

Thöny-Meyer, L., 2000. Heme-polypeptide interactions during cytochrome c maturation. *Biochimica et Biophysica Acta*, 1459, pp.316–324.

Thöny-Meyer, L. & Kunzler, P., 1997. Translocation to the periplasm and signal sequence cleavage of preapocytochrome c depend on sec and Zep, but not on the ccm gene products. *European Journal of Biochemistry*, 799, pp.794–799.

Truper, H.G., 1993. Dissimilatory sulphite reductase from Avchaeoglobus filgidus : physico-chemical properties of the enzyme and cloning , sequencing and analysis of the reductase genes. *Journal of General Microbiology*, pp.1817–1828.

Tsapin, a I. *et al.,* 2001. Identification of a small tetraheme cytochrome c and a flavocytochrome c as two of the principal soluble cytochromes c in Shewanella oneidensis strain MR1. *Applied and environmental microbiology*, 67(7), pp.3236–44.

Uchida, T. *et al.,* 2004. The interaction of covalently bound heme with the cytochrome c maturation protein CcmE. *The Journal of biological chemistry*, 279(50), pp.51981–8.

Ullrich, T.C., Blaesse, M. & Huber, R., 2001. Crystal structure of ATP sulfurylase from Saccharomyces cerevisiae , a key enzyme in sulfate activation. *The EMBO journal*, 20(3).

Urbanus, M.L. *et al.,* 2001. Sec-dependent membrane protein insertion : sequential interaction of nascent FtsQ with SecY and YidC. *EMBO reports*, 2(6), pp.524–529.

Van der Laan, M. *et al.,* 2001. Reconstitution of Sec-dependent membrane protein insertion: nascent FtsQ interacts with YidC in a SecYEG-dependent manner. *EMBO reports*, 2(6), pp.519–23.

Venkateswaran, K. et al., 1999. Polyphasic taxonomy of the genus Shewanella and description of Shewanella oneidensis sp. nov. *International journal of systematic bacteriology*, 49 Pt 2(1999), pp.705–24.

Vitry, C. De *et al.,* 2004. Biochemical and Spectroscopic Characterization of the Covalent Binding of Heme to Cytochrome b6. *Biochemistry*, pp.3956–3968.

Voulhoux, R. *et al.,* 2003. Role of a highly conserved bacterial protein in outer membrane protein assembly. *Science (New York, N.Y.)*, 299(5604), pp.262–265.

Wagner, M. *et al.,* 1998. Phylogeny of Dissimilatory Sulfite Reductases Supports an Early Origin of Sulfate Respiration. *Journal of Bacteriology*, 180(11), pp.2975–2982.

Wang, Z. *et al.,* 2008. Kinetics of reduction of Fe(III) complexes by outer membrane cytochromes MtrC and OmcA of Shewanella oneidensis MR-1. *Applied and Environmental Microbiology*, 74(21), pp.6746–55.

Wenz, L.S. *et al.,* 2014. Biogenesis and folding of B-barrel membrane proteins. *Cell Cycle*, 13, pp.169–170.

White, G.F. *et al.,* 2013. Rapid electron exchange between surface-exposed bacterial cytochromes and Fe(III) minerals. *Proceedings of the National Academy of Sciences of the United States of America*, 110(16), pp.6346–51.

White, S.H. & Wimley, W.C., 1999. Membrane protein folding and stability: physical principles. *Annual review of Biophysics and Biomolecular Structure*, 28, pp.319–365.

Wielinga, B. *et al.,* 2001. Iron Promoted Reduction of Chromate by Dissimilatory Iron-Reducing Bacteria. *Environmental Science & Technology*, 35(3), pp.522–527.

Wildung, R.E. *et al.,* 2000. Effect of Electron Donor and Solution Chemistry on Products of Dissimilatory Reduction of Technetium by Shewanella putrefaciens. *Applied and environmental microbiology*, 66(6), pp.2451–2460.

Wimley, W.C. *et al.,* 1998. Folding of β-sheet membrane proteins: a hydrophobic hexapeptide model. *Journal of Molecular Biology*, 277, pp.1091–1110.

Wimley, W.C., 2003. The versatile B-barrel membrane protein. *Current Opinion in Structural Biology*, 13, pp.404–411.

Woese, C.R., 2000. Interpreting the universal phylogenetic tree. *Proceedings of the National Academy of Sciences*, 97(15), pp.8392–8396.

Wu, T. *et al.,* 2005. Identification of a multicomponent complex required for outer membrane biogenesis in Escherichia coli. *Cell*, 121, pp.235–245.

Yoshioka, S. *et al.,* 2005. Biophysical Properties of a c -Type Heme in Chemotaxis Signal Transducer Protein. *Biochemistry*, pp.15406–15413.

Zhao, Y., Wang, Z.-B. & Xu, J.-X., 2003. Effect of cytochrome c on the generation and elimination of O_2 and H_2O_2 in mitochondria. *The Journal of biological chemistry*, 278(4), pp.2356–60.

2 | Materials and Methods

2:01 General Buffer preparation

20 mM HEPES pH 7.6 was the standard buffer used for most biochemical techniques. HEPES buffers was commercially obtained from Sigma™. 20 mM HEPES, 4.766 g was dissolved per litre of dH_20. Titrating small amounts of 10 M HCl to 7.6 the buffer's pH was then adjusted, the adjustments were measured by a Metrohm pH electrode. If sodium chloride was required then it was dissolved in the buffer at the necessary concentration (58.44 gL^{-1} for 1 M 5.844 gL^{-1} for 100 mM were the two most common concentrations). The buffer was then vacuum filtered through a 0.2 µm Sartorius™ filter and stored in sealed conical flasks.

2:02 SDS-PAGE analysis

Protein samples were prepared for electrophoresis by incubation in loading buffer composed of 1% (wt/vol) sodium dodecyl sulphate (SDS), 1% (wt/vol) 2-mercaptoethanol, 0.005% (wt/vol) bromophenol blue, 5% (wt/vol) glycerol, 30 mM Tris/HCl, pH 6.8. Between 12 and 15% (wt/vol) polyacrylamide gels were employed for resolution of the proteins, dependent on the size of the proteins to be resolved, with samples loaded via a 5 % (wt/vol) polyacrylamide stacking gel. Gels and sample buffers were prepared by standard methods, Laemmli (1970) and were run using a mini-gel system applying a constant potential of 120 V. In general, approximately 10 µL of sample was loaded per well. This corresponded to between 5 – 50 µg of protein sample.

Poly-acrylamide gels

Poly-acrylamide gels were made according to the following recipe: 7.5 mL Tris-HCl 1M pH 8.8, 150 µL of fresh 10% w/vol. ammonium persulphate, 300 µL of 10% w/vol. sodium dodecyl sulphate, 10.05 mL dH_2O water, 12.5 mL of 30 % acrylamide/bis-acrylamide mix (the ratio of dH2O to 30 % acrylamide/bis-acrylamide mix was adjusted to 10:12.05 mL for 10% resolving gels and 15:7.05 mL for 15% resolving gels) and finally 20µL of TEMED. The solution was poured into a 1 mm gel casting apparatus with a layer of aqueous butanol on top, creating a level surface. Once the resolving gel had set, a stacking gel, as described in Lamelli (1970), was poured on top of the resolving gel, filling the casting apparatus to the brim. A comb with appropriate teeth was inserted into the casting apparatus to create wells for protein loading.

2:03 Agarose Gel preparation

Agarose gels were used for electrophoresis and staining of DNA vectors and fragments, allowing estimations of the size of the DNA. 1% TAE Agarose gels were made through boiling 1g of agarose powder (from Sigma™) suspended in 100 mL of TAE buffer contained in a sponge-capped conical flask, in a microwave. The molten agarose was mixed with 5 µL of 100mM ethidium bromide and left to set in a casting tray with appropriate comb inserts. Once solidified, the gel was placed in a gel tank with TAE buffer, DNA samples mixed with loading buffer and then loaded into the wells of the gel. A constant voltage of 120 V was applied across the gel until the visible loading dye running front reached the end of the gel. The DNA was imaged under UV light in a BioRad gel Box and BioRad Quantity One imaging software.

2:04 Coomassie Staining

To gauge the total protein content in poly-acrylamide gels, Expedeon's Coomassie InstantBlue™ staining was used. Gels were immersed in Coomassie InstantBlue™ stain and then placed onto a rocking incubator and left for 1 hour. After 1 hour the gel was removed and washed with 30 mL of dH_2O. Protein bands were visible as blue stain.

2:05 Heme staining

To determine the presence of heme containing proteins, gels were stained through the following process. Gels were incubated in 45 mL 0.5M sodium acetate pH 5 for 20 minutes, allowing permeation of the solution into the gel matrix. 20 mg of TMBD was dissolved in 20 mL of methanol in a foiled wrapped falcon tube (to exclude light). This TMBD was then added to the sodium acetate solution and wrapped in foil. After 10 minutes 200uL of hydrogen peroxide was added to the solution, re-wrapped in the foil and then left for several hours or until the stain had fully developed.

2:06 Silver staining

Silver staining was used in place of Coomassie staining when the protein content of samples separated by SDS PAGE was required. With silver staining techniques it is possible to visualize much smaller concentrations of protein than with Coomassie staining.

SDS-PAGE gels were placed in a square petri-dish and incubated in 50 mL of 50% methanol and 5% acetic acid for 20 minutes. The solution was then removed and the gel was incubated in 50 mL of 50% methanol for 10 minutes. This solution was then removed and the gel was incubated in 50 mL of water for 10 minutes. After this, the gel was incubated in 50 mL of freshly made 0.02% $Na_2S_2O_4$ for 1 minute. Then the gel was washed in 50 mL water for 1 minute, twice. After the water wash had been removed, the gel was then incubated in 50 mL of freshly made $AgNO_3$ and kept in the dark by covering it in foil. The gel was incubated like this for 20 minutes. After 20 minutes, the $AgNO_3$ was removed and the gel was washed with 50 mL of water for 1 minute. This was completed twice removing the water each time.

The gel was then exposed to 50 mL of freshly made 2% Na_2CO_3, 0.04% formaldehyde. This caused the protein bands to be stained. Through close observation of the gel the

development process was tracked. Every thirty seconds, the 2% Na_2CO_3, 0.04% formaldehyde solution would be poured off and replaced until the protein bands became visible. At this point, the 2% Na_2CO_3, 0.04% formaldehyde was rapidly removed and the gel was immersed in 50 mL of 5% acetic acid for three minutes to quench the reaction. This 5% acetic acid incubation was repeated again for a second time and then the final stained gel was stored in 50 mL of 1% acetic acid.

2:07 Construction of mutant strains

The following molecular biology techniques were used for construction of bacterial mutants for protein expression.

Expression of a truncated form of MtrA

The vector pKP1C was constructed from pKP1 to enable the expression of MtrA C-terminus. A sequence containing the five C terminal C-XX-CH motifs and the predicted MtrA signal sequence was constructed using PCR, using the reaction scheme depicted in Figure 2.1. The strategy employed removed the MtrA N-terminus sequence from the full length MtrA via PCR of the whole pKP1 plasmid except of the N terminal section. The single stranded DNA overhanging ends of the PCR products were then removed via single stranded DNA endonuclease action. These were then de-phosphorylated and blunt-end ligated, reforming a new plasmid pKP1C. This joined the signal sequence with the MtrA C-terminus. The pKP1C contained the MtrA C-terminus with a his tag sequence with an inducible IPTG promoter. The plasmids were sequenced by Eurofins™ (www.eurofinsgenomic.eu)to check for fidelity.

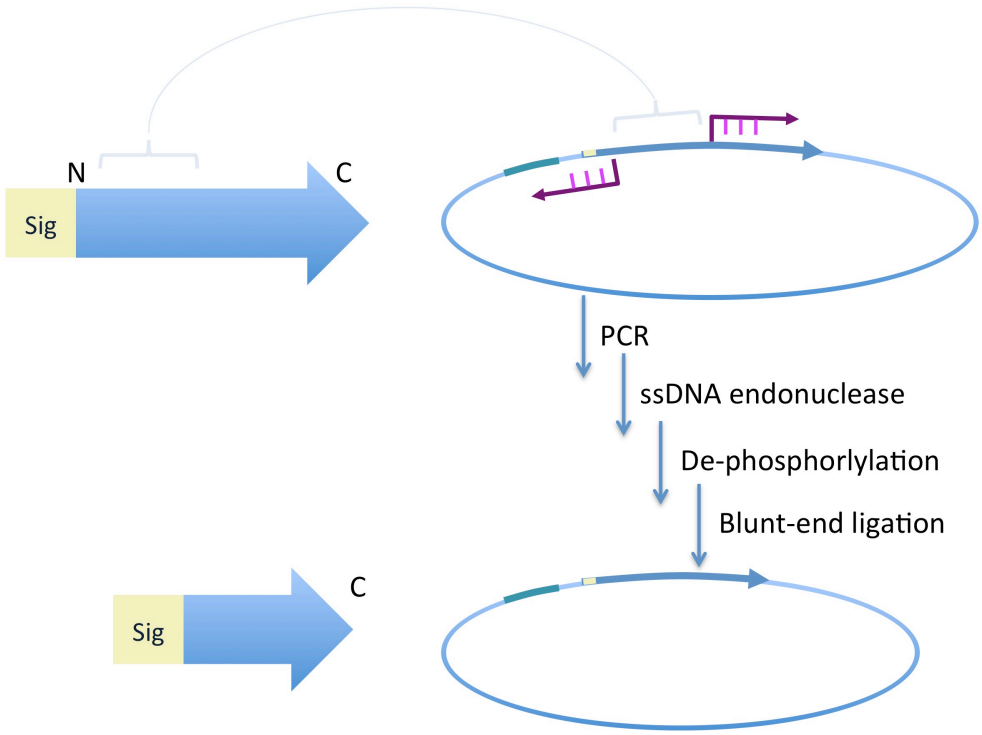

Figure 2. 1 Cartoon of the reaction scheme used to make MtrA C-terminus expression plasmids

The MtrA C terminal vector created using the primer pair **MtrA_Cterm_1_f** and **MtrA_Cterm_1_r** (table 2.1) was found to give the best expression of protein within host *E. coli* cells, however this was often only very weak expression compared to cells expressing MtrA N'. With MtrA N' a lot of pure protein could be harvested from 10 L worth of cell suspensions (produced by overnight growth after inoculation). Less than one tenth of the amount of MtrA C' could be produced from the same media quantity, and the MtrA C' smaples that were produced contained impurities. Other plasmids often produced inclusion bodies or failed to express at all. This indicated that the MtrA C terminus truncation was not a protein that suited E coli, and that Mtr C-terminus required the MtrA N-terminal half of the protein.

Polymerase Chain Reaction

Polymerase Chain Reaction (PCR) was performed with the following recipe: 1 µL of approximately 50ng.µL^{-1} genomic DNA, 84 µL of dH_2O, 10 µL 10x PCR buffer, 1 µL of 20pmol.µL^{-1} forward primer, 1 µL of 20pmol.µL-1 reverse primer, 2 1 µL of 10mM dNTP stock solution and 1 µL of 5U.µL^{-1} DNA polymerase. The mixture was then heated to 95°C for 300 seconds before thirty five cycles of denaturation annealing and polymerase extension steps (at 95 °C for 30 seconds, 60 °C for 60 seconds and 72 °C for 90 seconds, respectively) were carried out. A final extension step at 72 °C was carried out for a final 300 seconds. The PCR products were then cleaned using a Quiagen PCR product clean-up kit as per the manufacturer's instructions.

The following primers were created by Eurofins ™

Primer Name	Primer sequence
MtrA_Cterm_1_f	AGTCACCCACTCAAATGGGCACAAATGACCTGTAG
MtrA_Cterm_1_r	**TTTGAGTGGGTGACTCGCATAAGCGTTTGGTGTGA**

Table 2.1. The 5' – 3' nucleic acid sequence of the primers used for PCR.

Plasmid purification

Plasmids were purified using Quiagen plasmid miniprep kits, as per the manufacturer's instructions. The quality of the prepared plasmids was investigated through spectral assessment in a Thermo™ nano-drop spectrophotometer.

Restriction digest

Restriction digests were performed using enzymes from New England Biolabs and Sigma. The required enzyme was mixed with DNA, water and 10x enzyme buffer in the following amounts and then incubated at 37 °C in a hot-block or PCR machine for 1 hr before the reaction was heat terminated at 70 °C for 10 minutes. The products of the digestion were visualized and checked through electrophoretic separation on an agarose gel and ethidium bromide staining and UV light illumination.

De-adenylation digestions

Before some ligation reactions could be conducted, the single stranded regions of DNA added by polyermase action during PCR were removed so as to provide a suitable interface for vector – insert ligation. The reaction was completed using a thermo-scientific poly-A digest kit, as per the manufacturer's instructions. The sample was incubated with the Dpn1 adenine exonuclease with nuclease reaction buffer diluted to the required level in a 4 °C fridge overnight, allowing the nuclease to digest the exposed ssDNA.

Ligation

Ligation reactions were performed on poly-A digested inserts and dephosphorylated vectors. This ensured that the ligation reactions would join the correct components together. Ligation reactions were conducted and made up to 20 µL final volume, using the recipe in Table 2.2. The reaction was stored in a PCR tube at 4 °C overnight before use.

Reaction Component	20 µl reaction
10X T4 DNA Ligase Buffer*	2 µl
Vector DNA	50 ng
Insert DNA	37.5 ng
Nuclease-free water	up to 20 µl
T4 DNA Ligase	1 µl

Table 2.2. The reaction mixture for DNA ligation.

De-phosphorlyation

To stop self-ligation of plasmids in ligation reactions, a rapid-alkaline de-phosphorlaytion reaction was conducted on the restriction-digested vectors. This removed the terminal phosphate of the DNA strand essential for ligation. This was not

performed on fragment inserts. This reaction was carried out with rapid alkaline phosphotase from Roche and used the manufacture's supplied reagents and protocol. The reactions were incubated for 2hrs at 37°C in the Techne PCR thermocycler and the reaction stopped by heating to 75°C for 10 minutes.

2:08 Transformation of pKP1C into *E. coli* cells

Preparation of chemically competent *E. coli* cells

Chemically competent cells for vector transformation were created using the following method. Cells were stored in glycerol stocks held at -80 °C. These were streaked onto agar plates containing the required antibiotics to retain plasmids within the strain. After overnight incubation at 37 °C, single colonies were picked and used to inoculate 10 mL of LB (again with the antibiotics required for selection). After overnight growth at 37 °C in a shaking incubator, 1 mL of this culture was used to inoculate 100 mL of LB (again with any required antibiotics) contained within a sterile 250 mL flask. The culture was grown at 37 °C in a shaking incubator (RPM 180) until it reached an OD_{600} ~ 0.4 to 0.6. The cells were incubated on ice for 10 minutes before being pelleted by centrifugation in a bench-top Beckman Allegra 26R centrifuge at 3500 x g for 20 minutes. The pelleted cells were re-suspended in 20 mL of sterile, ice-cold 100 mM calcium chloride and incubated on ice for 20 minutes. These cells were pelleted by centrifugation again in the bench-top Beckman Allegra 26R at 3500 x g and re-suspended in 2.4 mL of sterile 100 mM calcium chloride 20% glycerol. The suspension divided into 50 µL aliquots before either being used fresh for transformations or being snap frozen by submersion in liquid nitrogen and then stored at -80 °C.

Transformation of competent cells

50 µL of chemically competent E *coli* cells, either from stocks stored at -80 °C defrosted on ice or from freshly prepared suspensions, were incubated on ice with 2 µL of the plasmid (at around 100 $ng.mL^{-1}$) for 30 minutes in a 1.5 mL centrifuge tube. The suspension was heat-shocked at 42°C for two minutes in a thermostatic water bath, then removed and stored on ice for 5 minutes. After this, the suspension had 1 mL of ice cold LB added and was incubated at 37 °C for 45 minutes with vigorous agitation. The cells in the suspension were pelleted in a bench top centrifuge and all but 200 µL of the supernatant removed. The cells were then gently re-suspended using a pipette before being plated out onto an LB agar plate containing the required antibiotics for selection.

The plates were incubated overnight at 37 °C. Colonies that grew during this period were then checked to ensure correct transformation either by PCR or rapid screening gel-retardation assays.

Rapid screening of recombinant plasmids with inserted vectors

Colonies from transformation plates were picked with a toothpick/pipette tip and streaked into a master plate before the remains of the colony was transferred to 30 µL of a pre-warmed and diluted lysis buffer with the following composition: 2 x Lysis buffer: 20% sucrose w/v, 200 mM NaOH, 120 mM KCl, 10 mM EDTA, 0.5% SDS, ~ 0.1% bromophenol blue. The 30 µL cellular suspensions were incubated for 5 minutes at 37 – 45 °C and then placed on ice for a further 5 minutes. After centrifuging the samples to remove any precipitate at 14000 x g for 10 minutes in a bench-top centrifuge, the samples were loaded onto an ethidium bromide containing agarose gel and run at a constant voltage of 100 V before visualization under UV light exposure. Plasmids with inserts were retarded in their movement compared to plasmids without inserts.

2:09 Growth of *Escherichia coli* strains

The following media recipes and growth protocols were used for *E. coli* strains.

Luria Broth media preparation

Luria Broth (LB) media was prepared using Formedium pre-mixed LB powder, of which 25 g was dissolved per 1 L of distilled water. The medium contained 10 g of yeast extract, 10g of trypone and 5 g of NaCl per 25 g pre-mix.

Growth and inductions

E coli cells from glycerol stocks stored at -80 °C were inoculated into 10 mL LB supplemented with kanamycin and chloramphenicol for plasmid retention and negative selection. These were grown overnight at 37 °C in a shaking incubator. 1 mL aliquots were taken and used to inoculate 100 mL of LB, again supplemented with antibiotics. This was grown overnight at 37 °C in a shaking incubator. 10 mL aliquots of this were used to inoculate 1 L of TB media supplemented with iron citrate (as stated below) and the required antibiotics. These were grown at 37 °C in a shaking incubator until an OD_{600} ~ 0.4 was reached, and then 1 mL of 100 mM IPTG was added for induction. The cells were grown at 37 °C in a shaking incubator overnight before harvesting.

2:10 Growth of *Shewanella oneidensis* strains

The following media recipes and growth protocols were used for different *Shewanella onedensis* strains.

Terrific broth media preparation

Terrific broth (TB) media was prepared via the following recipe: 10 $g.L^{-1}$ tryptone, 10 $g.L^{-1}$ NaCl, 5 $g.L^{-1}$ of yeast extract, and supplemented with 9.89 $mL.L^{-1}$ Lactate (60% w/v) and 4.5 $g.L^{-1}$ ferric citrate. The pH was then adjusted to 7.5 with NaOH and the media autoclaved. After the autoclave process, 100mL filter sterilized phosphate buffer pH 7.5 was added.

Supplemented Luria broth media preparation

Luria Broth (LB) media was prepared using Formedium pre-mixed LB powder, of which 25 g was dissolved per 1 L of distilled water. The medium contained 10 g of yeast extract,

10g of trypone and 5 g of NaCl per 25 g pre-mix. The media was supplemented with 9.89 $mL.L^{-1}$ Lactate (60% w/v) and 4.5 $g.L^{-1}$ ferric citrate for use with *Shewanella* cells. The media was then adjusted to pH 7.5 and autoclaved, ensuring the ferric citrate was fully dissolved.

Growth and induction for LS289 STC prep

1 mL glycerol stocks of *S. oneidensis* LS289, stored at -80°C, were thawed on ice then grown overnight at 30 °C in 10 mL of Luria broth with 100 ng mL^{-1} kanamycin supplement. 1 mL of this inoculum was added to 100mL of LB 100 ng mL^{-1} kanamycin and grown, again, overnight. 10 mL of this inoculum was added to 1 L terrific broth medium (supplemented with lactate and iron citrate and kanamycin) within baffled conical flasks and grown at 30 °C until they reached an optical density of approximately 0.5 AU. They were then induced with 10mM arabinose and grown under the same conditions overnight.

Growth of all other *S. oneidensis* MR-1 derived strains

1 mL glycerol stocks of cells stored at -80°C were defrosted on ice and used to inoculate 10 mL of TB with appropriate antibiotics for selection. This inoculum was grown overnight at 30°C. 1 mL of this cell suspension was used to inoculate 100mL LB, supplemented with appropriate antibiotics and grown overnight at 30 °C. 10 mL of this cell suspension was used to inoculate 1 L of supplemented TB medium contained in baffled conical flasks. This was incubated until reaching an OD ~0.6 and then induced with 1 mL of 1 M IPTG or 1 mL of 1 M arabinose, dependent upon the expression vector. The cells were then incubated at 30 °C for a total of 18- 24 hours (overnight).

2:11 General protein purification strategies

Cell harvesting via centrifugation

For all protein preparations 20 L worth of cells were grown and induced. These were harvested via centrifugation in a Beckman floor-standing J-26 centrifuge using an 8.1000 rotor, spun at 3000 x g for 15-20 minutes. The supernatant buffer was removed and autoclaved and the cell pellet collected and either snap-frozen via submersion in liquid nitrogen and stored at -80 °C or re-suspended in buffer at a ratio of 10-20 g of cells per 100 mL of 20 mM HEPES buffer pH 7.5, when immediate use was required.

Polymyxin B digest

Where it was necessary to extract the periplasm of the gram negative cells, the drug polymyxin B (from OXIOD) was administered. This forms complexes that act as pores in the outer membrane of gram positives, causing the periplasm to be released. 150 mg of polymyxin B was added per 300 mL of cell suspension in 20 mM HEPES pH 7.5. The suspension was incubated for 1.5 hours at 30 °C. The cellular remains were then separated from the periplasmic fraction through centrifugation at 12000 x g for 30 minutes in a sigma 3k30C bench-top centrifuge.

DEAE Sepharose ion exchange columns

DEAE columns were often used as the initial column for protein purification. After cell lysis Complete™ protease inhibitors were added to preserve proteins. These fractions were then loaded onto a 26/45 fast-flow DEAE sepharose column, equilibrated with 20 mM HEPES pH 7.5; using an AKTA prime system. After loading, the column was washed with 1 L of 20 mM HEPES pH 7.5 before the bound protein was eluted over a salt gradient from 0 – 1 M over 900 mL, with 11 mL fractions being collected. Every other fraction was analysed through SDS PAGE, and then stained with Coomassie Instant Blue™ or through Heme staining. Those fractions that were determined to contain the desired protein were pooled and dialyzed overnight to remove any salt, using 10 MWCO dialysis tubing and 20 mM HEPES pH 7.5.

Ion exchange metal affinity column (IMAC)

Where the protein of interest contained a histidine N-terminal tag, a nickel metal affinity column was used as the first step in purification. Three 5 mL IMAC columns (HiTrap Chelating HP from GE) were attached in series and prepared through washing with 50

mL of water and then loading 15 mL of 0.5 M $NiSO_4$. The composite column was washed with 15 mL of water (to remove the $NiSO_4$) before being equilibrated with 20 mM HEPES pH 7.5 200 mM NaCl. Pooled fractions were loaded onto the column, after which (to remove non-specific binding) the column was washed with 50 mL of 20 mM HEPES pH 7.5, 200 mM NaCl, 5 mM imidazole. Any remaining protein bound to the column was eluted via a gradient of 0 – 0.5 M imidazole in 20 mM HEPES pH 7.5, 200 mM NaCl. Fractions were collected every 1 ml over 50 mL. The fractions were analysed using SDS PAGE and these gels were stained for total protein content via Coomassie Instant Blue™ or heme stain.

Q Sepharaose ion exchange columns

Q Sepharose columns were usually used as a second step in protein purification. A 16/45 Q Sepharose column was equilibrated with 20 mM HEPES pH 7.5. The column was washed with 800 mL of this buffer before the bound protein was eluted over a salt gradient from 0 – 0.5 M NaCl over 400 mL collecting 5 mL fractions. These fractions were run in duplicate on SDS PAGE and then stained with Coomassie Instant Blue™ or Heme staining protocols. Those fractions that were determined to contain the protein of interest, with the least number of contaminants, were collated and concentrated in a Sartorius spin concentrator 10 kDa MWCO.

Gel filtration columns

Size exclusion chromatography was usually the third stage of purification. Fractions of protein containing the purest protein from previous stages were concentrated by 10 kD MWCO spin concentrator down to a volume of 2 - 0.5 mL. A 16/60 S75 (or S200 for larger proteins and protein complexes) gel filtration column was equilibrated with 20 mM HEPES 100 mM NaCl. The sample of protein was injected into the column and run at a flow rate of 0.2 mL per minute. All UV peaks were collected in 1 mL fractions. Alternate fractions were run in duplicate on SDS PAGE and then stained either with Coomassie Instant Blue™ or stained for heme. Those fractions that were determined to be purest were then collated.

Mono- Q anion exchange columns

High affinity Mono-Q columns were used as a final step to produce the maximum resolution for protein purification. Fractions from previous stages that contained the purest protein were collated and dialyzed to remove any salt. The fractions were then loaded onto a 1 mL Mono-Q column equilibrated with 20 mM HEPES pH 7.5. The proteins

were then eluted via a salt gradient of 0 – 600 mM NaCl over 60 mL, with 0.5 mL fractions collected whenever protein was detected in the flow through from the column via UV absorption. The eluent protein peaks were assessed by SDS PAGE and stained for total protein content via Coomassie Instant Blue™ or for heme content via Heme staining.

2:12 MtrA N-terminus purification (MtrA N)

MtrA N-terminus protein was purified from *E. coli* strains transformed with pEC86 and pKP1N and grown in media containing 30 $\mu g.ml^{-1}$ chloramphenicol and 100 $\mu g.ml^{-1}$ ampicillin. After suitable growth the cells were induced with IPTG. The cells were harvested then and digested with polymyxin B. The MtrA N-terminus protein was purified through DEAE, Q sepharaose, s75 gel-filtration size exclusion and mono-Q purification columns.

Figure 3.3 shows the SDS PAGE results after the purest fractions were taken from the Mono-Q eluant. The MtrA N-terminus is situated at just under 25 kDa, and is the only heme containing protein in the fractions. Two contaminants were detected in the Coomasie stain at ~45 kDa and 18 kDa. These contaminants were determined through UV-vis measurements to make up only a small fraction of the total protein, with the MtrA N-terminus determined to be above 90% purity. The MtrA N-terminus protein produces a smeared band on the heme stained gel. This is typical of MtrA based proteins.

2:13 Purification of MtrA-His

Cell harvesting via centrifugation

20 L of *S. oneidensis* strain LS306 were grown in a TB media containing 100 $\mu g.mL^{-1}$ kanamycin. These cells were induced with arabinose at a suitable time. The cells were harvested and digested with polymyxin B as described. The MtrA His protein was purified through IMAC, Q Sepharaose, s75 gel-filtration size exclusion and mono-Q purification columns.

Figure 3.2 shows the SDS PAGE results after the purest fractions were taken from the Mono-Q eluent. The MtrA protein runs at around 37 kDa and is the only heme containing protein in the fraction. Several minor contaminants were detected in the Coomasie stain, however these contaminants were only a small fraction of the total protein, with MtrA determined to be above 90% purity.

2:14 Purification of MtrA C terminal (MtrA C)

Cell harvesting via centrifugation

JM109 cells containing the pEC86 plasmid were freshly transformed with the pKP1C plasmid. These cells were grown with 100 $\mu g.mL^{-1}$ carbenacillin and 30 $\mu g.mL^{-1}$ chloramphenicol and induced with IPTG. The cells were pelleted and re-suspended in 20 mM HEPES pH 7.5 (at roughly 25 g or cell mass per 100 mL of buffer) with Complete™ protease inhibitors. The cells were then French pressed at 1000 psi three times to lyse the cells. The membrane fraction was pelleted by ultracentrifugation at 40,000g for 2 hours. The pelleted membranes were re-suspended and solubilised overnight in 20 mM HEPES 5% triton X100 before being re-centrifuged to remove any insoluble deposits. The solubilised proteins were separated via Q-sepharose, DEAE, s75 gel filtration and Mono-Q columns.

Figure 3.4 shows the SDS PAGE results after the purest fractions were taken from the Mono-Q eluant. The MtrA C-terminus protein runs at around 20 kDa and is the only heme containing protein in the fraction. Several contaminants were detected in the Coomassie stain notably those running at apparent 19 kDa and 17 kDa masses. MtrA C-terminus is the most abundant protein in the sample, however the contaminants do make up a significant proportion of the total protein content. MtrA C-terminus samples were subjected to multiple gel filtration columns (with up to 0.5 M NaCl added to the equilibration buffer), but this did not separate the MtrA C-terminus from all of the contaminants.

2:15 Purification of MtrCAB

20 L worth of *S. oneidensis* cells were cultured and the cells pelleted with floor standing Avanti J-26 centrifuges using a 8.600 rotor at 3500 x g for 20 minutes. These cell pellets were re-suspended in 20 mM HEPES pH 7.5, 2% sarkosyl and stirred at 4 °C for one hour. This preferentially solubilised the cytoplasmic membrane of the cells. The solution was then ultracentrifuged in a Beckman floor-standing XL-A using a Ti-45 at 40,000 x g for 1.5 hours. This separated the solubilised cytoplasmic membrane from the outer membranes which were pelleted. The pellet was removed and then re-suspended in 20 mM HEPES pH 7.5, 5% triton for 18 hours. The solution was then ultracentrifuged in the Beckman XL-A using a Ti-45 rotor at 40,000 x g for one hour to remove any un-solubilized membrane fragments. The pellets were discarded and the supernatant taken for further purification via Q Sepharose, s200 gel filtration size exclusion chromatography and Mono-Q columns.

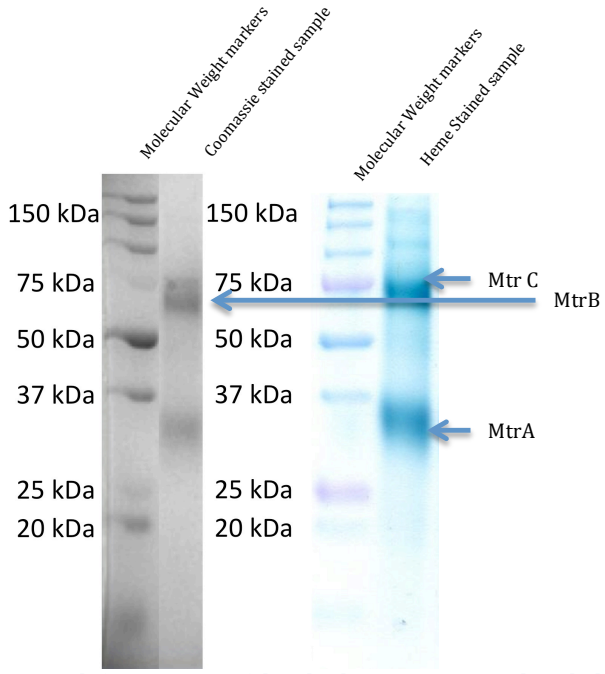

Figure 2. 2 12.5% SDS PAGE result for MtrCAB. Left hand gel Coomasie stained. Right hand gel heme stained.

Figure 2.2 shows the SDS PAGE results of the purest sample preparations of MtrCAB. The Coomassie stain shows three bands with apparent molecular masses of 32 kDa, 75 kDa and 76 kDa, typical of MtrA, MtrB and MtrC respectively. The heme stain shows only two bands at 32 kD and 76 kDa correlating with MtrA and MtrC as these contain heme cofactors.

2:16 Purification of small tetra-heme cytochrome (STC)

20 L of LS 306 culture were grown and the cells pelleted by centrifugation in a floor standing Beckman J26 at 600 RPM for 20 minutes. The pellets were removed and then re-suspended in 20 mM HEPES pH 7.5 with 100 mL of buffer per 10-20 grams of cells. The periplasms were extracted through polymyxin digest and STC was purified through the use of IMAC, Q sepharose, s75 gel filtration and Mono-Q columns. Protein samples were assessed by SDS PAGE and were then stained for total protein content with Coomasie Instant Blue ™ or for heme content via heme staining. Those fractions that had pure STC were retained, pooled and used for experimentation.

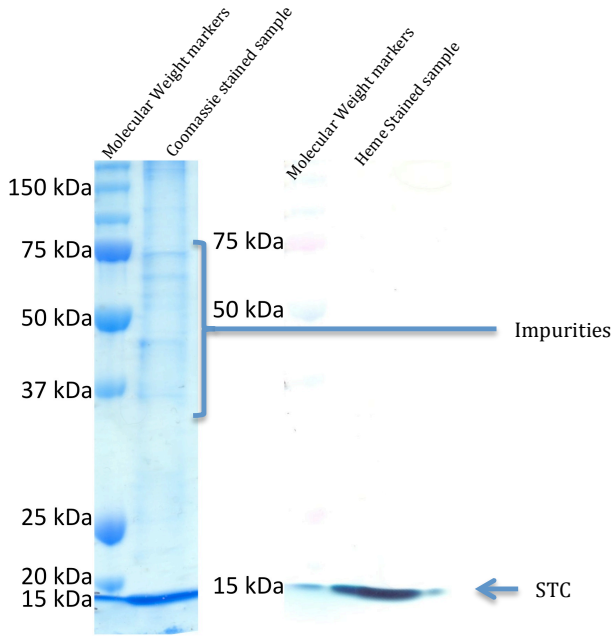

Figure 2.3 12.5 % SDS PAGE results for STC fractions used in experimentation. Left gel Coomasie stained. Right gel heme stained.

Figure 2.3 shows the SDS PAGE results after the purest fractions were taken from the Mono-Q eluent. The STC protein runs at around 14 kDa, and is the only heme containing protein in the fraction. Several minor contaminants were detected in the Coomassie stain with masses ranging from 37 kDa to 75 kDa, however these contaminants were only a small fraction of the total protein, with STC determined to be above 90% purity.

2:17 UV-visible absorption spectroscopy

UV-vis absorbance spectroscopy was an essential tool for for assessing proteins, liposomes and small molecules. Its practical applications arise from absorbance of electromagnetic waves with specific energies (and wavelengths) by specific chemical bonds. The Beer-Lambert law states the relationship between absorbance of a sample and the concentration of a specific component of that sample Equation 2.1.

$$\ln \frac{I}{I_0} = \varepsilon . c . L$$

Equation 2.1. The Beer Lambert Law. I_0 the intensity of light at source. I, the intensity of light after it passes through the sample. ε, the absorption coefficient ($mol^{-1}.cm^{-1}$) of the molecules absorbing light at specified wavelength. L, the path length (in cm) the light takes through the sample

The Beer-Lambert law relates concentration to absorbance in a linear fashion within a range of sample molecule concentrations dependent on the intensity of the light source used. To determine the molecule concentration range in which the Beer-Lambert law is linear, an assessment was made of the spectrophotometer used.

Assessing the linear limits of the spectrophotometer

Ten samples of methylene blue in water across a range of concentrations from 0.025 mM to 10 mM was made. The absorbance of each of these samples at 650 nm was assessed and then plotted against concentration. The point at which the concentration increase stopped being linearly proportional to the absorbance increase was then calculated from figure 2.4.

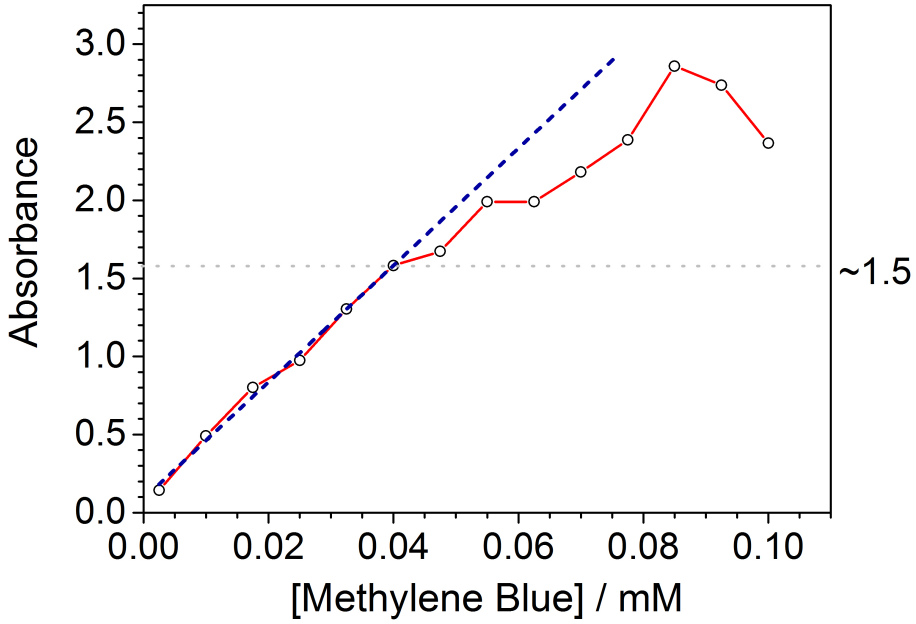

Figure 2.4 Detecting the linear absorbance limits of the Hitachi spectrophotometer used for UV-vis experiments. [black circles connected with red line] the absorbance of methylene blue at 650 nm across a concentration range. [blue dashed line] A linear regression fit of the absorbance of low concentrations of methylene blue.

The linear limit of the Hitachi U-3310 spectrophotometer used was calculated to be 1.5 absorbance units. Only samples that gave absorbance readings below this limit were used to calculate molecule concentration.

2:18 UV-vis monitored spectro-potentiometric redox titrations

Redox titrations were carried out on the MtrA, MtrA N-terminus and MtrA C-terminus proteins. Protein was buffered in 20 mM HEPES pH 7.5 and adjusted in concentration to have an absorbance at 410 nm between 0.1 and 0.8 AU. To allow the protein solution to have a stable potential across a range of voltages, redox mediators were added. These were small redox species that could react with the protein, acting as a buffer to slow voltage changes. The mediators used are listed in Table 2.3

Mediator	Formula	E_0' vs S.H.E. (V)	Mr ($g.mol^{-1}$)	Soluble in:
2,3,5,6-Tetramethyl-p-phenylenediamine (DAD)	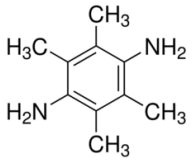	+276	164	Warm H_2O
Phenazine methosulfate (PMS)	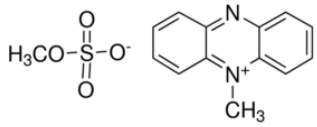	+80	334	H_2O
Phenazine Ethosulfate (PES)	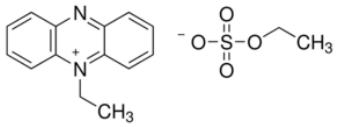	+55	306	H_2O
Jugulone	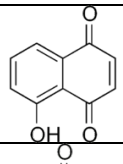	+30	174	DMF
Duroquinone	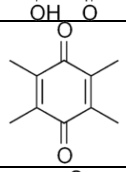	+5	164	DMSO
Menadione	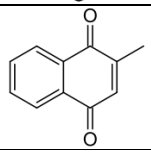	-70	172	DMSO
Anthraquinone Disulfonate (AQDS)	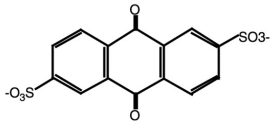	-185	413	DMSO
Anthraquinone Sulfonate (AQS)	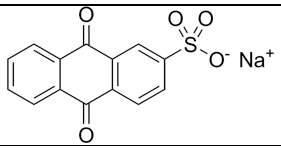	-225	328	DMSO
Benzyl viologen	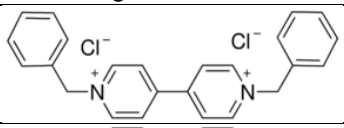	-350	409	H_2O
Methyl viologen	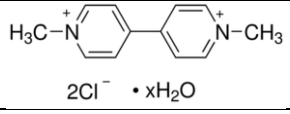	-440	257	H_2O

Table 2.3. List of mediator compounds used in UV-vis redox titrations, detailing their midpoint potentials, concentration when used and solubility.

To determine the correct concentration of mediators to use in the titrations, a control experiment was conducted surveying the absorbance of the mediator master mix over different potentials. Each of the mediators was added to 4 mL of 20 mM HEPES pH 7.5 to a final concentration of 15 nM. This solution was placed inside an anaerobic cuvette, which had access ports and a dual calomel / counter electrode within it Figure 2.5.

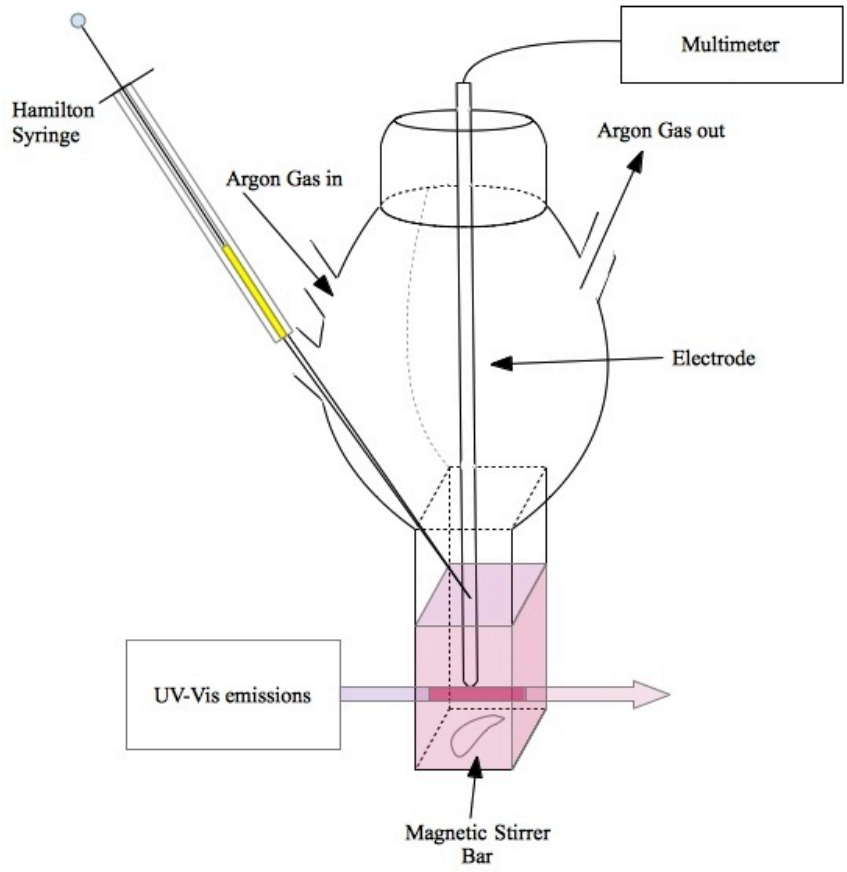

Figure 2.5 Cartoon representation of the redox titration. This anaerobic cuvette was placed inside a Hitachi U-3310 spectrophotometer to measure UV-vis absorbance of the solution inside the cell.

The cuvette was sealed and then incubated for an hour with a continuous flow of argon through it sparging any oxygen present. With the cuvette placed in the spectrophotometer and a magnetic flea vigorously stirring the solution, the potential of the solution was then altered through injecting small quantities of sodium dithionite and potassium ferricyanide from similarly sparged 10 µM anaerobic solutions. At each solution potential, a wavelength spectrum was taken. These spectra are shown in Figure 2.6.

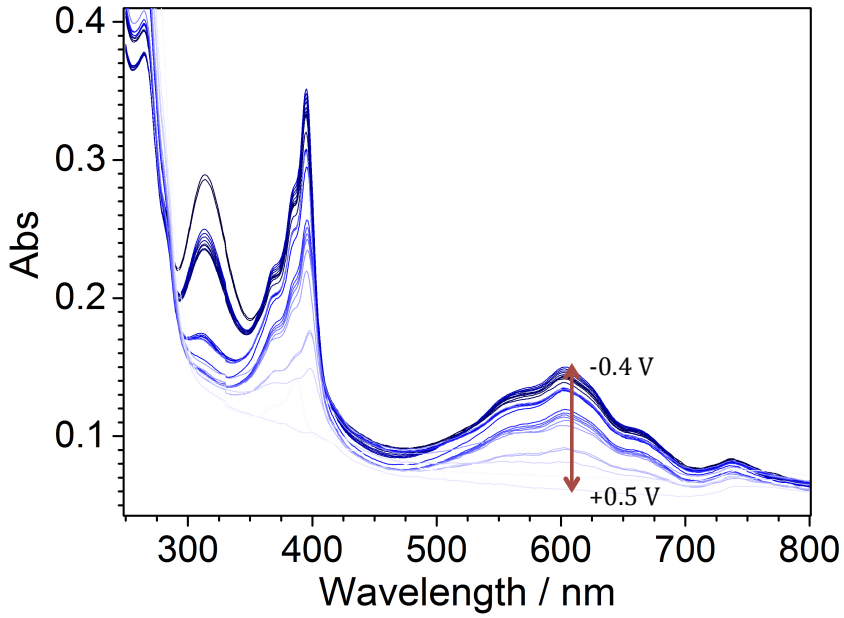

Figure 2.6 UV-vis absorbance spectra of the redox titration of mediators when at a final concentration of 15 nM. Each of the spectra has been colour coded from light to dark blue for high to low potential over the range +0.5 V to -0.4 V.

Most of the mediators did not produce, at any potential, any absorbance in the wavelength range the heme proteins would be assessed in. The methyl viologen and benzyl viologen mediators, when at a 15 nM final concentration and in reducing conditions, produce absorbance that are detectable on the scale being measured in the 552 nm region. This absorbance would superpose with the 552 nm α/β region absorbance of the heme proteins. Thus the concentration of mediators used for this experiment were deemed too high, as only absorbance at 552 nm made by heme co-factors should be measured. A repeat experiment altering the concentration of mediators from 15 nM to 1.25 nM final concentration was conducted. The results are shown in Figure 2.7.

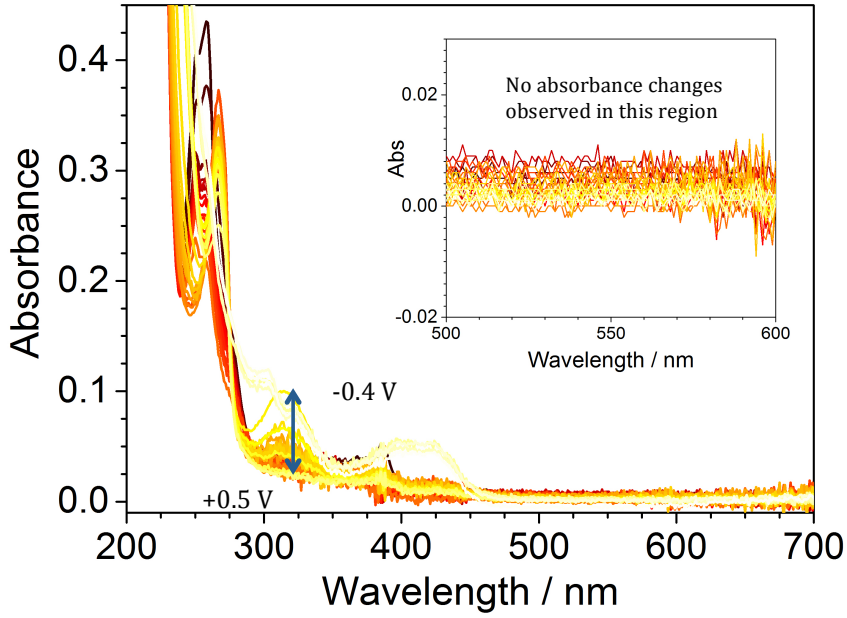

Figure 2.7 UV-vis absorance spectra of redox titration when the mediators were at a final concentration of 1.25 nM. Each of the spectra has been colour coded from red to yellow for high to low potential over the range +0.5 V to -0.4 V.

In Figure 2.7 the mediators did not produce any significant absorbance in the wavelength range the heme proteins would be assessed in. This is highlighted by the insert in Figure 2.9, which has an enlarged view of this region. At this concentration, no viologen absorbance can be detected on the scale used. Each of the mediators was made into a stock solution at a concentration of 10 mM. 100 µL of each of these stocks was mixed together to form a mediator master mix. 4 mL of the protein solution was then added to an anaerobic fluorescence cuvette along with 5 µL of mediator master mix solution described. This, when added to 4 mL of protein, would give a final mediator concentration of 1.25 nM.

Rapid mixing of fluids

Because the experimental technique relied on adding solutions together, and then those solutions reacting, the time needed for adequate mixing of the solutions was needed so that equilibrium was reached. This was so that when an absorbance reading was taken for each potential it could be certain that the protein components of that solution were experiencing the same potential as the electrode. MtrA protein solution not under rapid

mixing (the magnetic flea was not stirring) was anaerobically sealed inside the anaerobic cuvette. The absorbance of the protein solution at 552 nm was recorded over time after 10 µL of 100 mM sodium dithionite reducant was added, Figure 2.8.

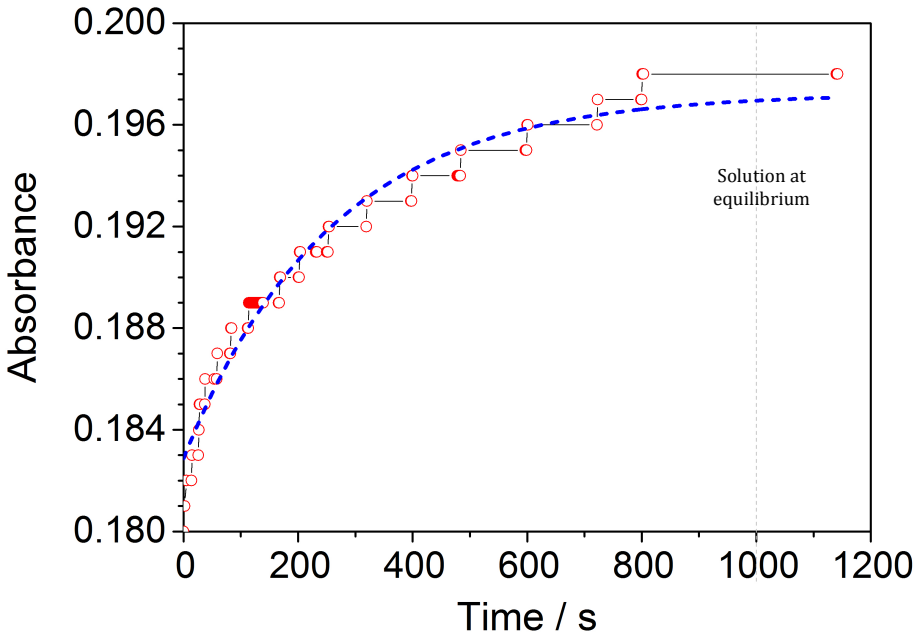

Figure 2.8 Non-rapid mixing of fluids over time. [red dot connected with black lines] The absorbance of 4 mL of 0.25 mg.mL^{-1} MtrA protein over time after the addition of 10 µL of 100 mM sodium dithionite; without any stirring from a magnetic flea. [blue dashed line] line of best fit for data. [grey dashed line] time at which solution had been at equilibrium for three minutes, a suitable time for a reading to be taken.

Figure 2.8 shows how the absorbance of the MtrA at 552 nm increases over time. Up until 800 seconds the protein is still being reduced. After 800 seconds no more absorbance increases are observed, thus the solution must have reached a state of equilibrium. With the magnetic flea causing rapid mixing the solution will reach equilibrium sooner. In the redox titrations after each chemical adjustment made to the protein solution at least 800 seconds were waited before an absorbance spectrum and associated potential reading were taken. This ensured that even if rapid mixing by the magnetic stirrer had failed the solution was at equilibrium.

Using the set up described in Figure 2.6, redox titration experiments on MtrA, MtrA N-terminus and MtrA C-terminus proteins were conducted. 4 mL of the protein solution was added to an anaerobic fluorescence cuvette along with 5 µL of mediator master mix. The solution was then altered through injecting small quantities of sodium dithionite and potassium ferricyanide from similarly sparged 10 µM anaerobic solutions. At each solution potential, a wavelength spectrum was taken after 800 seconds of incubation to reach solution equilibrium.

2:19 Optically transparent Tin-Electrode potentiometric titrations

UV-vis monitoring of protein adhered to an optically transparent tin electrode was conducted for MtrA, MtrA N-terminus and MtrA C-terminus proteins. Conductive tin-oxide coated glass slides were first cut to the correct dimensions to fit inside a 1 x 1 x 4 cm fluorescence cuvette. The slide was then cleaned through heating in an oven at 400 °C for one hour. Concentrated 20 $mg.mL^{-1}$, MtrA, MtrA N-terminus or MtrA C-terminus proteins in 20 mM HEPES pH7.5 were carefully applied to the tin oxide surface covering all the electrode with an even coat of protein. After letting the protein solution dry a little on the slide, any unbound protein was carefully washed off (and collected) with more 20 mM HEPES pH 7.5. This left a film of bound protein on the tin oxide surface. A platinum wire was then secured to the tin-oxide slide with heat shrink tubing. A solid connection between the wire and the slide was ensured. This process is demonstrated in figure 2.9.

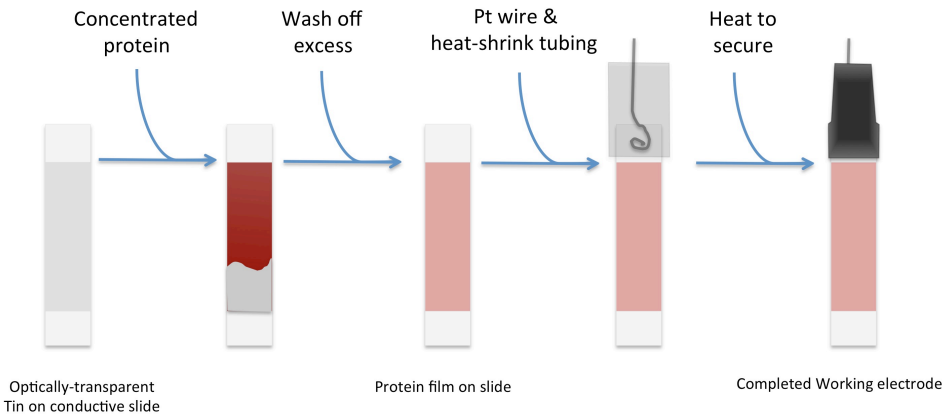

Figure 2.9 A cartoon demonstrating the process of making a tin-oxide electrode with protein adhered to the surface.

Once the working electrode had been constructed, it was placed in a fluorescence cuvette filled with 20 mM HEPES pH 7.5, 100 mM NaCl. A silver chloride-coated (silver-wire) reference electrode and a platinum counter electrode were inserted into the cuvette and finally connected into a potentiostat forming an electrochemical cell.

The silver chloride-coated reference electrode was created by wiring a silver wire onto the terminals of a battery and then submerging these wires into hydrochloric acid. The reference electrode was then calibrated against a commercial calomel electrode. An electrochemical cell was set up in an anaerobic glove box with a polished carbon

electrode, a platinum counter electrode and the Ag/AgCl reference electrode. A cyclic voltammogram measurement of 10 mM potassium ferricyanide, was taken. The reference electrode was changed for a commercial calomel electrode and another cyclic voltammogram taken. The mid point potentials of the two voltammograms were then compared to calculate a calibration factor for the Ag/AgCl reference electrode that would be used in the tin-oxide cell, Figure 2.10. This process was repeated before and after each use of the Ag/AgCl electrode to ensure an accurate calibration was used for each experiment and that there was no change in the calibration during the experiment. If any drift was detected the experiment was repeated.

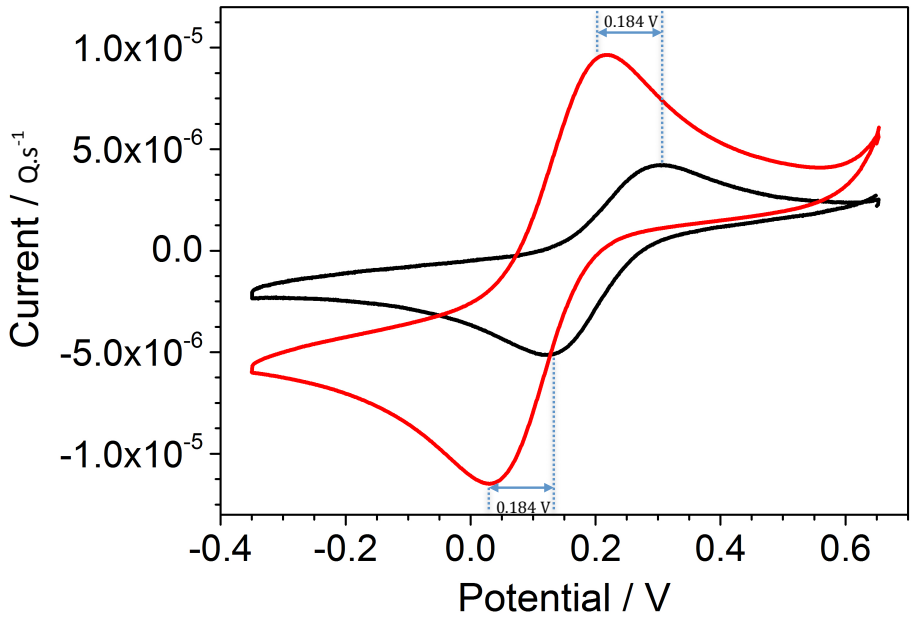

Figure 2. 10 Cyclic voltammogram of 10 mM potassium ferricyanide using a commercial calomel electrode [black line] and the Ag/AgCl reference [Red line].

The calibration factor was determined to be around +0.184 V for each experiment, with minor variations around this value for each experiment. Once the reference electrode was calibrated the tin oxide electrode cell was constructed as described in Figure 2.11. The cell was placed in a Jasco V-650 UV-vis spectrophotometer. Argon gas was then flushed over the cell to provide an anaerobic environment for the cell. This experimental set up allowed measurements of any absorbance changes of the protein on the tin-oxide

electrode. The potentiostat was controlled by the program GPES, and it allowed exact control of the potential of the cell, and thus the potential of the protein adsorbed onto the working electrode. A cyclic voltammogram cycle was run through the cell from +0.2 V to -0.7 V at 0.01 $V.s^{-1}$. The cycle was paused after each 10 mV change and the potential held for 3 minutes, allowing full equilibration of the adhered protein to the potential. A UV-vis wavelength absorbance scan was then taken.

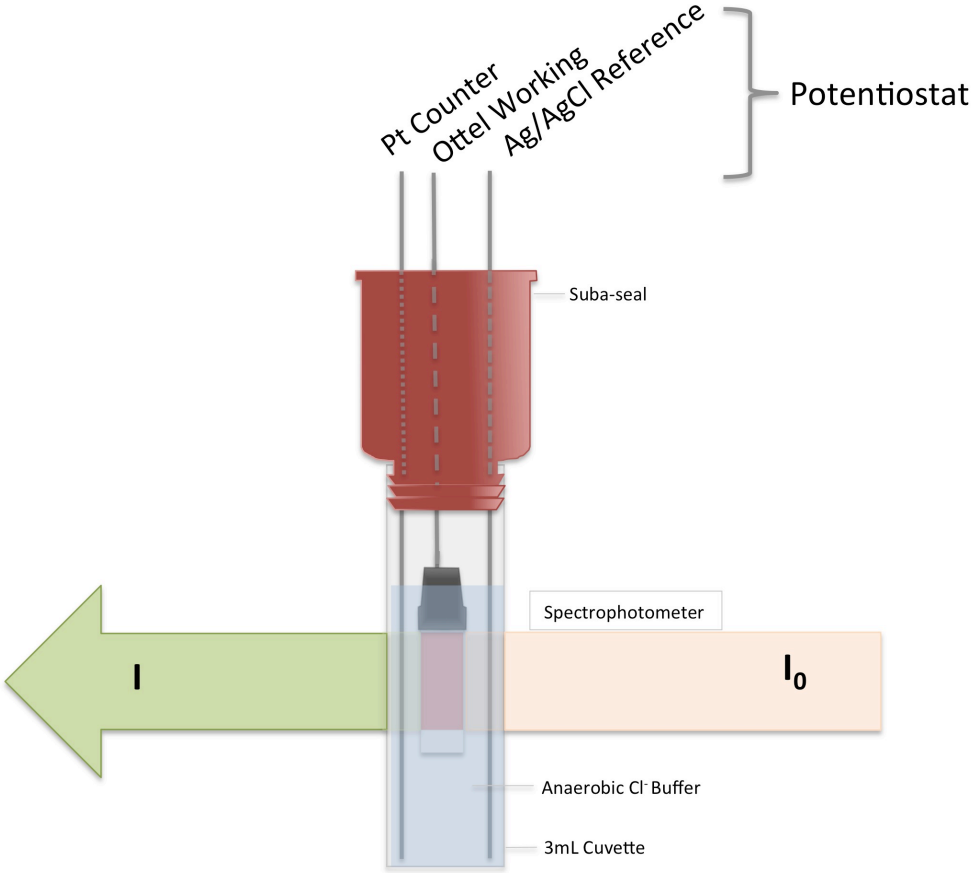

Figure 2. 11 Cartoon set up of the tin-oxide electrochemical cell set up. The cell was placed in a Jasco V-650 spectrophotometer allowing measurements of the absorbance of the tin-oxide slide at different potentials. Ottel is an abbreviation for optically transparent tine electrode.

2:20 Analytical Ultra-Centrifugation Velocity-experiments

Analytical ultracentrifugation was used to investigate the proteins MtrA, MtrA N-terminus, MtrA C-terminus and MtrCAB. It allowed investigation of the proteins in solution through tracking them spectrophotometrically whilst sedimenting under centrifugal forces.

Samples for ultracentrifugation were prepared at three different concentrations. These concentrations were typically based on the absorbance of the 410 nm Soret band of the proteins as they all contained heme co-factors. The concentrations were calculated so that the absorbance of the 410 nm soret peak was in the linear limit of the spectrophotometer. The useable linear limits were roughly 0.1 to 1 absorbance units. The concentrations of MtrA examined were 1 μM, 0.5 μM and 0.25 μM. The concentrations of MtrA N and C-terminus that were used were 2 μM, 1 μM and 0.5 μM. Those for MtrCAB were 0.37 μM, 0.22 μM and 0.13 μM. 120 μL of these protein samples were loaded into the left hand chamber of a two channel Beckman ultracentrifuge cell. 340 μL of matching buffer (typically 20 mM HEPES pH 7.5 with 100 mM NaCl for MtrA, MtrA N-terminus and MtrA C-terminus and 2% LDAO for MtrCAB) was loaded into the right hand channel of the cell. The cells were sealed with brass screws.

Two of the cells (along with a reference balance) were then paired and adjusted to be within 0.25 grams of each other, and placed into the AN Ti 50 8 channel Beckman analytical ultracentrifugation rotor at opposite positions. The rotor was then loaded into a Bekman XLA floor standing ultracentrifuge and a monochromatometer secured around it. The ultracentrifuge was accelerated to 42,000 RPM and absorbance scans taken of each of the protein containing cells over the radius of the quartz window of each channel. The results were collected in the Beckman XLA ultracentrifuge operating software and then analysed by ULTRASCAN, SEDFIT and SEDANAL programs.

2:21 Small angle X-ray scattering (SAXS) experiments

SAXS was performed at the Diamond Light Source Synchrotron (Harwell, Oxfordshire, UK) on BL 21. The experiments were performed using a 10.5 keV 250 µm square X-ray beam with a flux of 10^{12} photons/s. Data was collected at 4°C on a 1024 x 1024 pixel CCD detector at a sample-to-detector distance of 4 m; the transmission intensity was measured with a PIN diode beamstop. Scattering from protein solutions of MtrA, MtrA N-terminus and STC (all in 20mM HEPES, pH 7.5 200 mM NaCl) were collected from dilution series of protein concentrations from around 0.3 mg.mL^{-1} to 5 mg.mL^{-1}. 25µL of the samples were loaded via capillary tubes (with a pathway of 2 µm) into the X ray beam and were static throughout 180, 1 second exposures, Figure 2.12. The first and last of these exposures were compared for any changes indicating radiation damage. If no radiation damage was observed, average scattering profiles were created from the 180 images. This average image was then radially averaged creating a 2D plot of intensity (I) versus momentum transfer (q). Background scattering from HEPES/salt buffer-only plots were then subtracted. The momentum transfer q (or its analogous "s") is related to the scattering angle away from the incident X-ray beam where $q = 4\pi/\lambda \sin\theta$, where λ is the X-ray wavelength and 2θ is the scattering angle.

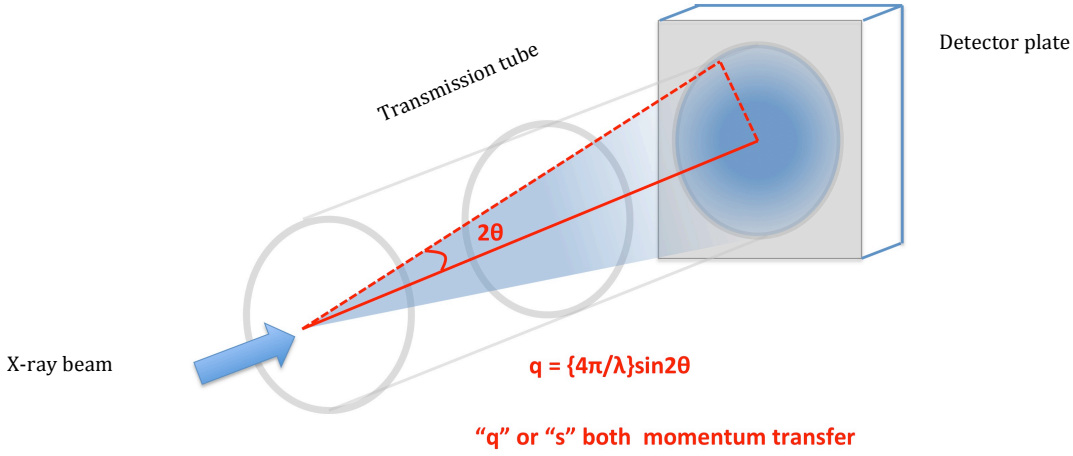

Figure 2. 12 3D Cartoon demonstrating how the scattering of X-rays from a single point [blue arrow] cause a scattering pattern [blue circle on the grey square]. The degree of scattering is measured by the momentum transfer the X-ray undergoes. This is calculated from the angle of scattering [2θ] and the energy of the X-rays.

Merged scattering profiles were created through combining the most accurate sections of each of the scattering profiles over the concentration series. This process was completed in PRIMUS. The program GNOM was used to calculate a real space function, the 'pair distribution function', P(r), from the merged scattering profiles.

To visualize the overall shape of the protein, *ab-initio* shape reconstructions were performed on P(r). Bead models were generated with the program DAMMIF using slow annealing and an oblate spheroid starting parameters. These models were then averaged using the program DAMAVER and aligned with the intersecting consistent features of all the simulated models produced from DAMFILT. These two surface envelopes were then aligned using the SUPCOMB program.

2:22 Small angle neutron scattering (SANS) experiments

Neutron scattering experiments were performed at the Rutherford Appleton Laboratories ISIS (Harwell, Oxfordshire, UK) with the help of beamline scientists. The experimental set up was similar to SAXS experiments, with neutron scattering recorded instead of X-ray scattering. Neutrons scatter due to interactions with atomic nuclei, unlike X-rays that scatter off electron density. The purpose of using SANS instead of SAXS was to distinguish between scattering caused by lipid moieties and scattering caused by proteins. The purified MtrCAB complex requires a lipid toroid to surround the hydrophobic region of MtrB, which canonically sits within the outer membrane. This lipid region would cause X-ray scattering in SAXS experiments that would obscure scattering from MtrCAB, as lipids and proteins have a very similar electron density. The nuclei density of lipids and proteins is sufficiently different for SANS experiments to differentiate between them. Through introducing deuterated water (D_20) into the MtrCAB buffer, the nuclear density change was changed. If the nuclear density of the buffer is increased to match the nuclear density of lipids (the "match point") then any scattering caused by lipids will appear as background noise and can be easily subtracted. This would differentiate protein scattering from lipid scattering. Lipid nuclear densities can be altered, making them increasingly different from protein densities through introducing deuterated components. This widening of the relative match points of lipids and proteins increases the quality of data that can be collected.

SANS experiments

75 µL samples of protein (one 5 $mg.mL^{-1}$ MtrC and three 4.7, 2.8 and 1.4 $mg.mL^{-1}$ MtrCAB) in 20 mM HEPES pH 7.5, 5 mM lauryldimethylamine oxide (LDAO) 10% D_2O were placed in quartz cuvettes. These were placed in the sample chambers of the neutron beamline apparatus. Neutron scattering was then collected from these samples for 45 minutes three times each. These scattering profiles were averaged, radially averaged and then processed to make real-space bead models using the same computational methods as the SAXS data.

Determining the deuterium match point of LDAO

50 - 75 µL of 20 mM HEPES pH 7.5, 5 mM LDAO was set up in a dilution series with increasing amounts of D_2O. These samples ranged from 0 to 30 % D_2O. Neutron scattering from these samples was the collected and compared to scattering from

samples of 20 mM HEPES (no LDAO). From these it was determined that 10 % D_2O 20 mM HEPES 7.5, 5 mM LDAO matched the scattering of 20 mM HEPES pH 7.5.

Preparation of deuterated detergent MtrCAB samples

To increase the signal to noise ratio, samples of MtrCAB in deuterated detergents were prepared. Deuterated n-dodecyl β-D-maltoside (DDM) and octyl β-D-fluropyranoside (OGP) were sourced from Anatrace™. 20 mM HEPES pH 7.5, 25 mM OGP and 20 mM HEPES pH 7.5, 0.25 mM DDM were then used to buffer exchange 5 $mg.mL^{-1}$ MtrCAB in 20 mM HEPES pH 7.5, 5 mM LDAO, through a 5 mL Q-sepharose anion exchange column. These samples were ready to take to the STFC ISIS Harwell neutron source, however there was an unexpected closure due to equipment failure the day before the scheduled experimental window. This delayed the collection of these results beyond the timeframe of this thesis.

2:23 Crystallization trials

MtrA and MtrA-terminus crystallization trials were attempted. A wide variety of commercial screens were used in a 96 well vapor diffusion plate, with 10 $mg.mL^{-1}$ and 20 $mg.mL^{-1}$ samples tested for each at both 15 °C and 5 °C. None of the trials were found to produce crystals of any sort for either protein. Most of the trials caused MtrA and MtrA N-terminus proteins to aggregate.

2:24 Liposome and proteoliposome creation for UV-vis experiments

Liposomes and proteoliposomes were made for experimentation using the following methodology. Between 1 mL and 10 ml of approximately 10mM redox indicator (in 50mM HEPES pH7, 2mM $CaCl_2$) was mixed with phosphatidyl choline to a final concentration of 10 $mg.mL^{-1}$. The phosphatidylcholine was stored at -20 °C and allowed to de-frost to room temperature in desiccator, to avoid any condensation. The mixture was then thoroughly vortexed. 1 mL portions were passed through a 0.1µm membrane, at least 10 times, using a syringe extruder. The extruded liposome suspension was then transferred into screw cap centrifuge tubes and either used immediately or stored at -80°C. The extruded samples were sonicated using a small probe for 3 x 40 seconds with 1 minute breaks on ice, this was to enhance the monodispersity of the samples. To make proteoliposomes, 1 µl of 10 µM MtrCAB stock and 10 µl of 10µM valinomycin were added to each mL of suspension. To make control liposomes, 10 µl of 10µM valinomycin and 2 µl 2% triton detergent was added to the suspension. Samples were then mixed well and put through a -80°C freeze-thaw cycle, four times, this was to encourage incorporation of protein into the lipid bilayer. 0.25 g of BioRad™ BioBeads were added to each 1 mL of liposome or proteoliposome suspension, removing any detergent in the sample. These were then agitated for 1 hour on a flat bed shaker at 5°C. The suspension was removed through drawing up into a syringe with a thin needle, with a bore smaller than the BioBead diameter. The liposomes or proteoliposomes were then ready for washing. The suspension was then transferred to 1mL ultracentrifuge tubes and spun at 80,000 RPM in a Beckman 70.3 Ti rotor (in a benchtop ultracentrifuge) for 40mins at 4°C. The supernatant was removed, analysed by UV-vis spectrophotometry and then either discarded or saved for making future liposomes. 1 mL of 50mM HEPES pH7, 2mM $CaCl_2$, 10mM KCl, was used to re-suspend the liposome pellets. This was done using a 1ml pipette. This washing process was then repeated twice more. After the final wash step, no redox indicator absorbance was detected in the supernatant after centrifugation and the pellets were re-suspended in 1 mL of 50mM HEPES pH7, 2mM $CaCl_2$, 10mM KCl and stored at 5°C (as freezing it caused disruption). These suspensions were found to be stable for a few days.

A range of different redox indicators was trialed for use within liposomes. From those tested, only methyl viologen, small tetraheme cytochrome (STC) and cytochrome c, were found to be suitable.

Methyl viologen proteoliposome advance washing technique

When preparing methyl viologen proteoliposomes for use with a thimble shaped glassy carbon pot electrochemical-cell Figure 2.17. a more thorough procedure was developed to remove any external methyl viologen. This was because this technique is highly sensitive and would be susceptible to false positive readings if any methyl viologen was free and un-encapsulated. After the four washing steps described in the section above were completed, additional washing steps described as below were then enacted.

Bio Rad™ Chelex 100 beads have iminodiacetic groups which have a high affinity for divalent cations, such as methyl viologen. Thus, these can be used to bind any free methyl viologen and separate it from proteoliposomes. 250 $mg.mL^{-1}$ of Chelex 100 was added to the proteoliposome suspension after the fourth wash. This was agitated for 30 minutes on a platform rocker, giving the beads an opportunity to mix with the entire solution. The proteoliposome suspension was separated from the Chelex beads with a small bore needle and syringe and then added to another 250 $mg.mL^{-1}$ of fresh Chelex beads. This was left to agitate for a further 30 minutes on a platform shaker, fully mixing the suspension and the beads. The proteoliposome suspension was separated from the Chelex beads with a needle and syringe. This two-step treatment with Chelex has been shown to remove over 99% of 50 μM methyl viologen from both aqueous solutions and liposome solutions. Further treatments of Chelex were used to remove any methyl viologen that had leached out of burst liposomes over time.

2:25 UV-vis monitored spectro-potentiometric liposome experiments

The UV-vis absorbance changes of liposomes and proteoliposomes (containing redox indicators) were measured when exposed to reductants and oxidants. The redox state of the internalized redox indicators could be deduced from the absorbance spectra recorded, and any changes tracked over time. These measurements were completed using a xenon and tungsten lamp Hitachi U-3310 UV-vis spectrophotometer.

Liposome and proteoliposome samples were sealed inside an anaerobic cuvette and left for 1-2 hours whilst argon was flushed through the cell to remove any oxygen present, Figure 2.13. The cells were not subjected to any rapid mixing at this stage, as the movement of the magnetic flea could cause disruption of the phosphatidylcholine membranes and thus cause the release of the un-encapsulated redox indicator. This would lead to false positive changes of absorbance, not mediated by MtrCAB. 17.5 mg of fresh sodium dithionite, 32 mg of potassium ferricyanide and 24mg of ferric citrate were placed inside separate universal tubes sealed with a suba-seal and sparged the nitrogen for 1 hour. Additionally, 3 mL of analytical water was sparged with nitrogen in a similar fashion. After sparging, 1 mL of anaerobic water was taken by gas tight syringe and injected into each of the suba-sealed universal tubes containing the chemical reductant and oxidants. This created 100 mM solutions of each of these solutions. These were the solutions used for each of the additions described below.

To fully characterize the liposome and proteoliposome redox state changes, a series of absorbance measurements tracking any changes over time were taken. For these, the liposomes were subjected to rapid mixing by a magnetic flea and stirrer plate. Firstly the initial redox state of the liposomes and proteoliposomes was examined through a wavelength scan from 800 nm to 250 nm. The liposomes and proteoliposomes should be partially or fully oxidised due to the presence of oxygen. After this scan, between 5- 10 µL of sodium dithionite reductant was injected into the sample suspension (this was calculated to be a roughly stoichiometric amount of reductant to the amount of redox indicator). As the samples were not entirely oxygen free, the amount of reductant added was always enough to scrub this oxygen and fully reduce all the redox indicators, but with only a very small excess of reductant. During this process a time scan measuring absorbance at 603nm for methyl viologen suspensions and 552 nm for the heme

suspensions was recorded. This tracked absorbance peaks linearly proportional to the redox status of the indicators. After all of the absorbance changes at these wavelengths had finished (at around 1000 seconds) another wavelength scan was recorded to track how the overall spectrum had changed. After this, 15 -20 µL of potassium ferricyanide or ferric citrate was added to the suspension. During this, the absorbance of the liposomes was measured (again at 603 nm and 552 nm for methyl viologen and heme containing suspensions respectively). After this, another wavelength scan was taken to track how the addition of oxidant had changed the absorbance spectrum of the respective suspensions.

Finally 3 µL of triton X100 was added to the suspension, to disrupt all the liposomes or proteoliposomes. After this, another wavelength scan producing a final absorbance spectrum was recorded. Then, 20 µL of sodium dithionite was added to fully reduce all of the redox indicator and a final wavelength was recorded to measure the maximal absorbance peaks at each wavelength in a reduced sample.

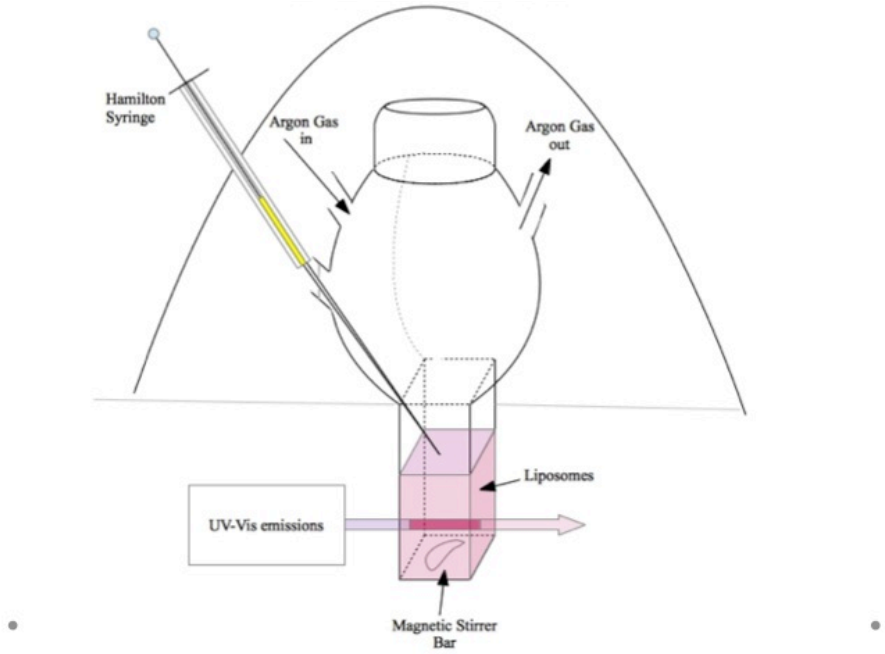

Figure 2. 13 The set up for an anaerobic cell to measure chemical reduction and oxidation of liposomes. The anaerobic cell comprises of a fluorescence cuvette with sealed access ports to allow argon to be continually flushed over the sample and chemical oxidants and reductants to be added via Hamilton syringe. When placed in a UV-vis spectrophotometer the additional bulk of the cuvette did not allow the built-in chamber cover to close thus black out cloth (detailed in the cartoon) was used as a substitute to block out any light.

2:26 Carbon-Pot cyclic voltammetry upon liposomes and proteoliposomes

The use of an electrochemical cell enables proteoliposomes to be non-chemically reduced and oxidised. A glassy carbon pot was used as a working electrode, a platinum wire as a counter electrode and a commercial calomel electrode as the reference electrode. The carbon pot experiments were set up as described in Figure 2.14. For cyclic voltammetry 300 μL of sample was pipetted into the carbon pot. Roughly 3 mL of electrolyte buffer was used to fill each of the side arms that were positioned in the cooling jacket to sit with tips immersed in the sample within the carbon pot. The cell was rigged within a Faraday cage within a Belle Perspex glovebox that maintained an O_2 level of below 1 ppm. The cell was connected to a potentiostat controlled by computer running GPES software.

Before experiments were conducted, the carbon pot was thoroughly polished with aluminum oxide to remove any substances trapped in the glassy carbon outer surfaces. All the glass components were washed with distilled water. Negative control experiments analyzing electrolyte buffer were performed to observe the non-Faradaic currents produced and to determine if the cleaning process had been sufficiently thorough. Any impurities would have produced Faradic responses, indicating that the equipment should be cleaned again. These negative controls were performed at the scan rates/step potentials that would be used for experimental samples.

Cyclic voltammetry

Cyclic voltametry (CV) experiments were conducted using linear sweep programs with an initial conditioning potential of 0 mV for 5s and then two vertex potentials that covered the potential range of -0.6 V to 0.1 V. This covered the range of potentials over which methyl viologen is redox active for interchange between MV^{2+} and MV^{1+} states. Crucially, the range is not negative enough to cause the double reduction of MV^{2+} to MV^{0} (~-0.75 mV). In this uncharged state MV is membrane soluble and could leak out of liposomes. The range in potential was less than 0.8 V to avoid excessive heating of the carbon pot.

Amperometry

Amperometry experiments were performed through modulating the cell potential between +0.1 V to -0.64 V and measuring the current passing through the cell due to these changes. The magnetic stirrer was active during the amperometry experiments as the interference noise it created could be subtracted.

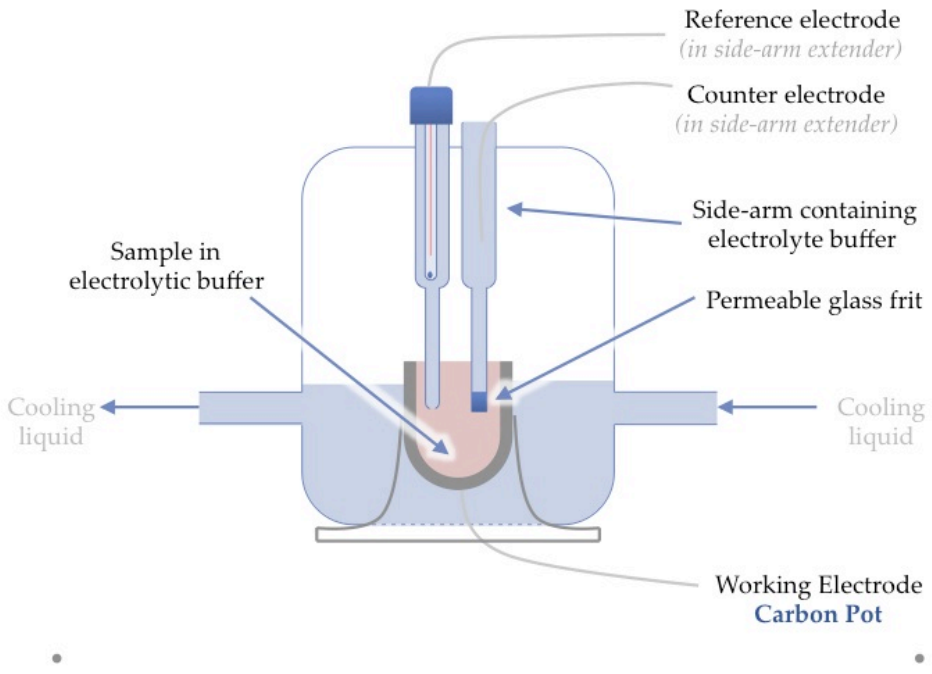

Figure 2. 14 Electrochemical cell inside cooling jacket. The working electrode is a "thimble" shaped, glassy/amorphous carbon-pot. This sits in a glass holder and is directly connected to a standard plastic coated electrical wire. The counter electrode is a platinum wire. This platinum wire sits inside a glass arm extender. The extender has a permeable frit at its base and is filled with the electrolyte buffer of the sample under examination in the carbon pot cell. The reference electrode is an Ag/AgCl standard electrode bought in from Metrohm. It sits in a reference arm extender filled with the same electrolyte buffer as the sample. The reference arm extender has a small opening at its base to allow direct buffer-sample contact in the reference arm – carbon pot. The electrode screws into the top of the reference arm extender creating a seal stopping the electrolyte buffer leaking out into the carbon pot. The cooling jacket is a glass cradle for the carbon pot that allows cooling liquids, pumped by a thermostatic water bath, to securely flow through it

2.27 Bibliography

Laemmli, U.K., 1970. Cleavage of Structural Proteins during the Assembly of the Head of Bacteriophage T4. *Nature*, 227(5259), pp.680–685.

3 | Structural and functional studies on MtrA

3.01 Structural and functional studies on MtrA

Investigation of the shape of MtrA and its ability to function as an electron transporter will enable insight into the contribution that MtrA makes to the structure and function of the hetro-trimeric MtrCAB complex. Currently, the only published work on the shape of MtrA comes from Firer-Sherwood *et al*., (2011). In this paper, the authors perform small angle X-ray scattering (SAXS) and analytical ultracentrifugation (AUC) experiments. Using these results, they produced a molecular envelope for MtrA and sedimentation coefficients and molecular weights. Although very illuminating, the results do not allow the topology of MtrA within MtrCAB to be investigated. Defining the parts of the molecular envelope likely to be the N and C termini would facilitate predictions as to the end of MtrA that interacts with the MtrB pore.

The work published in Pitts *et al*., (2003) seeks to investigate the mid-point potentials of the heme co-factors of MtrA. In this paper two different groups of hemes with distinct mid-point potentials at -200 mV and -375 mV were predicted. The ability to assign these potentials to specific hemes within the sequence of MtrA would be useful in characterizing the movement of electrons through MtrA, but this cannot be done with the currently published data.

This chapter will seek to further the understanding of the shape and functional orientation of MtrA and will investigate the midpoint potentials of the hemes contained with specific regions of MtrA. This will be achieved through the production and then characterization of truncated forms of MtrA, which are either missing the N or C terminal halves of the full-length sequence.

The MtrA N truncation (MtrA N) of MtrA is a protein designed to be truncated after the 160th amino acid in MtrA and so only contains only five hemes as opposed to the full ten in MtrA. The protein was created and purified as in the Materials and Methods section 2.12. The MtrA C truncation (MtrA C) of MtrA is a protein composed of the signal sequence of MtrA and the section of MtrA after the 160th amino acid of the full length MtrA (the section that was removed in the MtrA N terminus truncation). The amino acid sequences for both these truncations are shown in Figure 3.1. Like the MtrA N, MtrA C only contains only five hemes, instead of the full ten found in MtrA. MtrA C was purified as in the Materials and Methods section 2.14.

Through truncating MtrA to only the N or C terminal sections, these specific sections can be independently investigated for their structural and functional properties. In the future, this may lead to the identification of structural features belonging to only one truncation which can be used to differentiate sections of full-length MtrA models. Investigations into whether the two truncations of MtrA can complement each other and combine to mimic the structure and function of the full length MtrA, would be very informative.

3.02 The purification and characterization of MtrA, MtrA N and MtrA C.

Strains expressing constructs that produced proteins with amino acid sequences described in Figure 3.1 were made as per the Materials and Methods section 2.10.

A MtrA

MKNCLKMKNLLPALTITMAMSAVMALVVTPNAYASKWDEKMTPEQVEATLD
KKFAEGNYSPKGADSCLMCHKKSEKVMDLFKGVHGAIDSSKSPMAGLQCEACH
GPLGQHNKGGNEPMITFGKQSTLSADKQNSVCMSCHQDDKRMSWNGGHHDN
ADVACASCHQVHVAKDPVLSKNTEMEVCTSCHTKQKADMNKRSSHPLKWAQ
MTCSDCHNPHGSMTDSDLNKPSVNDTCYSCHAEKRGPKLWEHAPVTENCVTC
HNPHGSVNDGMLKTRAPQLCQQCHASDGHASNAYLGNTGLGSNVGDNAFTG
GRSCLNCHSQVHGSNHPSGKLLQRHHHHHH

B MtrA N

MKNCLKMKNLLPALTITMAMSAVMALVVTPNAYASKWDEKMTPEQVEATLD
KKFAEGNYSPKGADSCLMCHKKSEKVMDLFKGVHGAIDSSKSPMAGLQCEACH
GPLGQHNKGGNEPMITFGKQSTLSADKQNSVCMSCHQDDKRMSWNGGHHDN
ADVACASCHQVHVAKDPVLSKNTEMEVCTSCHTKQKADM

C MtrA C·

MKNCLKMKNLLPALTITMAMSAVMALVVTPNAYASKSHPLKWAQMTCSDCH
NPHGSMTDSDLNKPSVNDTCYSCHAEKRGPKLWEHAPVTENCVTCHNPHGSV
NDGMLKTRAPQLCQQCHASDGHASNAYLGNTGLGSNVGDNAFTGGRSCLNCH
SQVHGSNHPSGKLLQR

Figure 3. 1 The amino acid sequence of the MtrA and MtrA truncations. Panel A. The full length of MtrA, including the signal sequence that would be cleaved upon protein maturation. Panel B. The MtrA N truncation, including the signal sequence. Panel C. The MtrA C truncation, including signal sequence. [Green text] Signal sequence. [Red text] CXXCH heme binding motif. [black text] N-terminal section of MtrA. [Blue text] C-terminal section of MtrA.

These strains were then used to produced samples of MtrA, MtrA N and Mtr C proteins, which were purified as described in the Materials and Methods section 2.11. The results of each of the purifications are detailed below.

Figure 3.2 shows the SDS PAGE results of the MtrA purification stained with Coomassie and Heme stains. The MtrA protein runs with an apparent molecular weight of 37 kDa, and is the only heme containing protein in the fraction. Several minor contaminants were detected in the Coomassie stain however these contaminants were only a small fraction of the total protein, with the MtrA determined to be above 90% purity.

MtrA

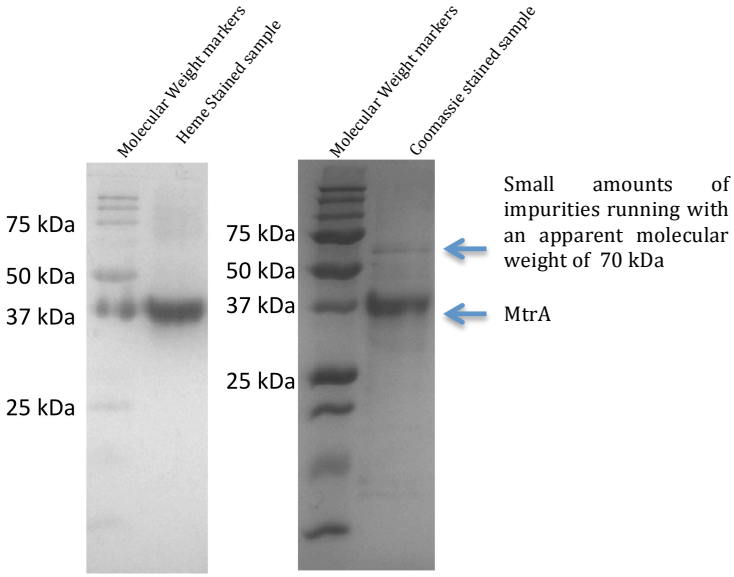

Figure 3. 2 12.5% SDS PAGE results for MtrA. The gel on the left has been heme stained, the gel on the right has been Coomassie stained.

Figure 3.3 The MtrA N runs with an apparent molecular weight of just under 25 kDa, and is the only heme containing protein in the solution. Two contaminants were detected in the Coomassie stain at ~45 kDa and 18 kDa. These contaminants were determined through UV-vis measurements to make up only a small fraction of the total protein, with MtrA N determined to be above 90% purity.

MtrA N

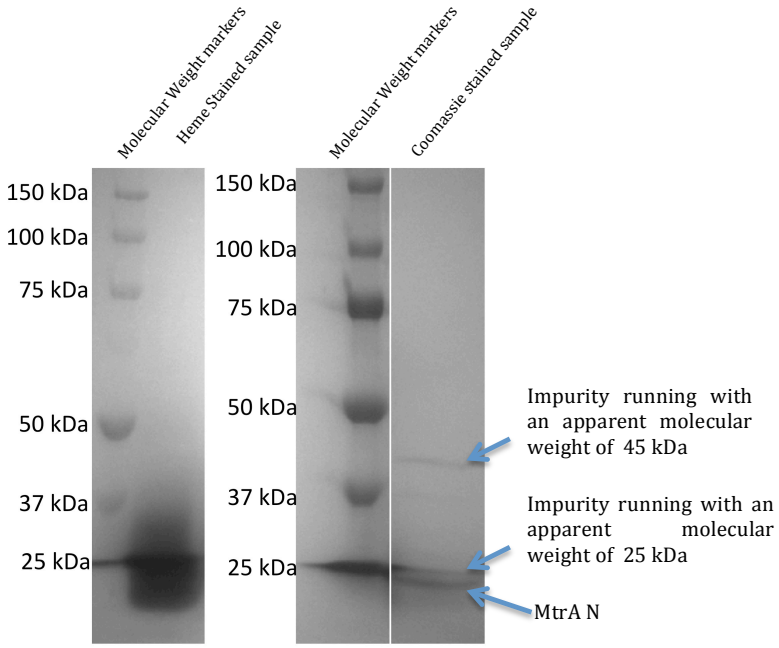

Figure 3. 3 SDS PAGE of purest fractions MtrA N fractions after Mono Q elution. The gel on the left has been Heme-stained, the gel on the right has been Coomassie stained.

Figure 3.4 shows the SDS PAGE results after the final stage of MtrA C purification. The MtrA C protein runs with an apparent molecular weight of around 22 kDa, and is the only heme containing protein in the fraction. Several contaminants were detected in the Coomassie stain. MtrA C is the most abundant protein in the sample, however the contaminants do make up a significant proportion of the total protein content. Throughout the purification, several strategies were employed to separate MtrA C from impurities but this was the best that could be achieved whilst retaining sufficient quantities of MtrA C for experimentation.

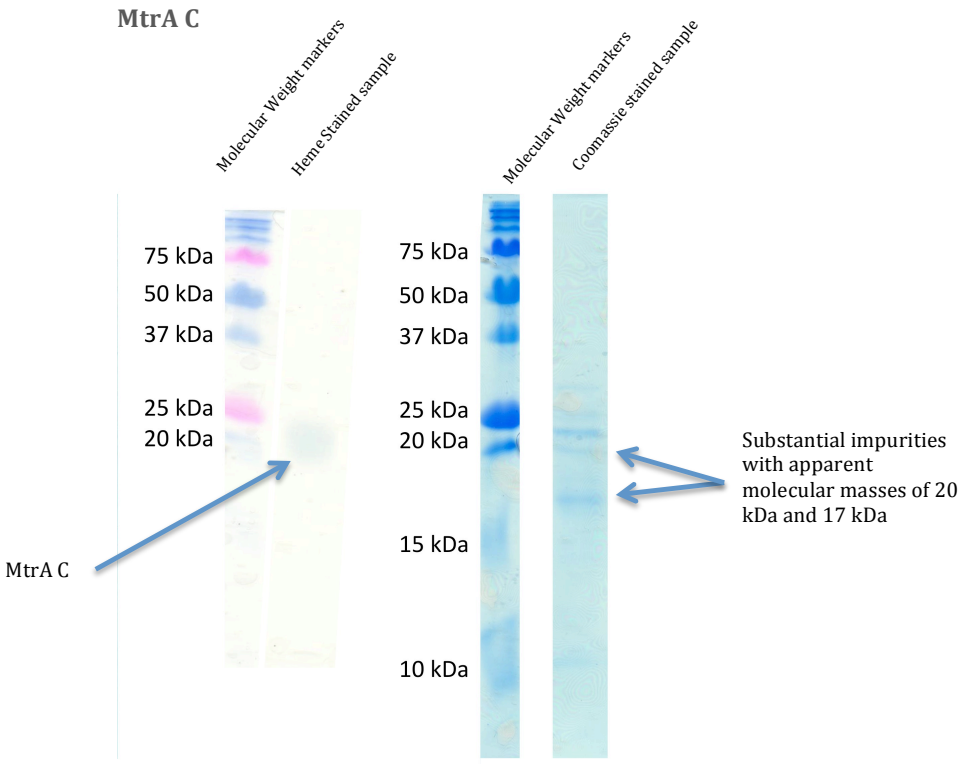

Figure 3. 4 12.5% SDS PAGE result for MtrA C. The gel on the left has been heme stained, the gel on the right has been Coomassie stained.

These protein solutions were then used for AUC, SAXS and redox titration experiments. MtrA C was not purified to the standard of purity and high concentration as that of MtrA N or MtrA. Thus, it was only suitable to perform analytical ultracentrifugation experiments upon it.

3.03 Analytical Ultracentrifugation

Analytical ultracentrifugation was conducted on samples of MtrA, MtrA N and MtrA C. Examining how MtrA or MtrA truncations behaved whilst sedimenting gave an insight into the shapes and sizes of each of these proteins. The Svedberg equation (Equation 3.1) describes the relationship between sedimentation, time and the physical properties of the molecule (Demeler, 2001).

$$\frac{s}{D} = \frac{M(1 - \bar{v}\rho)}{RT}$$

Equation 3.1. The Svedberg equation. The sedimentation coefficient (s), the diffusion coefficient (D), molecular weight (M), partial specific volume ($\bar{v}$), density of the buffer (ρ) Real Gas Constant (R), temperature (T).

Using the relationship in Equation 3.1, an ultracentrifugation experiment that tracks the movement of a molecular species by UV-vis spectroscopy over time, whilst under a known centrifugal force, in a known buffer and at a stable temperature, can be used to determine the molecule's sedimentation coefficient, molecular weight and predict frictional coefficients and axial ratios. The calculation of these values are the result of fitting ideal Lamm equations to the data, which enables specific parameters describing the sedimenting species to be calculated (Demeler, 2001). Thus, AUC experiments are ideal for investigating MtrA proteins as they are small and highly soluble, and contain heme cofactors which have a distinctive and easily detectable absorption band at 410 nm.

There are published results from sedimentation velocity (SV) AUC experiments on MtrA in Firer-Sherwood *et al.*, (2011). In this publication the authors reported a single sedimenting species with a sedimentation coefficient of 3.4 S correlating to between a 37 – 43 kDa species. Comparing these results to this particular preparation of MtrA and those for MtrA N and MtrA C will give insight into the shape and form of MtrA and how it can change. Hartshorne *et al.*, (2009) published data showing the sedimentation equilibrium of MtrA, reporting a molecular weight of around 40 kDa, which is within the range reported by Firer-Sherwood *et al,*. (2011).

Analytical Ultracentrifugation of MtrA

AUC sedimentation velocity experiments were conducted on MtrA cytochromes using concentrations of 0.1, 0.05 and 0.005 mg.mL^{-1}. The experiment was set up as described in Materials and Methods section 2.20. The proteins centrifuged at a rotational speed of 42,000 rpm in a floor standing Beckman XL-A using a Ti45 rotor. Absorbance data was then collected for each of the samples at timed intervals as the protein sedimented. These results were analysed with the programs SEDFIT and ULTRASCAN (Demeler *et al.*, 1997; Schuck, 2000; Schuck, 2003; Demeler & van Holde, 2004; Demeler, 2005; Cölfen *et al.*, 2010).

Figure 3.5. Panel A shows the radial absorbance at 410 mn of different time points when MtrA protein solution was centrifuged at 40,000 rpm in a Ti45 rotor in a Beckman XLI centrifuge . Using the program SEDFIT, these scans were collated and fitted to ideal Lamm equations (Schuck, 2000). These can be seen as the lines passing through the real data points. The fitted lines have only small residuals indicating that the solved Lamm equations are a good fit to the real data. Sedimentation analysis was then performed using these fits. Panel B demonstrates the coefficient of sedimentation histogram plot. This shows that there was one major sedimenting species for the scattering data with a sedimentation coefficient of 3.2 S. This corresponds to a molecular weight of around 40 kDa. This correlates with the molecular weight calculated from in-silico sequence analysis. A smaller subsidiary peak at 5.5 S was also detected in the c(s) analysis. This could correspond to a contaminant containing hemes with a molecular weight higher than MtrA. This would make the sample unsuitable for experiments such as SAXS, as this species would cause scattering that would interfere with the scattering from MtrA.

To investigate the reliability of these results the analysis was repeated using the program ULTRASCAN. Much stricter controls on which scans were used for modeling where put in place. Any anomalous scans were excluded and data smoothing techniques were applied. Figure 3.5. Panel C shows the resulting c(s) analysis report. The output indicates that there is one species sedimenting with a coefficient of 3.2 S. The prediction of a 3.2 S peak through ULTRASCAN analysis is in line with the SEDFIT analysis, however with a much stricter scan selection in the ULTRASCAN analysis, the peak at 5.5S was lost. This highlights how the processing of data using AUC analysis programs can be biased. The molecular weight of MtrA reported by ULTRASCAN analysis was 42.55 kDa. ULTRASCAN

also allowed the F/F_0 ratio to be calculated. The frictional coefficient ratio F/F_0 compares the surface friction expected of a protein of a certain size if it was exactly spherical compared to the observed value. The F/F_0 of MtrA was calucated to be 1.44. This suggests that the protein was not likely to be spherical. Using the axial ratio simulator in ULTRASCAN and presuming that that the protein was prolate then its major axis was estimated to be larger than 110 Å and its minor axis around 12 Å.

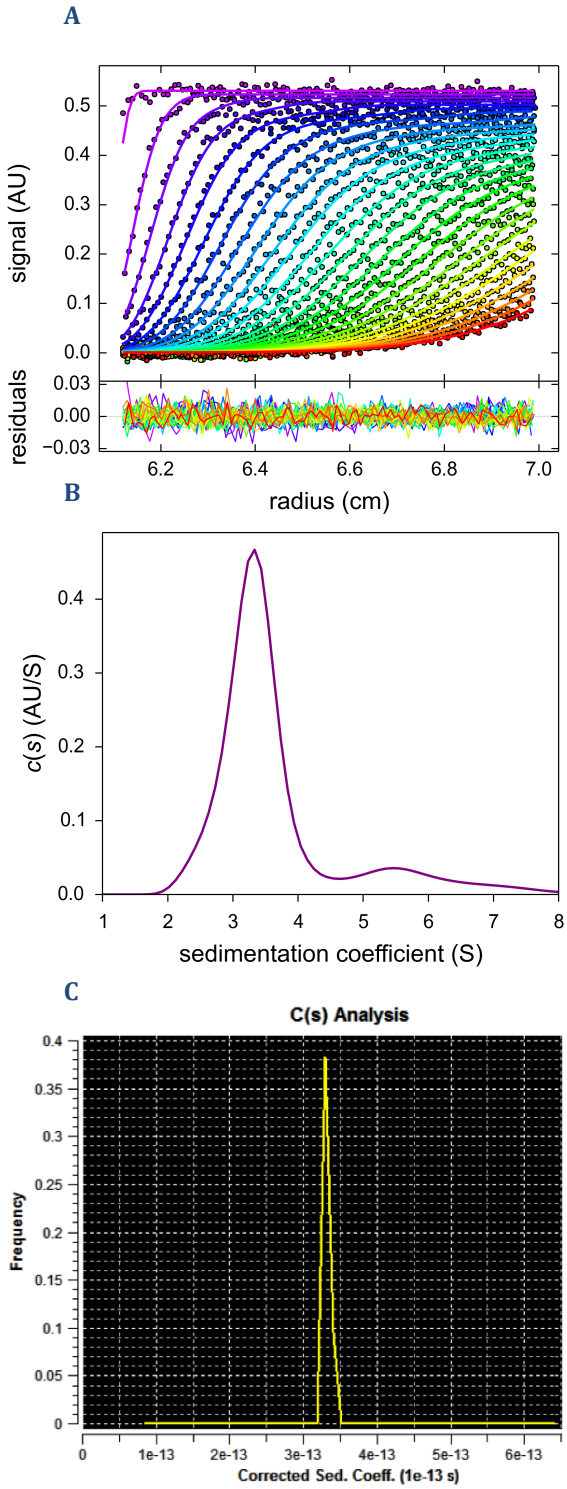

Raw data fitted in SEDFIT

SEDFIT c(s) analysis

ULTRASCAN c(s) analysis

Figure 3. 5 Analytical Ultracentrifugation of MtrA, sedimentation velocity experiments.
Panel A. Selected absorbance profiles of MtrA N over time, with the fitted Lamm equations and the residuals of these fits presented using SEDFIT.
Panel B. The c(s) analysis output for MtrA N from SEDFIT.
Panel C. The c(s) analysis output for MtrA from ULTRASCAN.

Analytical Ultracentrifugation of MtrA N

AUC velocity experiments were conducted on MtrA N cytochromes using a concentration range of 0.2, 0.1 and 0.01 $mg.mL^{-1}$. The experiment was set up as in the Materials and Methods section 2.20, with the same centrifuge speed used, absorbance measurements taken and analysis conducted, as in the MtrA AUC experiments.

Figure 3.6. Panel A shows the radial absorbance at 410 mn of MtrA N-terminal protein solutions, at different time points. Using the program SEDFIT, these scans were collated and fitted to Lamm equations (Schuck, 2000). These can be seen as the lines passing through the real data points. The Lamm equations produced are a good fit to the real data, as demonstrated by the low deviance in the residuals.

Using the Lamm equations produced by the fitted data, sedimentation analysis was performed. Panel B demonstrates the coefficient of sedimentation histogram plot. This shows that there was only one predicted species for the scattering data with a sedimentation coefficient of 2.3 S. From the molecular weight distribution analysis, the protein causing this peak was predicted to have a molecular weight of 22 kDa. This is very similar to the in-silico predicted molecular weight of MtrA N based on sequence composition. Figure 3.6 Panel C shows the Holde-Weischet plot of the data produced using ULTRASCAN (Demeler & van Holde, 2004). This analysis indicates that all of the collected absorbance aligns well, predicting a single sedimenting species of 2.3 S. It also indicates that the apparent molecular weight doesn't change over the course of the experimentas as the protein solution concentrates.

ULTRASCAN was also used to calculate the frictional coefficient ratio F/F_0 of MtrA N-temrinus. It was calucated to be 1.42. As with the F/F_0 ratio calculated for MtrA, this ratio indicates that MtrA N is elongated along at least one axis. Estimate of the length of the axis were made using the axial ratio prediction software of ULTRASCAN. Applying the presumption that MtrA N is prolate in shape, the major axis was predicted to be 75 Å and the minor axis 11Å.

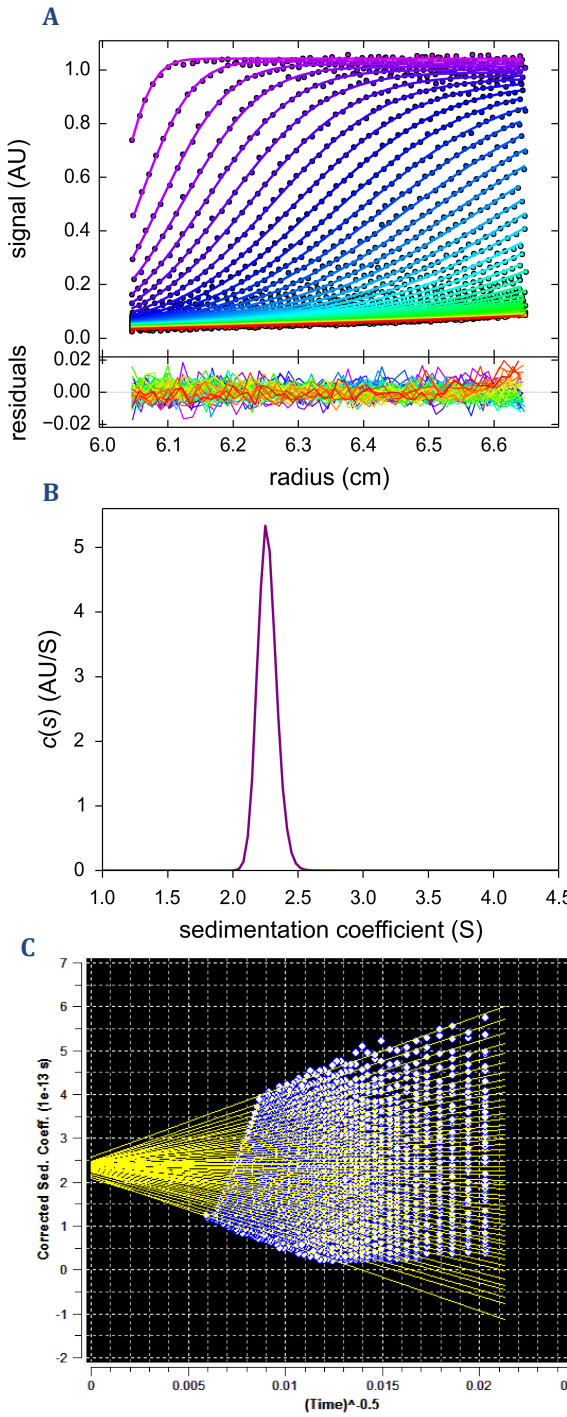

Raw data fitted in SEDFIT

SEDFIT c(s) analysis

ULTRASCAN Holde-Weischet plot

Figure 3.6. Analytical Ultracentrifugation of MtrA N, sedimentation velocity experiments.
Panel A. [coloured dots] Selected 410 nm radial absorbance profiles of MtrA N protein solutions, [coloured lines] fitted Lamm equations. The residuals of these fits are presented beneath the radial scans. All data processed using SEDFIT.
Panel B. The c(s) analysis output for MtrA N from SEDFIT.
Panel C. Holde-Weischet plot of MtrA N AUV velocity experiment; made using ULTRASCAN.

Analytical Ultracentrifugation of MtrA C terminus

Sedimentation velocity experiments mirroring those performed upon the MtrA and MtrA N proteins were completed on a sample of MtrA C. Radial absorbance scans measuring 410 nm absorbance were collected as the sample was centrifuged at 42,000 rpm in a Beckman XL-A using a Ti-45 rotor. A concentration range of 0.1, 0.05 and 0.01 $mg.mL^{-1}$ MtrA C was tested. These results were then interpreted using the SEDFIT and ULTRASCAN programs as before, shown in Figure 3.7.

Figure 3.7. Panel A. shows the radial absorbance at 410 mn of MtrA C protein solution at different time points throughout the experiment. Using the program SEDFIT, these scans were collated and fitted to ideal Lamm equations (Schuck, 2000). The Lamm equations are displayed as the line overlaying the real data points. It is apparent from the deviations of the residuals of the Lamm equations to the actual absorbance data, shown at the bottom of Panel A, that there are some disparities between the fits and the real data. This could mean there is a lot of noise within the data, or that the signals produced from MtrA C are not very strong. These residuals are larger than those for the MtrA N and MtrA AUC sedimentation velocity experiments, and thus any calculations based on this fit are therefore less reliable.

Using the Lamm equations that had been fitted to the data c(s) analysis was performed using SEDFIT, with the resulting distribution shown in Figure 3.7 Panel B. A single sedimentation peak at 2.3 S can be observed, with a distribution bias towards higher S. This may indicate that there are multiple sedimenting species overlapping within the distribution. Despite the non symmetrical peak distribution, the predicted sedimentation coefficient for MtrA C was 2.1 S. The same sedimentation coefficient as that predicted for MtrA N. The molecular weight of MtrA C was calculated to be 21 kDa, again similar to MtrA N. Comparing this result to the AUC sedimentation velocity experiments conducted on MtrA, both MtrA N and MtrA C appear to be half the molecular weight of MtrA, which is consistent with the sequences and compositions of the truncations compared to the full-length protein.

The MtrA C data was also analysed using ULTRASCAN. Lamm equations that fit the data better, with smaller residuals, were calculated. This was achieved through excluding a larger proportion of scans used and sections of each individual scan. Although still not as

accurate as the fits produced for MtrA and MtrA N AUC experiments, some improvement was made in the reduction of the residuals. ULTRASCAN was then used to produce c(s) analysis, shown in Figure 3.7. Panel C. This analysis predicts a main peak at 2.3 S, with one much smaller peak at 37 S. The MtrA C-terminal sample was not purified to homogeneity, unlike the MtrA and MtrA C samples. Nevertheless, the MtrA C was the only heme containing protein in the sample, allowing the characteristic 410 nm soret-absorbance to be used in tracking the radial distribution of MtrA C during the experiment. MtrA C was presumably interacting and tightly associating with contaminants (which may explain why it was extremely difficult to get rid of them) or with itself, causing peaks corresponding to larger proteins to appear in the analysis. This association with other proteins changed the sedimentation profile of only a small subset of the MtrA C, which caused a small population to be seen with a high sedimentation coefficient. The majority of the detected MtrA C was seen at 2.3 S.

ULTRASCAN was used to calculate the frictional coefficient ratio F/F_0 of MtrA C. It was calucated to be 1.43. This indicated that the protein was not likely to be globular and instead be highly extended in one axis, which is similar to MtrA and MtrA N. Assuming that the protein was prolate (as MtrA N and MtrA were theorised to be), the axial ratio prediction program in ULTRASCAN calcualted MtrA C to have a major axis 75 Å long and a minor axis making it 10 Å wide. This is similar the the dimensions of MtrA N.

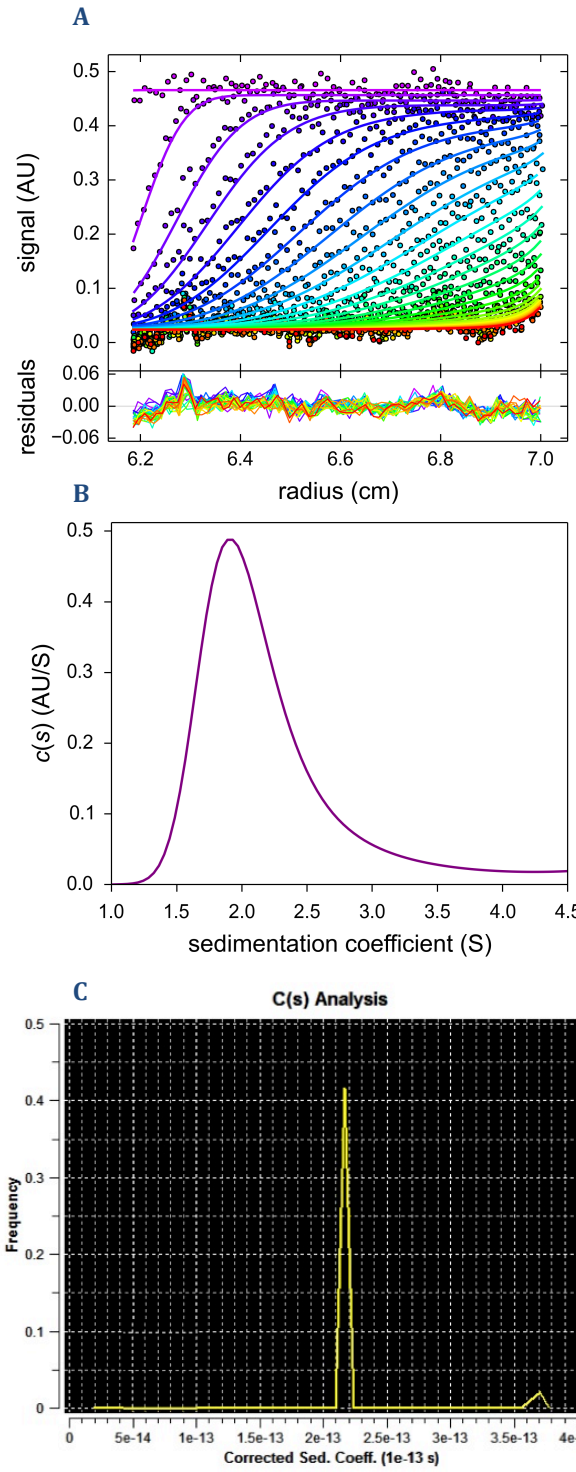

Raw data fitted in SEDFIT

SEDFIT c(s) analysis

ULTRASCAN c(s) analysis

Figure 3.7 Analytical Ultracentrifugation of MtrA C sedimentation velocity experiments.
Panel A. Selected absorbance profiles of MtrA C over time, with the fitted Lamm equations and the residuals of these fits presented using SEDFIT.
Panel B. The c(s) analysis output for MtrA C from SEDFIT.
Panel C. The c(s) analysis output for MtrA C from ULTRASCAN.

3.04 SAXS of multi-heme cytochromes

Small angle X-ray scattering (SAXS) was used to investigate the shapes of several multi-heme cytochromes. Small angle scattering works through placing freely soluble samples in a particle beam, in this case an X-ray beam, and then collecting and interpreting the radially isotropic scattering pattern that is created. Unlike crystallographic methods the molecules used in SAXS experiments are not bonded within a crystal lattice, thus may have a less constrained form. Therefore, this technique is particularly useful for investigating molecules or proteins that do not readily crystallize or contain co-factors that would complicate NMR experiments (such as hemes).

Experiments were conducted as described in the Materials and Methods section 2.21. The experiments relied on the pipeline suite of software (Petoukhov *et al.*, 2007; Petoukhov *et al.*, 2012; Franke, 2012) to automatically process raw data, taking two dimensional scattering patterns and radially averaging them to produce a scattering curve of momentum transfer q.$Å^{-1}$ (scattering angle) against the average radial intensity I. Background noise and scattering caused by the buffer was removed through subtracting buffer-only scattering profiles from the full protein scattering profiles. This process was repeated for a concentration series of the protein, with at least ten scattering profiles being collected and then averaged for each concentration. The radius of gyration was calculated from each concentration's scattering curve by the Guinier approximation, Equation 3.2.

$$I(q) = I(0)\exp\left[-\frac{(q^2R_G^2)}{3}\right]$$

Equation 3.2 The Guinier approximation of Rg

This is the average distribution of mass around the axis of the protein passing through the center of mass. It gives an indication of the protein shape. The scattering curve can then be analysed in various different graphical means that can give insight into the shape of the protein.

To allow full simulation of the protein's shape, the pair distribution function P(r) needs to be calculated through creating a line of best fit through the scattering profile. This was completed by the program GNOM, which calculated a fit based on Equation 3.3.

$$P(r) = \frac{r}{2\pi^2}\int_0^\infty I(q)q\sin(qr).dr$$

Equation 3.3. The pair distribution function, which links the scattering intensity over all angles to the distribution of scattering components of an object.

The calculated pair distribution function was then used in conjunction with the program, DAMMIF (Franke & Svergun, 2009), which took spheres (or beads) in real space and rearranged them into positions that satisfied the P(r) distribution profile. As there are many potential configurations in which the beads could be arranged to satisfy the P(r) curve, multiple simulations were run and an average taken. This average was then checked against other independent data to ensure its validity.

Characterization of small tetraheme cytochrome

Small tetraheme cytochrome (STC) is a periplasmic protein expressed by *S. oneidensis* MR-1. It is thought to be involved with the electron transfer to MtrA, with it possibly acting as a periplasmic electron shuttle (Ross *et al*., 2007; Hartshorne *et al*., 2009). It was therefore an interesting protein to study because comparisons could be made between it and MtrA.

STC was purified to a very high standard by Christopher Beckwith (UEA), with purity exceeding 99% w/w and concentrations of 2.83 mg.mL^{-1} reached. Dynamic light scattering (DLS) measurements were taken during purification which indicated that the sample was less than 9% polydisperse. Results were produced from DLS experiments collecting over 100 positive scattering counts. The results made it an ideal sample to trial for SAXS experiments.

SAXS measurements were taken by Dr Andrew Hemmings (UEA) at the ESRF B26 beam-line in Grenoble. Each step of a five step concentration gradient from 0.18 to 2.83 mg.mL^{-1} of STC in 20 mM HEPES pH 7.5 100 mM NaCl was irradiated ten times, each scan radially averaged and then an overall average scattering profile produced. Data reduction was performed using the ATSAS software suite (Petoukhov *et al*., 2007; Petoukhov *et al*., 2012; Franke *et al*., 2012).

Figure 3.8. Panel A shows the Guinier scattering profiles of the range of concentrations examined. Each of the scattering curves produced a straight line within the Guinier region, indicating that there is no aggregation. Each of the curves also shows a scalar increase in scattering intensity proportional to the concentration of the protein in each sample. Panel B shows the calculated radius of gyration (Rg) and the theoretical intensity of scattering at the zero momentum transfer (I_0) values calculated for each experiment. At each concentration, the Rg values remain constant, irrespective of the concentration of the experimental sample of STC. This indicates no aggregation in any of the samples. There are slight differences between the Rg values calculated, but these are small and do not follow a concentration dependent trend. The I_0 values are also fairly consistent, irrespective of concentration. There is a negative correlation of I_0 with increasing concentration, however the changes observed are minor. These factors indicate a reliable data set suitable for further analysis. Panel C shows a scattering profile composed of the best sections from each of the scattering profiles. This merged scattering profile was compiled through the ATSAS software suite program PRIMUS (Konarev *et al*., 2003). When this data is arranged in a Guinier plot, a straight line is observed in the Guinier region, shown as an insert in Panel C. The calculated Rg and I_0 values were 1.42 and 12.88 respectively, which matched well with the values shown in Panel B.

Figure 3.8 Panel D shows a Kratky plot of the merged scattering profile from Panel C. The plot shows one peak at around 1.3 q. At higher q the I.(q^2) does not increase and it forms a level tail on one side of the single peak. This suggests that there is one globular region of STC with no flexible tail region. Panel E shows the merged scattering data as grey circles. The fit used to calculated the P(r) function of STC using the program GNOM (Svergun, 1992), is shown as the black line on Panel E. The closeness of the line to the data points demonstrates that the fit produced from the STC scattering data was representative of the actual data, as the line overlays the data well. Panel F shows the pair distribution function calculated for STC. The function shows one main peak, which is indicative of a globular protein.

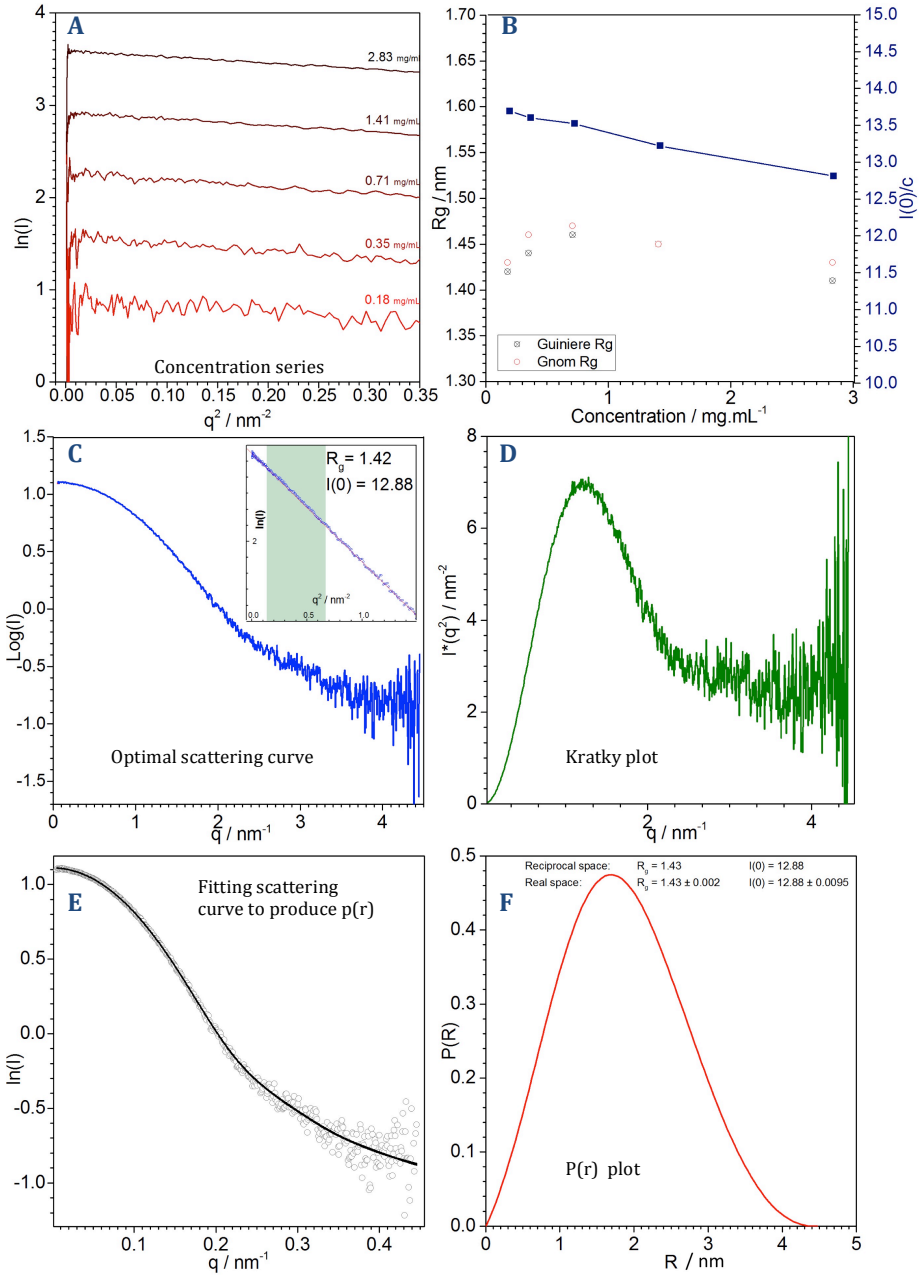

Figure 3. 8 Small angle x-ray scattering results for `STC purified from *Shewanella oneidensis*.
Panel A guinier plot of the Guinier region of each scattering curve of a concentration series
Panel B [connected blue squares] the I_0 calculated for each experimental concentration. [red circles] the Radius of gyration calculated through the guinier plot of each STC concentration. [black crossed circles] radius of gyration calculated through the program GNOM.
Panel C. [blue line] the scattering curve created by merging the best sections of each scattering curve from the concentration series. [insert graph] Guiner plot of the merged scattering curve. The highlighted green section is the Guinier region.
Panel D. Kratky plot of the merged scattering curve.
Panel E. [grey circles] merged scattering data points. [black line] simulated fit of merged scattering data points created by GNOM.
Panel F. Pair distribution plot produced by GNOM from merged scattering data set.

The program DAMMIF (Volkov & Svergun, 2003) was used to simulate a bead model based on the P(r) function in Figure 5. Panel F. This model was constructed from ~1300 beads and set to slow annealing settings. This process was repeated ten times and the individual results for each simulation are shown in Figure 3.9.

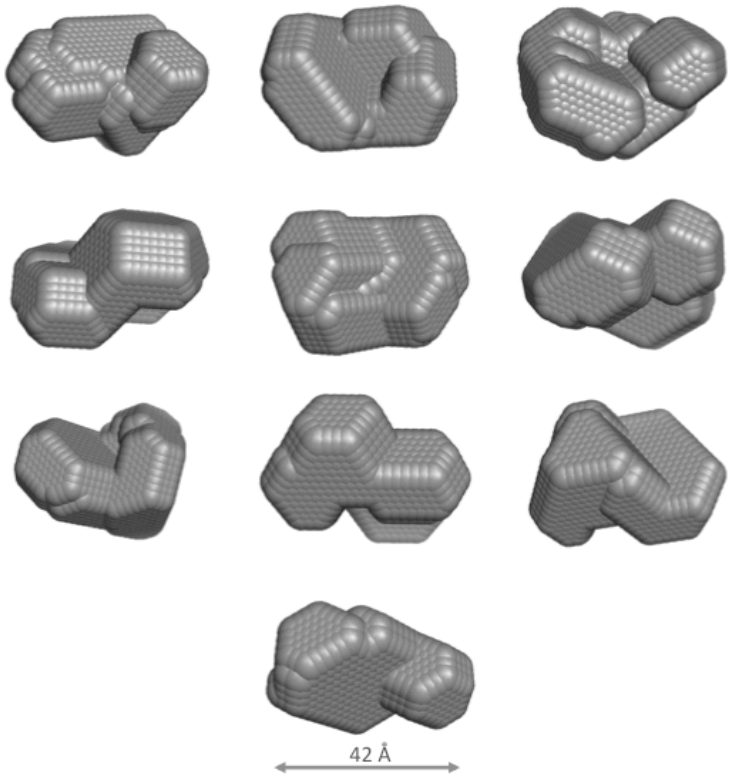

Figure 3. 9 Ten slow annealing bead model simulations created by DAMMIF. Based on the pair distribution plot of STC.

Figure 3.9 demonstrates all ten simulations of STC produced by DAMMIF. Each of the simulations is unique, but bear some similarities to each other. Each of the simulations is globular and slightly oblate. All the simulations contain a small cleft in the center of the minor-axis face. To further understand how each of these simulations contributes to the overall understanding of the shape of STC, an average of all the simulations was then calculated.

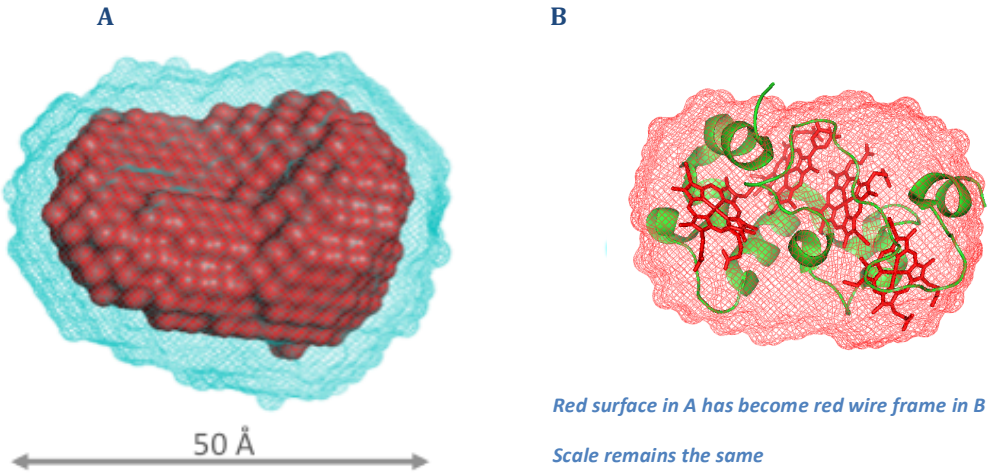

Figure 3. 10 SAXS models of STC.
Panel A. [red surface envelope] bead model predicted by DAMFILT, containing common structures in all DAMMIF simulations. [blue wire mesh] Average bead model envelope of all DAMMIF simulations, produced by DAMAVER.
Panel B. [wire mesh envelope] DAMFILT bead model of STC DAMMIF simulations. [cartoon protein structure] crystallographic protein structure of STC published in the protein data bank, heme co-factors highlighted in red. PDB entry 1m1p.

Figure 3.10 Panel A shows two average dummy atom simulations that have been aligned and overlaid using the program SUPCOMB (Kozin & Svergun, 2001). The red surface is the filtered molecular envelope produced by DAMFILT (Volkov & Svergun, 2003). This is the shape consistently contained within all the DAMMIF simulations. This gives a strong indication that these are highly probable features. The green wire frame is the average dummy atom arrangement of all the DAMMIF simulated shapes. This average was produced by the program DAMAVER (Volkov & Svergun, 2003). This molecular envelope gives an average representation of what the STC simulations look like and takes a weighted account of any unique features present in one simulation. The DAMFILT and DAMAVER simulations fit well together, the DAMFILT model being more condensed and smaller than the DAMAVER model with the DAMAVER model being approximately 50 Å x 30 Å x 20 Å and the DAMFILT model being roughly 40 Å x 25 Å x 15 Å. Both models have a cleft or indent on one of the major faces of the globular structure.

Figure 3.10 Panel B shows the filtered DAMFILT molecular envelope, depicted in a blue wire-frame, aligned with the crystal structure of STC from *S. onediensis* PDB entry 1m1p (Leys *et al.*, 2002). This was completed by using the program SUPCOMB. The crystal structure aligns within the SAXS envelope with a high degree of similarity. All of the crystal structure fits within the DAMFILT molecular envelope, except for three specific regions; the final section of the N terminus, a highly contorted loop region joining two α

helices and the edge of the porphyrin ring of the first heme cofactor. This similarity between the crystal structure and the SAXS envelope is convincing evidence that the SAXS model is representative. The sections of the STC amino acid chain that do not fit with the SAXS molecular envelope could be regions that are constrained when forming a crystal lattice and thus do not adopt a native conformation. Likewise these regions of mismatch, including the heme co-factor, could indicate areas of the SAXS molecular envelope that are incorrectly modeled by using the DAMFILT molecular envelope. When aligning the larger DAMAVER molecular envelope with the STC crystal structure, there are no regions that protrude from the molecular envelope.

Small Angle X-ray Scattering of MtrA N

No crystallographic-based techniques have so far been successful in providing a structure of MtrA, and similar trials conducted on MtrA N were similarly unsuccessful. During crystallographic trials where 5 and 10 $mg.mL^{-1}$ MtrA N samples were incubated in a wide variety of commercial crystallographic screens at both 10 and 5 °C, the MtrA N predominantly formed aggregates instead of crystals. Like STC, the small cytochrome MtrA N was a suitable candidate for SAXS experiments and these experiments were conducted as described in the section 2.21. A concentration range of 0.21 through to 3.38 $mg.mL^{-1}$ MtrA N was used for experiments at the ESRF B26 in Grenoble, conducted by Dr A Hemmings (UEA).

Figure 3.11. Panel A shows a Guinier plot of each of the concentrations of MtrA N experimentally examined. All of the concentrations tested produced a linear Guinier region and the scattering intensity increased proportionally with concentration. This indicates that none of the samples are aggregating. Panel B shows the calculated radius of gyration (Rg) and the theoretical intensity of scattering at zero momentum transfer (I_0) of the samples. The Rg values calculated either from AUTORG (Konarev *et al*., 2003) using the Guinier approximation method or through the GNOM program (Svergun, 1992), both produce a value of around 1.95 Å. This similarity in Rg helps support the idea that the data collected is reliable. The calculated values of I_0 exhibit a negative correlation with increasing concentration, however the overall change is minor.

Figure 3.11 Panel C shows a scattering profile composed of the best sections from each of the scattering profiles, maximizing the low q regions by using high concentration scattering profiles and other regions from lower concentration curves. The program PRIMUS (Konarev *et al*., 2003) was used to achieve this. When plotted on a Guinier graph this merged scattering profile produced a straight line in the Guinier region, shown in the insert in Panel C. The calculated Rg and I_0 values were 1.95 and 48.73 respectively, which matched well with the values shown in Panel B. Panel D shows a Kratky plot of the merged scattering profile. The data displays one peak and then a positively sloping tail, with increasing q^2. This indicates that there is likely to be a globular region of MtrA and then a flexible tail region. Panel E shows the merged scattering data for MtrA N, represented as grey circles. The program GNOM (Svergun, 1992) was used to fit a curve to this data, which allowed the calculation of a P(r) function for MtrA N. This fit is shown as a black

line, overlaying the grey circles. The black line fits the data well. Panel F shows the pair distribution function calculated for MtrA N. The function shows one main peak with an extended tail towards higher R. This is possibly indicative of a globular protein with an elongated tail at one end.

Using the P(r) function calculated in Figure 3.11 Panel F, the program DAMMIF, (Franke & Svergun, 2009) was used to create dummy atom models that had the same distribution of pairs of atoms. This was completed ten times using slow annealing settings. The results of each of the simulations are depicted in Figure 3.12.

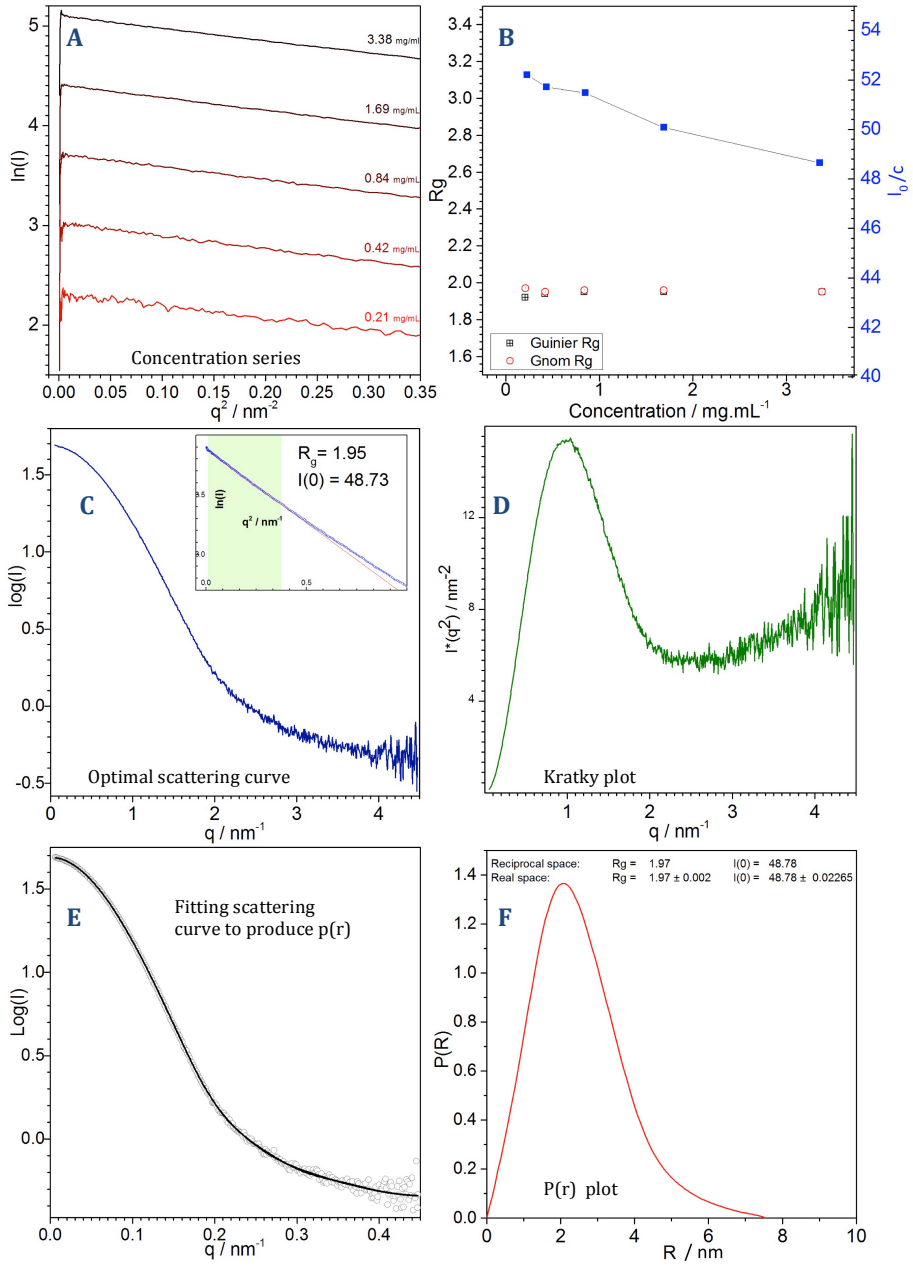

Figure 3. 11 Small Angle X-Ray Scattering of MtrA N purified from recombinant *E coli*.
Panel A. Guinier plot of the guinier region of each scattering curve produced from the concentration series experimentally examined.
Panel B [connected blue squares] the I_0 calculated for each experimental concentration. [red circles] the radius of gyration calculated through the guinier plot of each STC concentration. [black crossed circles] radius of gyration calculated through the program GNOM.
Panel C. [blue line] the scattering curve created by merging the best sections of each scattering curve from the concentration series. [insert] Guiner plot of the merged scattering curve.
Panel D..Kratky plot of the merged scattering curve.
Panel E. [grey circles] merged scattering data points. [black line] simulated fit of merged scattering data points created by GNOM.
Panel F. Pair distribution plot produced by GNOM from merged scattering data set.

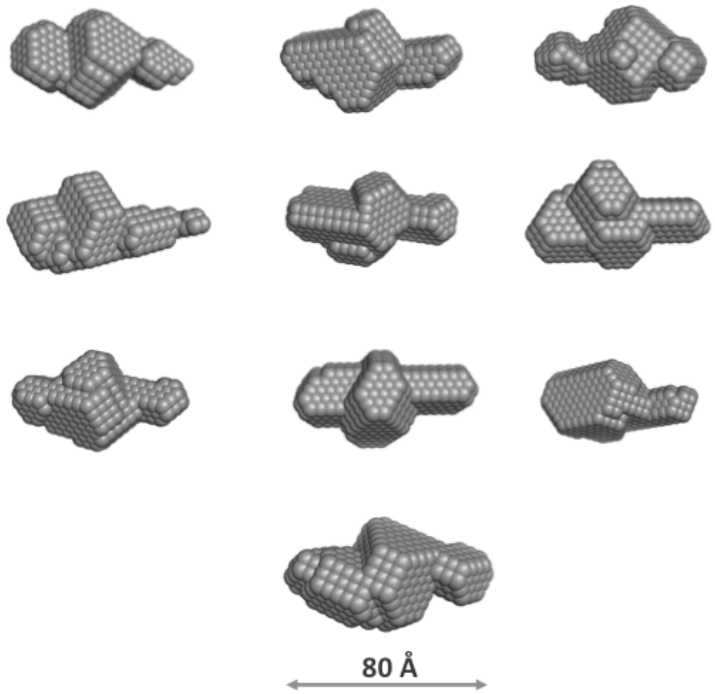

Figure 3. 12 Ten slow annealing bead model simulations of based on the calculated pair distribution function of MtrA N scattering data.

All of the bead models resulting from simulations shown in Figure 3.12 are approximately 80 Å in length and are present in a roughly prolate form. They have a globular region, which is around 50 Å x 20 Å x 20 Å and a thinner elongated tail region that is around 30 x 15 x 15 $Å^3$ in dimension. These suggested models produce characteristics that are congruent with the findings resulting from analysis of MtrA N using analytical ultracentrifugation. The ten DAMMIF simulations were then averaged and filtered using DAMFILT and DAMAVER (Volkov & Svergun, 2003) shown in Figure 3.13.

Figure 3.13 Panel A shows the DAMAVER average molecular envelope aligned with a DAMFILT filtered molecular envelope, both of which were calculated using the ten DAMMIF simulations in Figure 3.12. The DAMAVER average is shown as a blue wire mesh and the DAMFILT filtered molecular envelope as a red surface. The DAMAVER and the DAMFILT models were then aligned using the program SUPCOMB (Kozin & Svergun, 2001). As can be seen, the DAMAVER and DAMFILT models are very similar to each other, with the DAMFILT model being slightly smaller than the DAMAVER model. Both contain

the same features; a globular region and a small protruding tail region. The globular region has a small indented section on one of its major faces.

Figure 3.13. Panel B shows the DAMFILT model for MtrA N oriented to optimally superpose the crystal structure of STC within it (Leys *et al.*, 2002). This was achieved though the program SUPCOMB (Kozin & Svergun, 2001). The crystal structure is represented in cartoon form, colour coded blue for the STC N-terminus and red for the STC C-terminus. Heme co-factors are highlighted in red. The STC crystal structure fits neatly within the MtrA N DAMFILT molecular envelope, with no sections of the crystal structure extruding from the SAXS reconstructed molecular envelope. The hemes of the STC structure are oriented along the major axis of the MtrA N molecular envelope, as would be predicted if MtrA functions as a protein "wire". The superposition of STC and MtrA N can be compared and contrasted with the superposition of MtrA N and NrfB. As is shown in Figure 3.14. Panel C, NrfB is predicted to be an evolutionary ancestor of MtrA, based on sequence similarity (Clarke *et al.*, 2011). In this paper, the authors predict that a duplication event of NrfB led to the evolution of MtrA, which is the reason it contains ten hemes.

The crystal structure of NrfB (Clarke *et al.*, 2007) was aligned with the MtrA N DAMFILT molecular envelope, again using the program SUPCOMB. The alignment of the crystal structure and the SAXS molecular envelope shows that the five hemes of NrfB fit inside the DAMFILT molecular envelope. This alignment predicts that the five hemes align along the major axis of MtrA N. However, certain protein chains of NrfB do not fit within the DAMFILT molecular envelope. The amino acid chain that links the second and third alpha helices of NrfB protrudes. This linker region may have inherent flexibility when not confined within a crystal lattice and does not protrude form the SAXS envelope very far. The C-terminal alpha helix of NrfB also does not fit within the DAMFILT molecular envelope, although it only protrudes a slight distance. It protrudes through a small globular hump protruding slightly from the surface of the SAXS molecular envelope, indicating that this region of the SAXS envelope may have been modeled to be slightly too small. If this hump were bigger it would encompass the currently protruding amino acid chain. Alternatively, it may be the case that the helix protrudes because it is extended in an unnatural way due to crystal packing interactions.

Alignments of the MtrA N molecular envelope to NrfB and STC can be compared. The crystal structure of STC is smaller than the crystal structure of NrfB. This reduction in size means that the STC crystal structure does not have any regions that protrude from the SAXS molecular envelope when aligned together. This is in contrast to the NrfB crystal structure when aligned with the SAXS molecular envelope. The alignment of STC with MtrA N does leave a space within the MtrA N SAXS molecular envelope, at the C-terminal end of STC, which appears to be approximately the space required to fit a fifth heme. This could mean that MtrA N evolved through STC gaining an additional heme and then underwent a gene duplication event, instead of evolving through NrfB.

Panel D shows the MtrA N DAMFILT SAXS molecular envelope aligned with an in-silico prediction of the crystal structure of MtrA, developed by Dr A. Hemmings (unpublished work). This *in silico* structure was created from hidden Markov models based on common heme packing motifs. The alignment was completed using SUPCOMB (Kozin & Svergun, 2001). The predicted structure of MtrA did not align well with the SAXS molecular envelope of MtrA N. MtrA N is composed of roughly half of the amount of protein and exactly half of the number of heme cofactors as MtrA. Thus, there are sections of the MtrA structure that are aligned outside the SAXS molecular envelope. The N terminal heme of the MtrA in-silico crystal structure sits outside the globular region of the MtrA N SAXS molecular envelope, with the next four hemes sitting inside the globular region. The final five hemes of the MtrA in-silico crystal structure (the C terminal hemes) are aligned with the short tail in the MtrA N SAXS molecular envelope. The width of the secondary structure of this C terminal region is wider than the short tail in the SAXS molecular envelope. As a result, some of the protein and parts of the heme cofactors do not reside molecular envelope, with major sections being too wide and too long. As the small tail region of the MtrA N SAXS molecular envelope is too small to encompass a heme cofactor, it can be deduced that the globular region described in the MtrA N SAXS molecular envelope would contain all the heme co-factors in the MtrA N.

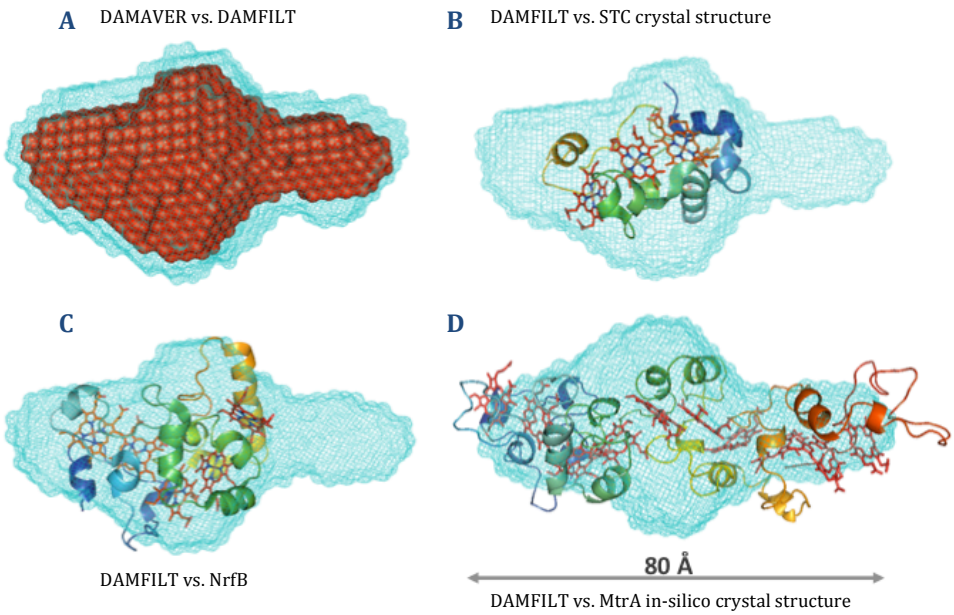

Figure 3. 13 The average molecular envelopes calculated by DAMMIF for the MtrA N SAXS data.
Panel A. [red surface envelope] the DAMFILT calculated bead model of all the common components of all the MtrA N simulations. [Blue wire surface] the average molecular envelope of the MtrA N bead model simulations, calculated by DAMAVER.
Panel B. [Blue wire mesh] the DAMFILT molecular envelope. [cartoon protein structure] The crystal structure of STC published in the protein data bank (code 1m1p).
Panel C. [Blue wire mesh] the DAMFILT molecular envelope. [Cartoon protein structure] the structure of NrfB published in the protein data bank (code 2OZY)
Panel D. [Blue wire mesh] the DAMFILT molecular envelope. [cartoon protein structure] In-silico prediction of the structure of MtrA (unpublished data, Dr A Hemmings).

Small Angle X-ray Scattering of MtrA

Extensive screening of crystallographic conditions was conducted with the aim of producing diffracting crystals of MtrA. Commercially available screens of TMPro, PACT, MBX Class 2 were set up with concentrations of MtrA at 10 and 20 mg/mL and incubated at both 16 and 4 degrees centigrade. All of the trialed conditions failed to produce diffracting crystals. The experimental conditions usually caused the protein to aggregate. Crystallographic conditions tested by Dr T. Clarke (UEA) did on one occasion produce a single crystal. This crystal diffracted but produced a perfectly twinned dataset, meaning a structure could not be constructed. Repeats of the condition failed to reproduce any crystals, and nor did any similar conditions.

Due to the lack of crystallographic data, alternate methodologies for gaining structural information were investigated. Firer-Sherwood *et al*., (2011) used a combination of SAXS and AUC to build a model of the molecular envelope of MtrA. In this paper the authors found the molecular weight of MtrA to be 42 kDa and the shape of MtrA to be 104 Å x 40 Å x 30 Å, with a paddle or spoon shape containing a concave semi globular head region. The relationship of the protein sequence to this molecular envelope was not made clear, presumably due to the resolution of SAXS re-constructions. Therefore, no indication was given as to how the MtrA sequence forms the shape predicted and how the heme cofactors are align within it.

The purpose of this section is to compare the molecular envelopes of MtrA with those of MtrA N. Using these alignments, predictions can then be made as to which end of the molecular envelope maps to specific parts of the amino acid sequence. Additionally this would allow hypotheses about the orientation of MtrA within the MtrB barrel to be developed if MtrA is unsymmetrical along one axis.

The shape of MtrA was investigated through small angle X-ray scattering. Three separate experiments were conducted, all as described in the Materials and Methods section 2.21. The first two experiments investigated a concentration range of MtrA from 0.20 through to 10 $mg.mL^{-1}$. In each of the experiments, the buffer composition was slightly altered. The first experiment repeated the experimental buffer conditions of Firer-Sherwood *et al*., (2011) using HEPES 20 mM tris pH 8, 50 mM NaCl, which was carried out on the beamline B26 at the ESRF (conducted by Dr A Hemmings). The second experiment used Tris-Cl 50

mM pH 7.5, 50 mM NaCl and was completed at Diamond Light Source beamline B21. Both these experiments were shown to have aggregating MtrA, Figure 3.14 Panels A and B. In the final experiment all of the remaining stocks of MtrA protein were combined and then concentrated into a single sample, buffered with 20 mM HEPES pH 7.5 150 mM NaCl. Just before exposure to X-rays, the sample was subject to size-exclusion chromatography, ensuring a non-aggregated sample was used. Unfortunately, the SAXS experiment set up was not a capillary linked SEC-SAXS and therefore SAXS was not performed on MtrA as it came off the column. Only one scattering curve was produced as only one sample was collected from the size-exclusion column. This final scattering profile appeared different to previously collected scattering profiles of samples of MtrA at the same concentration. It bore more resemblance to scattering profiles of low concentration samples of MtrA, leading to the hypothesis that this sample of MtrA was behaving in a non-aggregating manner in the X ray beamline.

Figure 3.14 Panel A shows the radially averaged scattering profiles of a concentration series of MtrA, which is an example of one of the first SAXS experiments performed on MtrA. The scattering profiles appear to be aggregating or behaving in a way which is atypical of a freely soluble protein at high concentrations. Panel A shows that as concentrations of MtrA are changed, the shape of the scattering profile changes. New features emerged, dependent on concentration, as opposed to the same features being apparent in each scan to a higher or lower degree of intensity depending on concentration. Panel B shows the Kratky plots for each of the experiments shown in Panel A. These graphs show that there is a peak in the low q regions for all of the concentrations tested. In the high q region there is a positively sloping tail. Together, these features suggest a globular region and a flexible region. Higher concentrations of MtrA seem to have higher degrees of flexibility of this tail, compared to low concentration samples, as the slope in the Kratky plot increases. The aggregation and concentration dependence of MtrA in the SAXS experiment could indicate that MtrA does not have a particularly stable form in isolation, which may suggest that MtrA requires the presence of the MtrB barrel in order to be stabilized.

Figure 3.14 Panel C shows the scattering profile of MtrA from the final experiment that was determined to be non-aggregating. This scattering profile is shown as the red squares and is contrasted to the scattering profile of MtrA of similar concentration from the second experiment that was concluded to be aggregating or unfolding, shown in blue squares. The

two scattering profiles are different, particularly at mid to high q, where the red squares have higher values of intensity than the blue squares. Differences between the two scattering profiles are also observable in Panel D. This compares the Kratky plots of the two MtrA data sets. As can be seen, the blue Kratky plot of the aggregated or misbehaving data has a positively sloped tail region at high q values. This is contrasted with the red scattering profile, which has a more level tail in the high q region. This indicates that the blue (aggregating) sample has a flexible or disordered region, whereas the red MtrA scattering profile does not. Both data sets have a similar peak at low q, indicative of a globular region.

The sequence of MtrA was analysed using DISPro for sections of structural disorder (Cheng *et al*., 2005). Sections of disordered protein were predicted using the amino acid sequence of MtrA, and were compared to template proteins where disorder is known. There were disordered regions predicted in the C terminus of MtrA, after the tenth heme binding site in the last 20 amino acids, of MtrA's sequence. This potential region of disorder could explain why some samples of MtrA appeared aggregated in SAXS experiments. This result would also explain why MtrA C samples were difficult to purify, as it would have a high level of intrinsic disorder.

Panel E shows the well-behaving scattering profile of MtrA (previously depicted in red square) and a fit produced by the program GNOM (Svergun, 1992). This fit was used to calculate the pair distribution function. The program GNOM was limited to calculating a scattering profile of maximal dimension of 200 Å. This was longer than the D-max chord length predicted in Firer-Sherwood *et al*., (2011), but was in line with the predicted axial length from AUC experiments and produced the best fit of the data. As can be seen, the simulated fit of the data is consistent with the actual scattering profile for most of the range. Deviations between the actual data and the simulated fit occur only at the very low and high q regions. From this simulated fit, the pair distribution function was calculated, Panel F. The pair distribution function shows one main peak at around 45 Å and then an extended tail toward high Å. This indicates a globular region with a thick tail on one side.

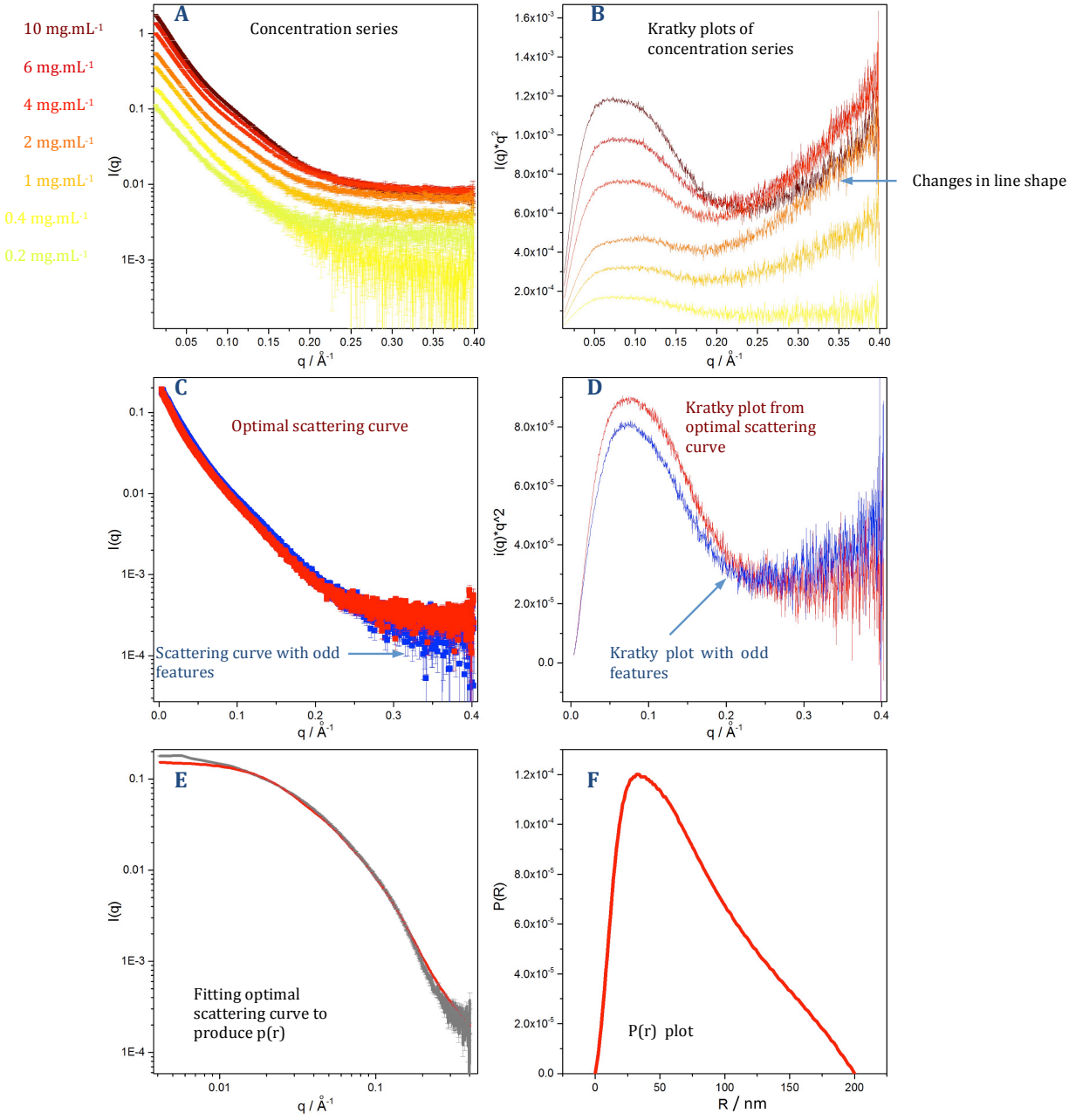

Figure 3. 14 Small angle X-ray scattering of MtrA purified from *S. oneidensis*.
Panel A. Radially averaged scattering profiles from SAXS experiments on MtrA from a concentration series of experiments. These showed signs of aggregation or non-standard scattering behavior,
Panel B. Kratky plots of scattering profiles from Panel A (same concentration series of experiments as Panel A).
Panel C. [Red Squares] Semi log plot of the optimal scattering profile obtained for samples of MtrA. This profile taken directly after size exclusion chromatography. [Blue squares] Semi-log plot of the scattering profile of MtrA behaving in an aggregated or non-canonical manner.
Panel D. [Red line] Kratky plot of the optimal scattering data for MtrA [Blue line] Kratky plot of MtrA behaving in an aggregated or non-canonical manner.
Panel E. [grey line] Radial average of the scattering profile of MtrA. [Red line] Simulated scattering profile created by the program GNOM to allow pair distribution function to be calculated.
Panel F. [Red line] calculated pair distribution function of MtrA.

Using the P(r) function shown in Figure 3.14 Panel F the program DAMMIF (Franke & Svergun, 2009) was used to produce bead model simulations of molecular shapes that comply with the P(r). Figure 3.15. shows twelve bead model simulations produced by DAMMIF, run on its slowest annealing settings.

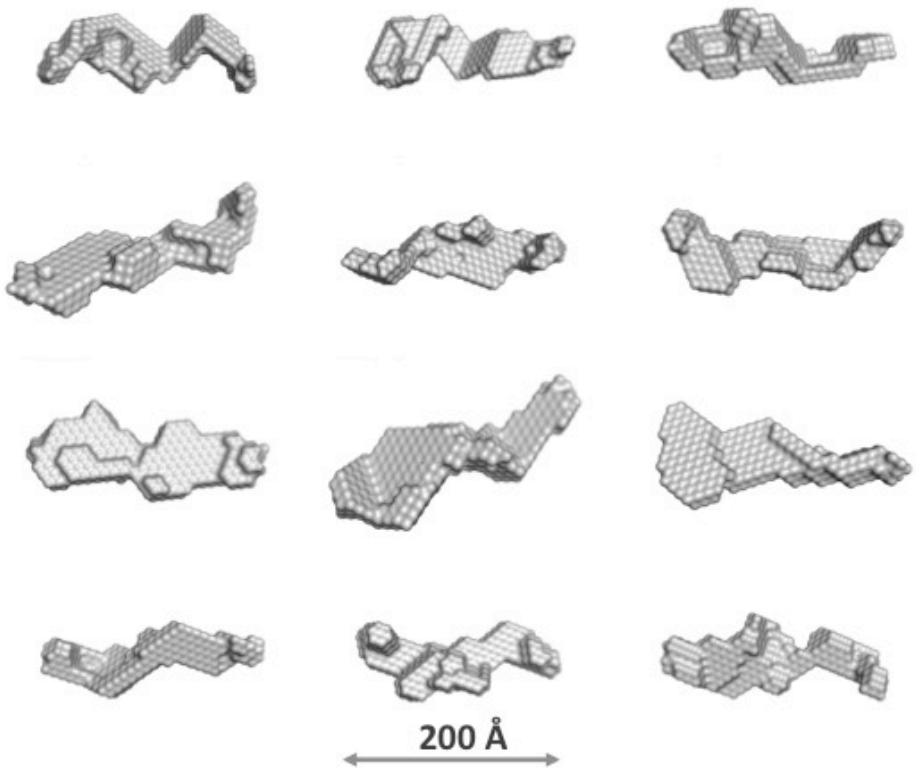

Figure 3. 15 Twelve slow annealing bead model simulations based on the calculated pair distribution function of MtrA scattering data.

Using all of the bead models, average and filtered molecular envelopes were produced using the programs DAMAVER and DAMFILT (Volkov & Svergun, 2003). The two molecular envelopes were then aligned using the program SUPCOMB (Kozin & Svergun, 2001).

Figure 3.16. Panel A shows the alignment between the DAMAVER average molecular envelope and the DAMFILT molecular envelope. The average molecular envelope of MtrA is shown as a red mesh, and the DAMFILT molecular envelope is shown as a blue surface. The simulations show MtrA to be roughly prolate and between 160 Å and 200 Å long. Panel A shows the simulation of MtrA to have a broadly globular domain, presented on the left hand side of the figure, with an indent on one of the major faces and then a thinner tail-like region to the right of the figure. This gives it a spoon or paddle shape. The average molecular envelope is larger in every dimension than the DAMFILT molecular envelope, but bearing the same shape and proportions. Panel B is an alignment of the DAMFILT molecular envelope and an *in silico* prediction of the MtrA crystal produced by Dr A. Hemmings (UEA). The size difference between the two models is large, with the *in silico* crystal structure having a maximal dimension of 100 Å and the DAMFILT molecular envelope having a maximal dimension of 165 Å. This is a substantial difference in size and possibly indicates that the SAXS model of MtrA and/or the *in silico* crystal structure is not representative of the actual shape of the protein. When the two structures are aligned, they do not superpose particularly well, with the SAXS molecular envelope protruding on both sides of the *in silico* crystal structure's major axis.

Panel C shows an alignment of the DAMAVER average molecular envelope of MtrA N (Figure 3.13 Panel A) with the DAMFILT molecular envelope of MtrA. The molecular envelope of MtrA N has several structural features as well as a size that aligns it well to the globular region of the MtrA molecular envelope. Both molecular envelopes have an indent on one of their major faces, aiding the alignment process. The tail region of the molecular envelope of MtrA, that MtrA N does not reside within, seems to be a continuation of the slight tail feature of the MtrA N.

Panel D shows an alignment of the DAMFILT MtrA and DAMFILT MtrA N average molecular envelopes. The two molecular envelopes have structural features that are common between the two. Like Panel C, the two molecular envelopes of Panel D both have an indent on one of their major faces. Like Panel C, this means the MtrA N aligns with a reasonable degree of accuracy to the globular region of the MtrA molecular envelope. Because the MtrA N DAMFILT molecular envelope is smaller than the DAMAVER model of MtrA N, the size difference between MtrA and MtrA N increases when comparing Panel C to Panel D. Because the DAMMIF-produced models are simulations of shapes that merely could be what MtrA or MtrA N looks like, it is hard to say with a high degree of certainty

what the shapes are exactly. It is, however, relevant that the indent or "spoon" shape re-occurs in different models of MtrA.

Panels E and F show the SAXS molecular envelope of MtrA produced by Firer-Sherwood *et al*., (2011). This clearly demonstrates a spoon or paddle-like portion that is of similar size to the globular region of the models produced in this thesis. Because the spoon shape is a common feature between all the models of MtrA, the orientation of each of the models with respect to each other can be determined. The Firer-Sherwood *et al.,* model is also similar to the model in Panel A as it has a small protrusion, similar to the tail structure, coming out of the paddle globular domain. This section is much less extended than the tail sections in Panel A, being only 25 Å in length compared to the 80 Å calculated for the tail in the DAMAVER SAXS molecular envelope. The published MtrA envelope is much shorter and smaller than the MtrA SAXS envelope in every dimension; it is only 20 Å longer than the MtrA N SAXS envelope along the major axis.

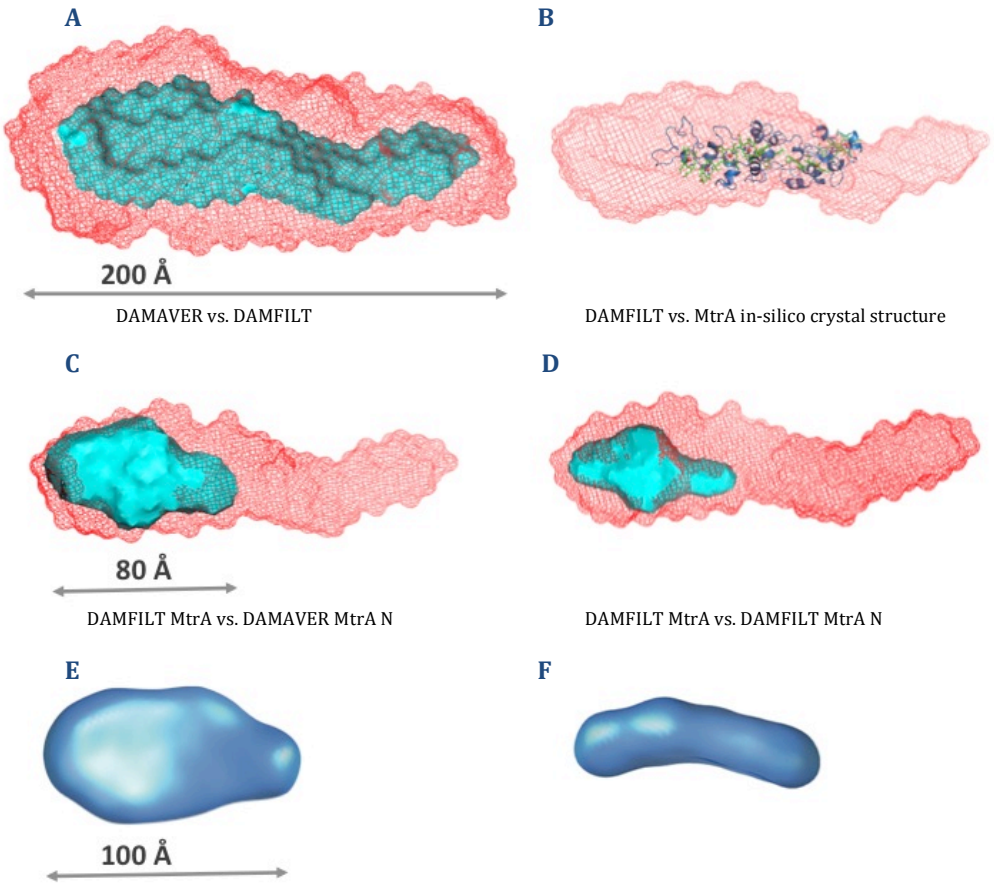

Figure 3. 16 SAXS reconstructions of MtrA.
Panel A. [Red Mesh] Average molecular envelope of the 12 MtrA simulations created by DAMAVER. [Blue surface] the model of all the common components of all the simulations created by DAMFILT.
Panel B. [Red mesh] The molecular envelope of MtrA created by DAMFILT. [cartoon protein structure] The in-silico created, hypothetical structure of MtrA.
Panel C. [Red mesh] The molecular envelope of MtrA created by DAMFILT. [Blue surface] The average molecular envelope of MtrA N.
Panel D. [Red mesh] The molecular envelope of MtrA created by DAMFILT. [Blue surface] The DAMFILT-created molecular envelope of MtrA N.
Panel E and Panel F. [Blue surface] Two views of the average molecular envelope of MtrA as published by Fier-Sherwood *et al* (2011).

3.05 Solution and Electrode redox titrations of MtrA, MtrA N and MtrA C

The role of MtrA as an electron transporter means that redox potentials of the heme groups within the structure may provide insight to the function of the MtrCAB complex. Calculations of redox potentials from a deca-heme protein were investigated through a combination of different redox titrations. Work in Pitts *et al*., (2003) produced a soluble redox titration of MtrA, where two groups of hemes were distinguished at -200 mV and -375 mV. In Hartshorne *et al*., (2009) cyclic voltammetry studies on MtrA adhered as a film on a working electrode had an active redox range of -400 – 0 mV. To expand upon these results, comparisons of redox titrations of MtrA with the N and C-terminus truncations (MtrA N and MtrA C) would allow investigations into the differences between sub sets of hemes within MtrA with known locations. This could increase the resolution with which the redox potentials were described if the potentials of the hemes stayed the same between the full length and truncated MtrA versions. However changes in the structure could cause redox-Bohr effects. These are changes in the heme environment (charge, hydration etc) that cause changes in the heme mid-point potential. Heme environment changes are usually caused when structural changes of protein around the heme occur. Thus the removal of sections of supportive amino acid chains could certainly affect nearby heme environments.

Redox titration experiments were the main method used to investigate the redox properties of the c-heme co-factors within MtrA. They involved varying the potential of MtrA samples and measuring the overall redox state; thereby finding out the proportion of heme co-factors that had been reduced at each potential. Simultaneous monitoring of the overall system potential and the redox state of the cytochromes allowed the experimental calculation of the mid-point potential of redox species. The calculations required to do this are based on the Nernst equation: Equation 3.4.

$$E = E_{0\,Red} - \frac{RT}{nF} ln\left\{\frac{[Red]}{[Ox]}\right\}$$

Equation 3.4. The Nernst equation. E the potential of the environment. E_0 the mid-point potential of the redox species. R, the real gas constant 8.314472 $J.K^{-1}.mol^{-1}$. T, temperature °K of the experiment. n, the number of electrons involved in the redox change. F, the Faraday constant 9.64853x10^4 $C.mol^{-1}$. [Red], the concentration of reduced species. [Ox], the concentration of oxidised species.

Using the algebraic simplification in Equation 3.5 and the relationship describing the ratio of oxidised to reduced species in a closed system Equation 3.6, an equation describing the mid point potentials purely in terms of the concentration of reduced species can be written, Equation 3.7.

$$\frac{[Red]}{[Ox]} = e^{\left[\frac{-nF}{RT}(E-E_0)\right]} = \theta$$

Equation 3.5 Algebraic simplification of terms used in Equation 3.4 in terms of θ.

$$[Ox] + [Red] = 1$$

Equation 3.6. Equation describing the relation between concentrations of oxidised and reduced species when normalized between zero and 1.

$$[Red] = \frac{\theta}{1+\theta}$$

Equation 3.7. The Nernst equation written solely with [Red] being the dependent variable and E being the dependent variable.

Through Equation 3.7, the measurable concentration of the reduced species (expressed as a percentage of total concentration) is equated to the solution potential, certain physical constants, the system's temperature (which is kept constant) and crucially the mid point potential of the redox species. The program ORIGINLAB PRO was used to fit the experimental data to a series of mid point potentials. This was achieved through the program iteratively changing heme mid-point potential parameters and heme-group absorbance contribution weightings within an equation comprised of multiple independent Nernst equations described in Equation 3.7 summed together.

Measuring the overall solution potential is achieved through the use of a Metrohm (Micro PT Titrode) electrode, while monitoring the concentration of the reduced species of heme can be achieved using UV-vis spectroscopy. The α/β region of the heme UV-vis absorbance spectrum has a peak at 552 nm that has a height linearly proportional to the concentration of reduced heme species. This was used to measure the overall redox state of the MtrA hemes and allowed the determination of the proportion that were reduced once the fully reduced and fully oxidised 552 nm peak heights were known. Data was collected on

multiheme cytochromes through two methodologies: soluble redox titrations and optically transparent tin electrode experiments.

Soluble redox titrations

4 mL of protein at a concentration that produced an absorption of 0.5 to 0.8 AU at 410 nm in 20 mM HEPES pH 7.5, 100 mM NaCl was mixed with 4 uL of the redox mediator master mix described in Materials and Methods section 2.18. This protein solution was placed in an anaerobic cuvette and sealed under a continuous flow of argon, causing it to become anaerobic over time, as described in section 2.18. Small additions (between 1-10 µL) of 100 mM sodium dithionite or potassium ferricyanide were added to the cuvette and the overall potential was recorded along with the UV-vis absorbance. The change in absorbance at 552 nm was normalized, based on the highest and lowest absorption measurements, and plotted as a function of potential. The results for MtrA, MtrA N and MtrA C are shown in Figure 3.17.

Figure 3.17. Panel A shows the full UV-vis spectrum of MtrA at each of the potentials assayed. The isobestic point at 560 nm was used to align each scan correcting for absorbance drift of the spectrophotometer. The MtrA scans are coloured according to potential, with gradient from blue (oxidised) to yellow (reduced) in increments in the order of 1-2 mV (this was the same for all soluble redox titrations). This clearly demonstrates the shift in the Soret peak from 401 nm to 420 nm and the appearance of peaks in the α/β region at 530 nm and 552 nm when the protein was reduced. This is indicative of heme reduction. Panel B shows the normalized height of the 552 peak plotted as a function of potential from the data presented in Panel A. The program ORIGINLAB has been used to plot a Nernstian derived curve, consisting of three potential parameters simulating heme groups. Fits with less than three heme-groups produced results that had larger Chi squared values and were therefore less accurate simulations. Fits simulated with more than three heme-group parameters produced results that had multiple heme-groups each of the same potential. Panel B demonstrates that the potential window of MtrA was between -0.05 V and -0.35 V. This is close to the conclusions reached in Hartshorne *et al*., (2009). The Nernstian fit of the data using three heme groups was calculated with a floated contribution from each heme group. The potentials of these are -0.3 V -0.2 V and -0.11 V, with 2.5, 4 and 3.5 hemes in each group respectively.

Panel C. shows the full UV-vis spectrum of MtrA N at each of the potentials assayed. As with Panel A, the isobestic point at 560 nm was used to calibrate each scan. The MtrA N scans are coloured according to potential, with gradient from grey (oxidised) to blue (reduced). The shift in the Soret peak from 410 nm to 420 nm and the appearance of peaks in the α/β region at 530 nm and 552 nm are clearly observed when the protein was reduced. The 552 nm peak height as a function of potential is shown in Panel D. Like Panel B, this data was fitted with a Nernstian derived equation containing two heme group parameters. When the data was fitted using only one heme parameter, Chi squared values indicated a less accurate fit. When the data was fitted using three or more heme parameters, the Chi square value of the fits was not any higher than for two heme parameter fits. The additional parameters duplicated heme potentials found in the two heme parameter fit. The potential window of MtrA N was defined as -0.05 V to -0.25 V. This is smaller than the potential window defined for MtrA, however MtrA N has five fewer hemes contributing to the range of its potential window than MtrA. The potential range encompasses the higher (less negative) section of the potential range observed in MtrA. The predicted heme mid point potentials produced by the fit were -0.12 V and -0.2

V, with 2 and 3 hemes in each group respectively. This places the heme-group mid point potentials found in MtrA N to be almost exactly mapping the highest and the middle heme-groups found in the full length MtrA protein.

Panel E shows the full UV-vis spectrum of MtrA C at each of the potentials assayed. As with Panels A and C, the isobestic point at 560 nm was used to calibrate each scan. The MtrA C scans are coloured according to potential, with gradient from purple (oxidised) to yellow (reduced). The shift in the soret peak from 410 nm to 420 nm and the appearance of peaks in the α/β region at 530 nm and 552 nm are clearly observed when the protein was reduced. However additional absorbance changes can be noted at 600nm. These are much smaller that those found in the α/β region used to calculate heme redox state. His-Met penta-coordinate hemes can be active at 600 nm, and this could indicate partially unbound heme cofactors. Another alternative is that this absorbance is due to impurities within the MtrA C protein solution. The purification of this protein was extremely difficult and the final preparation was about 70 % total purity but only composed of MtrA C heme species. Panel F shows the 552 nm peak height (which is only affected by MtrA C heme proteins, not any potential contaminants) as a function of potential. Panel F shows that the potential window of MtrA C is from -0.12 V to -0.35 V. The 0.22 V potential range of MtrA C is similar to the 0.20 V potential range of MtrA N, however the range covers more negative potentials, being 0.1 V lower than MtrA N. The predicted heme-group mid point potentials from the simulated fit of MtrA C are -0.2 V and -0.29 V. Similar to MtrA N, only two heme groups could be calculated without redundancy occurring in the potentials of heme groups. The heme groups predicted in MtrA C match quite closely to two of the heme-groups found in MtrA, the lowest potential heme group and the middle potential heme group at -0.3 V and -0.22 V respectively. The -0.2 V or middle heme group seems to be recurrent and common throughout all the different forms of MtrA within the soluble redox titration data sets.

MtrA

MtrA N

MtrA C

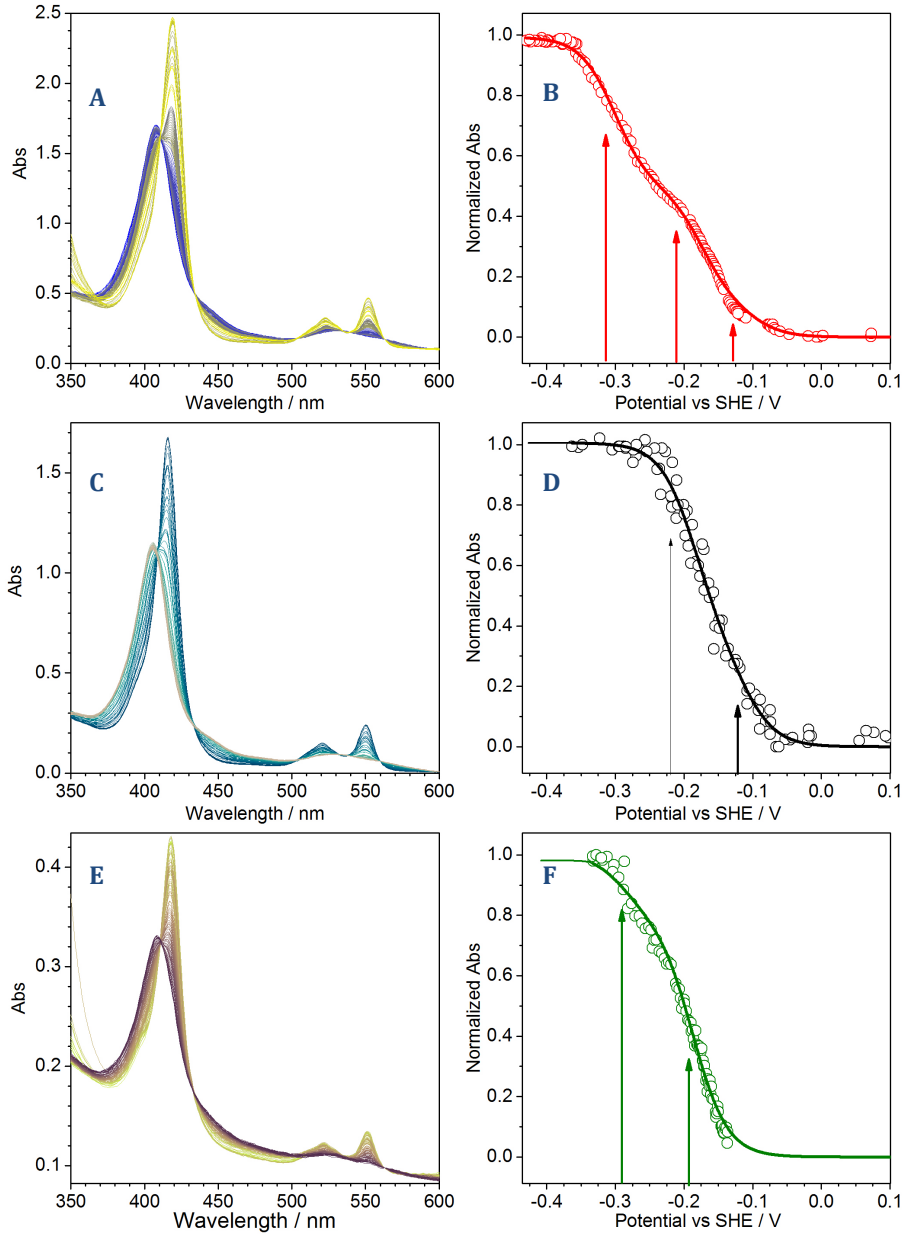

Figure 3.17 Redox titrations from MtrA, MtrA N and MtrA C terminus proteins, chemically poised in free solution.
Panel A. Absorbance spectra of MtrA in free solution at different potentials over which heme components changed redox state; blue = high potential, yellow = low potential.
Panel B. [Red circles] Normalized 552nm heme-absorbance of MtrA at different solution potentials (vs SHE). [Red line] Three heme-group parameter Nernstian curve fitted to the titration data through the ORIGINLAB data fitting package. [Red arrows] potentials of the three heme groups from the Nearnstian
Panel C. Absorbance spectra of MtrA N in free solution at different potentials over which heme components changed redox state; gray = high potential, blue = low potential.
Panel D [Black circles] Normalized 552nm heme-absorbance of MtrA N, at different solution potential (vs SHE). [Black line] Two heme-group parameter Nernstian curve fitted to the titration data through the ORIGINLAB data fitting package. [Black arrows] potentials of the two heme groups from the Nernstian fit.
Panel E. Absorbance spectra of MtrA C in free solution at different potentials over which heme components changed redox state; purple = high potential, yellow = low potential.

Panel F. [Green circles] Normalized 552nm heme-absorbance of MtrA C terminus at different solution potentials (vs SHE). [Green line] Two heme-group parameter Nernstian curve fitted to the titration data through the ORIGINLAB data fitting package. [Green arrows] potentials of the two heme groups from the Nernstian fit.

Optically transparent tin electrode (Ottel) Redox titrations

Redox titrations of freely soluble proteins allowed unbound MtrA to be experimentally examined. The validity of these experiments relied on the stability of the heme potential whilst a UV-vis absorption measurement was taken. All scans had small amounts of fluctuation in the potential, in the order of one or two mV, as each scan was taken. This was due to the dynamic interchange of electrons, within mediators and protein. An alternate methodology that overcomes any biases inherent within free solution redox titrations was needed to confirm any conclusions. Ottel experiments involved adsorbing MtrA proteins to a glass slide coated with a conductive tin oxide film that was optically transparent between 800 and 350 nm. The experiment was performed as described in the Materials and Methods section 2.19 and allows the tin oxide electrode to be connected to an adjustable electric cell whilst being placed in a UV-vis spectrophotometer. In this way, the potential of the protein adhered to the slide could be precisely controlled.

Figure 3.18 Panel A shows the full UV-vis spectrum of MtrA at each of the potentials assayed. The isobestic point at 560 nm was used to calibrate each scan. The MtrA scans are coloured according to potential, with gradient from blue (oxidised) to yellow (reduced). This clearly demonstrates the shift in the soret peak from 401 nm to 420 nm and the appearance of peaks in the α/β region at 530 nm and 552 nm when the protein was reduced, indicative of heme reduction. Panel B shows the normalized height of the 552 peak plotted as a function of potential from the data presented in Panel A. The program ORIGINLAB has been used to plot a Nernstian derived curve, consisting of three potential parameters simulating heme groups. This was found to be the optimum number of heme parameters to use without causing duplicate potentials to be calculated. Panel B demonstrates that the potential window of MtrA was between -0.05 V and -0.35 V. This is the same potential window as observed in Figure 3.17. Panel B. The change in potential between points in the tin oxide electrode redox titration was 0.01 V. This is the smallest possible change in potential for the potentiostat used. 0.01 V steps are a bigger potential change between points than achieved in the free solution redox titration, which was from 0.001 to 0.005 V change per point. Thus, the resolution of the tin oxide electrode redox titration is lower than the free solution redox titration. Despite this, a 10 mV step change is more than accurate enough to resolve multiple heme species over a potential window of

0.3 mV. The heme-group potentials were calculated to be -0.14 V -0.22 V and -0.30 V, with 3, 5 and 2 hemes in each group respectively. These broadly match the -0.12 V -0.2 V and -0.31 V heme group mid point potentials calculated for free solution redox titrations of MtrA. These matching groups were subsequently described as high, middle and low potential heme-groups respectively.

Figure 3.18 Panel C shows the full UV-vis spectrum of MtrA N at each of the potentials assayed. As with previous experiments, the isobestic point at 560 nm was used to calibrate each scan. The MtrA N scans are coloured according to potential, with gradient from grey (oxidised) to blue (reduced). Similarly to Panel A the shift in the soret peak from 410 nm to 420 nm and the appearance of peaks in the α/β region at 530 nm and 552 nm are clearly observed when the protein was reduced. The normalized height of the 552 peak as a function of potential was plotted in Panel D. This data was fitted with a Nernstian derived equation containing two heme group parameters similar to the fits of the data in Figure 3.18 Panel B. Two heme parameters was determined to be the optimal number of heme parameters for fitting as any fewer heme groups made the fit less accurate and any more heme groups replicated one of the two potentials already predicted. The potential range for the titration was -0.02 V to -0.25 V. This is similar to the free solution redox titration for MtrA N in Figure 3.18 Panel D. The potential range maps onto the top half of the tin oxide electrode redox titration for MtrA in Panel A. This is similar to the relationship between the soluble redox titration of MtrA and MtrA N in Figure 3.18. The Nernst fit produced two unique heme groups with mid point potentials of -0.13 V and -0.21 V. These are similar values to the middle and higher potential heme groups predicted in the tin oxide redox titration on MtrA. They are also similar to both the heme groups predicted in the MtrA N terminus free solution redox titration.

Panel E shows the full UV-vis spectrum of MtrA C at each of the potentials assayed. As with Panels A and C the isobestic point at 560 nm was used to calibrate each scan, removing any shifts in absorbance produced by the spectrophotometer. The MtrA C scans are coloured according to potential, with gradient from purple (oxidised) to yellow (reduced). Once again the shift in the soret peak from 410 nm to 420 nm and the appearance of peaks in the α/β region at 530 nm and 552 nm are clearly observed when the protein was reduced. This is consistent with all previous redox titrations, however the concentration of MtrA adsorbed to the tin oxide electrode was only high enough to generate small absorbance changes. An inserted graph in Panel E demonstrates the absorbance profile of

the data set at an increased scale, so that α/β region absorbance changes are visible. As well as failing to adsorb to the electrode in high concentrations, any MtrA C that was adsorbed did not adsorb with high affinity. Thus the protein was easily knocked off the electrode. This would cause changes in the levels of absorbance peaks. Data was excluded when the concentration of MtrA C on the electrode changed. This led to fewer absorbance profiles being included in the data set than in previous redox titrations. The potential window of the titration goes from -0.1 V to -0.35 V, which is the same as for the free solution redox titration of MtrA C. The Nernst fit produces two unique heme groups, much like the MtrA C free solution redox titration. Similarly to previous fits, increasing the number of heme groups fitting the MtrA C tin oxide data causes redundant potentials to be predicted and reducing the number of heme groups in the fit reduces the Chi squared value. The mid point potentials of the fit are calculated to be -0.21 V and -0.32 V, with 4 and 1 hemes per group respectively. These are broadly similar to the mid point potentials of the two heme groups calculated in the free solution MtrA C redox titration in Figure 3.18 Panel D and the middle and lower potential heme-groups found in the MtrA tin oxide redox titration.

MtrA

MtrA
N-terminus

MtrA
C-terminus

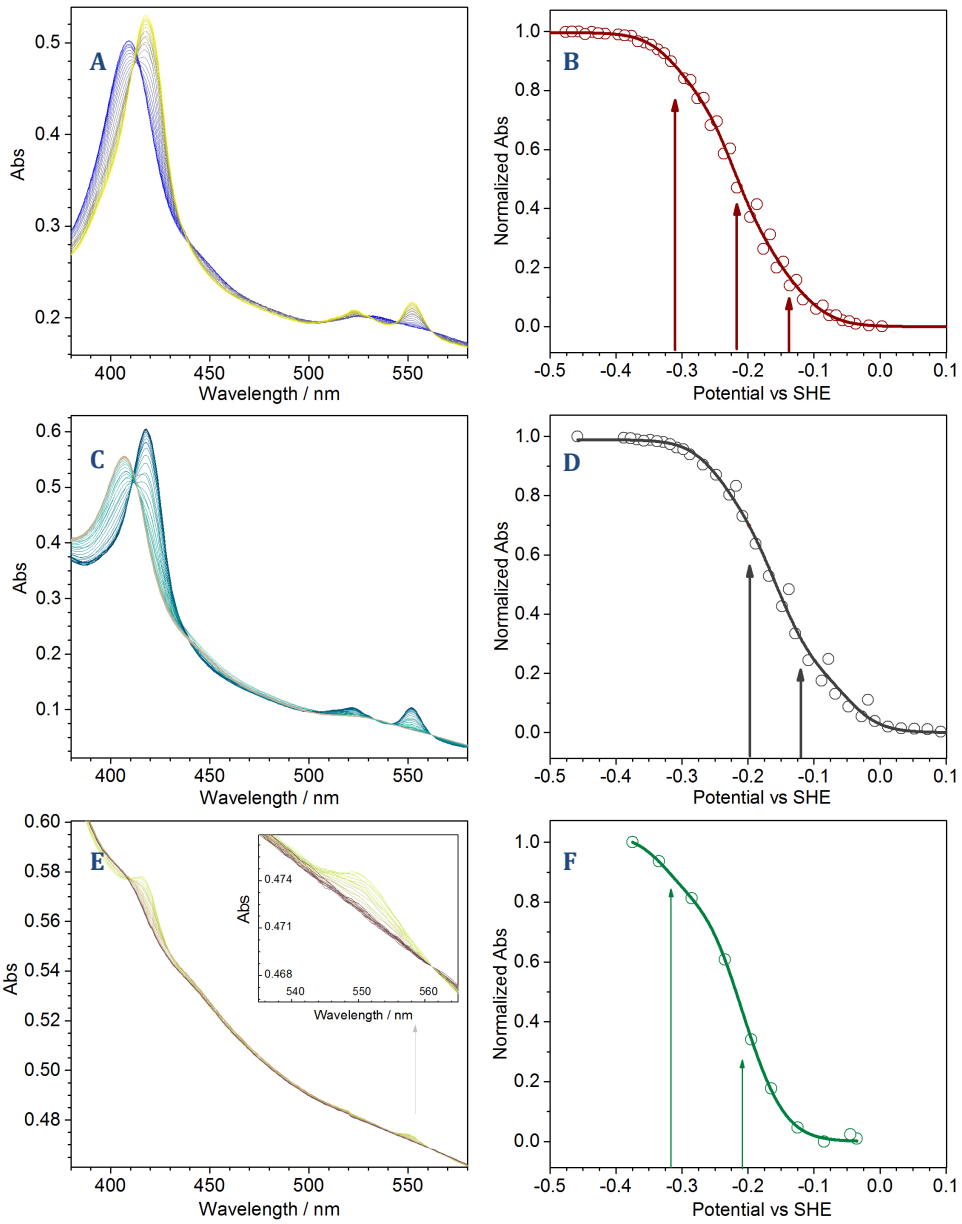

Figure 3. 18 Redox titrations from MtrA, MtrA N and MtrA C terminus proteins adhered to a tin oxide electrode.
Panel A Absorbance spectra of MtrA at different potentials over which heme components changed redox state; blue = high potential, yellow = low potential.
Panel B [Red circles] Normalized 552nm heme-absorbance of MtrA at different solution potentials (vs SHE). [Red line] Three heme-group parameter Nernstian curve fitted to the titration data through the ORIGINLAB fitting package. [Red arrows] potentials of the three heme groups predicted by the fit.
Panel C Absorbance spectra of MtrA N- at different potentials over which heme components changed redox state; gray = high potential, blue = low potential.
Panel D [Black circles] Normalized 552nm heme-absorbance of MtrA N, at different solution potential (vs SHE). [Black line] Two heme-group parameter Nernstian curve fitted to the titration data through the ORIGINLAB data fitting package. [Black arrows] potentials of the two heme groups from the Nernstian fit.
Panel E Absorbance spectra of MtrA C at different potentials over which heme components changed redox state; purple = high potential, yellow = low potential.
Panel F [Green circles] Normalized 552nm heme-absorbance of MtrA C terminus at different solution potentials (vs SHE). [Green line] Two heme-group parameter Nernstian curve fitted to the titration data through the ORIGINLAB data fitting package. [Green arrows] potentials of the two heme groups from the Nernstian fit.

Table 3.1 tabulates all the mid point potentials calculated from each of the redox titration experiments. It is clear from this table that MtrA N and MtrA C have redox potentials that fully overlap with MtrA potentials but only partially overlap with each other. In order to gain further insight into the properties of both penta-heme domains it was necessary to simulate a fit to both MtrA N and MtrA C simultaneously.

	High potential heme group Volts (No. hemes)	Middle Potential heme group Volts (No. hemes)	Low potential heme group Volts (No. hemes)
MtrA soluble	-0.12 (3)	-0.22 (5)	-0.31 (2)
MtrA ottel	-0.14 (3)	-0.22 (5)	-0.30 (2)
MtrA N sol.	-0.13 (2)	-0.19 (3)	
MtrA N ottel	-0.13 (2)	-0.21 (3)	
MtrA C sol.		-0.19 (4)	-0.29 (1)
MtrA C ottel		-0.20 (4)	-0.32 (1)

Table 3.1 The calculated mid point potentials vs SHE of different heme groups from Nernst derived fits of different redox titrations, with the number of predicted hemes within that potential group in brackets.

Simulating the heme potentials of MtrA from combining data sets of MtrA N and MtrA C free solution redox titrations

Because the proteins MtrA N and MtrA C contain the two halves of MtrA, through combining the results of redox titrations for both these proteins, a redox titration of MtrA can be simulated. Comparing this simulation to the real redox titration of MtrA will allow insight to be gained into the degree to which the MtrA truncations MtrA N and MtrA C are representative of the respective N and C terminal sections of the full length MtrA protein.

Figure 3.19 shows the redox titration of MtrA in free solution from Figure 3.17. Panel B (in red) and compares it to a Nernstian curve, shown in green-black dash, created by combining equally weighted MtrA N and MtrA C data sets. This was achieved through fitting separate 1500 point Nernst curves to each of the MtrA N and C data sets (green and black circles) and then fitting a three heme group parameter fit of these two curves combined. The mid point potentials for each of the three heme groups of each of the curves are marked with arrows, red for the redox titration fit and black for the simulation. As shown in Figure 3.18 Panel A, MtrA free solution redox titration calculates three heme groups of high, middle and low potential at -0.12 V -0.22 V and -0.31 V respectively. Similarly to the MtrA free solution simulation, the MtrA N and C combined Nernst simulation also produced three unique heme groups. These groups had very similar mid point potentials to those calculated for MtrA. They were -0.13 V, -0.19 V and -0.29 V. This demonstrated that the mid point potentials of MtrA could be reconstituted from the MtrA N and MtrA C truncations. Red and green-black dash lines do not overlay. This is because a different number of hemes is predicted to be contributing to each of the three corresponding heme groups, in the two Nernst curves. In the high potential heme group, the red redox titration fit predicted 3 hemes to be contributing to the absorbance signal at -0.13 V. In the green-black dash simulation this has changed to 2 hemes contributing to the absorbance signal at -0.13 V. Comparing the middle heme groups, the red redox titration fit calculated 5 hemes to be contributing to the absorbance at -0.22 V, whereas the green-black dash simulation calculated 6 to 7 hemes changing the absorbance at -0.19 V signal. In the low potential heme group the red redox titration fit calculated two hemes changing the absorbance at -0.31 V, whereas the green-black dash simulation calculated 1 to 2 hemes changing the absorbance signal at -0.29 V. These results show that the green-black dash simulation calculated more hemes to be present in the middle heme group than the

red redox titration fit, and less hemes to be present in the high and low heme groups than the red redox titration fit.

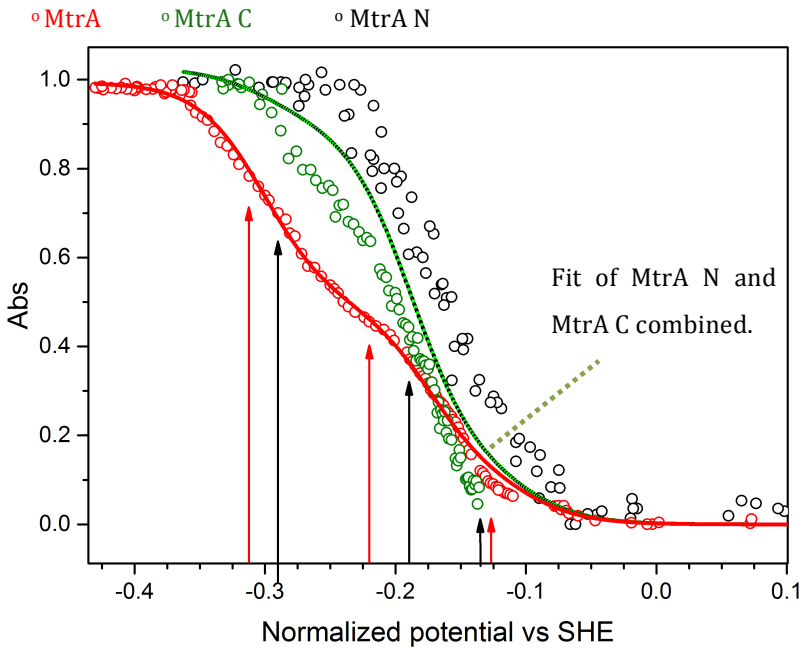

Figure 3.19 A graph of the redox titrations of MtrA, MtrA N and MtrA C chemically poised in free solution.
[Red circles] Plot of the normalized height of the 552nm heme-absorbance band of MtrA at different solution potentials (vs SHE).
[Red line] Three heme-group parameter Nernstian curve fitted to the titration data through the ORIGINLAB data fitting package.
[Black circles] Plot of the normalized height of the 552nm heme-absorbance band of MtrA N, at different solution potential (vs SHE).
[Green circles] Plot of the normalized height of the 552nm heme-absorbance band of MtrA C terminus at different solution potentials (vs SHE).
[Green and Black dashed line] Three heme-group parameter Nernstian curve fitted to the combined data sets of fits to both MtrA N and MtrA C.
[Red arrows] potentials of the three heme groups from the Nernstian fit to MtrA produced by ORIGINLAB.
[Black arrows] potentials of the three heme groups from the Nernstian fit to the combined MtrA N and MtrA C data-set.

Simulating the heme potentials of MtrA from MtrA N and MtrA C tin-oxide redox titrations

As well as simulating Nearst curves for MtrA through combining fits of MtrA N and MtrA C from free-solution redox titration data sets, simulations using the tin-oxide electrode redox titration data sets were also carried out. Figure 3.20. shows the redox titration of MtrA from Figure 3.18. Panel B (in red) and compares it to a Nernstian curve, shown in green-black dash, created by combining equally weighted MtrA N and MtrA C data sets. Again, this was achieved through fitting separate 1500 point Nernst curves to each of the MtrA N and MtrA C data sets (green and black circles) and then fitting a three heme group parameter fit of these two curves combined. The mid point potentials for each of the three heme groups of each of the curves are marked with arrows, red for the redox titration fit and black for the simulation.

The red redox titration fit and the green-black dash simulation fit very closely together. As described in Figure 3.18, the MtrA redox titration produced three unique heme-groups with potentials at -0.14 V, -0.22 V and -0.30 V. These matched the high, middle and low potential heme groups observed previously. Similarly to the MtrA fit, the MtrA N and C-terminus combined Nernst simulation also produced three unique heme groups. The potentials of these heme groups were -0.15 V, -0.22 V and -0.32 V. This demonstrated that the mid point potentials of MtrA could be reconstituted from the MtrA N and MtrA C truncations. In contrast to Figure 3.20, the red and green-black dash lines of Figure 3.20 do overlay with a high degree of accuracy. This is because the same number of hemes is predicted to be contributing to each of the three corresponding heme groups, in the two Nernst curves. In the high potential heme group, the red redox titration fit predicted 3 hemes to be contributing to the absorbance signal at -0.14 V, very closely matching to the green-black dash simulation which calculated 3 hemes to be contributing to the absorbance signal at -0.15 V. Comparing the middle heme group, both the red redox titration fit and the green-black dash simulation calculated 5 hemes to be contributing to the absorbance at -0.22 V. In the low potential heme group, the red redox titration fit calculated two hemes changing the absorbance at -0.30 V, whereas the green-black dash simulation calculated the same number of hemes to be contributing to absorbance changes at -0.29 V. The similarity in the parameters of these fits meant that the lines overlaid with a high degree of similarity, Table 3.2.

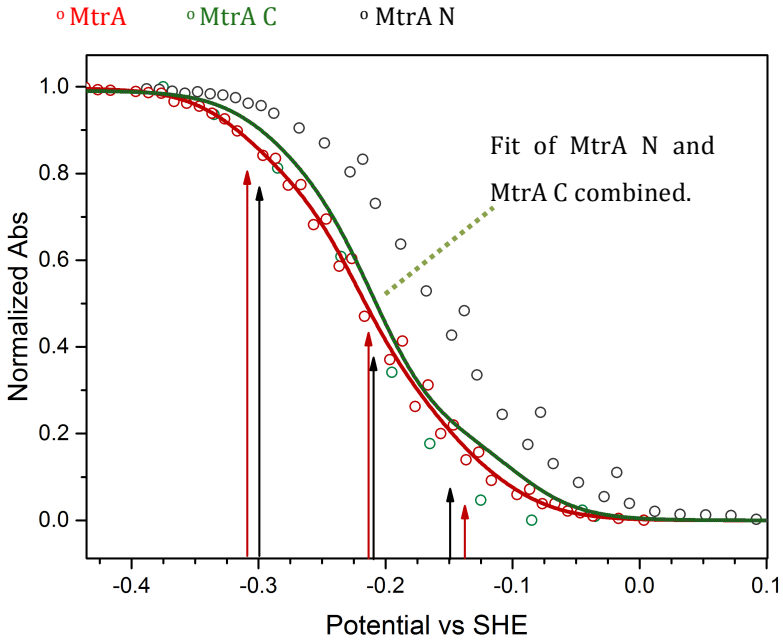

Figure 3. 20 Redox titrations from MtrA, MtrA N and MtrA C terminus proteins, poised by potentiostat whilst adhered to a tin electrode.
[Red circles] Plot of the normalized height of the 552nm heme-absorbance band of MtrA at different potentials (vs SHE).
[Red line] Three heme-group parameter Nernstian curve fitted to the MtrA titration data through the ORIGINLAB data fitting package.
[Black circles] Plot of the normalized height of the 552nm heme-absorbance band of MtrA N, at different potentials (vs SHE).
[Green circles] Plot of the normalized height of the 552nm heme-absorbance band of MtrA C at different potentials (vs SHE).
[Green and Black dashed line] Three heme-group parameter Nernstian curve fitted to the combined data sets of fits to MtrA N and MtrA C.
[Red arrows] potentials of the three heme groups from the Nearnstian fit to MtrA produced by ORIGINLAB.
[Black arrows] potentials of the three heme groups from the Nearnstian fit to the fits of MtrA N and MtrA C data-sets.

	High potential heme group Volts (No. hemes)	Middle Potential heme group Volts (No. hemes)	Low potential heme group Volts (No. hemes)
MtrA soluble	-0.12 (3)	-0.22 (5)	-0.31 (2)
Soluble simulation	-0.13 (2)	-0.19 (6-7)	-0.29 (1 -2)
MtrA ottel	-0.14 (3)	-0.22 (5)	-0.30 (2)
Ottel simulation	-0.15 (3)	-0.22 (5)	-0.32 (2)

Table 3.2 The calculated mid point potentials vs SHE of different heme groups from Nernst derived fits of MtrA in free solution and adsorbed to a tin oxide electrode; as well as the mid point potentials calculated from simulations of the MtrA N and C-terminal redox titrations for both these methodologies. The number of predicted hemes within that potential group is presented in brackets.

3.06 Discussion

Investigating physical properties of MtrA through AUC

MtrA was investigated by AUC sedimentation velocity. The data analysis shows one sedimenting protein with a sedimentation coeficient of 3.2 S and a molecular weight of around 42 kDa. Based on this data, simulations of size could be made. The simulations theorizes MtrA to be long and thin, yet signficantly smaller in size than the molecular envelope produced by SAXS in Firer-Sherwood *et al*., (2011). It is possble that MtrA is a very flexible protein, and this flexibility may affect the way it behaves in solution and therefore how it sediments, possibly folding up upon itself. The simulation of the axial ratio performed in ULTRASCAN only predicts dimensions based on a very limited number of basic shapes inlcuding spheres and rods as well as prolate and oblate ellipsoids. This is a limit of the analytical ultracentrifugation technique. These limitations could account for the discrepancies between the SAXS model and the AUC predictions, where SAXS models predicted for MtrA and MtrA N in this thesis were slightly longer than in AUC simulations.

Investigating the physical properties of MtrA N and MtrA C through AUC and comparing them to those of MtrA

No structural data on MtrA N or MtrA C exists in published literature, therefore any insights into the size and shape of these two proteins is interesting. Determining physical characteristics of MtrA N or MtrA C would give insight into how they fit together to for the fulllength MtrA. AUC sedimentation velocity experiments performed upon MtrA N and MtrA C showed that like MtrA they were long, thin proteins with one axis much bigger than the other two. These results demonstrated that MtrA N had a sedimentation coefficient of 2.2 S and MtrA C had a sedimentation coefficient of 2.3 S. Both of these are significantly smaller than the sedimentation coefficient of MtrA which was calculated to be 3.2 S. MtrA N and MtrA C were both calculated to have a molecular weight of 22 kDa, which matches the sequence based molecular weight calculations. This could be expected, as MtrA N and MtrA C are both roughly equal truncations of the MtrA protein, potentially created by a gene duplication event.

The structural predictions for MtrA N made from the AUC experiments were based on the proteins being prolate. These roughly agree with the SAXS structures made through bead

model simulations. The structures are long, thin and around 80 – 100 Å along the largest axis. However the SAXS models were generally slightly larger than the AUC axial ratio simulations.

Although the MtrA C protein sample contained impurities, it was heme pure. This allowed the MtrA C to be tracked in isolation through out the experiment due to the characteristic 410 nm Soret absorbance of heme co-factors. The quality of the data collected was useable but not as precise as the AUC data collected for MtrA or MtrA N. A small subset of MtrA C seemed to bind and sediment with contaminants in the sample that did not contain heme cofactors. This is another indication that MtrA C usually exists in a complex, again lending weight to the theory that MtrA C, rather than MtrA N, is the section of MtrA that interacts with the MtrB pore.

Using SAXS to describe the structure of STC

The STC protein is one possible evolutionary precursor to MtrA. Through investigating the protein by small angle scattering experiments, a molecular envelope of the protein was developed. This enhanced the published crystal structure of STC (PBD entry 1m1p). The SAXS model that was created has a high degree of similarity to published crystal structures, except in specific locations. These instances of discord between the two models could be due to inaccuracies in the SAXS envelope reconstruction process or could represent real differences in STC when in free solution compared to when confined in a crystal lattice.

In the paper Fischer *et al*., (2010), the authors describe a method that uses information contained within Kratky plots to form an estimate of the volume and therefore molecular weight of proteins using only scattering data. As long as the experimental system has proteins that are monodisperse and randomly orientated, homogeneous and dilute enough to avoid spatial correlation effects, and the scattering curve produced is free from experimental smearing effects, then the protein volume V is proportional to the ratio between I(0) and the invariant Q. This means that the volume can be determined directly from SAXS data in relative (non-absolute) units Equation 3.8.

$$V = 2\pi^2 \frac{I(0)}{Q}$$

Equation 3.8. The equation linking volume of a protein to scattering intensity.

The above equation was found by the authors to link volume to two constants I(0) and Q that can be calculated directly from scattering curves. The I(0) is the estimated intensity of scattering at zero degrees, whereas Q is the area under the Kratky plot from q = 0 to q = infinity (or in real terms the maximum q for which scattering was detected) Equation 3.9.

$$Q = \int_0^{q_{max}} I(q)q^2 \,.\, dq$$

Equation 3.9. The equation used to calculate the parameter Q.

The molecular weight of the protein can therefore be calculated by multiplying the volume by the average protein density, which is 0.83×10^{-3} kDa. $Å^{-3}$. This method could be used to approximate molecular weights for proteins. There will be some inaccuracies that arise by use of the aforementioned value for the average protein density, as cytochromes will have a slightly different value due to the presence of heme c cofactors. The method was originally developed for globular proteins, however Fischer *et al*., (2010), state that calculating the volumes of non-globular elongated protein should be accurate enough to produce an answer within ±10% accuracy. However flexible elongated proteins may not have been considered when the authors undertook the mathematics, and this may cause errors. In addition, the calculation of the value of Q will rely on the integration function of ORIGINLAB, which may lead to inaccuracies, particularly with datasets that have large error bars at high q regions of Kratky plots.

Using the Fischer *et al*., (2010) method, the molecular weight of STC was calculated to be ~13 kDa, which is very close to the 12.5 kDa molecular weight predicted from the known sequence. This is expected as STC is a small globular protein which is relatively inflexible, and has excellent calculations of I(0) and Q (due to data density and small error bars).

Examining the structural features of MtrA N using SAXS

In addition to using AUC to determine the size and shape of MtrA N, MtrA N was investigated through small angle x-ray scattering. Results from these two types of experiment can often have size and shape biases introduced into them through the modeling procedures. Therefore completing AUC and particularly SAXS experiments in tandem with other structural experiments allows for any models or shape conclusions to be independently corroborated. In the SAXS experiments for MtrA N ten bead models were created and these simulations were averaged and then compared to other structures of potential interest, STC and NrfB. The shape of MtrA N was calculated to be a prolate

structure 80 Å in length. It contained a globular domain and a thinner tail domain. When aligned with the small cytochrome proteins STC and NrfB, these structures were fitted inside the globular domain. The tail domain was too small to encompass heme cofactors and associated proteins. The *in silico* prediction of the crystal structure of MtrA did not align well with the MtrA N SAXS molecular envelope. Neither the N or C terminal sections of the *in silico* crystal structure matched particularly well with the MtrA N SAXS envelope when they were manually aligned. The default alignment did place the N-terminal half of the *in silico* crystal structure within the MtrA N-terminal SAXS envelope, however not all of the five N-terminal hemes were encompassed within the molecular envelope. This was presumably due to the bias in the alignment created by the presence of the C terminal section of the *in silico* crystal structure.

Using the Fischer *et al*., (2010) method for calculating the molecular weight of proteins from SAXS scattering, it was predicted that MtrA N had a molecular weight of ~22 kDa. This is very close to the molecular weight predicted from sequence analysis. This is expected as MtrA N is a globular protein which is relatively inflexible. As with the data for STC, an accurate I(0) and Q could be calculated due to the high quality data.

The MtrA N molecular envelope was found to be only 20 Å smaller than the SAXS molecular envelope of MtrA published in Firer-Sherwood *et al*., (2011). The volume of MtrA must be significantly larger than MtrA N, as it is made up of ~160 more amino acids and five more heme cofactors. This could indicate that either MtrA N was modeled to be too big, or that the published MtrA model contained some inaccuracies.

Investigating the structure of MtrA through SAXS

One SAXS molecular envelope of MtrA has been published in Firer-Sherwood *et al*., (2011). AS has been stated this model was dissimilar in some respects compared to SAXS models of MtrA N that had been produced. Therefore repeating SAXS experiments on MtrA and obtaining a SAXS model would allow a deeper analysis of how MtrA and MtrA N SAXS models fit align. SAXS experiments on MtrA were initially difficult due to the nature of MtrA causing distortions in the scattering profiles, possibly because it aggregated, Firer-Sherwood *et al*., (2011) made no mention of this in there publication. These characteristics of MtrA could be due to MtrA being inherently unstable when not in complex with MtrB. Any aggregation is most likely caused by the C-terminal section of MtrA (similar to the MtrA C protein), as MtrA N is known to be highly soluble and stable in isolation, whereas

MtrA C was difficult to purify away from interacting contaminants, and had regions of disorder predicted within it.

A scattering profile of MtrA was produced through minimizing the time between the final size exclusion purification step and the SAXS experiment. This was the best attempt that could have been made to obtain an accurate profile, as it used the most highly purified and mono-disperse sample of MtrA that was feasibly available. However to confirm that this scattering profile was representative of monodisperse MtrA, scattering profiles of a concentration series of this sample should have been collected. This was not done due to the time restraints and lack of equipment availability. The incorporation of sequential SEC-SAXS would have overcome these problems. Therefore, the model of MtrA produced from this experiment must be treated with a degree of skepticism.

Using the single SAXS profile, MtrA was modeled to be a 200 Å long prolate structure with one globular region and a tail region. Overall, the model had a larger volume than expected based on assumptions from the published SAXS model and *in silico* structure predictions. This may be due to the data quality, or it may indicate that certain aspects of MtrA (such as its flexibility and tendency to aggregate) are very difficult to model accurately using the SAXS method. When comparing the SAXS models for MtrA and MtrA N, the MtrA models were noted to have a higher degree of difference between the DAMAVER molecular envelope average and the DAMFILT molecular envelope. This indicates a greater diversity in the shape of DAMMIF bead model simulations of MtrA. This could stem from the lower quality SAXS data collected for MtrA compared to MtrA N. The SAXS model of MtrA has a globular region thay had an indent on one of its major faces, causing it to have a likeness of a spoon or paddle. This feature was recurrent in both the MtrA N SAXS model and the SAXS model of MtrA developed by Firer-Sherwood *et al* (2011). This similarity of features in the different models allows the conclusion that the globular paddle section of MtrA is the N-terminal section and the handle or tail section of MtrA is the C–terminal half. As the tail section of the model appears thinner then the supposed N-terminal half of MtrA, it has dimensions that better suit it to fitting inside the opening of MtrB. This allows for the postulation that this is the location where the C terminus of MtrA interacts with MtrB. Additionally this also fits with the conclusions that C-terminal half of MtrA has disordered regions. This is because these disordered regions may only take on a stable form when in complex with another protein, which in this case is MtrB.

These conclusions must be considered alongside the following information: the SAXS structures are models that fit the scattering profiles collected and they are not direct visualizations of the proteins, therefore their appearance may not accurately describe MtrA's structure. In addition, even if the models are accurately describing MtrA in free solution, this may not be useful. MtrA may only assume a functional shape when in complex with MtrB. These factors would also influence the conclusions investigating the heme mid point potentials of MtrA. The redox Bohr effect may alter heme mid point potentials of MtrA when it is in complex with MtrB.

Using the technique described in Fischer *et al*., (2010) the molecular weight of MtrA was calculated to be ~130 kDa. This is far larger than the ~40 kDa protein predicted from AUC and by sequence analysis. The difficulty in collecting SAXS data for MtrA could indicate that the SAXS structure is of an oligomersied MtrA complex, with approximately three MtrA proteins joined together. Alternatively, the long flexible MtrA structure could make it difficult to capture accurate SAXS data, leading to inaccurate bead model simulations and SAXS molecular weights.

Investigating the redox properties of MtrA through redox titration experiments

Performing redox titrations on MtrA, MtrA N and MtrA C proteins using both free solution and tin oxide electrode based methods allowed the thorough exploration of the heme mid point potentials of MtrA. It was predicted that there are three unique and distinguishable groups of hemes within MtrA. These were around -0.1 V, -0.2 V and -0.3 V, and were given the names high, middle and low respectively. It is not wholly unexpected that three distinct groups of hemes would emerge from simulations of a 0.3 V potential range when the individual potential range of one heme is around 90 mV. Thus, having more than three heme groups overlapping of individual heme group ranges would occur when confined to a 300 mV range. When MtrA was truncated to form the MtrA N and MtrA C proteins, the five N terminal hemes could be separated from the five C terminal hemes. This advances the description of heme mid point potentials compared to Pitts *et al.,* (2003).

Both MtrA N and MtrA C contained the middle -0.2 V heme group. MtrA N additionally contained the high -0.1 V group and lacked the low -0.3 V group. In contrast, MtrA C did not contain the high -0.1 V heme group but did contain the low -0.3 V heme group. When the MtrA N redox titrations and the MtrA C redox titrations are combined they effectively

recreated the three high, middle and low heme-groups found in full-length MtrA redox titrations. This suggests that the N terminal half of MtrA contains high potential hemes and the C terminal half contains low potential hemes. This suggests that there is some directionality in the heme mid point potential order throughout MtrA. As MtrA functions to translocate electrons from the (moderately) high potential periplasm to low potential MtrC or the cell exterior, and there appears to be a gradient of mid point potentials along MtrA where the N terminus is high potential and the C terminus is low potential, then it could be that the N terminus more likely interacts with the high potential periplasmic electrons and the C terminus interacts with the lower potential MtrC hemes or extracellular heavy metal deposits. If this were correct, it would be likely that the C terminal section of MtrA inserts into the MtrB barrel. MtrA C was also not easily bound to the tin oxide electrode. This could have been due to the impurities within the MtrA C sample that could not be removed, as postulated previously MtrA C seems to form complexes for stability.

3.07 Bibliography

Beer, 1852. Determination of the absorption of red light in colored liquids. *Annalen der Physik und Chemie*, 86, pp.78–88.

Clarke, T.A. *et al*., 2011. Structure of a bacterial cell surface decaheme electron conduit. *Proceedings of the National Academy of Sciences*, 108(23), pp.9384–9389.

Clarke, T.A. *et al*., 2007. The crystal structure of the pentahaem c-type cytochrome NrfB and characterization of its solution-state interaction with the pentahaem nitrite reductase NrfA. *Biochemical Journal*, 406(1), p.19.

Cheng, J.L., Sweredoski, M.J. & Baldi, P., 2005. Accurate prediction of protein disordered region by mining protein structure data. *Data Mining and Knowledge Discovery*, 11(3), pp.213–222.

Cölfen, H. *et al*., 2010. The Open AUC Project. *European biophysics journal : EBJ*, 39(3), pp.347–59.

Demeler, B., 2001. Methods for the Design and Analysis of Sedimentation Velocity and Sedimentation Equilibrium Experiments with Proteins. In *Current Protocols in Protein Science*. John Wiley & Sons, Inc.

Demeler, B., 2005. UltraScan – A Comprehensive Data Analysis Software Package for Analytical Ultracentrifugation Experiments. *LSD AUC* ,Chapter 11 pp.210–230.

Demeler, B. & van Holde, K.E., 2004. Sedimentation velocity analysis of highly heterogeneous systems. *Analytical Biochemistry*, 335(2), pp.279–88.

Demeler, B., Saber, H. & Hansen, J.C., 1997. Velocity Boundaries. *Biophysical Journal* , 72(January), pp.397–407.

Firer-Sherwood, M.A. *et al*., 2011. Solution-based structural analysis of the decaheme cytochrome, MtrA, by small-angle X-ray scattering and analytical ultracentrifugation. *Journal of Physical Chemistry B*, 115(38), pp.11208–11214.

Fischer, H. *et al*., 2010. Determination of the molecular weight of proteins in solution from a single small-angle X-ray scattering measurement on a relative scale. *Journal of Applied Crystallography*, 43, pp.101–109.

Franke, D., Kikhney, A.G. & Svergun, D.I., 2012. Automated acquisition and analysis of small angle X-ray scattering data. *Nuclear Instruments and Methods in Pysics Research A*, 689, pp.52–59.

Franke, D. & Svergun, D.I., 2009. DAMMIF , a program for rapid ab-initio shape determination in small-angle scattering. *Journal of Applied Crystallography*, 42(2), pp.342–346.

Hartshorne, R.S. *et al*., 2009. Characterization of an electron conduit between bacteria and the extracellular environment. *Proceedings of the National Academy of Sciences*, 106(52), pp.22169–22174.

Konarev, P. V *et al*., 2003. PRIMUS : a Windows PC-based system for small-angle scattering data analysis PRIMUS : a Windows PC-based system for small- angle scattering data analysis. *Biophysical Journal*, pp.1277–1282.

Kozin, M.B. & Svergun, D.I., 2001. Automated matching of high- and low-resolution structural models. *Journal of Applied Crystallography*, 34(1), pp.33–41.

Leys, D. *et al*., 2002. Crystal structures at atomic resolution reveal the novel concept of "electron-harvesting" as a role for the small tetraheme cytochrome c. *The Journal of Biological Chemistry*, 277(38), pp.35703–11.

Petoukhov, M. V *et al*., 2007. supported small-angle scattering data analysis. Journal of *Applied Crystallography*, pp.223–228.

Petoukhov, M. V. *et al*., 2012. New developments in the ATSAS program package for small-angle scattering data analysis. *Journal of Applied Crystallography*, 45(2), pp.342–350.

Pitts, K.E. *et al*., 2003. Characterization of the Shewanella oneidensis MR-1 decaheme cytochrome MtrA: expression in Escherichia coli confers the ability to reduce soluble Fe(III) chelates. *The Journal of Biological Chemistry*, 278(30), pp.27758–65.

Ross, D.E. *et al*., 2007. Characterization of protein-protein interactions involved in iron reduction by Shewanella oneidensis MR-1. *Applied and Environmental Microbiology*, 73(18), pp.5797–808.

Schuck, P., 2003. On the analysis of protein self-association by sedimentation velocity analytical ultracentrifugation. *Analytical Biochemistry,* 320(1), pp.104-124

Schuck, P., 2000. Size-Distribution Analysis of Macromolecules by Sedimentation Velocity Ultracentrifugation and Lamm Equation Modeling. *Biophysical Journal*, 78(March), pp.1606–1619.

Svergun, D.I., 1992. Determination of the regularization parameter in indirect-transform. *Journal of Applied Crystallography*, 25, pp.495–503.

Volkov, V. V & Svergun, D.I., 2003. Uniqueness of ab initio shape determination in small-angle scattering. *Journal of Applied Crystallography*, 36(3 Part 1), pp.860–864.

4 | Investigating the operation of MtrCAB incorporated in liposomes

4.01 The role of MtrCAB in the outer membrane

Shewanella oneidensis has an incredibly diverse range of redox proteins that can accept and transfer electrons. A large number of redox proteins can be found in the *S. oneidensis* periplasm, with over 40 putative C-type cytochromes being expressed, (Meyer *et al.,* 2004). Many of these proteins have high heme to protein ratios and similar mid point potentials, which means that many of them have structural and functional similarities, (Firer-Sherwood *et al.,* 2011; Pitts *et al.,* 2003; Hartshorne *et al.,* 2009; Myers & Myers 2003). Therefore, there are many different cytochromes within *S. oneidensis*, with the MtrCAB complex representing only a small fraction. MtrCAB is not unique in being a cytochrome complex within the outer membrane; the paralogous MtrDEF is most notably also contained within the outer membrane (Coursolle & Gralnick 2010; Clarke *et al.,* 2011). For these reasons, it was not possible to study the isolated electron transportation abilities of MtrCAB in live cells. To overcome this, the MtrCAB complex was isolated by purification, allowing investigations into its functioning independent from competing cytochromes.

4.02 Incorporating MtrCAB into liposomes to make proteoliposomes

The purification of MtrCAB was published in Ross *et al.,* (2007) and Hartshorne *et al.,* (2007). An adaptation of this method is detailed in section 2.15. Redox analysis of MtrCAB by protein film voltammetry and soluble redox titrations have been used to investigate the properties of MtrCAB in isolation, (Hartshorne *et al.,* 2009). These experiments elucidated the potential range over which MtrCAB was active, which was measured to be from 0 to -400 mV (versus standard hydrogen electrode). Stopped flow analysis of soluble iron compound reduction by MtrC and associated factors was carried out by (Wang *et al.,* 2008). In this paper the authors determined the rates of electron transfer of MtrC when interacting with freely soluble redox partners, giving insight into how one component of MtrCAB functions. To probe the properties of MtrCAB further, kinetic assays were developed using MtrCAB inserted into liposomes, facilitating investigations into the redox behaviour of MtrCAB when interacting with partners, Figure 4.1. These assays were described in the work of White *et al.,* (2013) and Hartshorne *et al.,* (2009). Currently there is no other literature published describing similar work. In their 2013 paper, White *et al.,* describe the creation and characterization of phosphatidylcholine liposomes incorporated with MtrCAB. The MtrCAB complexes were oriented in a unidirectional manner and were

termed proteoliposomes. The proteoliposomes were made containing a membrane-impermeable redox indicator that could exchange electrons with the MtrCAB complex. The methyl viologen acted as a sink or source for electrons to flow into or out of, which facilitated their passing through the MtrCAB complex. The redox indicator, methyl viologen, has a distinctive UV-vis absorbance spectrum for both its oxidised (+2) and single reduction (+1) states. This is useful as when analyzing bulk absorbance properties of methyl viologen solution, the 603 nm absorbance band has a linear proportionality to the concentration of reduced species of methyl viologen (linked via the Beer- Lambert law Beer, (1852)). In this way White *et al.,* could observe the bulk flow of electrons passing through the MtrCAB complex in real time.

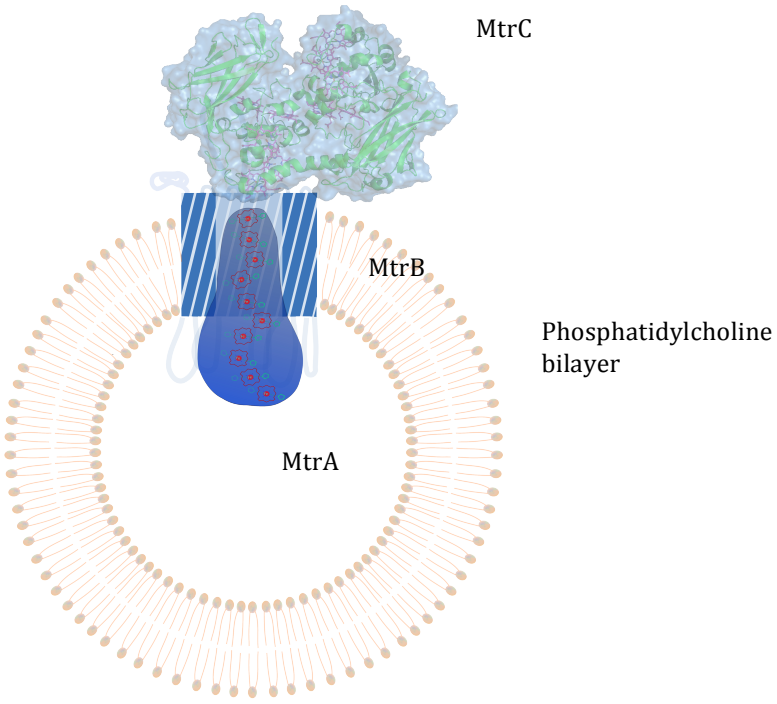

Figure 4. 1 A cartoon diagram of MtrCAB inserted into a phosphatidylcholine bilyaer, demonstrating a internal cavity with the potential to be filled with redox indicators.

Methyl viologen has a mid-point potential (E_m) of -0.43 V. Thus, sodium dithionite, which has a E_m = -0.660 V, (Mayhew 1978), was used as a chemical reductant of the proteoliposomes. Potassium ferricyanide, with an E_m = +0.48 V, (Kolthoff & Tomsicek 1934; Rao *et al.,* 1978), was used as an oxidant. The use of these compounds created potential gradients across MtrCAB that are larger than those predicted to occur naturally. The redox compounds used were also not physiologically relevant as they are small molecules that would not normally come into contact with MtrCAB when functioning in the *Shewanella* cell.

4.03 Development of different proteoliposome interiors

Shewanella oneidensis contains many soluble, small cytochromes within its periplasm (Meyer *et al.,* 2004). These heme proteins are thought to act as electron shuttles, linking processes occurring in or on the inner membrane to processes occurring in the periplasm, and on the outer membranes, (Ross *et al.,* 2007; Hartshorne *et al.,* 2009; Shi *et al.,* 2012; Fonseca *et al.,* 2012). In this way they act as a biological capacitor, electronically linking physically separated systems. A heme protein that is abundant in the *S. oneidensis* periplasm is STC (small tetra heme cytochrome). STC is a 12 kDa protein containing four heme cofactors, for which there is a published crystal structure (Leys *et al.,* 2002). In addition, a SAXS envelope was described in Chapter 3. Harada *et al.,* (2002) found that the mid point potentials of the hemes at high salt and pH 9 were -143, -194, -218 and -231 mV (for hemes III, IV, II and I respectively). Fonseca *et al.,* (2009) found that redox Bohr effects altered heme III the most but at pH 7 the active potential range of STC was from -100 to -300 mV. The use of STC instead of methyl viologen enables a better model of the *Shewanella* periplasm to be developed, as STC is a physiologically relevant protein, already involved with the canonical functioning of MtrCAB with less negative redox potentials than that of methyl viologen in an oxidised state.

The small heme protein cytochrome c is a 104 amino acid protein containing a single c type heme, which is found in eukaryotic mitochondria (Bushnell *et al.,* 1990). In the mitochrondria, it mediates one step in the electron transport chain of respiration (Mathews 1985). Its single heme species has a mid point potential of +244 V at pH 7, (Pande & Myer 1978). As cytochrome c is involved with membrane-gated electron transport chains but is of much higher potential than either methyl viologen or STC, using it as a redox indicator inside MtrCAB proteoliposomes would provide an interesting contrast to both methyl viologen and STC. The aims of this chapter were to extend the work of White *et al.,* (2013) by comparing the functioning of MtrCAB in proteoliposomes containing methyl viologen with proteoliposomes containing cytochrome c or STC redox indicators, as these would be more physiologically relevant. Investigating how these three types of proteoliposomes differed in their respective abilities to transport electrons both into and out of the proteoliposomes would enable investigation into how MtrCAB functioned in different periplasmic and extracellular redox environments. Experiments were conducted to create and characterize each of these three types of proteoliposomes, as well as investigate any differences in the oxidation and reduction of these proteoliposomes.

4.04 Redox indicators unsuitable for encapsulation within liposomes

When initially designing experiments to investigate the functioning of MtrCAB with proteoliposomes, many different redox indicators were considered for incorporation and then trialed. The majority of these indicators were found to be lipid soluble, and thus were released from the liposomes over time or successive washing steps. Others could not be concentrated sufficiently to enable detectable signals when within liposomes. Table 4.1 shows the list of mediators that were not suitable for liposome incorporation and summarizes why each redox indicator was inappropriate. All trials were carried out following the method detailed in section 2.24, with the concentration of redox indicator stated in Table 4.1. Trial experiments were carried out as per section 2.25.

Compound Name	Formula	Em (mV)	Concentration (mM)	Problems Encountered
Methylene Blue (MB)	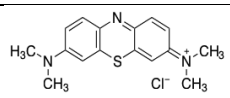	+10	10	MB stuck to membranes, interfering with liposome production especially washing
AQDS	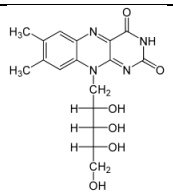	-183	~0.2 (limit of solubility)	AQDS blank liposomes produced false positives. AQDS was therefore presumed permeable (to some degree) through the liposome membranes.
Riboflavin	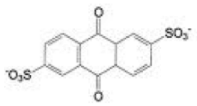	-200	~0.3 (limit of solubility)	The aqueous solution of riboflavin produced liposomes that had spectral changes too minute to detect.
Phenosafranin	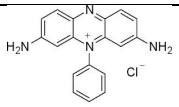	-250	10	Phenosafranin blank liposomes produced false positives. Phenosafranin also leaked out of liposomes considerably during washing process.
NADH & Diaphorase	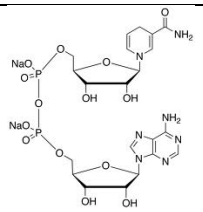	-320	10	NADH & diaphorse did not interact with the MtrCAB complex, no redox changes were observed.
Benzyl Viologen (BV)	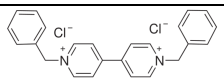	-350	10	BV, slowly leaked out of liposomes, see figure 2.17.

Table 4.1 The redox indicators trialed for incorporation into liposomes that were deemed unsuitable.

One example of an unsuitable redox indicator was benzyl viologen. Although having a structure similar to methyl viologen, which was successfully used in liposome preparations, benzyl viologen was found to be permeable through phosphatidylcholine membranes. Analyzing the UV-vis absorbance of the supernatants removed during washing steps showed that after consecutive washing steps the amount of benzyl viologen in the supernatant decreased. This was the same as seen for successfully cleaned liposomes containing methyl viologen, as will be demonstrated later in this chapter. The characteristic absorbance profile of benzyl viologen can be seen in Figure 4.2, with the amount of benzyl viologen determined by the absorbance at 603 nm. The 603 nm absorbance decreases from the green to the yellow line, the first and second wash steps. After the second wash step, the re-suspended benzyl viologen liposomes were left for 12 hours at 5°C and then washed for a third time. The red absorbance spectrum shows an increased absorbance at 603 nm. This indicates that benzyl viologen was leaked into the supernatant, from inside the liposome, during the 12 hour incubation after the second wash. After the fourth wash, the 603 nm absorbance decreased again. This cleaning process continued until there was no 603 nm absorbance from any part of the liposome pellet or supernatant after centrifugation. This indicated that all of the benzyl viologen both inside and out of the liposomes had been removed, and that benzyl viologen was soluble in phosphatidylcholine.

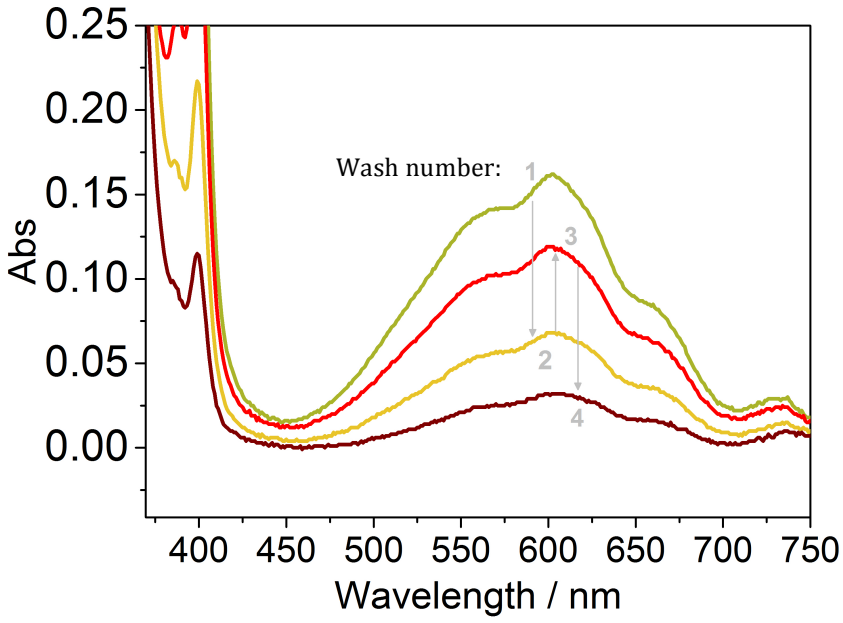

Figure 4. 2 Absorbance spectra of successive supernatants removed after successive benzyl viologen liposome suspension ultracentrifugation steps. The sequential washes are labeled 1 through to 4 and the grey arrows denote how the 603 nm absorbance peak changes.

4.05 Creating and cleaning functional proteoliposomes containing: methyl viologen, STC and cytochrome c

To create a functioning proteoliposome suitable for investigating the function of MtrCAB, the method detailed in section 2.24 was followed. The process required the following steps: extrusion of lipids suspensions within solutions of the redox mediator, sonication, addition of MtrCAB followed by freeze thawing and then washing. The washing process involved sedimenting the liposomes and proteoliposomes by ultracentrifugation. Any excess redox indicator was then separated from liposomes through removing the supernatant. The pelleted liposomes were then re-suspended in fresh buffer. After each washing step a UV-vis spectrum of the supernatant was taken to determine the concentration of excess redox indicator surrounding the liposomes or proteoliposomes when in suspension. Repeat washes resulted in a suspension of liposome in a buffer free from excess redox indicator.

Liposome washing

Figure 4.3 demonstrates the UV-vis spectra for successive supernatants taken from successive washes of both liposomes and proteoliposomes prepared in the presence of three types of redox indicator.

Figure 4.3 Panels A and B show the UV-vis spectra of supernatants, taken from sequential washes of liposomes (that did not contain any MtrCAB) and proteoliposomes encapsulating methyl viologen, after reduction by sodium dithionite. As can be seen in both panels, the respective 603 nm peak absorbance gets smaller with successive washes (dark to light blue) indicating that with successive washes, less methyl viologen is present in the supernatant. After four wash steps, no peak at 603 nm can be observed in either panel. This indicates that the residual amount of methyl viologen left within the buffer supernatant surrounding the liposomes or proteolipsomes is so small as to be undetectable. Thus, any methyl viologen redox status changes in subsequent experiments must be from methyl viologen encapsulated inside the liposomes or proteoliposomes, and so mediated by the presence of the lipid bilayer. Liposomes or proteoliposomes were used on the day they were created or within a few days of being created, during which time they were stored at 5 °C. If the liposomes and proteoliposomes were left for an extended period of time, the methyl viologen could leach out slowly or instability of the phosphatidylcholine membrane could cause the liposomes and proteoliposomes to burst as they aged, which would release methyl viologen. However older liposome suspensions

could be re-washed if necessary. These results were in line with the findings of White *et al.,* (2013), indicating that a suitable and repeatable methodology was used.

Figure 4.3 Panels C and D show the UV-vis spectra of the supernatants collected from sequential washes of liposomes and proteoliposomes made with STC. Concentrated STC was purified from *Shewanella oneidensis* as detailed in the Materials and Methods section 2.16. Within these spectra, the absorbance peak of oxidised heme (Soret) is visible at 410 nm, as is the α/β region at 552 nm. The spectra are coloured from dark to light orange, in order of the successive washes. The peak height of the Soret absorbance decreases in each sequential wash, indicating that there is less STC in the supernatant after each successive wash. By the third wash step, little or no STC is observed in the supernatant. Although a small 410 nm absorbance peak is still visible after three washing steps, no absorbance at 552 nm is observable. Experiments using liposomes containing STC and proteoliposomes depend on absorbance measurements in the 552 nm region, thus any observable change in this region must be due to encapsulated STC. Liposomes containing STC were found to be more fragile when compared to liposomes containing methyl viologen, they were more liable to bursting during re-suspension from pellets. Minimizing the number of washing steps helped to maximize the quality of liposomes containing STC or proteoliposomes produced. Further washes did show a total removal of STC from the supernatant of the pelleted STC liposome suspensions, but these reduced the amount of liposome or proteoliposome suspension available for experimentation. Additional difficulties were found when incorporating high concentrations of STC into liposomes or proteoliposomes. To increase the concentration of STC with liposomes or proteoliposomes, a less disruptive sonication process, a less extreme freeze-thawing and a more gentle pelleting and re-suspension (during the wash stages) were employed. Once made, the liposomes containing STC had a smaller time frame in which they could be used, typically within 48 hours of the final washing step.

Figure 4.3 Panels E and F show the UV-vis spectra of the supernatant removed from pelleted liposomes containing cytochrome c and proteoliposomes. Within these spectra, the absorbance peak of oxidised heme (Soret) is visible at 410 nm, as is the α/β region at 552 nm. The spectra are coloured from dark to light red, in order of the successive washes. The 410 nm absorbance peak decreases in successive washes in both panels. After three washes, the 410 nm Soret peak is no longer visible, thus any cytochrome c in the liposome or proteoliposome suspensions must have been encapsulated.

Horse heart cytochrome C was commercially available from Sigma™. This overcame the issues of low protein quantity faced with STC and enabled liposomes with a greater internal concentration of heme to be made, which made the relative absorbance of the characteristic heme signals much greater than background noise. Cytochrome c was washed from the exterior of liposomes with greater ease than either methyl viologen or STC. This increased the yield of liposomes made. Liposomes containing cytochrome c seemed to last longer than liposomes containing STC, without background cytochrome c escaping from liposomes (which was presumably due to liposomes bursting). Liposomes containing cytochrome c seemed to last as long as liposomes containing methyl viologen, being clean and functional a few days after the completion of the last wash step. The cytochrome c that was obtained from Sigma™ came with ~ 30% of heme in a reduced state. This can be seen in the distinctive 552 nm peak in the α/β region of the UV-vis spectra. The partially reduced cytochrome c could still produce a large enough 552 nm absorbance change to be detected, through the reduction of the remaining ~ 70% oxidised protein.

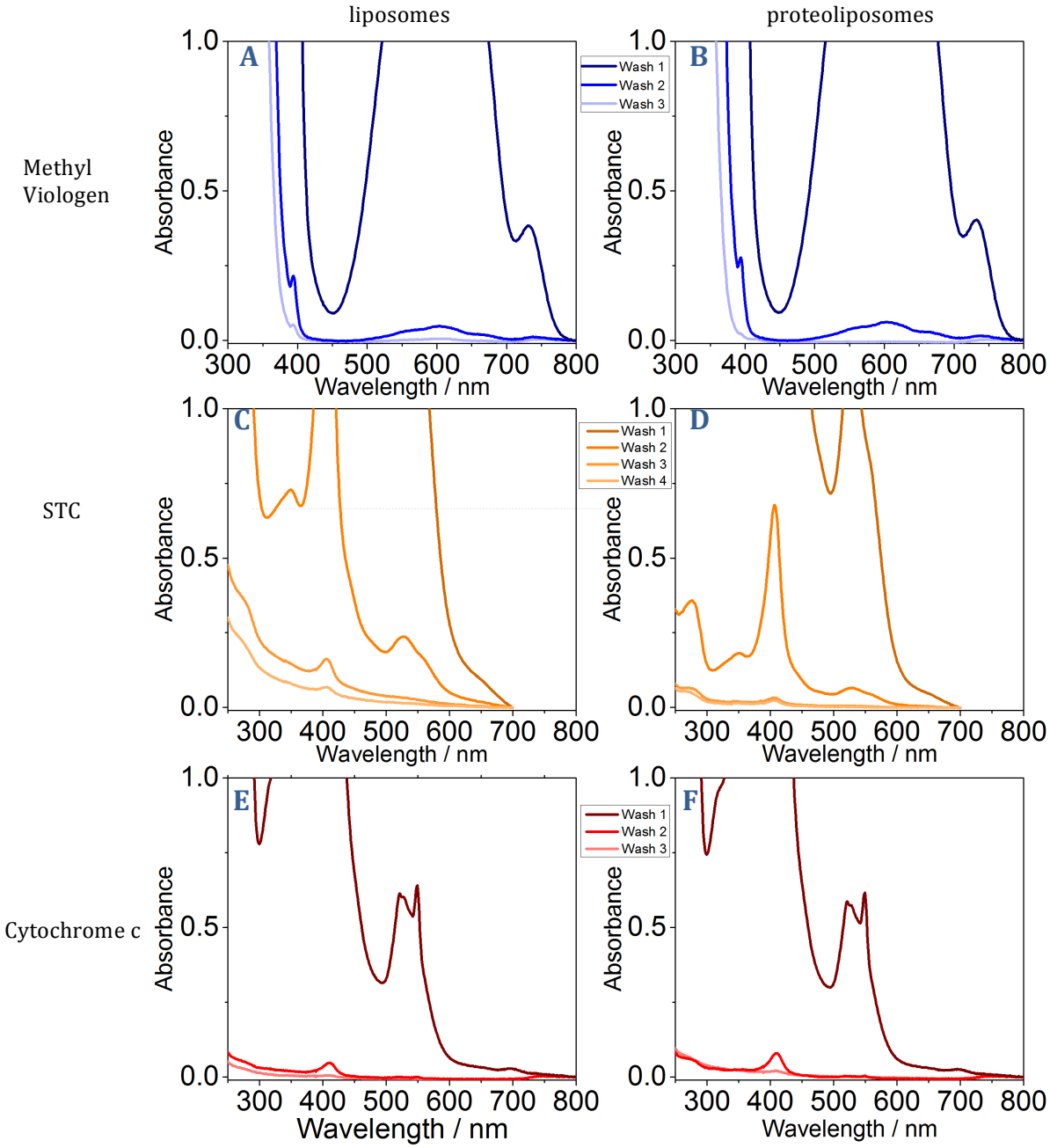

Figure 4.3 The absorbance spectra of the supernatant removed from serial washes of liposomes and proteoliposomes.

Panels A and B. [Blue Lines] The absorbance spectra of the supernatant removed from serial washes of liposomes and proteoliposomes containing methyl viologen; after sodium dithionite was added completely reducing the methyl viologen and inducing a quantifiable 603 nm absorbance band. The spectra are colour coded from dark to light blue in order of sequential washes.

Panels C and D [Orange lines] The absorbance spectra of the supernatant removed from serial washes of liposomes and proteoliposomes containing STC. The spectra are colour coded from dark to light orange for sequential washes.

Panels E and F. [Red lines] The absorbance spectra of the supernatant removed from serial washes of liposomes containing cytochrome c. The spectra are colour coded from dark to light red for sequential washes. .

4.06 Liposome dynamic light scattering

In addition to checking that the clean liposomes and proteoliposomes could be repeatedly created, the quality of those liposomes created needed to be assessed. One method of assessing the liposomes created was dynamic light scattering (DLS) experiments. These used 2 μL of liposome/proteoliposome stock which was mixed gently by pipette into 18 μL of 20 mM HEPES pH7, 2mM $CaCl_2$, 10mM KCl,. This was placed into a clean DLS cuvette and measured in a DynaPro Titan DLS machine (Wyatt Technology Corporation). A minimum of 100 counts were then performed for each sample, Table 4.1.

The DLS experiments, of Table 4.1, showed a distribution of the hydrodynamic radii of the liposomes and proteoliposomes. This allowed assessment of how uniform the liposomes were in size. Work by White *et al.,* (2013) had found the average hydrodynamic radii of the liposomes containing methyl viologen and proteoliposomes they created was approximately 150 nm, with a range of size distributions above and below this average. Theoretically the 100 nm pores of the filter used in the extrusion step when preparing liposomes and proteoliposomes should introduce size uniformity. Compared to the previously published result, the DLS experiments on methyl viologen containing liposomes and proteoliposomes were calculated to have slightly smaller average a hydrodynamic radii of 106 nm (38.2% polydisperse) and 105 nm (34.4% polydisperse) respectively. Hydrodynamic radii of up to 360 nm for liposomes and proteoliposomes were detected, showing that there was a high degree of variation, and the extrusion step had not limited the size of the liposomes or proteoliposomes. The smallest hydrodynamic radius was around 100 nm. This could be caused by the steric limitations of the lipid bilayer being unable to bend freely to sharp enough angles to create a liposome of such small size. A high proportion of liposomes and proteoliposomes containing methyl viologen where found to have a hydrodynamic radius of 150 nm, which is the same as the average result in White *et al.,* (2013). The relative similarities of liposomes to proteoliposomes indicate that the insertion of the MtrCAB complex may not affect the overall size. However, when pelleted by ultracentrifugation, qualitative investigations indicated that liposomes formed a denser pellet than proteoliposomes. Proteoliposome pellets after ultra centrifugation were larger, less compacted and easier to re-suspend than liposome pellets.

Compared to liposomes and proteoliposomes containing methyl viologen, liposomes and proteoliposomes containing STC were larger and more polydisperse. The quality of the results collected was not high, with most readings being rejected by the DLS software. Those results that were deemed valid predicted hydrodynamic radii of 148.1 and 150.5 nm with high polydispersity in each sample. This average hydrodynamic radii is very similar to the average radii predicted for liposomes and proteoliposomes containing methyl viologen, White *et al.,* Hydrodynamic radii in the range of 100 – 1000 nm were detected, which is a larger range than liposomes and proteoliposomes containing methyl viologen, and is possibly due to the lower quality of the results.

Liposomes and proteoliposomes containing cytochrome c were calculated to have hydrodynamic radii of 95 nm (with 38 and 32 % polydispersity respectively). This is slightly smaller than the average hydrodynamic radii calculated for liposomes or proteoliposomes containing methyl viologen. The range of the hydrodynamic radii was from 90 to 360 nm, which is very similar to liposomes or proteoliposomes containing methyl viologen. For the liposomes and proteoliposomes containing either STC or cytochrome c, the differences in ultracentrifugation pellet density were similar to those noted for liposomes containing methyl viologen and proteoliposomes. This indicates that this difference is due to the presence of MtrCAB in the phosphotidyl choline membrane.

	R (nm)	Polydispersity (%)
Liposomes containing methyl viologen	106.7	38.2
Proteolipsomes containing methyl viologen	105.4	34.4
Liposomes containing STC	148.1	42.6
Proteoliposomes containing STC	151.5	46.2
Liposomes containing cytochrome c	95.23	38.2
Proteoliposomes containing cytochrome c	95.21	31.8

Table 4.1 Dynamic light scattering experiments on liposomes and proteoliposomes.

4.07 Liposome and proteoliposome reduction

Comparisons between the oxidation and reduction of liposomes and proteoliposome suspensions, which were proven to be free of any excess un-encapsulated redox indicator, allowed the assessment of MtrCAB's role in any observable redox changes. In White *et al.,* (2013) the methyl viologen held within liposomes (without MtrCAB) were observed to be inaccessible to soluble reductants (and presumably soluble oxidants too). Methyl viologen encapsulated in proteoliposomes (with MtrCAB) could be oxidised and reduced through the addition of oxidants or reductants to the external solution. This proved that electrons were being transported across the phosphatidylcholine membrane via the MtrCAB complex, and that methyl viologen was interacting with the internal side of the MtrCAB complex. Wang *et al.,* (2008) described the rate of reduction of reduced freely soluble MtrC or OmcA with Fe-ethylenediaminetetraacetic acid (Fe-EDTA), Fe-nitrilotriacetic acid (Fe-NTA) and Fe-citrate oxidants. The rate was calculated through tracking absorbance changes of hemes within MtrC or OmcA over time. These rates were determined to be bi-phasic and were described by parallel, second order, bi-molecular rate equations. The bi-phasic nature of the rate of reduction showed a very fast initial rate for few milliseconds and then a very slow secondary rate until completion after a few seconds. The rate of oxidation of MtrC was shown to be faster than OmcA, with the oxidants ranked in the following order for both proteins: Fe-EDTA > Fe-NTA > Fe-citrate. MtrC was maximally reduced by Fe-EDTA at a rate of 0.872 $\mu M^{-1}s^{-1}$; and OmcA had the slowest rate of oxidation recorded, when oxidised by Fe-citrate at 0.012 $\mu M^{-1}s^{-1}$.

In White *et al.,* (2013) bi-phasic rates of reduction and oxidation were found for proteoliposomes containing methyl viologen. In the first few milliseconds after oxidant or reductant had been added a very fast rate of reduction was observed, and then a much slower rate of reduction followed this. The initial rates of oxidation of proteoliposomes containing reduced methyl viologen by suspensions of iron minerals ranged from 8500 ± 916 $e.s^{-1}$ to 1133± 266 $e.s^{-1}$ (0.88 to 2.35 $\mu mol.e.m^{-2}.s^{-1}$). These rates are considerably slower than those for free solution oxidation of MtrCAB, but they do reflect the increased complexity of the proteoliposome system, which is a membrane gated tri-molecular reaction, (Davidson, 1996; Davidson, 2000; Jin & Bethke, 2002). However, these rates are much faster than estimated the rate of Fe(III) reduction by MtrC and OmcA during bacterial respiration calculated by Ross *et al.,* (2009), who found the maximal rate of electron transport to be ~5 $e{\cdot}s^{-1}$. This rate is two or three orders of magnitude slower than

the observed rate of electron transport through MtrCAB in the methyl viologen proteoliposome experiments. This shows that with a suitable potential difference across the proteoliposome lipid bilayer, the rate of electron transport through the MtrCAB complex is sufficient to support, anaerobic, solid-phase iron respiration. To extend the understanding of how MtrCAB transports electrons, experiments investigating the relative reduction and oxidation of proteoliposomes containing methyl viologen, STC and cytochrome c were conducted and compared with these results.

Figure 4.4. Panel A shows the wavelength spectra of liposomes containing oxidised methyl viologen before (grey line) and after (blue line) 10 µL of 100 mM sodium dithionite (to make a final concentration of ~0.25 mM) was added to the 4 mL suspension of liposomes in in 50mM HEPES pH7, 2mM $CaCl_2$, 10mM KCl (this buffer was used throughout). Both the grey and the blue lines show a typical absorbance spectrum of +2 oxidised methyl viologen superposed with liposome scattering. Upon addition of sodium dithionite, any accessible methyl viologen should be reduced, as sodium dithioinite has a lower reduction potential than methyl viologen. As no increase in the 603 nm absorbance was observed, while a strong 330 nm absorbance peak was retained, the conclusion must be that the soluble reductant, was unable to reach and reduce the encapsulated methyl viologen. Thus, the methyl viologen in liposomes was insulated from the soluble redox compounds.

Figure 4.4 Panel B shows the wavelength spectra of methyl viologen containing proteoliposomes. In a similar fashion to Panel A, the grey line represents the proteoliposomes containing methyl viologen absorbance profile before reductant addition, and the blue line represents the absorbance profile of the proteoliposomes after sodium dithionite was added (to make a final concentration of ~0.25 mM). There is a clear increase in the 603 nm (and 400 nm) absorbance upon sodium dithionite addition, indicating that the methyl viologen had been reduced.

Figure 4.4 Panel C shows the absorbance changes at 603 nm of proteoliposomes containing methyl viologen after the addition of sodium dithionite. Starting with oxidised methyl viologen, the addition of sodium dithionite causes the 603 nm peak to increase in two phases. Initially, an extremely fast rate of absorbance increase is observed. This occurs in the first few seconds after reductant addition. After this initial phase, the rate of absorbance change decreases. This lower rate of absorbance increase continues until the methyl viologen within the proteoliposomes is fully reduced at 1000 seconds. After the

proteoliposomes containing methyl viologen stopped showing an absorbance increase at 603 nm, ferric citrate oxidant was added to the suspension (to make a final concentration of ~0.5 mM). The 603 nm absorbance changes associated with this addition of oxidant are shown in Panel D. Panel D shows a rapid decrease in the absorbance at 603 nm after the addition of ferric citrate. Unlike the absorbance increases observed in Panel C, the absorbance decreases in Panel B appear to have only one phase, with the decrease in 603 nm peak height rapidly occurring within the first few seconds. The total 603 nm peak that was observed under reducing conditions returned to its original absorbance under oxidizing conditions, indicating that the reduction and oxidation of the liposomes was fully reversible.

The change in 603 nm peak height was confirmed to be the result of methyl viologen oxidation and reduction, through taking additional wavelength scans before and after the reductive and oxidative time scans (data not shown). These were used to check that there was a 603 nm peak upon reduction as observed in Panel B, rather than any changes in 603 nm absorbance being caused by changes in background scattering absorption or non methyl viologen peaks. The absorbance profile of the liposomes under oxidizing conditions mirrored the grey line in Panel B and the absorbance profile of proteoliposomes in reducing conditions mirrored the blue line in Panel B. This confirmed that the absorbance changes did relate to methyl viologen oxidation and reduction, and that the proteoliposomes had not burst during the process, confirming the conclusions made by White *.et al.,* (2013) who observed the same reduction and oxidation time-scan absorbance changes.

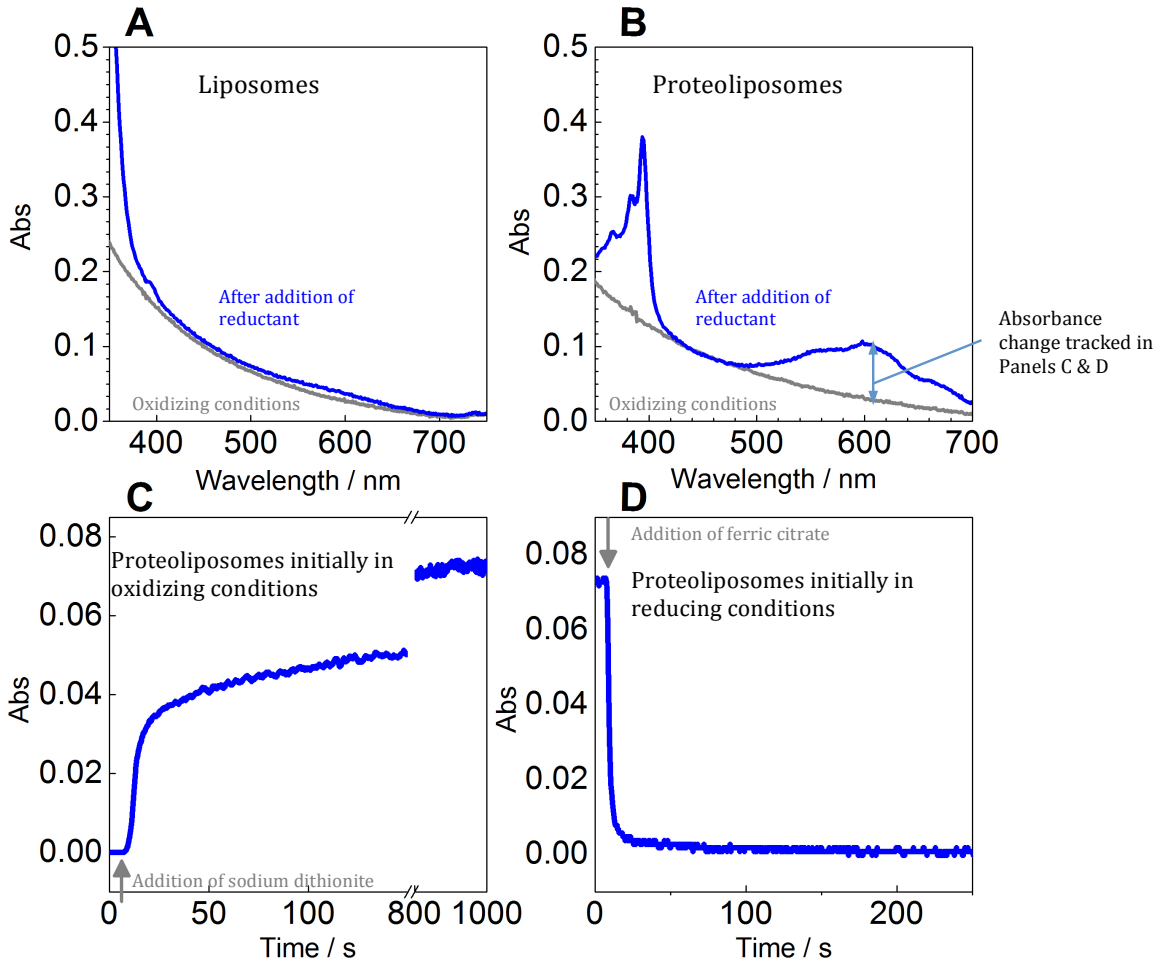

Figure 4.4 Absorbance changes of methyl viologen containing liposome and proteoliposomes in 50mM HEPES pH7, 2mM $CaCl_2$, 10mM KCl.

Panels A and B. [grey line] liposomes or proteoliposomes containing methyl viologen in an aerobically oxidised environment. [Blue line] liposomes or proteoliposomes containing methyl viologen in a anaerobic environment with 0.25 mM sodium dithionite.

Panels C and D. The absorbance of methyl viologen proteoliposome suspensions at 603 nm over time, as the environment changed from oxidizing to reducing (Panel C) and reducing to oxidizing (Panel D). The grey arrows indicates the time when sodium or dithionite ferric citrate was added to a final concentration of 0.5 mM.

To investigate how liposomes or proteoliposomes containing STC behave a similar set of experiments (to those detailed in Figure 4.4) were conducted. Figure 4.5 Panel A shows the absorbance profiles of STC containing liposomes and proteoliposomes before (grey line) and after (orange line) 10 µL of 100 mM sodium dithionite was added to the 4 mL suspension (again to make a final concentration of ~0.25 mM). The grey line in Panel A shows an absorbance spectrum with a peak at 410 nm, typical of oxidised heme. The spectra also shows some background absorbance created by liposome light scattering at lower wavelengths. The orange line shows no change in the absorbance spectra compared to the grey line, thus after sodium dithionite addition there was no heme reduction. This meant that the sodium dithionite present in the sample could not reduce the STC encapsulated within liposome membranes. In contrast to the liposomes represented in Panel A, the MtrCAB proteoliposomes shown in Panel B were reduced when sodium dithionite was added to the suspension. Again, the grey line shows the absorbance profile of the proteoliposomes before the addition of 10 µL of 100 mM sodium dithionite to the 4 mL proteoliposomes suspension, while the red line shows the absorbance profile after 10 minutes after the addition of the reductant, ensuring the sample was at equilibrium. The grey line shows absorbance peaks at 410 nm and 550 nm typical of oxidised heme absorbance, as well as background absorbance due to proteoliposome light scattering at shorter wavelengths. The orange line shows differences to the grey line at the Soret and α/β regions, with a 420 nm, 520 nm and 552 nm peaks all emerging. This demonstrates that the sodium dithionite added to the proteoliposome suspension could reduce the STC encapsulated within the proteoliposomes. This must be due to the presence of MtrCAB in the phosphatidylcholine membrane.

In Panel C, the absorbance of proteoliposomes containing STC at 552 nm was recorded over time as 10 µL of 100 mM sodium dithionite was added to the 4 mL suspension (at the time indicated by the grey arrow). Immediately after the addition of sodium dithionite the absorbance at 552 nm increased. The absorbance changes that occurred had two distinct phases, but the size and duration of the phases of reduction were different to methyl viologen proteoliposome reduction. Immediately after the addition of sodium dithionite, there was a rapid increase in the absorbance at 552 nm, similar to methyl viologen proteoliposomes. After a few seconds this fast initial rate decreased and a slower rate of absorbance increase occurred and continued until an absorbance plateau was reached. Compared to the proteoliposomes containing methyl viologen in Figure 4.3 Panel C, the proteoliposomes containing STC took less time to reach an absorbance plateau. The

proteoliposomes containing methyl viologen took 530 seconds longer to finish reducing. This means that a greater proportion of the STC heme species were reduced in the initial rate phase compared to the proportion observed in the comparative methyl viologen experiments.

Panel D shows the 552 nm absorbance changes over time of the reduced STC proteoliposome suspension when 10 μL of 100 mM ferric citrate oxidant was added (to make a final concentration of ~0.5 mM). Similar to Figure 4.3 Panel D, the absorbance immediately decreased and occurred in one phase. Unlike the oxidation of proteoliposomes containing methyl viologen, the oxidation of proteoliposomes containing STC occurred at a slower rate. The time to total re-oxidation of proteoliposomes containing STC was around 100 seconds. The proteoliposomes containing methyl viologen (Figure 4.3 Panel D re-oxidised) two orders of magnitude faster than this, becoming re-oxidised in the order of seconds. Through this reduction and re-oxidation, the proteoliposomes containing STC were demonstrated to be fully redox reversible. The absorbance changes were confirmed to be changes in the 552 nm peak height caused by heme species redox status change, rather than background absorbance changes. This was achieved through measuring absorbance profiles of the proteoliposome suspension before and after the reductive and oxidative time-scans (data not shown).

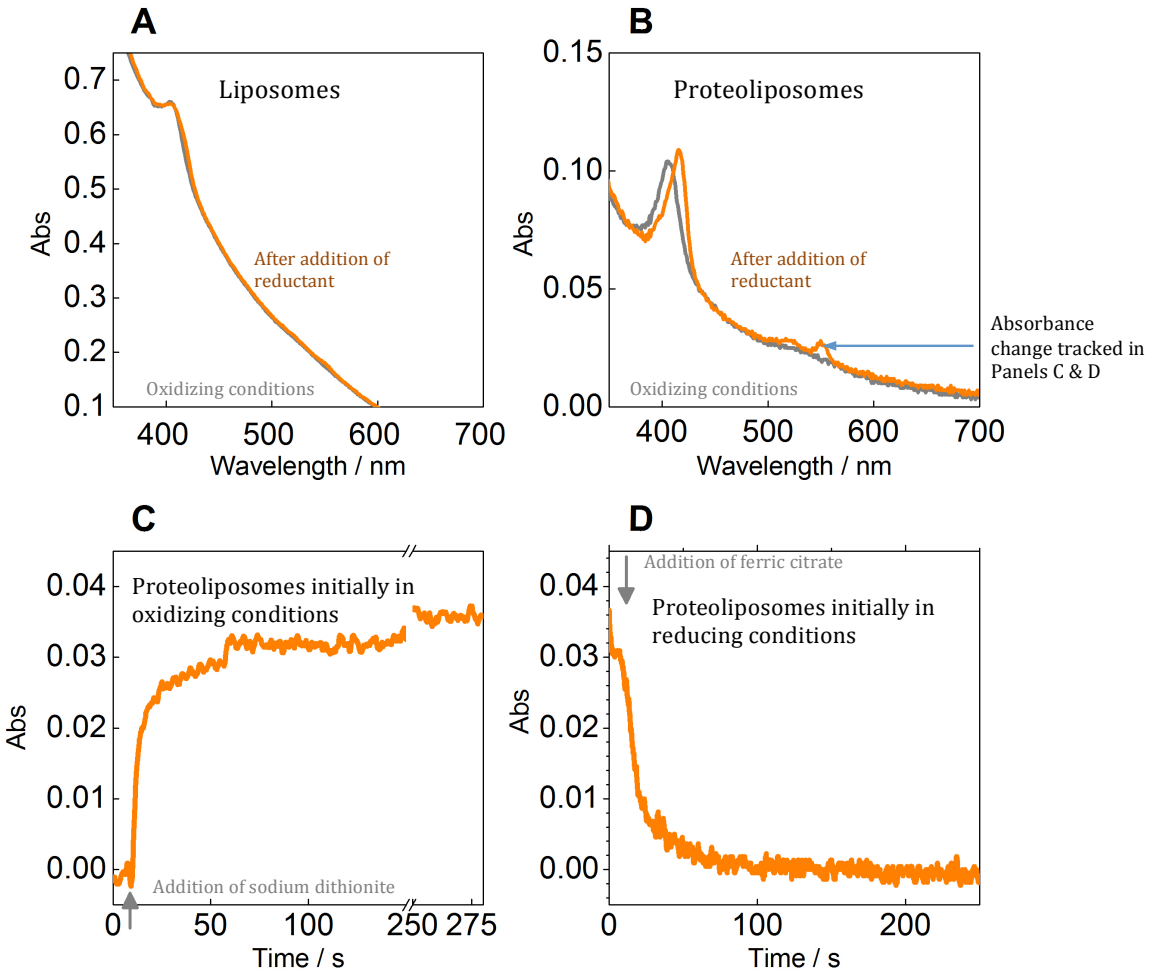

Figure 4. 5 Redox changes of STC containing liposome and proteoliposomes in 50mM HEPES pH7, 2mM $CaCl_2$, 10mM KCl..

Panels A & B. [grey lines] liposomes or proteoliposomes containing STC in an aerobically oxidised environment. [Orange line] liposomes or proteoliposomes containing STC in an anaerobic environment with 0.25 mM sodium dithionite.

Panels C & D. The absorbance of STC proteoliposome suspensions at 552 nm over time either from oxidizing to reducing conditions (Panel C) or reducing to oxidizing conditions (Panel D). The grey arrow indicates the time when sodium dithionite or ferric citrate was added to a final concentration of 0.25mM and 0.5 mM.respectively

Similar to Figures 4.4 and 4.5, experiments were conducted on cytochrome c containing liposomes and proteoliposomes to investigate how they behaved in different redox conditions. Figure 4.6 Panels A and B show the absorbance profiles of both liposomes and proteoliposomes containing cytochrome c before (grey lines) and after (red lines) 10 µL of 100 mM sodium dithionite was added to the 4 mL suspension (again to make a final concentration of ~0.25 mM). The grey line in Panel A shows an absorbance spectrum with a peak at 410 nm this is typical of oxidised heme. The spectrum also has background absorbance created by liposome light scattering at lower wavelengths. The red line shows no change in the absorbance spectrum compared to the grey line, thus after sodium dithionite addition there was no heme reduction. The grey and red lines overlay. This indicates that the hemes contained within the liposomes, were not reduced upon addition of sodium dithionite. In Panel B, the grey line also shows an absorbance spectra with peaks at 410 nm, which is again typical of oxidised heme, however the red line shows a canonical reduced heme spectrum, with peaks emerging at 410 nm, 520 nm and 552 nm. This indicates that the MtrCAB in proteoliposomes allowed the sodium dithionite to reduce cytochrome c encapsulated within proteoliposomes, which would otherwise be insulated due to the phosphotidylcholine membrane. This is similar to both the proteoliposomes containing methyl viologen and STC (Figures 4.4 and 4.5).

Panel C shows the change in absorbance at 552 nm over time that proteoliposomes containing cytochrome c undergo when 10 µL of 100 mM sodium dithionite was added to them, at the time indicated by the grey arrow. Similarly to proteoliposomes containing STC, the proteoliposomes containing cytochrome c underwent a rapid increase in the 552 nm absorbance in the first few seconds after sodium dithionite addition. Unlike previous proteoliposome experiments, the absorbance change occurred in phase. The absorbance reached a maximum and plateaus after the first few seconds, with only the first initial rate observed.

In Panel D the absorbance at 552 nm of reduced proteoliposomes containing cytochrome c is monitored whilst 10 µL of 100 mM of ferric citrate was added to the suspension (to make a final concentration of ~0.5 mM). Unlike proteoliposomes containing methyl viologen or STC, only a very minor change in 552 nm absorbance is observed when ferric citrate is added. There is a small reduction in 552 nm absorbance but the absorbance change does return to the pre-reduction values. In unpublished experiments, ferric citrate was not observed to re-oxidise cytochrome c when it was in free solution. The mid point

potential of cytochrome c was calculated to be +0.224 V (Pande & Myer, 1978), and the mid point potential of ferric citrate +0.212 V (Wang *et al.,* 2008). Therefore, the reduction of ferric citrate by cytochrome c is unfavorable.

The change in 552 nm absorbance observed in Panel D was not attributed to a change in 552 nm peak height. It is most likely that the change observed was due to a change in background scattering absorbance at 552 nm. A stronger oxidant, potassium ferricyanide (Em = +0.436 V) was observed to oxidise cytochrome c in free solution. However, when potassium ferricyanide was added to reduced proteoliposomes, the 552 nm peak also did not diminish. This is demonstrated in Panel E, where the grey line shows the absorbance spectra of proteoliposomes containing cytochrome c in aerobic conditions, the dark red line shows the absorbance spectra after sodium dithionite was added to a final concentration of 0.25 mM, and the bright red line was the absorbance spectra of the cytochrome c after potassium ferricyanide was added to a final concentration of 1 mM. Before any reductant was added, the wavelength spectrum of the proteoliposomes shows the proteoliposome encapsulated cytochrome c to be in a partially reduced state. This is consistent with Figure 4.6 Panels A and B. After reduction by sodium dithionite, an increase in the 552 nm and 520 nm peaks were observed. This indicated that the encapsulated cytochrome c had become reduced. After potassium ferricyanide was added to the reduced liposomes, the peak heights of the 552 and 520 nm peaks were not observed to diminish. This indicated that the proteoliposomes containing cytochrome c remained reduced in the presence of the oxidant potassium ferricyanide. This demonstrates that once reduced, the encapsulated cytochrome c was not able to be re-oxidised via the MtrCAB complex.

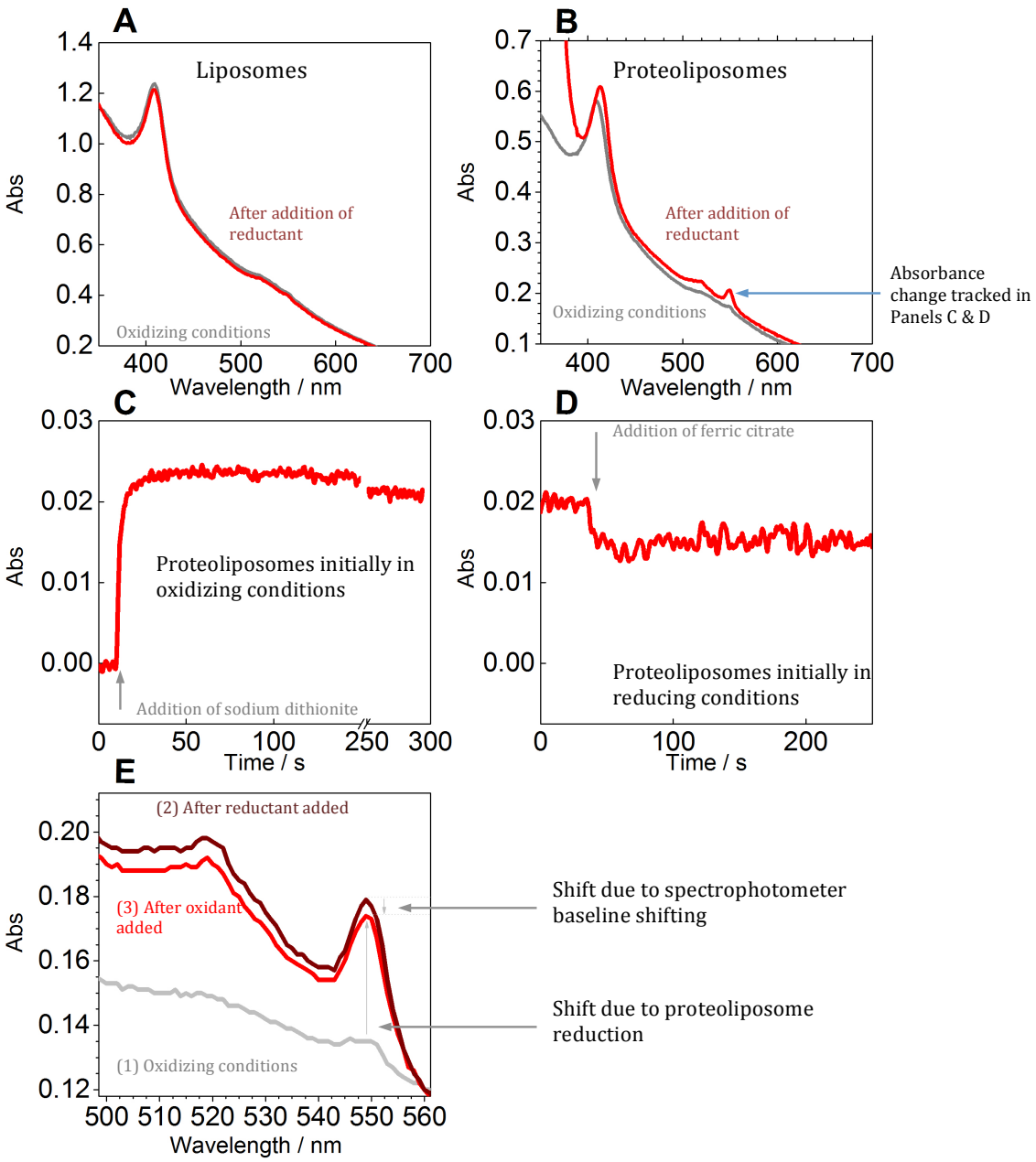

Figure 4. 6 Absorbance changes of cytochrome c containing liposome and proteoliposomes in 50mM HEPES pH7, 2mM $CaCl_2$, 10mM KCl..

Panels A & B. [grey lines] liposomes or proteoliposomes containing cytochrome c in an aerobically oxidised environment. [Red line] liposomes or proteoliposomes containing cytochrome c in a anaerobic environment with 0.25 mM sodium dithionite.

Panel C and D. The absorbance of cytochrome c proteoliposome suspensions at 552 nm over time, going from oxidizing to reducing conditions (Panel C) and reducing to oxidizing conditions (Panel D). The grey arrow indicates the time when sodium dithionite was added to a final concentration of 0.5 mM.

Panel E. Sequential absorbance profiles of proteoliposomes containing cytochrome c in different redox conditions. [(1) grey line] Absorbance profile of proteoliposomesin an oxidizing environment. [(2) Dark red line] Absorbance profile after sodium dithionite has been added to a final concentration of 0.25 mM. [(3) Light red line] Absorbance after potassium ferricyanide has been added to a final concentration of 1 mM.

Rates of proteoliposome reduction and oxidation

To compare the rates of electron transport in and out of the three types of proteoliposomes, linear approximations were made for each of the sections in the oxidative and reductive graphs. The linear fits for each experiment are shown in Figure 4.7

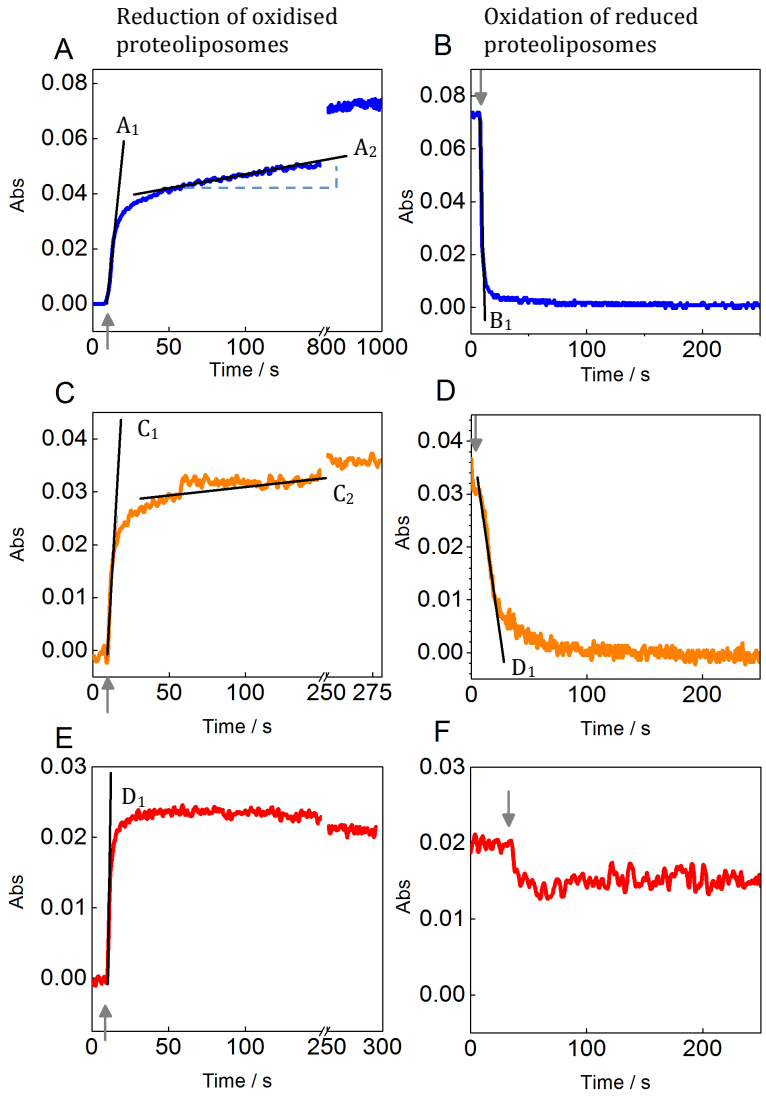

Figure 4. 7 The absorbance of proteoliposomes in 50mM HEPES pH7, 2mM $CaCl_2$, 10mM KCl exposed to reductants and oxidants over time, both oxidants and reductants were added until a final concentration of 0.25 mM was achieved
Panels A & B. The respective reduction and oxidation of methyl viologen proteoeliposomes
Panels C & D. The respective reduction and oxidation of STC containing proteoliposomes.
Panels D & E. The respective reduction and oxidation of cytochrome c containing proteoliposomes.
The black lines on the panels (A_1, A_2, B_1...etc.) are the linear fits for different parts of the graphs, These were used (as demonstrated in Panel A) to calculate gradients from which the rate of absorbance changes could be calculated. The grey arrows indicate time at which either reductant or oxidant was added to the proteoliposome suspensions.

Table 4.2 details the observed rate of reduction and oxidation for each type of proteoliposome, based on the gradients of the linear fits in Figure 4.7.

Proteoliposome Interior		Reductive Exterior	Lines from Figure 4.7	Oxidative Exterior	Lines from Figure 4.7
Methyl Viologen	Initial Rate (Abs/s)	4.17×10^{-3}	A_1	-2.54×10^{-2}	B_1
	Initial Rate (e^-/s)	8.88×10^{14}		-5.40×10^{15}	
	2nd Rate (Abs/s)	9.79×10^{-5}	A_2	n/a	
	2nd Rate (e^-/s)	2.09×10^{13}		n/a	
STC	Initial Rate (Abs/s)	5.38×10^{-3}	C_1	-1.60×10^{-3}	D_1
	Initial Rate (e^-/s)	5.00×10^{14}		-1.38×10^{14}	
	2nd Rate (Abs/s)	2.06×10^{-5}	C_2	n/a	
	2nd Rate (e^-/s)	4.40×10^{12}		n/a	
Cytochrome C	Initial Rate (Abs/s)	6.42×10^{-3}	E_1	n/a	
	Initial Rate (e^-/s)	5.52×10^{14}		n/a	
	2nd Rate (Abs/s)	n/a		n/a	
	2nd Rate (e^-/s)	n/a		n/a	

Table 4.2. The rate of change in absorbance of the 603 nm peak in proteoliposomes containing methyl viologen and the 552 nm peak in STC and liposomes containing cytochrome c when being reduced from an oxidised state and re-oxidised from a reduced state. The calculated rate of mass electron movement onto redox indicator species inside proteoliposomes; based on absorbance changes of redox indicators.

These rates in absorbance change have been converted into estimates of the number of electrons reacting per second in each experiment. This was achieved through using the Beer-Lambert Law Equation 2.1 (as well as the respective extinction coefficients of 11,000 $M^{-1}.cm^{-1}$, 440,000 $M^{-1}.cm^{-1}$ and 110,000 $M^{-1}.cm^{-1}$ for methyl viologen STC and cytochrome c respectively) to calculate the concentration of either the methyl viologen, STC or cytochrome c being reduced over time. As it is known that both methyl viologen and cytochrome c accept a single electron upon reduction, and STC accepts four electrons, using Avagadro's number and the volume of the proteoliposome suspension a rate of electrons per second can be calculated.

$$The\ gradient\ of\ line\ A_1 = 4.17.10^{-3}\ Abs/sec$$

$$(Beer\ Lambert) \qquad Concentration_{MV} = \frac{Abs}{\varepsilon_{MV}.l}$$

$$Number\ of\ \acute{e} = Concentration_{MV}.Vol.\mathbb{N}$$

$$Rate\ of\ \acute{e}/s = \left(\frac{4.17.10^{-3}}{11000.1}\right).4.10^{-3}.6.10^{23} = 8.10^{14}\ \acute{e}/s$$

The rates displayed in Table 4.2 represent the rate of change in absorbance in the initial periods of reduction and oxidation and the secondary rate in the reductive process (once the fast initial rate phase was complete). The initial rates of reduction for each of these experiments are of the same order of magnitude, however clear difference in the rates of oxidation between the different proteoliposome types are observed. Proteoliposomes containing methyl viologen re-oxidised two orders of magnitude faster than those containing STC. Proteoliposomes containing cytochrome c did not re-oxidise at all.

If accurate estimates of the number of MtrCAB complexes in the sample could be made then estimates of the number of electrons transported per MtrCAB complex per second could be calculated. Numerical estimates of MtrCAB complexes could be made based on the amount of MtrCAB used in proteoliposome preparation, the incorporation rate of MtrCAB into proteoliposomes and the amount of the preparation used in each experiment. Between 0.01 to 0.02 nmol of MtrCAB was used for each proteoliposome preparation, with an incorporation rate of 40-80 % (unpublished data from E. Ainsworth, who investigated the amounts of MtrCAB free within the suspension at different stages of making proteoliposomes) and approximately 10-30% of each preparation being used for each experiment. This gives a range of between 2.4×10^{11} and 2.9×10^{12} MtrCAB complexes per experiment. Each preparation had a different proportion of MtrCAB incorporation, and each experiment used different amounts of proteoliposome suspension. The DLS experiments show that there is a range in the sizes of the proteoliposomes prepared and substantial differences between the different types of proteoliposome, particularly proteoliposomes containing STC. Consequently, it is difficult to compare quantitatively the rates of oxidation and reduction of different proteoliposome experiments. This is because these rates are derived from the superposed absorbance of unknown numbers of proteoliposomes which contain unquantified concentrations of redox indicators, and have unknown numbers of MtrCAB complexes available per liposome, However, taking these biases into consideration and using the predicted range of MtrCAB numbers, an electron transport rate of between 200 – 3000 $e.s^{-1}$ for each MtrCAB was calculated. No attempt to distinguish the differences between different proteoliposome types could be made but this result is in line with published results (White *et al.,* 2013) where approximately 1000 $e.s^{-1}$ was predicted for the initial rate.

As proteoliposome aliquots were used for both the reduction and oxidation experiments, the rates of electron transport are directly comparable between these processes. Ratios were calculated from the reductive and oxidative initial rates for each proteoliposome type. These are shown in Table 4.3. Proteoliposomes containing methyl viologen oxidise faster than they initially reduce. The opposite is true for proteoliposomes containing STC, which reduce at a rate that is faster than they are oxidised. Proteoliposomes containing cytochrome c only reduce, being unable to re-oxidise. This produces correlation where the more positive the mid-point potential of the redox indicator, the larger the ratio of initial rate of reduction to oxidation.

Redox indicator	Methyl Viologen	STC	Cytochrome C
$\left\lvert\frac{[Int.\,Rate\ in\ (reduction)]}{[Int.\,Rate\ out\ (oxidation)]}\right\rvert$	$1.64\text{x}10^{-1}$	3.3625	n/a

Table 4.3 The bulk flow of electrons into proteoliposomes, during reduction, divided by the bulk flow of electrons out of the same proteoliposomes during re-oxidation.

4.08 Electrode based proteoliposome reduction and oxidation

The work by White *et al.,* 2013, relied on chemical reduction of the proteoliposomes. This process required the addition of redox chemicals to the proteoliposome suspension. These chemicals and chemical products (typically sodium dithionite) would be present in the suspension and available to interfere with any subsequent experiments, such as oxidation of reduced proteoliposomes. Therefore, the development of a methodology to circumvent the need for chemical reduction or oxidation would allow experimentation upon reduced proteoliposomes in a mediator free buffer. Non-chemical redox experiments on liposomes and proteoliposomes were attempted using a carbon-pot electrochemical cell set up, as detailed in Materials and Methods section 2.26. These were conducted in a Belle™ anaerobic glove box with oxygen levels below 5ppm. The carbon pot would provide a surface for proteoliposomes to exchange electrons with, dependent on the potential difference between the pot and a counter electrode. This potential difference could be exactly controlled through the use of a potentiostat. The current passing through the electrochemical cell chamber would then be exactly the same current that passes into or out of the liposomes or proteoliposomes. Initial experiments using liposomes containing methyl viologen were used to test the methodology, as these were the most well studied and most easily and repeatedly produced.

Reduction of methyl viologen in solution using a carbon pot electrode

To be able to accurately determine that the functioning of MtrCAB complexes facilitated a current passing through the cell, all other redox species external to the liposome need to be removed. These soluble-free species, like un-encapsulated methyl viologen, would be able to directly interact with the carbon pot, and so would be able to provide false positive current. Cyclic voltammograms are experiments where the potential of an electrochemical cell (containing substance of interest) is varied between two potential vertices at a prescribed voltage per second. The changes in the current through the cell are collected. Cyclic voltammogram scans were taken of a methyl viologen titration into a carbon pot, which also contained empty (with no redox indicators) phosphatidyl-choline proteoliposomes. This would simulate methyl viologen leaking out of proteoliposomes, and facilitate investigations into the tolerances for un-encapsulated methyl viologen within the experimental set up, Figure 4.8.

Figure 4.8 shows cyclic voltammograms of each concentration of methyl viologen titrated into a carbon pot with a background of proteoliposomes (with no internal redox indicator) in 20 mM HEPES pH 7.5 2 mM $CaCl_2$ 100 mM NaCl. Three scan rates (0.01, 0.05 and 0.1 $V.s^{-1}$) were used for each of the titration's stages to observe any changes dependent on this.

The green voltammograms in all the panels of Figure 4.8 show the baseline scans. These were scans of the proteoliposome suspension before any methyl viologen was added to the carbon pot. There are no redox species in these samples apart from the MtrCAB incorporated in the proteoliposomes. The voltammogram shows only non-Faradaic currents forming, which means that the blank proteoliposomes did not produce a signal that is large enough to be detected in the set up. If MtrCAB was incorporated into liposomes at a higher concentration, then it might be possible to observe a Faradaic response from them, however this was not the case with the proteoliposomes used. The baseline scans are therefore very useful as they enable the precise identification of non-Faradaic currents in later titrations.

The yellow lines in all the panels of Figure 4.8 show the first titration of methyl viologen. 1 µL of 200 mM methyl viologen was added to the proteoliposome suspension, making a final concentration of 0.6 µM. Faradaic current peaks were then detected at -0.46 V on the reductive sweep and -0.422 on the oxidative sweep. A further 2 µL of 200 mM methyl viologen was then added to the proteoliposome suspension making a final concentration of 1.8 µM.

The orange lines represent the cyclic voltammograms measured at this methyl viologen concentration. The Faradaic peaks -0.46 V and -0.422 V observed for the initial concentration of methyl viologen are present in this titration, this time with larger currents.

The final titration was made with a further 1 µL of 200 mM methyl viologen added to the liposome suspension. This made a final concentration of 2.4 µM. The cyclic voltammagrams from this titration are shown as red lines in Figure 4.8. The Faradaic peaks at -0.46 V and -0.422 V have an increased current compared to previous titrations. Although the carbon pot experiments do not enable exact background subtraction, which would allow precise integration of the Faradaic peaks for electron counting, rough calculations indicate that the number of electrons in the reductive peak matches the

number in the corresponding oxidative peak of each scan, indicating the reduction and oxidation of methyl viologen in this situation is reversible.

No scan rate dependence of the mid point potential of methyl viologen in free solution was observed between the three different scan rates of 0.01, 0.05 and 0.1 $v.s^{-1}$ in each of the respective panels. The -0.46 V and -0.422 V peaks observed for methyl viologen remained at the same potentials, irrespective of the scan rate used for the cyclic voltammogram. The non-Faradaic current increased with scan rate as expected, as did the current of each of the Faradaic peaks.

The average of the reductive and oxidative peaks in the cyclic voltamograms is -0.441 V, which is very similar to the published mid-point potential of methyl viologen of -0.446 V (Mayhew *et al* 1978).

Unencapsulated methyl viologen was detected at much lower levels with a carbon pot set up compared to UV-vis absorbance measurements. Trace amounts of methyl viologen would produce detectable currents in CV experiments, these trace amounts of methyl viologen gave rise to UV-vis absorbance's that were too small to be detected by a spectrophotometer. Thus proteoliposomes that were found to be suitable for experiments tracking absorbance changes were found to be unsuitable for carbon pot based experiments because they had trace amounts of methyl viologen present in the supernatant. As a result of this, a new cleaning protocol was developed. This helped to create liposomes and proteoliposomes that had minimal methyl viologen external to (or un-encapsulated by) the liposomes. The extra cleaning procedures introduced were, firstly, increasing the number of centrifugal washing steps and, secondly, incubating the liposomes with the divalent cation binding Chelex™ beads, as described in Materials and Methods section 2.24. These extra procedures effectively removed all detectable methyl viologen external to the liposomes and proteoliposomes.

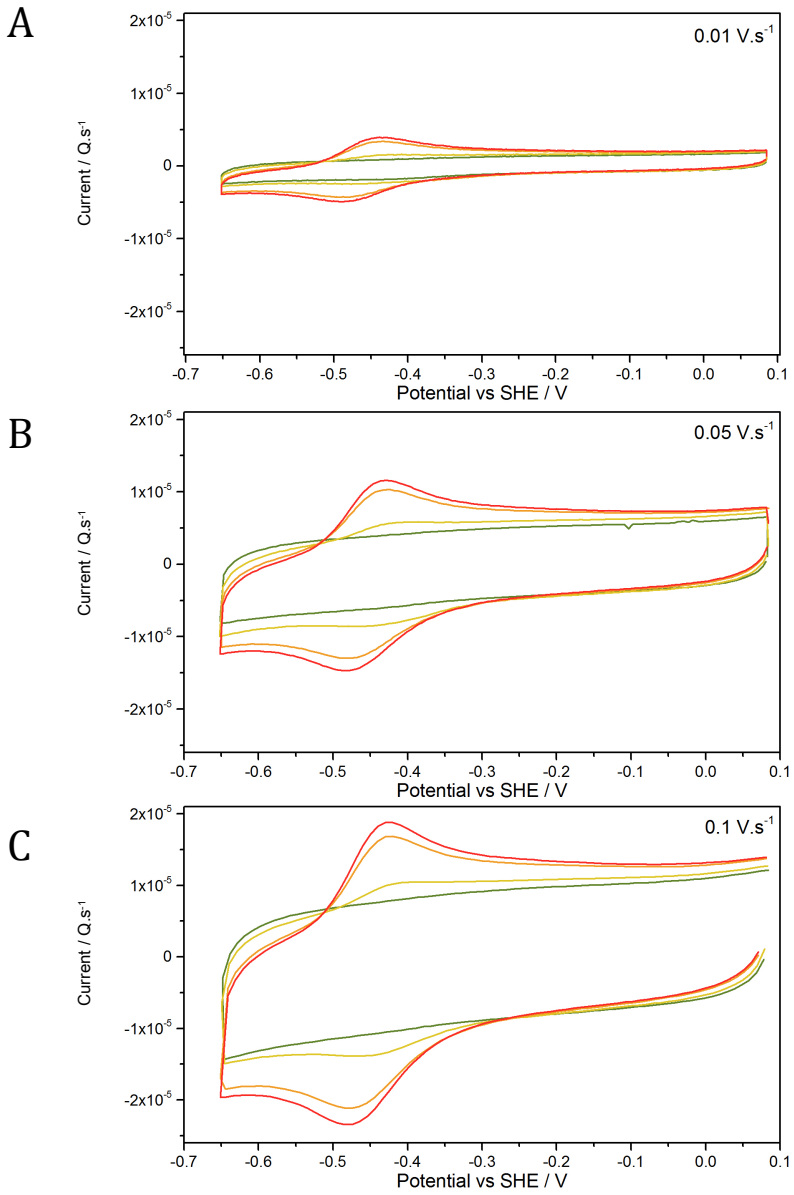

Figure 4. 8 Cyclic voltammograms rom 0.1 V to -0.7 V of MtrCAB proteoliposome suspensions in 20 mM HEPES pH 7.5 2 mM $CaCl_2$ 100 mM NaCl ,held within a glassy carbon pot with increasing concentrations of methyl viologen added to the solution. Panel A. was conducted at 0.01 $V.s^{-1}$ Panel B. at 0.05 $V.s^{-1}$ .Panel C. at 0.1 $V.s^{-1}$
[green traces] proteoliposomes containing no redox indicator.
[yellow traces] proteoliposomes suspension with 1 µL of 200 mM methyl viologen added.
[orange traces] proteoliposomes suspension 3 µL of 200 mM methyl viologen added.
[red traces] proteoliposomes suspension with 4 µL of 200 mM methyl viologen added.

Comparing cyclic voltammetry of methyl viologen with liposomes and proteoliposomes containing methyl viologen

Having fully characterized how methyl viologen in free solution behaves in a carbon pot, the voltammetric responses of proteoliposomes containing methyl viologen were investigated and then compared to methyl viologen liposomes and freely soluble methyl viologen. This enabled the determination of whether the non-chemical redox methodology was suitable for future experiments. The experimental set used a glassy carbon pot, as described in the Materials and Methods section 2.26. Results from a range of methyl viologen proteoliposome experiments are shown in Figure 4.9. Liposomes were first determined to be fully insulating encapsulated methyl viologen from any redox reactions, then that MtrCAB proteoliposomes allowed methyl viologen to become reduced and re-oxidised. An investigation into the effect of scan rate upon the oxidation and reduction of proteoliposomes was conducted. A comparison between the reduction and oxidation of methyl viologen in free solution and encapsulated within proteoliposomes was made, to try and discern any differences. Based on these results investigations into the longevity of liposomes was conducted, where methyl viologen that had leaked out of liposomes was tacked.

Figure 4.9. Panel A shows the cyclic voltammogram of 20 mM HEPES buffer 2 mM $CaCl_2$ 100 mM NaCl as a black line. This is the buffer used for liposome and proteoliposome suspensions, and as such the voltammogram is useful to determine the background current responses. The voltammogram profile has no Faradaic charge transfers, only non-Faradaic (or capacitive) currents of free ions moving in the cell. These results indicate that the carbon pot is clean and that there are no redox species in the buffer used. The presence of trace amounts of methyl viologen intercalated between the outer layers of carbon in the pot was a common problem. These produced detectable signals that interfered with results and they had to be removed through aluminum oxide abrasion and thorough washing before experimentation. Thus, the developments of rigorous control assays were essential to prove the pot's cleanliness. Panel A also shows a red line which is the cyclic voltammogram of 50 μL of liposomes containing methyl viologen added to the 300 μL of 20 mM HEPES buffer 2 mM $CaCl_2$ 100 mM NaCl already in the pot. These liposomes had no MtrCAB present within them. The red line has a larger non-Faradaic response than the (black) buffer baseline. This is due to the increased volume present in the carbon pot, from the addition of liposomes. The red line shows only very small

Faradaic responses at -0.42 V on the reductive sweep and -0.4 V on the oxidative sweep. Comparison with the free methyl viologen cyclic voltammetry in Figure 4.8 Panel C shows that the concentration of available methyl viologen is in the order of 10^{-10} M. The encapsulated methyl viologen (which is in the order of 10^{-3} M) is insulated from the carbon electrode surface by the phosophatidylcholine membrane. The effectiveness of the washing process of the liposomes and proteoliposomes was demonstrated by the lack of any meaningful Faradaic signal. Upon removal from the carbon pot and lysis of the liposome membranes, the released methyl viologen produced easily observable Faradaic responses, similar to the green line in Figure 4.9 Panel D and the blue line in Figure 4.9 Panel E.

These control experiments enabled experiments on MtrCAB proteoliposomes containing methyl viologen to be conducted with the knowledge that any signals recorded do not come from freely soluble methyl viologen, as long as the proteoliposome preparation was properly washed and the carbon pot set up was properly cleaned.

Figure 4.9 Panel B shows the cyclic voltammograms of proteoliposomes containing methyl viologen as a blue line and the associated 20 mM HEPES buffer 2 mM $CaCl_2$ 100 mM NaCl buffer baseline as a black line. These experiments were set up in the same way as those previously investigating liposomes containing methyl viologen (section 2.24). The proteoliposomes were washed and cleaned before removing all exterior methyl viologen. No Faradaic signals were detected in the buffer measurements (as shown by the black line), indicating that the equipment was clean of any free methyl viologen. In contrast to the liposomes containing methyl viologen, the proteoliposomes containing methyl viologen produce a large Faradaic response. Current peaks at -0.48 V on the reductive sweep and -0.42 V on the oxidative sweep were clear redox signals. This shows that MtrCAB complexes in proteoliposome membranes act to allow a current from the carbon pot to reduce and oxidise insulated methyl viologen. This therefore indicates that a conductive bridge can be formed between the carbon pot electrode surface and the MtrCAB complex. The mid point potential of the two Faradaic responses is -0.45 V, a lower mid point than measured for methyl viologen in free solution (or on the surface of liposomes and proteoliposomes). This change must be caused by the redox reactions depending on MtrCAB function. Panel C shows how the proteoliposomes containing methyl viologen respond to changes in the scan rate of cyclic voltammograms. Three different scan rates were investigated, 0.01, 0.05 and 0.1 $V.s^{-1}$ (labeled as dark to light blue

respectively). These showed no changes in the potentials of the Faradaic responses, either on the reductive or oxidative sweeps over all the scan speeds. This shows that the voltammetric response of liposomes containing methyl viologen is not diffusion limited in the time scale range investigated. A real difference in the mid point potential between freely soluble methyl viologen and proteoliposomes containing methyl viologen is occurring.

Figure 4.9 Panel D shows a direct comparison of the voltammograms of freely soluble methyl viologen (green line) and one of MtrCAB proteoliposomes containing methyl viologen (blue line). The different potentials inducing peak Faradaic responses between the two samples is clearly demonstrated. The reductive peak for proteoliposomes containing methyl viologen is clearly more negative than for freely soluble methyl viologen. In contrast, the oxidative peaks are fairly similar. This suggests liposomes containing methyl viologen require a more negative or greater reductive potential than methyl viologen in solution to become reduced. The magnitude of the reductive peaks of both freely soluble methyl viologen and methyl viologen in proteoliposomes were observed, in Figure 4.9 Panel C and in Figure 4.8 Panels A, B and C respectively, to not be dependent on voltage scan rate. Both Figure 4.9 Panel C and all the Panels in Figure 4.8 show reductive peaks at the same potential as their respective blue and green voltammograms in Panel D.

Panel E shows the cyclic voltammograms of week old liposomes containing methyl viologen (dashed red line) compared to fresh proteoliposomes containing methyl viologen (blue line). The methyl viologen proteoliposome cyclic voltammogram has the same Faradaic responses observed in Panel B: a reductive peak at -0.48 V and an oxidative peak at -0.42 V. The liposomes containing methyl viologen initially showed the same profile as those demonstrated in Panel A. This is demonstrated by the black line, where no Faradaic responses are observed. After a week of incubating these liposomes in an anaerobic glovebox in the dark, the liposomes were re-tested. Freely soluble methyl viologen signal was observed, with Faradaic responses at -0.46 and -0.42 V. This indicates that methyl viologen has escaped the confines of the liposomes and is freely soluble in the suspension solution. Slight differences in the freely soluble methyl viologen and proteoliposome encapsulated methyl viologen are observed in the reductive peak potential. It is possible that these differences could be used to differentiate between freely soluble methyl

viologen and MtrCAB proteoliposomes containing methyl viologen that are free from external methyl viologen contaminants.

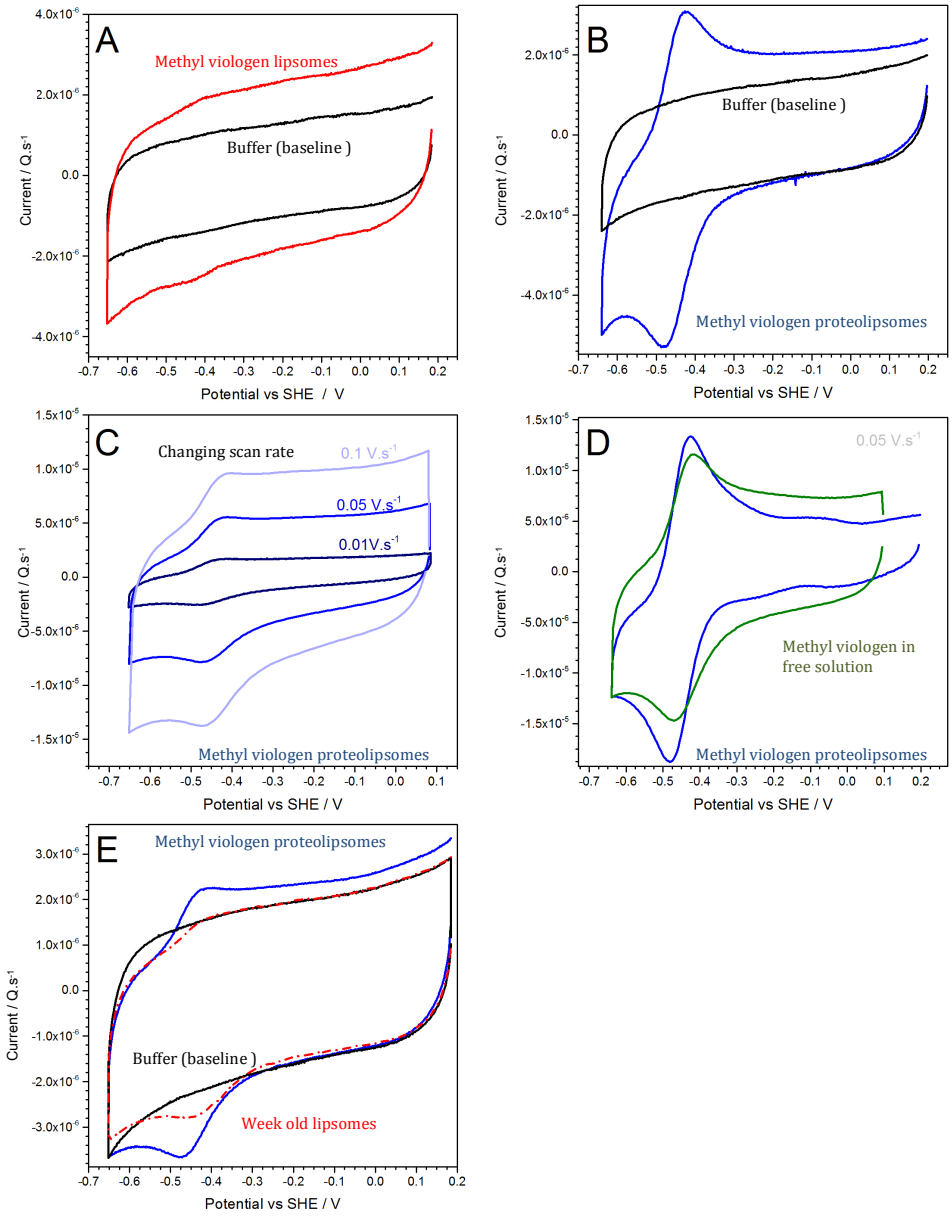

Figure 4. 9 Cyclic voltammograms of methyl viologen containing liposomes and proteoliposomes in a glassy carbon pot cell. The standard buffer (20 mM HEPES, 2 mM $CaCl_2$, 100 mM NaCl) was used in all experiments.

Panel A. [Black line] The standard HEPES buffer in isolation [Red line] liposomes containing methyl viologen in the standard HEPES buffer.

Panel B [Black line] The standard HEPES buffer in isolation. [Blue line] MtrCAB proteoliposomes containing methyl viologen in the standard HEPES buffer.

Panel C scan rate dependence of MtrCAB proteoliposomes containing methyl viologen at 0.01 $V.s^{-1}$ [Dark blue line], 0.05 $V.s^{-1}$ [blue line] and 0.1 $V.s^{-1}$ [light blue line].

Panel D comparing freely soluble methyl viologen [green line] with MtrCAB proteoliposomes containing methyl viologen [blue line].

Panel E liposomes of different ages. [Black line] Standard buffer in isolation [blue line] Fresh MtrCAB proteoliposomes [Red dashed line] seven day old liposomes

4.09 Amperometry of proteoliposomes containing methyl viologen

After proteoliposomes containing methyl viologen had been shown to be reduced and re-oxidised in cyclic voltammetry experiments, experiments were conducted to investigate how the flux of electrons into and out of these proteoliposomes behaved over time. These experiments would investigate whether the reduction and oxidation profiles of proteoliposomes containing methyl viologen in a carbon pot over time were similar to those absorbance changes detected in proteoliposomes by chemical reduction and oxidation over time. The methyl viologen containing proteoliposomes were therefore investigated using amperometry experiments (as set out in Materials and Methods section 2.26). All amperometry was conducted in a Belle™ anaerobic glove box with oxygen levels below 5ppm. In addition to the electrochemistry rig, a diode array UV-vis spectrophotometer was inserted into the glove box for complimentary UV-vis absorbance analysis on proteoliposome samples.

Figure 4.10 Panel A shows the coulombmetric response of proteoliposomes containing methyl viologen under rapid mixing when the cell potential was altered from +0.18 V to -0.6 V. The contents of the carbon pot were rapidly mixed, through the use of a magnetic flea rotated by a magnetic stirrer plate which was positioned under the carbon pot cell. This caused oscillating magnetic fields within the cell, inducing small resistive electrical currents in the cell that can be observed as noise in the experimental trace. At 600 seconds (marked with a grey arrow), the magnetic stirrer plate was switched off to demonstrate that the background noise was caused by this source. The potential +0.18 V was chosen as the oxidative potential for the proteoliposomes, as it is well above the mid point potential of proteoliposomes containing methyl viologen. -0.62 V was chosen as the reducing potential as it is below the potentials in the cyclic voltammetry experiments that had a reductive Faradaic response for proteoliposomes containing methyl viologen, but not so low as to cause methyl viologen to be doubly reduced to MV^0, which is membrane soluble. At +0.18 V there was no redox current observed, either into or out of the proteoliposomes. When the potential was switched from +0.18 V to -0.6 V there was an immediate negative current out of the cell (into the liposomes), maximally at -2.2×10^{-5} amps (or 1.4×10^{14} $e.s^{-1}$). This negative current had a rapid rate of decline in the first few seconds. This initial fast rate was then replaced after the first few seconds by a slower second rate that leveled off after around 600 seconds. The liposomes containing methyl viologen were removed from

the carbon pot and analysed in a UV-vis photospectrometer to confirm that the proteoliposomes were reduced.

Panel B shows the UV vis absorbance of proteoliposomes before and after carbon pot reduction. As the concentration of liposomes used was high, there was a large amount of background scattering causing very high absorbance readings on the edge of the linear limit of the spectrophotometer. Before reduction, no absorbance peak was observed at 603 nm. After reduction by the carbon pot as detailed in Panel A, an absorbance peak at 603 nm was detected. The high background noise pushed the absorbance levels cup to and beyond the linear limit of the spectrophotometer used, thus the exact peak height cannot be used to measure concentration. The evidence of proteoliposome reduction in Panel B is confirmed through the photograph insert in Panel A. This shows the proteoliposomes in a fluorescence cuvette after reduction by the carbon pot. The proteoliposomes are visibly blue. The colouration of the proteoliposomes did not fade when they were left overnight in the glovebox, which allowed the proteoliposomes reduced in this way to be used in further experiments. This indicated that the proteoliposomes were stably reduced in the carbon pot and could be removed and remain reduced.

To compare the reduction and oxidation of proteoliposomes containing methyl viologen in chemical and non-chemical methodologies, an amperometry experiment was conducted, mirroring the additions of sodium dithionite and ferric citrate using the carbon pot cell. The difference between the mid-point potentials of sodium dithionite (E_m=-0.66 V) and ferric citrate (E_m= +0.37 V) is over 1 V. Causing an instantaneous potential change of 1 V across the carbon pot could damage its surface and could cause it to disintegrate, even though it was undergoing thermostatic cooling. Thus, the potentials +0.18 V to -0.62 V were used. These were known to not damage the carbon pot and are fairly close to the potentials induced in the chemical reduction and oxidation of methyl viologen prtoeoliposomes. Panel C shows the changes in current over time, as the potential of the cell is switched from +0.18 V to -0.66 V and back to +0.18 V. The magnetic stirrer was in operation for the entire experiment to ensure that proteoliposomes would not settle on the carbon pot surface and impede the reduction of other proteoliposomes. This gave a large amount of background noise. Upon the potential change from +0.18 V to -0.66 V, a large negative current out of the cell into the proteoliposomes was observed, maximally at $1.6x10^{-5}$ amps (or $9x10^{-13}$ $e.s^{-1}$). The rate of current change was initially very fast but then slowed, before returning to zero. When the cell potential was switched from -0.66 V to

+0.18 V there was a large current of electrons into the cell (from the liposomes containing methyl viologen), maximally at $1.75x10^{-5}$ amps (or $1x10^{-14}$ $e.s^{-1}$). The rate of change of current then rapidly decayed away until it reached zero. These initial rates are one order of magnitude slower than those observed for solution based redox changes of proteoliposomes containing methyl viologen.

To further investigate any similarities or differences between the chemical and non-chemical reduction and oxidation of proteoliposomes, the background noise was removed from the amperometry trace in Panel D. This was achieved through 25 point smoothing of the data by the program ORIGINLAB PRO. This allowed investigation into the rate of change of current through calculating the derivative of the line. This was achieved through the standard derivative algorithm of ORIGINLAB PRO. Graphs of the calculated derivative functions of both the reduction and oxidation of the proteoliposomes are shown in Panels E and F. These are comparable to the absorbance changes observed in chemical reduction and oxidation experiments. The initial rates of charge transfer were calculated to be $-0.50x10^{-5}$ $q.s^{-1}$ for the reduction and $1.44x10^{-5}$ $q.s^{-1}$ for the oxidation. Converting these to electrons per second (through multiplying by $6.241x10^{18}$, which is the number of electrons per coulomb) gives a reductive rate of $3.1x10^{13}$ and an oxidative rate of $9.0x10^{13}$. These rates are slightly slower than the initial rates seen in Panel C. These changes could be due to the smoothing process. Similarly these rates are one order of magnitude (if $9.0x10^{13}$ is rounded to $1x10^{14}$) slower than those calculated for the free solution reduction and oxidation of proteoliposomes containing methyl viologen table 4.2. Electron exchange in the carbon pot set up requires the MtrCAB complex of proteoliposomes to make contact with the carbon pot surface. The rates observed could be influenced and slowed by diffusion of the proteoliposomes to the carbon pot surface and through obtaining the correct orientation for electron exchange. Proteoliposomes were observed to settle, forming loose deposits on the bottom of the carbon pot. Without mixing, the formation of these deposits would influence methyl viologen reduction. A reductive to oxidative rate ratio of 0.34 was calculated from the above rates. This is double the ratio calculated for chemical reduction methods, which was 0.16 (Table 4.2) but is still within the same order of magnitude. It indicates that the reductive rate is slower than the oxidative rate for proteoliposomes containing methyl viologen in non-chemical reductive methods, but could indicate that in chemical reduction methods the rate of reduction of proteoliposomes could be limited due to reductant concentrations.

Taking the derivative of the two parts of Panel D (which show changes in current over time) gives curves showing the number of electrons moving per second in the reduction and oxidation of proteoliposomes. These curves are then comparable to the respective curves that tracked the absorbance changes during oxidation or reduction of MtrCAB proteoliposomes containing methyl viologen (Figure 4.4, Panels C and D). Panel E (the reductive curve) has a slightly biphasic nature as it has fast initial rate and then a slower second rate of change. The oxidative curve in Panel F is monophasic. The oxidative curve in Panel F rises to zero within a few seconds, whereas the reductive curve in Panel E falls to zero after around 600 seconds. These times are similar to the absorbance changes tracked over time with chemically induced redox experiments Figures 4.4 Panel C and D.

The areas under the reductive and oxidative curves of Panel D were integrated using the integrate algorithm in ORIGINLAB PRO. The value calculated by this integration is an estimate of the number of electrons that have moved into or out of the MtrCAB proteoliposomes. The area under the reductive and oxidative curves was found to be roughly the same. The number of electrons that flowed into and out of the MtrCAB proteoliposomes in Figure 4.10 Panels C and D were $1.0x10^{-3}$ and $5x10^{-4}$ respectively. Considering the background noise of the experiment, the similarity in the numbers probably indicates that all of the electrons that flowed into the proteoliposomes through the MtrCAB complex also flowed back out again.

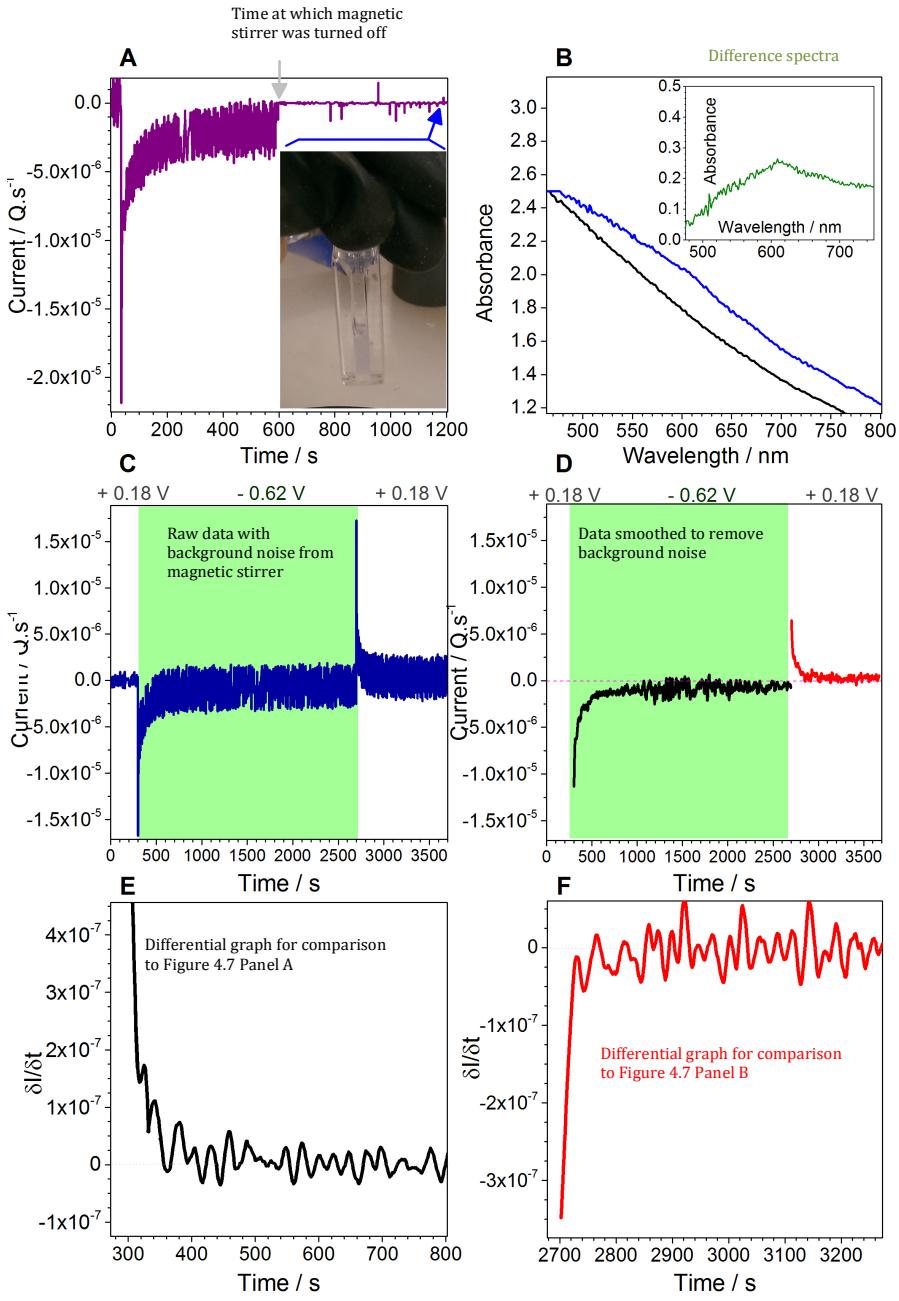

Figure 4.10 Amperometry experiments, investigating the reduction and oxidation of proteoliposomes containing methyl viologen in a glassy carbon pot cell. The the experiments were conducted in a standard buffer 20 mM HEPES, 2 mM $CaCl_2$, 100 mM NaCl.

Panel A. [Purple line] The current drawn over time through the cell containing proteoliposomes under rapid mixing [grey arrow] the time at which the magnetic flea stirrer plate was turned off [Insert picture] a photograph of the methyl viologen proteoliposome suspension in a cuvette after they had been reduced by the carbon pot cell at the time marked by the blue arrow.

Panel B. the absorbance spectra of proteoliposomes containing methyl viologen before reduction [black line] and after reduction [Blue line] by the carbon pot cell. [Insert graph] Difference spectra of blue and black lines.

Panel C. [Blue line] The current drawn through the cell containing proteoliposomes, over time, under rapid mixing, exposed to -0.6 V [green highlighted region] and +0.18 V [white regions] potentials.

Panel D [Black line] 25 point smoothing of the amperometry results in Panel C, the reductive curve [Red line] 25 point smoothing of the amperometry results in Panel C, the oxidative curve.

Panel E. [Black line] the derivative of the reductive curve in panel D.

Panel F. [red line] The derivative of the oxidative curve in Panel D.

4.10 Discussion

The encapsulation of mediators in liposome and MtrCAB proteoliposomes

Relatively little published work on MtrCAB proteoliposomes is currently available. Currently only Hartshorne *et al.,* (2009) and White *et al.,* (2013) explore the topic. Therefore much of the work here was devoted to investigating the suitability of methodologies or expanding directly upon the work carried out in these two publications.

Three types of MtrCAB proteoliposome were successfully created. In addition to methyl viologen, cytochrome c and STC solutions were shown to be stably contained within liposomes. In addition, it was proven that methyl viologen, STC and cytochrome C could be removed from the external phase of the liposomes or proteoliposome suspension to a level that it was not detectable by UV-vis measurements. From DLS measurements, the liposomes were determined to have roughly a 100 nm hydrodynamic radius, although a spread of liposome sizes was always seen. No dramatic changes were observed between liposomes and proteoliposomes made with or without MtrCAB. Comparisons between different types of liposomes showed STC-containing liposomes to have a wider range and larger average hydrodynamic radius than liposomes containing methyl viologen and or cytochrome c. The actual size of liposomes and proteoliposomes was not presumed to be of great importance, as long as the size was repeatable between different batches produced.

STC was incorporated into liposomes and MtrCAB proteoliposomes at a lower concentration than methyl viologen or cytochrome c. Low STC concentrations made observation of redox changes difficult, due to high background absorbance or scattering from the liposomes themselves. Slightly increased concentrations of STC (although never to the concentrations of methyl viologen or cytochrome c) were encapsulated within liposomes and proteoliposomes through modification of the freeze thaw section of the methodology. Faster freeze thawing by increasing the surface area to volume ratio of the liposome suspension and then using less extreme temperatures to induce thawing (for example, body temperature instead of water bath) seemed to allow higher concentrations of STC to be encapsulated.

Additional quantification of the number of MtrCAB complexes per proteoliposome and the amount of redox indicator contained within each proteoliposome would have enhanced the conclusions drawn from liposome and proteoliposome experiments. This would have

allowed more accurate calculations of the rate of electron transfer through individual MtrCAB complexes.

Oxidation and reduction of liposomes and proteoliposomes

Liposomes were proven to insulate the redox indicators that they contained from chemicals added to the solution within which they were suspended. This result was achieved through analyzing the wavelength spectra of liposomes in different redox conditions. The encapsulated redox indicators remained in the oxidised redox state that they were initially produced in, even though there was a detectable presence of reductant exterior to the liposomes. Due to the process of making liposomes being aerobic, it was not possible to create liposomes containing reduced redox indicators. Thus, only the liposomes' capacity to insulate redox indicators from sodium dithionite reductant was measured. However as the oxidants used were also impermeant through membranes, it can be extrapolated that they would have been insulated from the redox indicators inside the liposomes in a similar way.

The inclusion of MtrCAB complexes in liposomes to make proteoliposomes allowed encapsulated methyl viologen, STC or cytochrome c to be reduced from their initially oxidised condition. No methyl viologen, cytochrome c and STC were proven to be in the solution external to the proteoliposomes at detectable levels after the washing process. This proved that the absorbance changes observed came exclusively from the encapsulated redox indicators. This enabled the conclusion that the reduction of the proteoliposomes occurred due to the functioning of MtrCAB transporting electrons through the phosphotidylcholine membrane and allowing the reaction with redox species internal to the proteoliposome. This conclusion is founded on the assumption that there were not any redox indicator species adhered to the outside of the proteoliposome, which, if there were, would not have been removed by washing and would still be accessible for reduction. As no redox indicators were detected adhering to liposomes it is highly unlikely that indicators were adhering to the lipid bilayer of proteoliposomes. Due to the large amount of reduction going on in each experiment it is near impossible that redox species adhered solely to the MtrCAB complex would be able to give such a large signal.

Examining MtrCAB proteoliposomes containing methyl viologen

The absorbance changes of proteoliposomes containing methyl viologen arising through chemical reduction or oxidation were very similar to the results published in White *et al.,* (2013). The method of reading the absorbance changes was slightly different to the protocol used by White *et al.,* In that study, reductant or oxidant was added to the proteoliposomes and then a UV-vis measurements was started. The results here were obtained by using a method whereby the UV-vis measurements were started and then a pre-determined aliquot of oxidant or reductant was released to the proteoliposomes, allowing the initial redox changes to be captured. The use of a tungsten and deuterium lamp spectrophotometer, rather than a diode-array spectrophotometer, improved the accuracy of the absorbance measurements recorded.

The rate of electron transfer for proteoliposomes containing methyl viologen was very similar to the White *et al.,* study, with a similar two-stage reduction profile recorded. Although it is not possible to make absolute comparisons between the sets of proteoliposomes containing methyl viologen published by White *et al.,* and those described here, the rates of reduction recorded are similar. Both are in the same 10^{-3} AU.s^{-1} order of magnitude and both experiments show a faster oxidative rate than reductive rate of proteoliposomes.

Non-chemical reduction and oxidation of MtrCAB proteoliposomes containing methly viologen

Liposomes and MtrCAB proteoliposomes containing methyl viologen that had no external methyl viologen detectable in an electrochemical cell were successfully made. The electrochemical cell set up was much more sensitive to redox species than measuring absorbance changes in a UV-vis spectrophotometer. Free methyl viologen was detectable in the electrochemical cell set up, which clouded the functioning of MtrCAB, and as such complicatied the analysis of the experiments. Thus, the additional washing and cleaning steps instigated in the methyl viologen liposome protocol were essential.

Methyl viologen was found to give a distinctive Faradaic response during cyclic voltammetry experiments. This changed once the methyl viologen was encapsulated inside proteoliposomes. In the carbon-pot, free methyl viologen had Faradaic current peaks at -0.46 V and -0.42 V. This was broadly similar, but with key differences, to encapsulated methyl viologen, which had Faradaic peaks at -0.48 V and -0.42 V a more

negative potential was required to reduce encapsulated methyl viologen. This appeared to be independent of the cyclic voltammetry scan rate used. This difference in Faradaic peaks between free methyl viologen and methyl viologen encapsulated within MtrCAB proteoliposome could be due to the need for the MtrCAB complex to become reduced before passing electrons onto methyl viologen species. As MtrCAB has evolved to pass electrons from the periplasm out towards the cell exterior, the reduction of encapsulated methyl viologen, through the addition of a reductant external to the protoelipome, causes MtrCAB to work in the non-canonical direction. This could explain the increased potential required to reduce methyl viologen in proteoliposomes. The difference in responses between free methyl viologen and encapsulated methyl viologen allowed for the detection of burst liposomes in aged samples. This methodology could therefore be used in preparation protocols to ensure the highest quality of proteoliposome for experimentation.

Amperometry of MtrCAB proteoliposomes containing methyl viologen

Though performing amperometry at potentials able to reduce methyl viologen, proteoliposomes were stably reduced. These reduced proteoliposomes were shown to remain reduced when removed from the electrochemical cell, an observation that is extremely useful for future experiments where reduced proteoliposomes in chemical free solutions are required. The encapsulated methyl viologen would then be the only reductant acting in these future experiments. Such experiments could include examining the interactions of non-chemically reduced MtrCAB proteoliposomes with iron oxides or other forms of MtrCAB proteoliposome.

When comparing the line shapes of the derivative curves of amperometry experiments, it can be seen that both the reductive and oxidative derivative curves have similar features to the curves produced from tracking the 603 nm absorbance changes induced by chemical reduction and oxidation. Upon reduction in the carbon pot, a large initial current of electrons flows into the proteoliposomes, followed by a second phase where the current decreases steadily. In the oxidative curves there is only a large exodus of electrons. As 603nm absorbance is directly proportional to charge on methyl viologen species, the proteoliposomes in the carbon pot are behaving similarly to proteoliposomes in free solution when accepting or passing-out charge. The carbon pot experiment does not rely on chemical oxidants or reductants. Therefore, the rate of reduction of proteoliposomes through the carbon pot is not dependent on any changes in the concentration of oxidant or reductant. The same carbon pot was used every time, so the same surface area of electrode

was present in each experiment. Unlike the chemical reduction of proteoliposomes, the carbon pot experiments may be rate limited through proteoliposome access to the electron exchange interface (the surface of glassy carbon pot acting as a working electrode). The ratio of the reductive and oxidative rates of proteoliposomes in the carbon pot set up were calculated to be an order of magnitude slower than in solution based redox experiments. However, these rates were the product of bulk electron transport within the sample and are difficult to directly compare. The ratio of the reductive and oxidative rates was determined to be similar for carbon pot experiments compared to soluble proteoliposome experiments. This indicates that electrons flow faster out of MtrCAB than into MtrCAB, assuming its canonical orientation within the periplasmic membrane.

Future work using this technique would ideally include repeating these non-chemical oxidation and reduction experiments using proteoliposomes containing STC. These are the best models to use when making an artificial periplasm. It would be interesting to make a comparison with regards to the MtrCAB function between proteoliposomes containing methyl viologen and those containing STC. Similarly, confirmation that reduced proteoliposomes containing cytochrome c cannot be re-oxidised, even by a carbon-pot, would be very informative.

Reduction and oxidation of MtrCAB proteoliposomes containing cytochrome c or STC

Figure 4.11 brings together all the conclusions about how MtrCAB interacts with different redox species. These overall conclusions were based on all of the different proteoliposome experiments.

Comparing MtrCAB proteoliposomes containing methyl viologen to proteoliposomes containing STC, the ratio of initial reductive rate to initial oxidative rate is an order of magnitude larger for STC than methyl viologen containing proteoliposomes Table 4.3. This indicates that proteoliposomes containing STC reduce more easily than they oxidise, as compared to proteoliposomes containing methyl viologen. This is expected because methyl viologen has a more negative mid point potential than STC. The potential difference between methyl viologen and sodium dithionite is smaller than the potential difference between sodium dithionite and STC. Conversely, when proteoliposomes are oxidised, a greater potential difference is observed between reduced methyl viologen and ferric citrate than reduced STC and ferric citrate. This smaller potential difference during

the reduction and increased potential difference during oxidation could explain the ratios of initial reduction to initial oxidation observed for proteoliposomes containing methyl viologen compared to proteoliposomes containing STC. Proteoliposomes containing methyl viologen are more balanced towards oxidation and proteoliposomes containing STC are comparatively more balanced towards reduction. Theoretically, proteoliposomes containing cytochrome c have the largest ratio of initial reductive rate to initial oxidative rate, as they do not re-oxidise. Cytochrome c has the most positive mid point potential. Thus, it creates the largest potential difference with sodium dithionite when compared with methyl viologen and STC. Even when a very strong oxidant is used to try and re-oxidise reduced proteoliposomes containing cytochrome c, no oxidation occurs. This could be because the cytochrome c is so electropositive that it cannot reduce the MtrCAB complex. Without this ability, to reduce MtrCAB, electrons stored in reduced cytochrome c cannot be tunneled through the MtrCAB complex, however strong the oxidant exterior to the proteoliposomes.

The inability of cytochrome c to reduce MtrCAB in this way has implications as to how MtrCAB functions in *S. oneidensis*. Methyl viologen and cytochrome c have quite low and quite high respective mid point potentials when compared to MtrCAB. These two redox species could be so electronegative and electropositive respectively that MtrCAB may not function canonically when it reacts with them. STC has a mid point potential that sits close to the mid point potential of MtrCAB and it is a putative interacting partner. STC has a fast reductive and oxidative rate of MtrCAB and it functions as a better electron donor to MtrCAB than cytochrome c or methyl viologen. Proteoliposomes containing STC provide the best model of how MtrCAB functions within *S. oneidensis*, and thus why the proteoliposomes containing STC could be termed an “artificial-periplasm”. Figure 4.11 visualizes the interactions of MtrCAB described in these experiments.

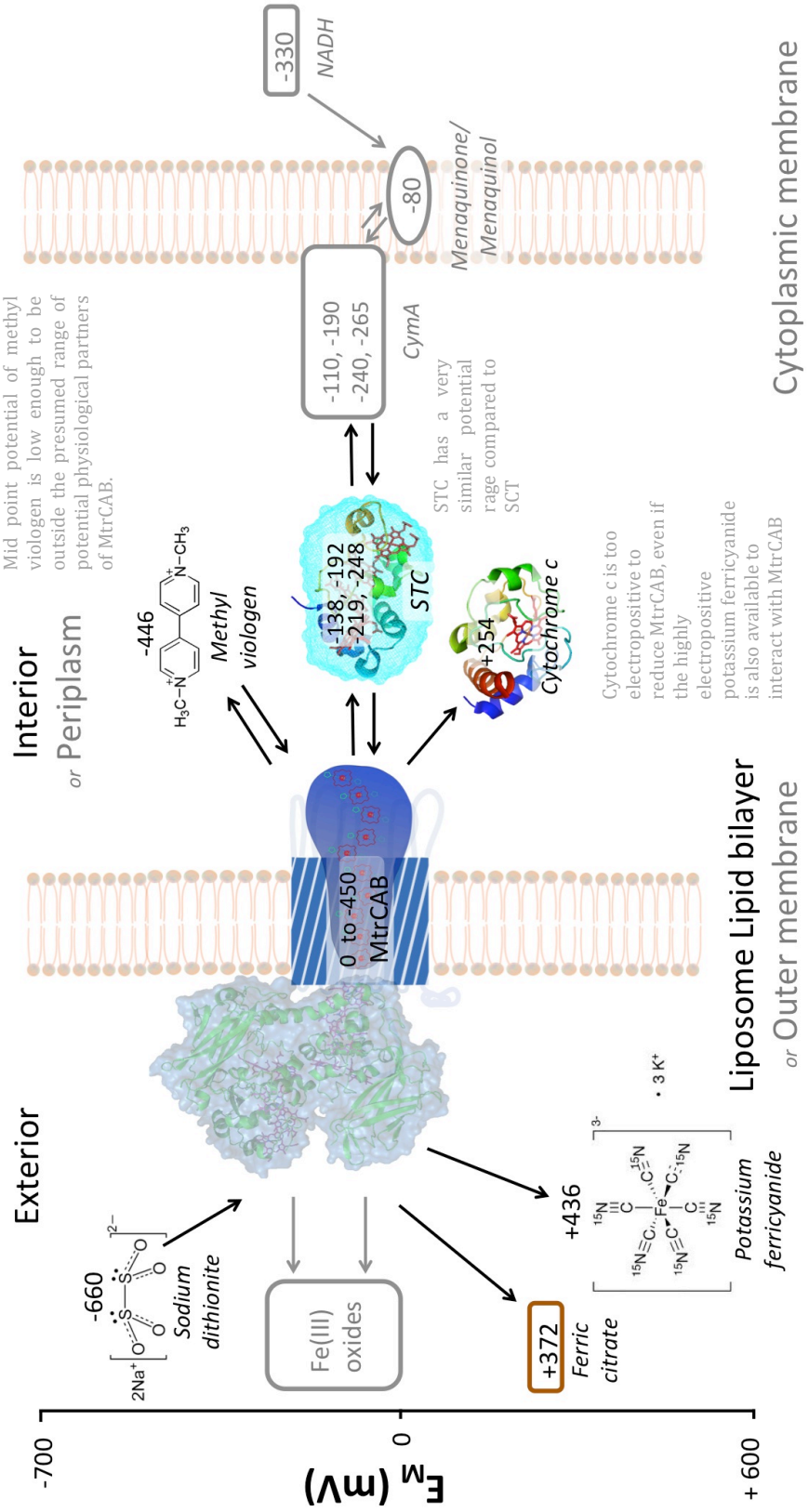

Figure 4.11 A Cartoon diagram representing the redox species that interact with MtrCAB during the proteoliposome experiments of Chapter 4 and those redox species naturally encountered by MtrCAB when in the outer membrane of *S. oneidensis*. The redox mi-point potentials of each redox species has been positioned along a electro-potential scale (mV). Arrows represent directional movement of electrons between species.

4.11 Bibliography

Beer, 1852. Determination of the absorption of red light in colored liquids. *Annalen der Physik und Chemie*, 86, pp.78–88.

Bushnell, G.W., Louie, G. V & Brayer, G.D., 1990. High-resolution three-dimensional structure of horse heart cytochrome c. *Journal of Molecular Biology*, 214(2), pp.585–95.

Clarke, T.A. *et al.,* 2011. Structure of a bacterial cell surface decaheme electron conduit. *Proceedings of the National Academy of Sciences*, 108(23), pp.9384–9389.

Coursolle, D. & Gralnick, J. a, 2010. Modularity of the Mtr respiratory pathway of Shewanella oneidensis strain MR-1. *Molecular Microbiology*, 77(July), pp.995–1008.

Davidson, V.L., 1996. Unraveling the kinetic complexity of interprotein electron transfer reactions. *Biochemistry*, 35(45), pp.14035–9.

Davidson, V.L., 2000. What controls the rates of interprotein electron-transfer reactions. *Accounts of Chemical Research*, 33(2), pp.87–93.

Firer-Sherwood, M. *et al.,* 2011. Tools for resolving complexity in the electron transfer networks of multiheme cytochromes c. *Metallomics : Integrated Biometal Science*, 3(4), pp.344–8.

Fonseca, B.M. *et al.,* 2012. The role of intramolecular interactions in the functional control of multiheme cytochromes c. *FEBS letters*, 586(5), pp.504–9.

Fonseca, B.M. *et al.,* 2009. The tetraheme cytochrome from Shewanella oneidensis MR-1 shows thermodynamic bias for functional specificity of the hemes. *Journal of Biological Inorganic Chemistry,* 14(3), pp.375–85.

Harada, E. *et al.,* 2002. A directional electron transfer regulator based on heme-chain architecture in the small tetraheme cytochrome c from Shewanella oneidensis. *FEBS letters*, 532(3), pp.333–337.

Hartshorne, R.S. *et al.,* 2009. Characterization of an electron conduit between bacteria and the extracellular environment. *Proceedings of the National Academy of Sciences*, 106(52), pp.22169–22174.

Hartshorne, R.S. *et al.,* 2007. Characterization of Shewanella oneidensis MtrC: a cell-surface decaheme cytochrome involved in respiratory electron transport to extracellular electron acceptors. *Journal of Biological Inorganic Chemistry*, 12(7), pp.1083–94.

Jin, Q. & Bethke, C.M., 2002. Kinetics of electron transfer through the respiratory chain. *Biophysical Journal*, 83(4), pp.1797–808.

Kolthoff, I.M. & Tomsicek, W.J., 1934. The Oxidation Potential of the System Potassium Ferrocyanide–Potassium Ferricyanide at Various Ionic Strengths. *The Journal of Physical Chemistry*, 39(7), pp.945–954.

Leys, D. *et al.,* 2002. Crystal structures at atomic resolution reveal the novel concept of "electron-harvesting" as a role for the small tetraheme cytochrome c. *The Journal of Biological Chemistry*, 277(38), pp.35703–11.

Mathews, F.S., 1985. The structure, function and evolution of cytochromes. *Progress in Biophysics and Molecular Biology*, 45(1), pp.1–56.

Mayhew, S.G., 1978. The Redox Potential of Dithionite and SO-2 from Equilibrium Reactions with Flavodoxins, Methyl Viologen and Hydrogen plus Hydrogenase. *European Journal of Biochemistry*, 85(2), pp.535–547.

Meyer, T.E. *et al.,* 2004. Identification of 42 possible cytochrome C genes in the Shewanella oneidensis genome and characterization of six soluble cytochromes. *Omics : A Journal of Integrative Biology*, 8(1), pp.57–77.

Myers, J.M. & Myers, C.R., 2003. Overlapping role of the outer membrane cytochromes of Shewanella oneidensis MR-1 in the reduction of manganese(IV) oxide. *Letters in Applied Microbiology*, 37(1), pp.21–5.

Pande, A. & Myer, Y.P., 1978. The redox potential of horse heart cytochrome c. *Biochemical And Biophysical Research Communications*, 85(1), pp.7–13.

Pitts, K.E. *et al.,* 2003. Characterization of the Shewanella oneidensis MR-1 decaheme cytochrome MtrA: expression in Escherichia coli confers the ability to reduce soluble Fe(III) chelates. *The Journal of Biological Chemistry*, 278(30), pp.27758–65.

Rao, S.P., Singh, S.R. & Banakavi, S.R., 1978. Formal redox potentials of ferricyanide-ferrocyanide couple in certain nonaqueous water mixtures. *Proceedings of the National Acadamy of Science: India A*, 44(6), pp.333–335.

Ross, D.E. *et al.,* 2007. Characterization of protein-protein interactions involved in iron reduction by Shewanella oneidensis MR-1. *Applied and environmental microbiology*, 73(18), pp.5797–808.

Ross, D.E., Brantley, S.L. & Tien, M., 2009. Kinetic characterization of OmcA and MtrC, terminal reductases involved in respiratory electron transfer for dissimilatory iron reduction in Shewanella oneidensis MR-1. *Applied And Environmental Microbiology*, 75(16), pp.5218–26.

Shi, L. *et al.,* 2012. Molecular Underpinnings of Fe(III) Oxide Reduction by Shewanella Oneidensis MR-1. *Frontiers In Microbiology*, 3(February), p.50.

Wang, Z. *et al.,* 2008. Kinetics of reduction of Fe(III) complexes by outer membrane cytochromes MtrC and OmcA of Shewanella oneidensis MR-1. *Applied and Environmental Microbiology*, 74(21), pp.6746–55.

White, G.F. *et al.,* 2013. Rapid electron exchange between surface-exposed bacterial cytochromes and Fe(III) minerals. *Proceedings of the National Academy of Sciences*, 110(16), pp.6346–51.

5 | Small angle neutron scattering analysis of MtrC and MtrCAB, and structural predictions of MtrB.

5.01 Low resolution structures of MtrC, MtrB and MtrA

In order to investigate how MtrCAB functioned, it would be very useful to obtain structures of the individual components of MtrCAB and the structure of the hetro-trimeric complex that form together. At present, only crystal structures of MtrF and the highly conserved UndA and OmcA are available to analyze (Clarke et al. 2011; Edwards et al. 2012; Edwards et al. 2014). In addition, the structure of MtrC has been solved and is due to be published in 2015. MtrF and UndA are thought to perform the same function as MtrC, sometimes interchangeably, perhaps to allow specialization of DMR to different heavy metals. OmcA is a decaheme protein found in the outer membrane of *Shewanella oneidensis*. It is thought to associate with the MtrCAB complex, increasing the connections to extracellular minerals (Hartshorne et al. 2007; Edwards et al. 2014).

The crystal structure of MtrF is composed of four domains. Domains I and III contain seven antiparallel β-strands folded in and contain a greek key motif, whereas domains II and IV contain α helices and bind five heme cofactors each. Domains II and IV are arranged centrally within MtrF (and UndA and OmcA), allowing loose packing of the c type hemes, which together form a staggered decaheme cross. Domains I and III sit either side of this central pair of heme containing domains. These regions could possibly be involved with reduction of solutes by heme 7 in the stagger of the decaheme cross (Edwards et al. 2012). UndA is an 11 heme (undecaheme) paralogue of MtrC. When comparing crystals soaked with Fe Nitrilotriacetic acid (NTA) and Fe citrate to unsoaked crystals, significant changes in difference density Fourier maps were observed. These changes were observed in the split b β-stranded domains I and III. The changes were modeled well with the placement of these solutes in this location, possibly indicating that these were the sites of electron transfer from UndA to metal ions. In additionally the crystal structure of OmcA has been determined (Edwards et al. 2014). This followed the same four domain pattern as MtrF and UndA and had a similar 3D structure.

The X-ray crystal structures of MtrB and MtrA have not been solved, with only SAXS molecular envelope simulations developed for MtrA (Firer-Sherwood et al. 2011). The molecular envelope of MtrA was predicted to have dimensions of 100 x 30 x 20 $Å^3$, and resembles a flat-paddle or spoon-head shape. In the absence of a suitable MtrB structure *in silico* sequence-based, modeling was used to predict the structure of MtrB.

5.02 Creating a homology model for MtrB

Obtaining structural information of a transmembrane protein such as MtrB is challenging due the presence of lipid molecules binding to surface hydrophobic regions. Protein crystals and therefore X-ray structures are difficult to produce. In principal, SANS experiments could be used to study MtrB in isolation, through phasing out scattering contributions from MtrB associated lipids. However, MtrB is very difficult to express, and, as of yet, has not been purified in isolation from MtrA (Schicklberger et al. 2011). Therefore, a sequence based *in silico* bioinformatics route was chosen to investigate the structure of MtrB in this thesis.

MtrB *in silico* predictions

A BLAST search of all non redundant protein sequences employing the full protein sequence of MtrB from *S. oneidensis,* as the query, reveals that MtrB is predicted to be a member of the outer membrane porin superfamily, abundant in the *Shewanella* and γ-proteobacteria family Figure 5.1 (Altschul et al. 1990).

Figure 5. 1 Results from a BLAST search using the protein sequence of MtrB. The results are displayed in a similarity distance tree. The MtrB sequence is highlighted in yellow. The genetic distance calculated by BLAST is shown by the scale, Kimura (1983).

The β-barrel pore outer membrane superfamily of proteins has been well studied and many applications have been developed for investigating them based on their sequence. Three such programs were used to investigate MtrB *in silico*. These were BOCTOPUS (renamed from OCTOPUS in 2012), Pred_TMBB and TMB_PRO.

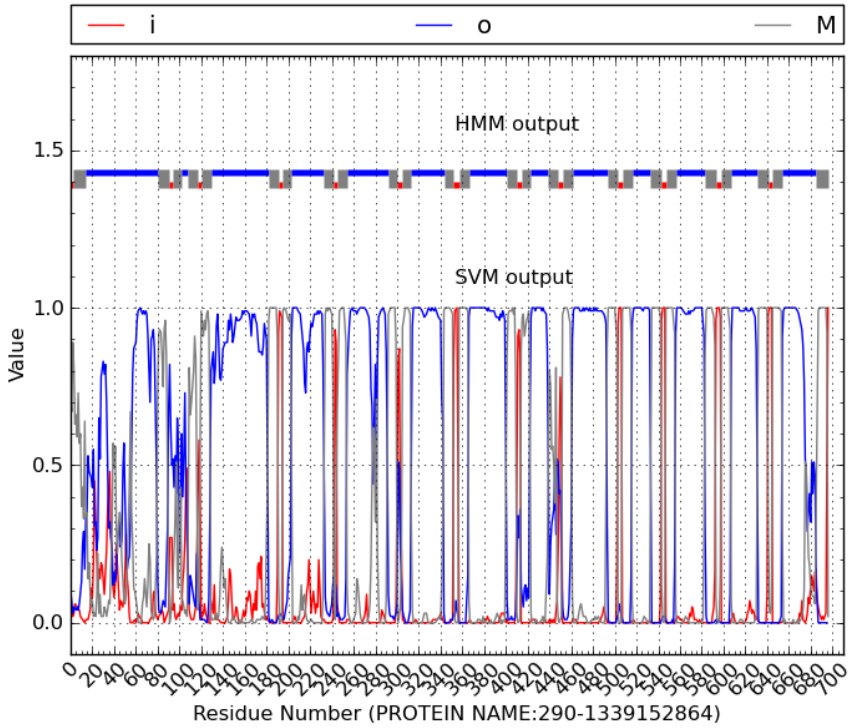

Figure 5. 2 The graphical output from running the BOCTOPUS program, analysing the MtrB sequence. The sequence position is displayed on the x axis, and the Sequence Sector Machine (SVM) probability and Hidden Markov Model (HHM) predictions of protein location within the membrane are displayed on the y axis. [blue lines] protein sequence is on the extracellur face [red lines] protein sequence is on the periplasmic face [grey lines] protein sequence is inside the membrane bi-layer. Hayat, S. & Elofsson, A., 2012

BOCTOPUS (Viklund & Elofsson 2008; Hayat & Elofsson 2012) used hidden Markov models and artificial neural networks to predict the correct topology for the amino acid sequence of beta barrel pores. In particular BOCTOPUS fully integrates the modeling of re-entrant/membrane-dipping regions and trans-membrane hairpins, important for the long loop regions found in MtrB. Using BOCTOPUS, MtrB was predicted to have a beta barrel structure with 28 strands crossing the membrane with 13 extended loops facing the extracellular space and 14 short loops and an N terminal tail facing the periplasm Figure 5.2.

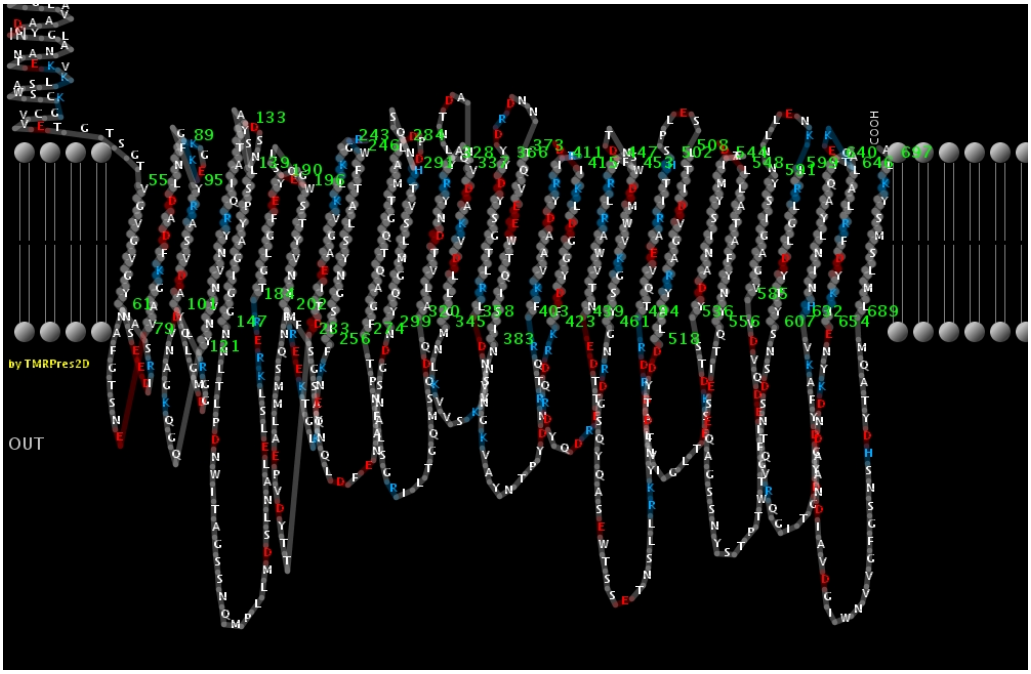

Figure 5. 3 The transmembrane regions predicted by Pred_TMBB using the Hidden Markov *Viterbi* method, from translated genomic sequence, showing the polypeptide sequence and positions of each of the predicted beta barrel strands and associated loops. Bagos, *et al.*, 2004.

In the 2013 paper by White et al., the authors predicted the topology of MtrB using the program Pred_TMBB. This result was confirmed by re-running the program Pred_TMBB using MtrB as the query. Figure 5.3 shows the output from the TMRPres2D part of the Pred_TMB program (Bagos et al. 2004). Similarly to BOCTOPUS, Pred_TMBB is another program based on hidden Markov modeling, however it was constrained according to the Conditional Maximum Likelihood criterion to predict β strands for β barrel regions (Bagos et al. 2004). PRED_TMBB predicted MtrB to have 28 transmembrane regions and large extra-celluar loops.

In addition to this *in silico* modeling, White et al. also performed proteinase K digestion of MtrCAB inserted into proteoliposomes. Through immune-blotting, MtrC and some sections of MtrB were detected to have been digested. MtrA and specific sections of MtrB where observed to be protected by the phospholipid bilayer of the liposome. The N terminal tail and the short loop regions of MtrB were found to be digested by proteinase K and were located on the outside of the proteoliposome, and therefore would be located facing the extra cellular space of *S. oneidensis*. These digested sections map onto the sections that are predicted by BOCTOPUS and TMBB to be on the periplasmic facing side of MtrB. The periplasmic facing components of MtrB should be protected from digestion, thus

BOCTOPUS and TMBB, when modeling it, inverted the orientation of MtrB in the membrane. This highlights that there are significant differences between the sequence-based models and the real structure of MtrB. Therefore, any model that is made using these programs needs to be treated with appropriate caution, and, at very least, the orientation within the membrane must be reversed.

The program TMB_PRO was used to develop a *de novo* structure based on sequence using fragmented stages of simulated annealing, (Randall et al. 2008). Pictures of the output of TMB_PRO_3D (part of TMB_PRO) are shown in Figure 5.4. TMB_PRO_3D modeled MtrB in 3D as a 24 β-strand pore, which is different to PRED_TMBB and BOCTOPUS prediction programs, which modeled MtrB in 2D as containing 28 strands, Figure 5.4 Panel A. The lower number of loop regions predicted by TMB_PRO presumably occurred as the program modeled MtrB with a 'plug' inside the pore. The 'plug' that is demonstrated by Figure 5.4 Panel B may have a sequence that in isolation may have a high likelihood to form but in reality never has the chance to due to sections being incorporated in the membrane. Through removing the sequences, which TMB_PRO_3D had assigned as the "plug", as well as some of the longer loop regions of MtrB, TMB_PRO_3D was then used to create a model of MtrB that had an open pore, Figure 5.4 Panels C and D. This could then be used as a rough approximation for the shape of MtrB. The real structure is likely to have a larger pore as any extra β-strands would increase the pore circumference. The structure is also likely to be affected by the long loop regions that may aid interaction with MtrA in the periplasm.

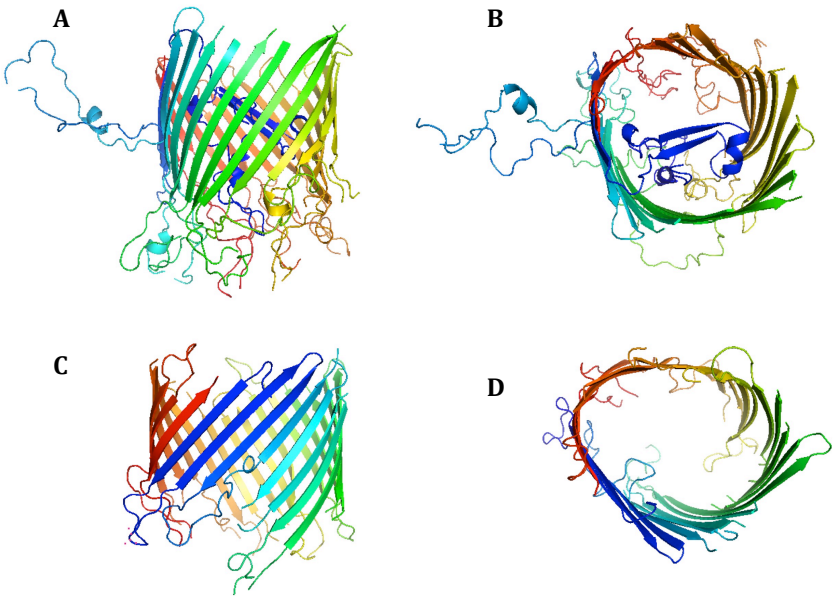

Figure 5. 4 In-silico prediciton of the MtrB structure using the TMB_Pro_3D program. Panel A and B Prediction of the structure of MtrB based on the full length protein sequence, Panel B further demonstrates the presence of a section of protein predicted to be acting as a 'plug' for the barrel of MtrB. Panels C and D Prediction of the structure of MtrB based on a truncation of the MtrB protein sequence, removing the 'plug' section and the extra cellular space extended loop regions. Panel D shows that no additional 'plug' is re-calculated within the barrel.

5.03 SANS analysis of MtrC

To complement the published crystal structure of the MtrC homologue MtrF (from *S. oneidensis*), SANS experiments were conducted on MtrC purified from *S. baltica* by Dr. M. Edwards (UEA). This was done with the aim of generating a molecular envelope of MtrC in free solution that could be aligned to and compared with suitable crystal structures (Edwards et al. 2012, Edwards et al 2015 in press). A sample of 5 $mg.mL^{-1}$ MtrC in 20 mM HEPES pH 7.5 was used for the SANS experiment. Due to limited beam time, only this one sample was run. Experimental details are provided in Section 2.22.

Figure 5.5 Panels A – C show the radially averaged scattering profile generated from this experiment in linear, semi-log and double-log formats. The low q, Guinier region of the data is linear, and therefore indicates that there is no aggregation or contamination in the sample. Panel D shows the Kratky plot of the data. The data shows one peak, indicating a globular domain. The $I(q).q^2$ rises towards higher q, possibly indicating a flexible region. The program GNOM (Svergun 1992) was used to calculate a pair distribution function for the dataset. The fit of the scattering data created by the program is very good, as shown in Panel E. At high q (0.4 $Å^{-1}$ and above) there are significant error bars due to the low density of the scattering points collected. At high q, lower scattering trending to zero is expected. Thus, the line of best fit tends to zero rather than leveling off at 0.01, as the scattering points might otherwise suggest, which is due to the inaccuracy of the data collected in this region. This process is completed automatically by the GNOM fitting algorithm. The p(r) function is displayed in Panel F. It shows one main peak at 36 Å and an inflection at 10 Å. The Rg calculated for this fit was 28.27 with a D_{max} of 80.62 Å.

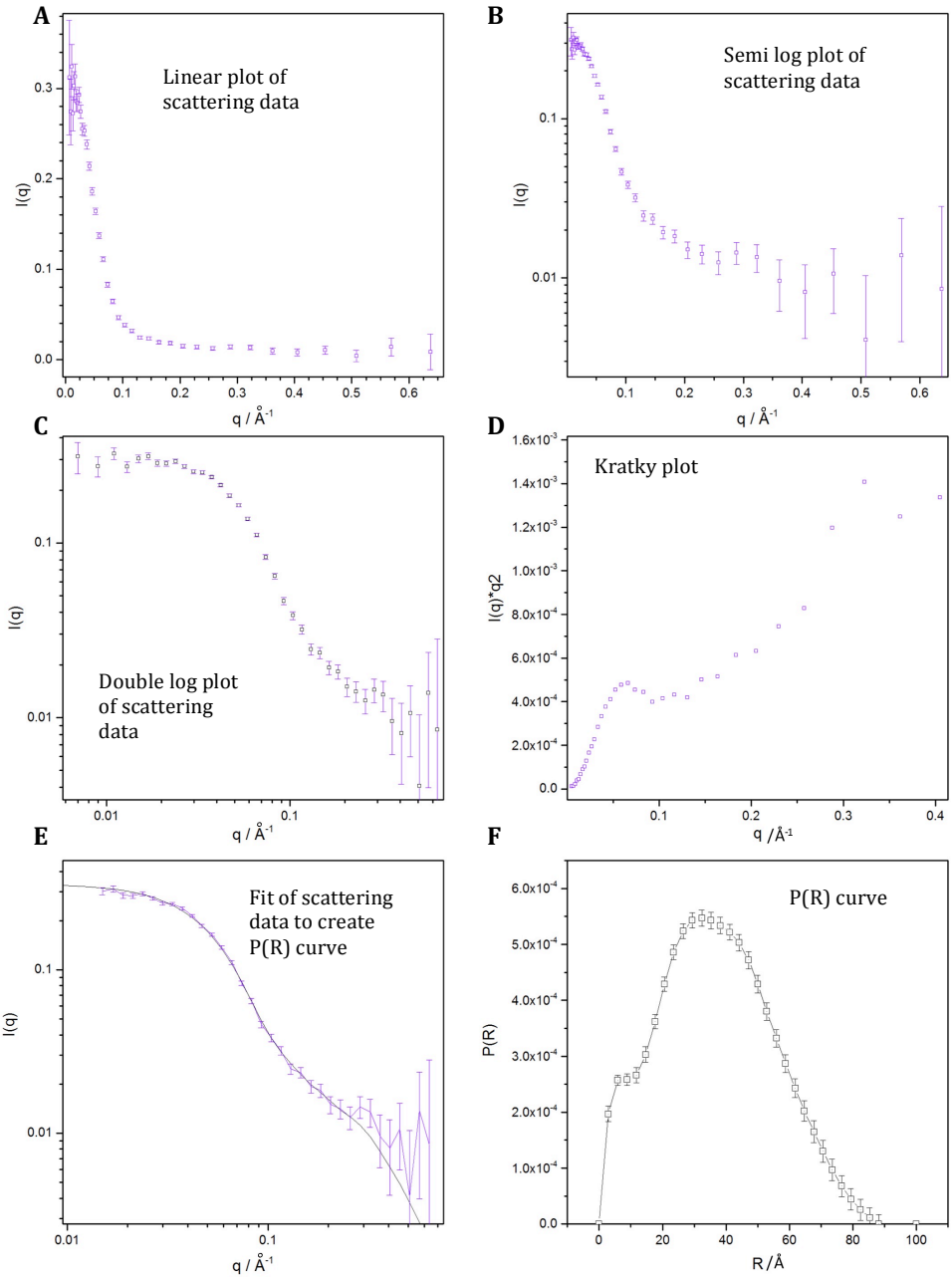

Figure 5.5 Results of neutron scattering experiments performed on 5 mg.mL^{-1} MtrC in 20 mM HEPES pH 7.5.
Panel A. The radially averaged neutron scattering profile of MtrC presented in linear scale format.
Panel B. The neutron scattering profile of MtrC presented in semi-log scale format.
Panel C. The neutron scattering profile of MtrC presented in double-log scale format.
Panel D. The Kratky plot of the MtrC scattering profile.
Panel E. [purple line] the radially averaged scattering profile of MtrC, [black line] The function calculated by GNOM to best fit the scattering profile.
Panel F. [Black line] The pair distribution function calculated for MtrC scattering data.

The p(r) curve generated from the scattering profile was then used with the program DAMMIF (in slow mode) to create bead model simulations (Franke & Svergun 2009). Ten models were created which are shown in Figure 5.6. These models did not seem to contain a globular region as predicted by the Kratky plot, which could be due to the size of the beads and solvent radius, factors that are influenced by user controlled parameters. Increasing these parameters beyond the limits normally used when modelling would lead to the models becoming fully globular. The models in Figure 5.6 seem to describe a folded tubular shape. If the solvent radius size and van de Waals radii of the beads were increased, the beads could 'fill in' the inner sections of the model, in between the folds which are curently empty. If these sections are real they will be similarly present in any average models constructed.

Using the ten DAMMIF bead models, the programs DAMAVER and DAMFILT (Volkov & Svergun 2003) were employed to create an average molecular envelope and a filtered molecular envelope comprising the components consistently present in all models. These models were then aligned using the program SUPCOMB (Kozin & Svergun 2001) and the results are presented in Figure 5.7 Panel A. The average molecular envelope is shown as an orange wire mesh. The filtered molecular envelope is shown as the green surface. The average molecular envelope is around 80 Å long and forms a globular shape. The filtered molecular envelope is similar to the individual DAMMIF bead models in that it is a folded tubular shape. This model appears to mimic the order in which the domains of MtrC are connected, but no structural detail is provided.

The average molecular envelope was aligned with the crystal structure for MtrC, (publication in review) using the program SUPCOMB and is shown in Panel B, (SUPCOMB rotates pdb file coordinates to maximize two structures overlap). The crystal structure aligns well with the SANS molecular envelope. The structure mirrors the contours of the SANS molecular envelope and only exceeds the space of the envelope in one extended loop region, with no secondary structure. The tip of the first heme of MtrC and the helix (that is nearby) cross the aligned molecular envelope. These parts of the structure still align with the general contours of the SANS molecular envelope, and only protrude in a very shallow manner. If the solvent radius of the SANS molecular envelope were increased, these protrusions would no longer occur, however in doing so, some detail would be lost. MtrC has a line of symmetry running along its minor oblate axis. Therefore, the comparison would be slightly changed if the structures were be switched along this axis.

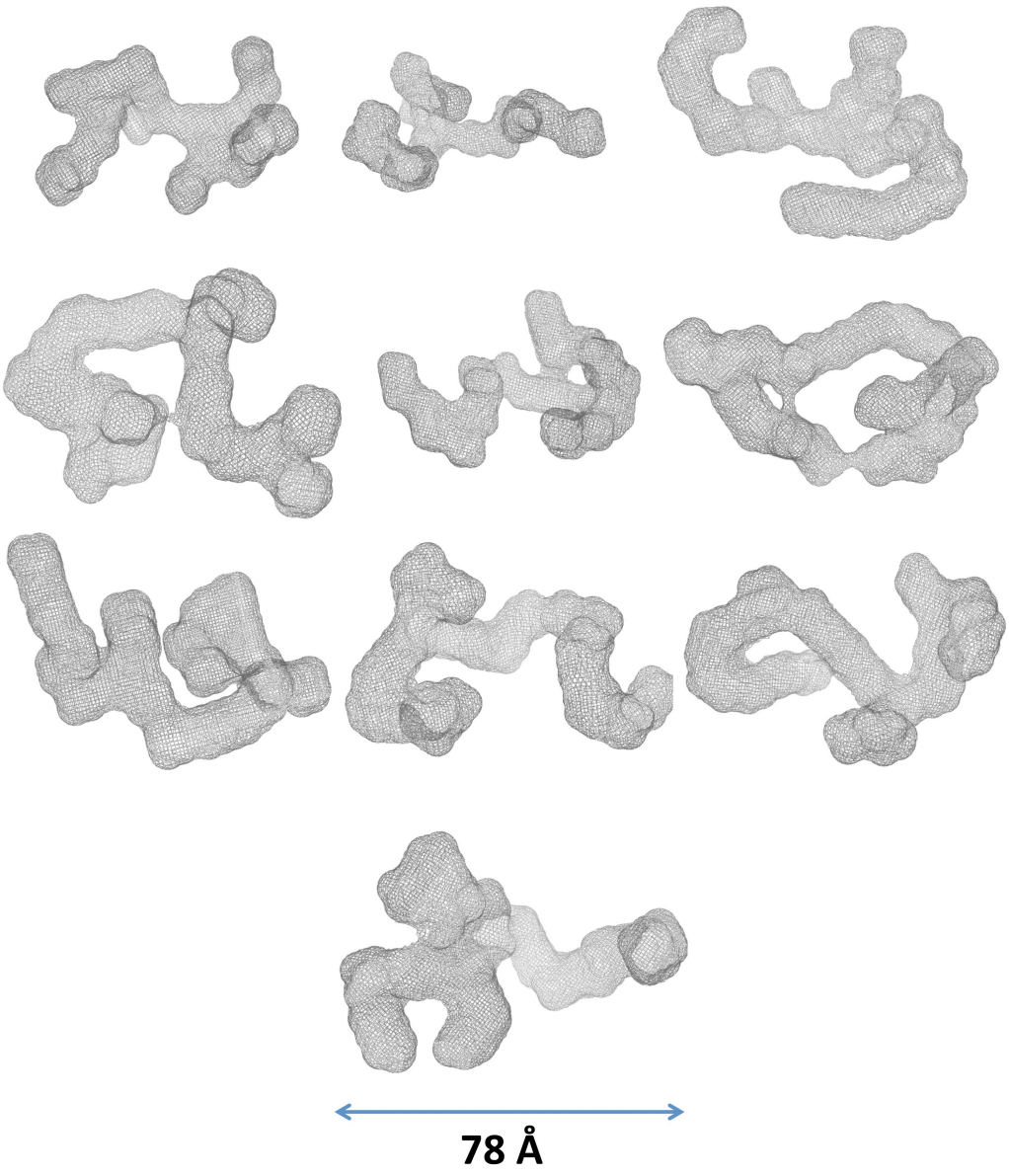

Figure 5. 6 Bead models produced by DAMMIF that replicate the pair distribution function calculated for MtrC. The bead models were calculated using the slow mode of DAMMIF. All molecular envelopes are presented using PYMOL.

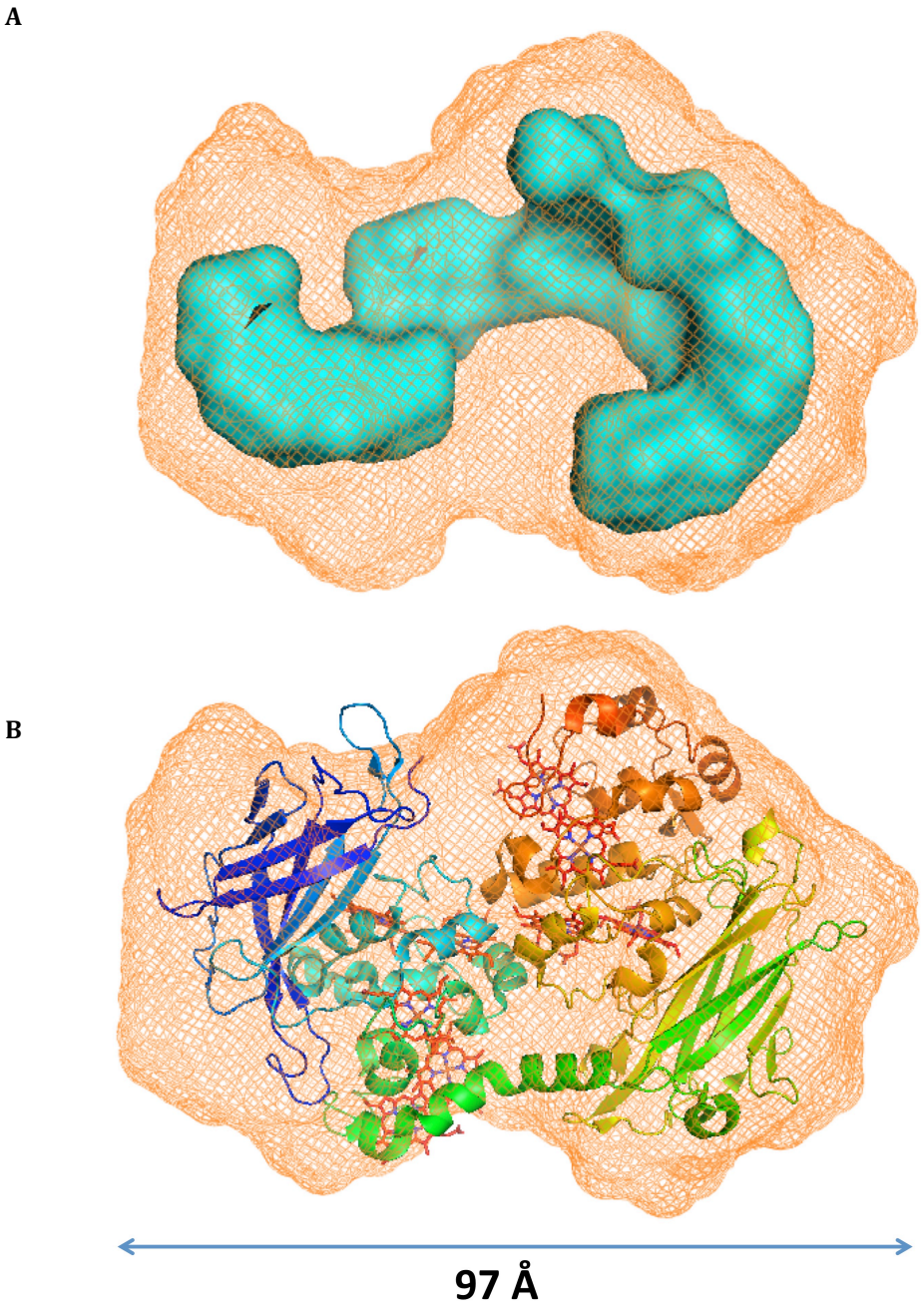

Figure 5. 7 The average molecular envelopes calculated from the ten DAMMIF simulations of the shape of MtrC.
Panel A. [orange wire mesh] The averge molecular envelope, of all the ten DAMMIF simulations, calculated using the program DAMAVER. [Blue surface] The filtered molecular envelope based on sections that were present in all DAMMIF simulations, calculated by DAMFILT.
Panel B. An alignment of of the crystal structure of MtrC [cartoon structure] and the DAMAVER average molecular envelope calculated for MtrC.

5.04 The shape of MtrCAB

There has not been any work published on how the subunits MtrA, MtrB and MtrC associate to form MtrCAB. Coursolle & Gralnick (2010) showed that MtrA was periplasmic, MtrB was located in the membrane and MtrC was extracellular. Developing a suitable methodology with which to study the shape of MtrCAB as a complex is therefore an unresolved problem.

Small angle neutron scattering (SANS) is a technique that uses the scattering patterns created by proteins or molecules in free solution to infer shape data. Unlike SAXS, which uses x-ray scattering, SANS uses neutron scattering. This provides an opportunity for scattering caused by protein, lipid, detergents and nucleic acids to be separated. Neutron scattering is caused by interactions with atomic nuclei, whereas X-ray scattering is caused by interactions with electrons. Both proteins and detergents have similar electron densities, but different nuclei densities. Berthaud et al. (2012) used SAXS, in conjunction with x-ray crystal structures, to develop models of the shape of the lipid halos surrounding the hydrophobic regions of purified membrane proteins. The scattering data they produced from SAXS experiments resulted in scattering by both protein and lipid. The protein crystal structure was then superposed to investigate the lipid content of the scattering.

This SAXS-based methodology could be used for investigating MtrCAB if a crystal structure was available, which unfortunately it is not. SANS is a technique that can overcome the problems faced in these experiments. SANS, combined with a technique called contrast variation and sophisticated data analysis approaches (Petoukhov & Svergun 2007; Neylon 2008; Madl et al. 2011), has been used to characterize the stoichiometry, conformational changes and topology of protein-protein and protein-nucleic acid complex (Niemann et al. 2008; Li et al. 2009; Chaudhuri et al. 2011; Christie et al. 2012). This is because, with SANS, it is possible to select scattering caused exclusively from specific components of a heteromeric complex. In relation to MtrCAB, this means that the protein components of the complex can be separated from the detergent toroid-associated MtrB (whic usually spans the membrane). The concentration of deuterium that is needed in buffers to provide scattering that matches various different detergents used for membrane protein solubilization is available in Breyton et al. (2013). At these match points the detergent or lipid scattering can easily be baseline subtracted, leaving other scattering arising from

other components of the sample to be detected. The greater the difference in the match point (or deuteration percentage) of detergent and protein, the better the quality of data that can be obtained from SANS experiments.

Replacing hydrogen for deuterium within the respective atomic structures can alter the match point of detergents, lipids, nucleic acids and proteins. More advanced experiments involving the combination of deuterated and hydrogenated components of a complex causes increased differences in the respective match point, and thus allows separation of scattering contributions from each component. Methodologies for creating deuterated proteins are described in Breyton et al. (2013). However, for SANS experiments on MtrCAB, solubilizing the hydrogenated protein complex in deuterated detergent was determined to be optimal considering budget, equipment and time constraints. Therefore, a set of experiments was designed to investigate the overall shape of MtrCAB. This included AUC, SANS and contrast-matched SANS on both hydrogenated and deuterated samples.

5.05 Purification of MtrCAB

MtrCAB was purified from both *Shewanella baltica* and *Shewanella oneidensis* using the method described in the Materials and Methods section 2.15. MtrCAB was buffered with 20 mM HEPES pH 7.5, 5 mM LDAO. Compared to other alternative detergents, such as Triton X100, LDAO micelles were found to have small enough diameters to fit through the pores of centrifugal concentrators, simplifying the purification process of MtrCAB. Initially, the MtrCAB from *S. baltica* was used for experimentation as a greater amount of higher concentration protein was produced. Further experiments were planned for the *S onedensis* MR-1 MtrCAB once the initial experiments with the *S. baltica* complex were concluded successfully.

5.06 Analytical ultracentrifugation of MtrCAB in H_2O

AUC techniques were employed to estimate structural parameters of MtrCAB. These experiments allowed investigation into the volume, axial ratios and molecular weight of MtrCAB. These parameters were helpful during the SANS modeling process. Additionally, AUC experiments help to confirm that MtrCAB samples are fit for use in the more expensive and time-consuming SANS experiments. AUC experiments can detect the presence of multiple species and provide sedimentation distribution estimations, thereby detecting if there is any aggregation, stability or purity issues. Both absorbance and interference sedimentation velocity experiments were conducted on 0.25, 0.15 and 0.1 $mg.mL^{-1}$ MtrCAB in 20 mM HEPES pH 7.5 5mM LDAO, as described in section 2.20. These experiments examined how the MtrCAB complex behaved in solution without D_2O.

AUC velocity sedimentation absorbance and interference measurements

Figure 5.8 Panel A shows the radial absorbance measurements resulting from sedimenting MtrCAB over time, processed using the program SEDFIT. Lamm equations can be fitted to the data with good alignment, (Schuck, 2000a; Schuck, 2000b; Schuck, 2003). The sedimentation distribution from c(s) analysis is presented in Panel B. One major component with a sedimentation coefficient of 6 S is predicted by SEDFIT. There is a less abundant component with lower sedimentation coefficients predicted at 3.2 S. At 9 S there is an increase in AU/S, indicating that there could be a higher molecular weight species beyond the parameters of the fit. This could be due to aggregated proteins, due to LDAO in the absorbance measurements, or due to artifacts arising from the Lamm equations that do not fit the data precisely. The absorbance data collected did have background noise created from LDAO scattering. This could have led to difficulty in assigning sedimenting species in the SEDFIT fitting algorithm. Instead of tracking protein sedimentation through absorbance measurements, tracking sedimentation using interference would provide data with greater clarity in this respect.

Panel C shows the dc/dt analysis of MtrCAB sedimenting in a velocity experiment, tracked by Rayleigh interference optics. The essential element of the dc/dt technique is to select a set of scans which span a time range that is short enough that the difference in concentration between first and last scans approximates to the derivative of concentration with respect to time. This method allows for multiple discreetly sedimenting substances to be identified (Stafford 1992). The dc/dt curve shows only one peak at 6 S. This is similar to

the largest sedimenting peak observed in Panel B. Panel D shows the g(s*) distribution computed using SEDANAL (Stafford & Sherwood 2004). Again, only one peak can be observed at ln(s*) = 1.8. This gives an apparent sediment coefficient of 6.04 S, again similar to the largest peak calculated in the c(s) analysis on Panel B. These results show that there is only one sedimenting object and this should be MtrCAB in LDAO. This is unlike the c(s) results, where one main peak and two smaller peaks are detected. These peaks can therefore be presumed to be due to optical scattering from LDAO or artefacts from the data processing.

Even if the protein solution does contain impurities, the 6 S body is the most common object in solution. When performing SANS experiments, this will therefore be the most prevalent source of scattering and thus most significant factor determining the scattering profile. Additionally, the 6 S body is probably the biggest object in the sample, thus each one will scatter much more than any individual potential impurities. Impurities or aggregations will distort the scattering profile, however heavily it is biased towards the most common or largest scattering protein. These impurities contribute to any conclusions drawn from the experiment, for example shape reconstructions. With these considerations in mind, the MtrCAB in 20 mM HEPES pH 7.5 5 mM LDAO sample was deemed appropriate for use in SANS experiments. It was then deemed important to see how the sample changed with the addition of D_2O. If the MtrCAB behaves differently in D_2O compared to H_2O buffers, then it may not be suitable for SANS D_2O contrast experiments.

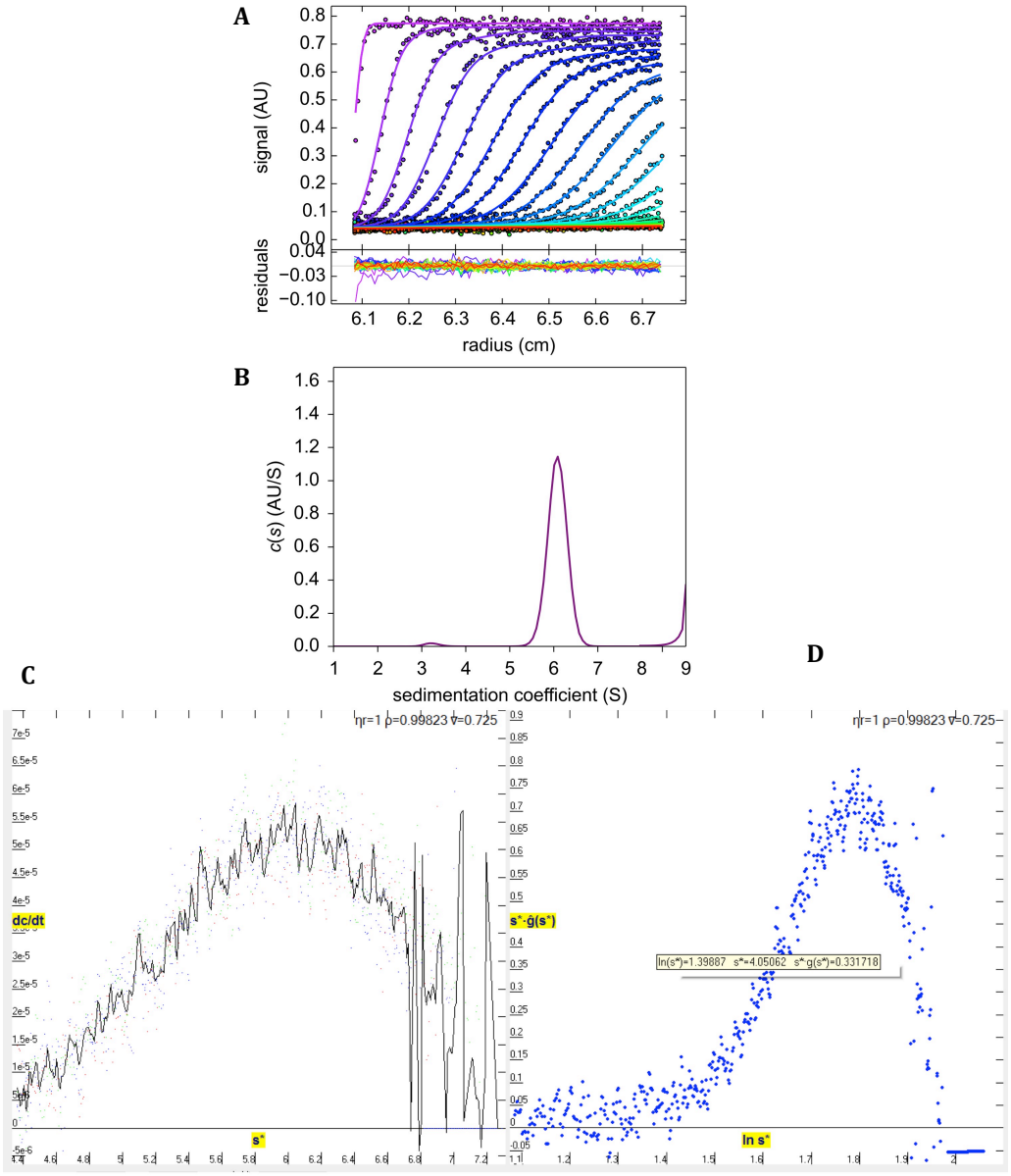

Figure 5. 8 Results from AUC experiments conducted on MtrCAB in 20 mM HEPES pH 7.5, 5 mM LDAO.
Panel A Radial absorbance at 410 nm of MtrCAB sedimenting over time [blue dots] data points, [black line] average of data points. Lamm equations were fitted to each scan, with the residuals of each scan displayed below the graph, processed in SEDFIT.
Panel B c(s) distribution calculated by SEDFIT.
Panel C Screenshots from the output of SEDANAL computing the dc/dt curve produced from sedimenting MtrCAB, tracked by radial interference measurements.
Panel D Screenshots from the output of SEDANAL computing the g(s*) distribution from sedimenting MtrCAB radially tracked by interference. Panels C and D have additional parameters displayed above the graphs and in a yellow box overlaying the data. This is part of the automated output from SEDANAL.

5.07 Analytical ultracentrifugation of MtrCAB AUC in D_2O buffers

AUC velocity experiments were conducted on 0.25, 0.15 and 0.1 mg.mL^{-1} MtrCAB in 20 mM HEPES pH 7.5, 5mM LDAO, 10% D_2O. This was to investigate whether the presence of D_2O affected the monodispersity of MtrCAB, and thus the potential suitability of the MtrCAB sample for SANS D_2O match-point experiments. 10% D_2O was chosen, as this was the predicted concentration of D_2O that would match out any neutron scattering from LDAO.

Figure 5.9 Panel A shows the radial absorbance at 410 nm over time of MtrCAB in 20 mM HEPES pH 7.5, 5 mM LDAO, 10% D_2O. Lamm equations were fitted to the sequential scans using SEDFIT. The Lamm equations fit neatly to the scans and there are only slight deviations in the residuals. SEDFIT was then used to calculate the c(s) distribution, Panel B. The c(s) distribution shows major peaks at 0.2 S and 5.9 S and minor species sedimenting at 11 S and above 14 S. The distribution is similar to the c(s) distribution of MtrCAB in figure 5.8 Panel A, where MtrCAB is sedimenting in the presence of H_2O instead of D_2O. The recurrence of a major peak sedimenting at around 6 S indicates that the sedimentation of MtrCAB does not change when D_2O is present in the buffer. The peaks at 11 S and 14 S correspond to very large objects, and could indicate an aggregate of MtrCAB. This would make the sample inadequate for SANS experiments. The validity of the other peaks calculated in the c(s) analysis were tested by once again performing a velocity experiment tracking the radial distribution of MtrCAB through interference. These results were then analyzed by the dc/dt method, Figure 5.10 Panel C. Panel C shows the dc/dt curve. This has only one peak at 5.8 S. This is within 0.1 S of the major peak detected in the c(s) analysis. No other peaks were calculated in this method, indicating that this is the main or only sedimenting species. Figure 5.2 Panel D shows the g(s*) distribution calculated from the MtrCAB interference data. This shows one major peak at g(s*) = ln(1.76), giving a sedimentation coefficient of 5.8 S. This is the same as in the dc/dt curve and once again shows that there is only one major peak.

With these results obtained it was decided that the D_2O-containing sample was suitable for SANS experiments. No aggregation was detected and the sample appeared to be mono-disperse.

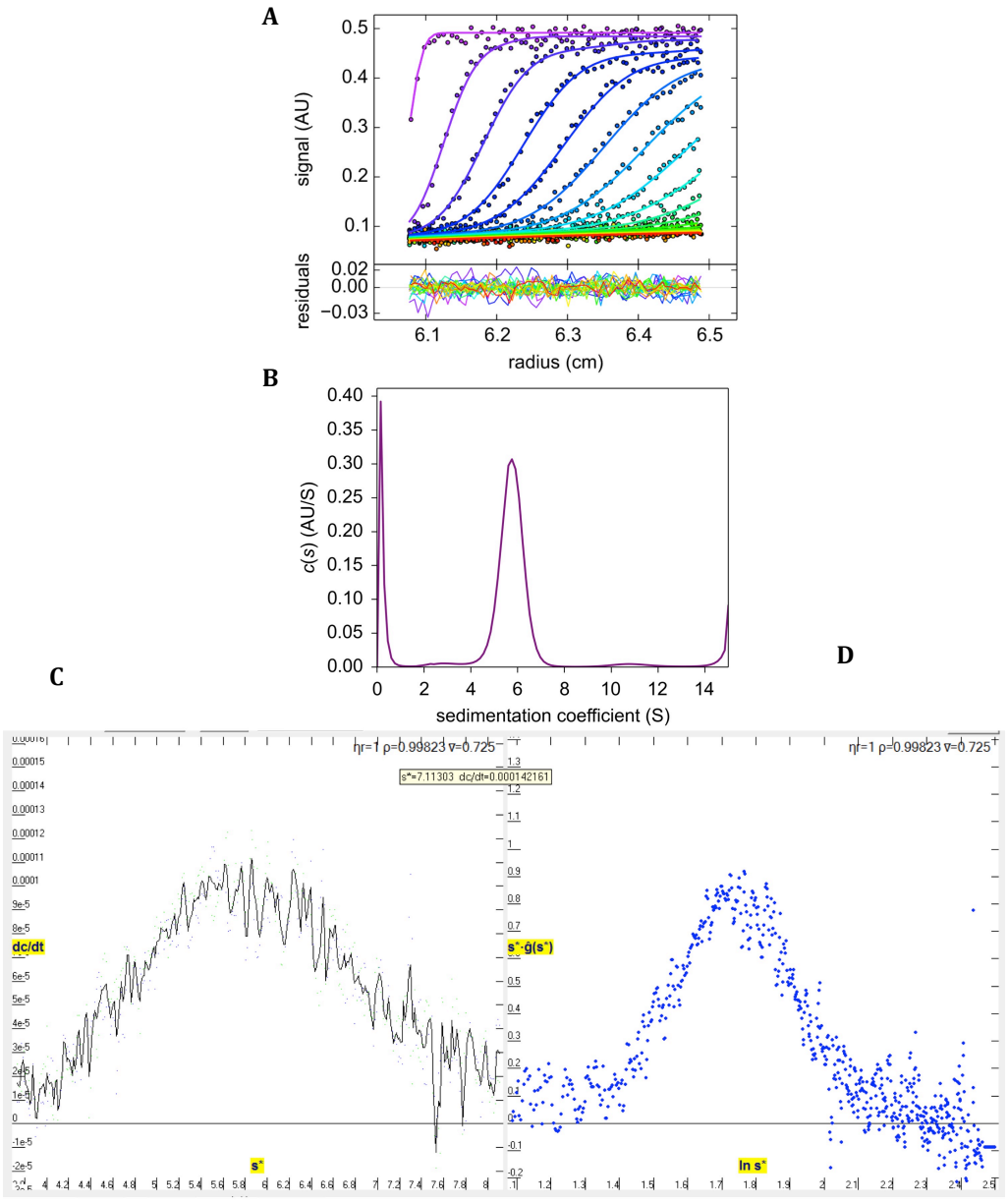

Figure 5.9 Results from AUC experiments conducted on MtrCAB in 20 mM HEPES pH 7.5, 5 mM LDAO, 10 % D_2O.

Panel A. Radial absorbance at 410 nm of MtrCAB sedimenting over time. Lamm equations have been fitted to each scan, with the residuals of each scan displayed below the graph, processed in SEDFIT.

Panel B. C(s) distribution calculated by SEDFIT.

Panel C. The dc/dt curve produced from sedimenting MtrCAB, tracked by radial interference measurements.

Panel D. The g(s*) distribution from sedimenting MtrCAB radially tracked by interference. Panels C and D have additional parameters displayed above the graphs and in a yellow box overlaying the data. This is part of the automated output from SEDANAL.

5.08 SANS analysis of MtrCAB in buffers solvated soley by H_2O

Once the MtrCAB sample was determined to be of sufficient quality and stability when in a D_2O-containing buffer, SANS experiments could be conducted. These were performed as described in the Materials and Methods section 2.22 with the help of Richard Heenan (ISIS) and Dave Scott (STFC).

MtrCAB samples in 20 mM HEPES pH 7.5 5 mM LDAO, with a range of concentrations, were irradiated in the neutron beam-line. Each of the radially-averaged scattering profiles collected are displayed in Figure 5.10 Panel A. All these profiles show a concentration dependence for intensity of scattering, with similar features at each degree of momentum transfer. The Rg and I_0/c values were consistent over the range of concentrations tested, Figure 5.10 Panel B. These factors indicate that the data is reliable, as only scattering intensity rather than scattering features change with protein concentration. However, the density of points taken during the data collection is much reduced compared to SAXS data. Only 40 data points were calculated. This was achieved by taking raw data and grouping it into bins of 0.05 q. This minimized the error bars whilst maintaining the highest degree of detail possible.

Figure 5.10 Panel C shows the Kratky plot for each of the scattering profiles. A single peak at low q, with an upward sloping tail at high q, indicates that the scattering profile is that of a complex with a globular region and a flexible tail. Figure 5.11 Panel D shows the fit of the scattering profile of the 11 $mg.mL^{-1}$ data created by the program GNOM (Svergun 1992). The fit closely matches the scattering profile, except at very low and very high q. This was expected from low-density scattering data produced by SANS.

Figure 5.10 Panel E shows the pair distribution function calculated by GNOM using the 11 $mg.mL^{-1}$ scattering profile. It has one major peak at low pair distances and a tail as pair distances get higher. The results from Panel E echo the results from the Kratky plot in Panel C, in indicating that the scattering was caused by an elongated molecule that has a small globular region. The Rg calculated for this fit was 112.4, and the D_{max} 400 Å. The Rg value is similar to the Rg values in Panel B.

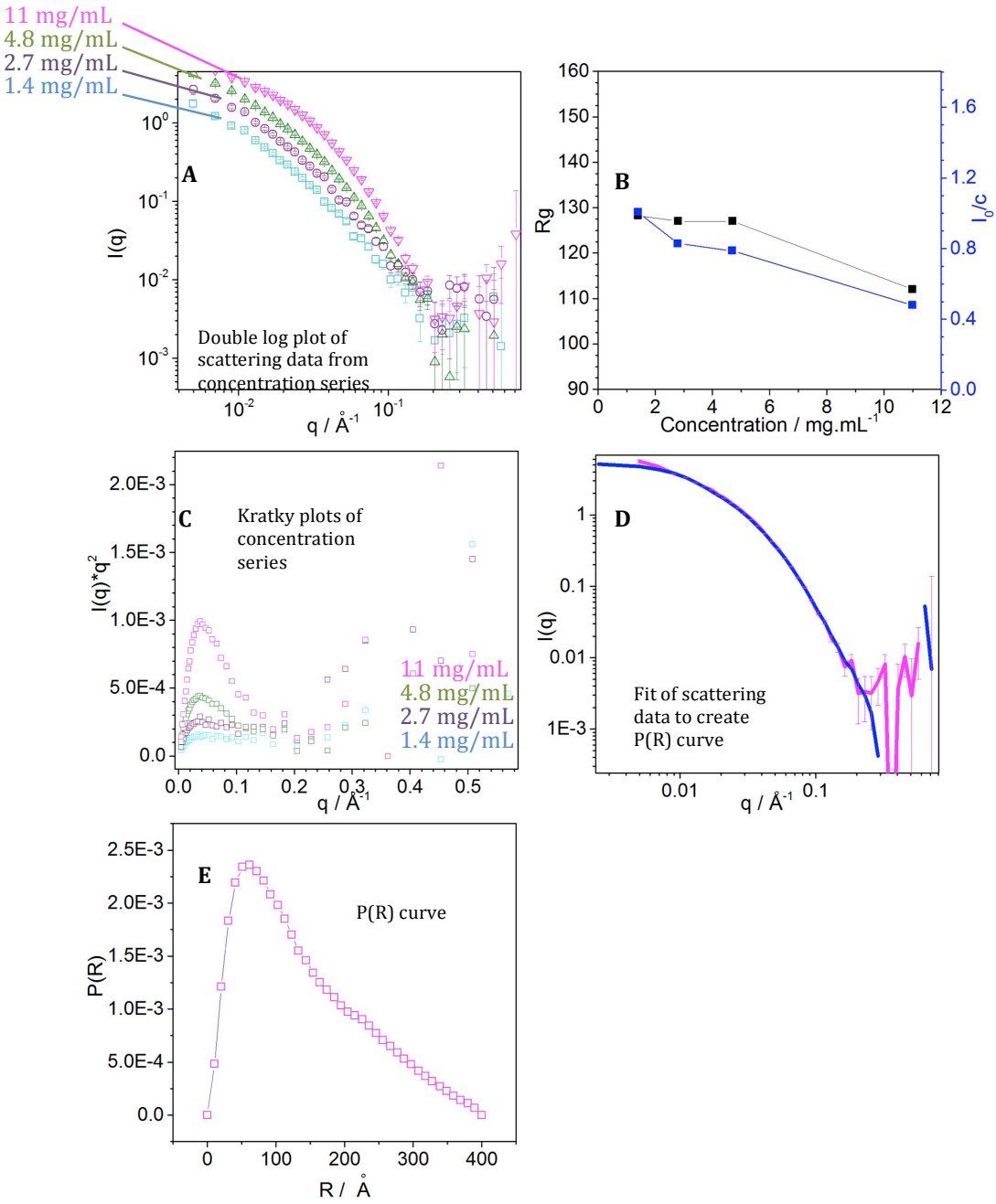

Figure 5. 10 Results from SANS experiments on MtrCAB in 20 mM HEPES pH 7.5, 5 mM LDAO.
Panel A. Radially averaged scattering intensity of neutrons over a concentraion series.
Panel B. Radius of gyration [Black dots and lines] and theoretical I_0/c [blue dots and lines] for scattering profiles over the concentration rage of MtrCAB tested.
Panel C. Kratky Plot of scattering data for MtrCAB over the same concentration series as Panel A.
Panel D. Radially averaged scattering profile of 11mg.mL^{-1} MtrCAB [purple line] with fit calculated by GNOM [black line].
Panel E. Pair distribution function, calculated by GNOM for 11 mg.mL^{-1} MtrCAB.

Using the program DAMMIF (Franke & Svergun 2009), ten bead model simulations were constructed based on the p(r) curve from Figure 5.10 Panel E. These simulations are shown in Figure 5.11 Panel A. The program DAMMIF was set to use a bead size range from 1 to 20 Å, with up to 50 harmonics in interactive mode. This gave the best possible chance of producing an accurate model. The simulations produced are shown in Figure 5.12. Due to the low signal to noise ratio in the scattering profiles collected, a low data density p(r) curve was constructed which contained only 40 points. From this, simulations were constructed using far fewer beads (100 – 140). This number of beads is one order of magnitude smaller than the number of beads used for SAXS based simulations.

The simulations displayed in Figure 5.11 Panel A exhibit a general pattern. They are long and thin with a small globular region at or near one end. The thin tail region is often only one bead thick and comprises most of the 400 Å length of the model.

These models were then used by the program DAMAVER (Volkov & Svergun 2003) to create an average bead model simulation and a filtered bead model simulation. The program SUBCOMB (Kozin & Svergun, 2001) was then used to align these two models, shown in Figure 5.11 Panel B. The red wire mesh shows the average molecular envelope of all the simulations, with the beads representing the shapes that were present in all of the simulations. These models clearly exhibit a globular region attached to a slender tail.

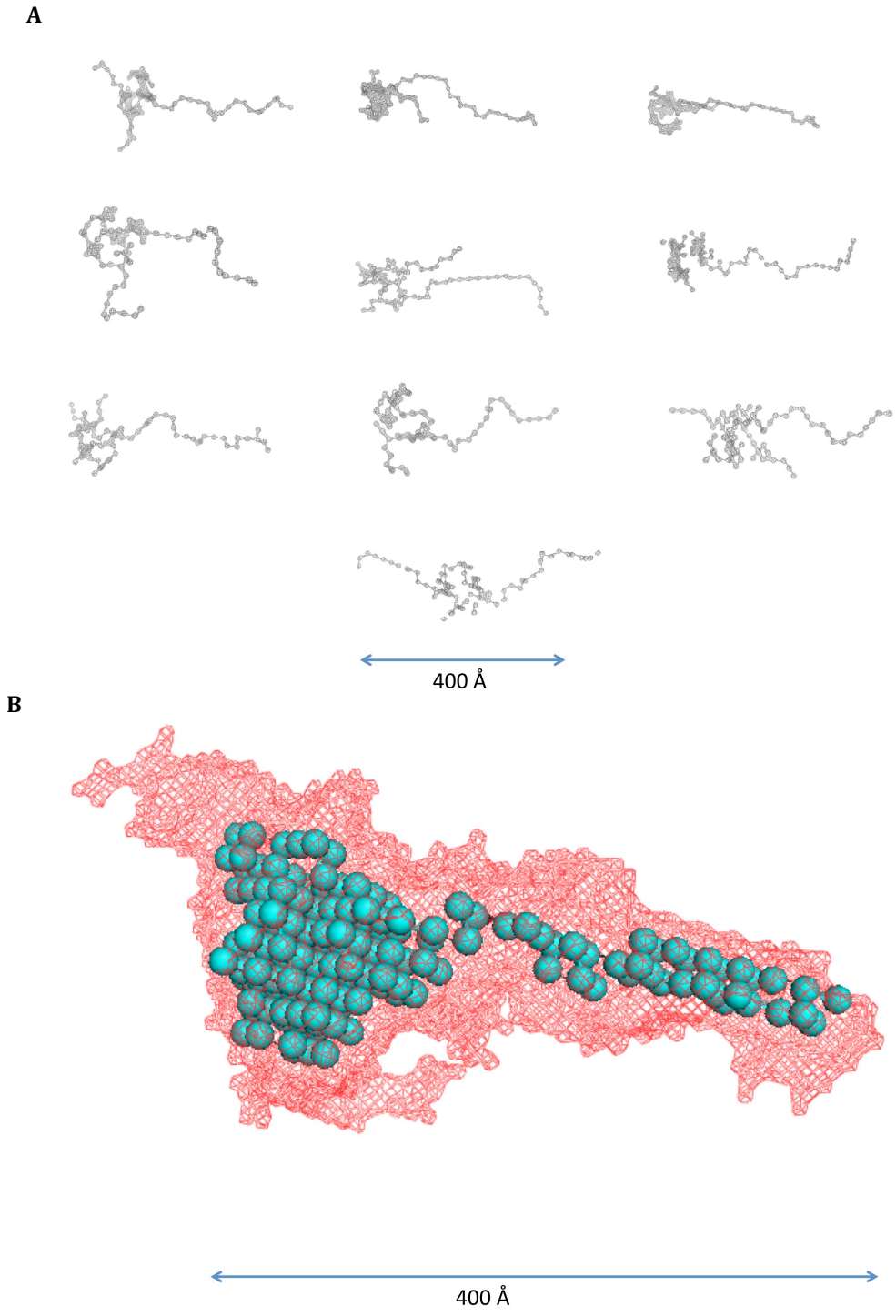

Figure 5. 11 SANS derived models of MtrCAB in 20 mM HEPES pH 7.5, 5 mM LDAO.
Panel A. Ten simulated bead models of MtrCAB calculated by DAMMIF in interactive mode.
Panel B. [Red wire mesh] Average molecular envelope calculated from all ten DAMMIF simulations of MtrCAB, constructed using DAMAVER. [Blue spheres] molecular envelope calculated by DAMFILT of the regions consistently within all of the ten DAMMIF simulations. The two molecular envelopes were aligned using SUPCOMB.

5.09 SANS analysis of MtrCAB in buffers containing D_2O

To fully interpret the neutron scattering developed by MtrCAB in isolation, the SANS contribution from LDAO was removed. This was achieved through creating a D_2O background with the same nuclei concentration as LDAO. In this way, the LDAO scattering contribution was indistinguishable from the background scattering and thus will was subtracted during signal processing.

A buffer series of 20 mM HEPES pH 7.5 5 mM LDAO, with a gradient of D_2O, was constructed. The range included 0%, 1% and 5% D_2O samples and then 10 – 80 % D_2O over 8 samples in 10% D_2O increments. The scattering patterns were collected and compared with those collected for 20 mM HEPES pH 7.5. It was found that the scattering pattern created for 20 mM HEPES pH 7.5 5 mM LDAO 10% D_2O best matched the scattering pattern of 20 mM HEPES pH 7.5. This indicated that the match point of the 5 mM LDAO was 10 % D_2O. This is similar to the match point of LDAO described previously in (Breyton et al. 2013). Sampes of MtrCAB were prepared with this concentration of D_2O and used for SANS experiments as detailed in section 2.22.

The radially averaged scattering profiles generated from SANS experiments on 4.7, 2.8 and 1.4 $mg.mL^{-1}$ MtrCAB are shown in Figure 5.12 Panel A. The scattering profiles show a concentration dependence, with increasing concentration of MtrCAB causing a proportional increase in the scattering detected over all q. Figure 5.12 Panel B shows the Rg and I_0/c values computed for each of the samples. There are only very small changes in Rg and I_0/c over the concentration range. This indicates that the results are reliable. Figure 5.12 Panel C shows the Kratky plot of the scattering profiles. This shows a small peak at low q followed by a rising tail towards high q. This is similar to the Kratky plot shown in Figure 5.10 Panel C for MtrCAB without the presence of D_2O. This indicates that the scattering was caused by a small globular region attached to a long flexible tail. The program GNOM was then used to create a pair distribution function for the scattering data. Panel D shows the fit created, which accurately describes the scattering profile except at very low and very high q. Panel E shows the p(r) curve. It has only one very broad peak, the calculated Rg of this fit was 124 which is similar to the calcualted Rg's in Panel B. The D_{max} of the fit was calculated to be 362 Å.

Comparing the scattering data from MtrCAB samples with and without the presence of D_2O will lead to potential structual insights about MtrCAB, as the contributions LDAO made to the scattering can be derived. Figure 5.12 Panel F shows the overlaid scattering profiles of 11 mg.mL MtrCAB in 20 mM HEPES pH 7.5, 5 mM LDAO (from Figure 5.10 Panel A) and 4.7 $mg.mL^{-1}$ MtrCAB 20 mM HEPES pH 7.5, 5 mM LDAO 10% D_2O (from Figure 5.12 Panel A). The scattering profiles are generated from different concentrations of MtrCAB, which means that they do not overlay, however it is possible to deduce that, if the scattering profiles were adjusted for concentration, they would have differences. At around $2.5x10^{-2}$ q the MtrCAB in H_2O has a more pronounced curve compared to that for MtrCAB in D_2O. This is especially apparent when comparing the p(r) curves for the two scattering profiles. Figure 5.12 Panel G shows the p(r) curves for the H_2O and D_2O MtrCAB samples, using different scales for each plot to enable easy comparisons. The H_2O sample has peaks at 80 Å and 230 Å that are not present in the D_2O sample, which has one peak at 120 Å. These differences are likely due to the absence of scattering from LDAO in the D_2O sample.

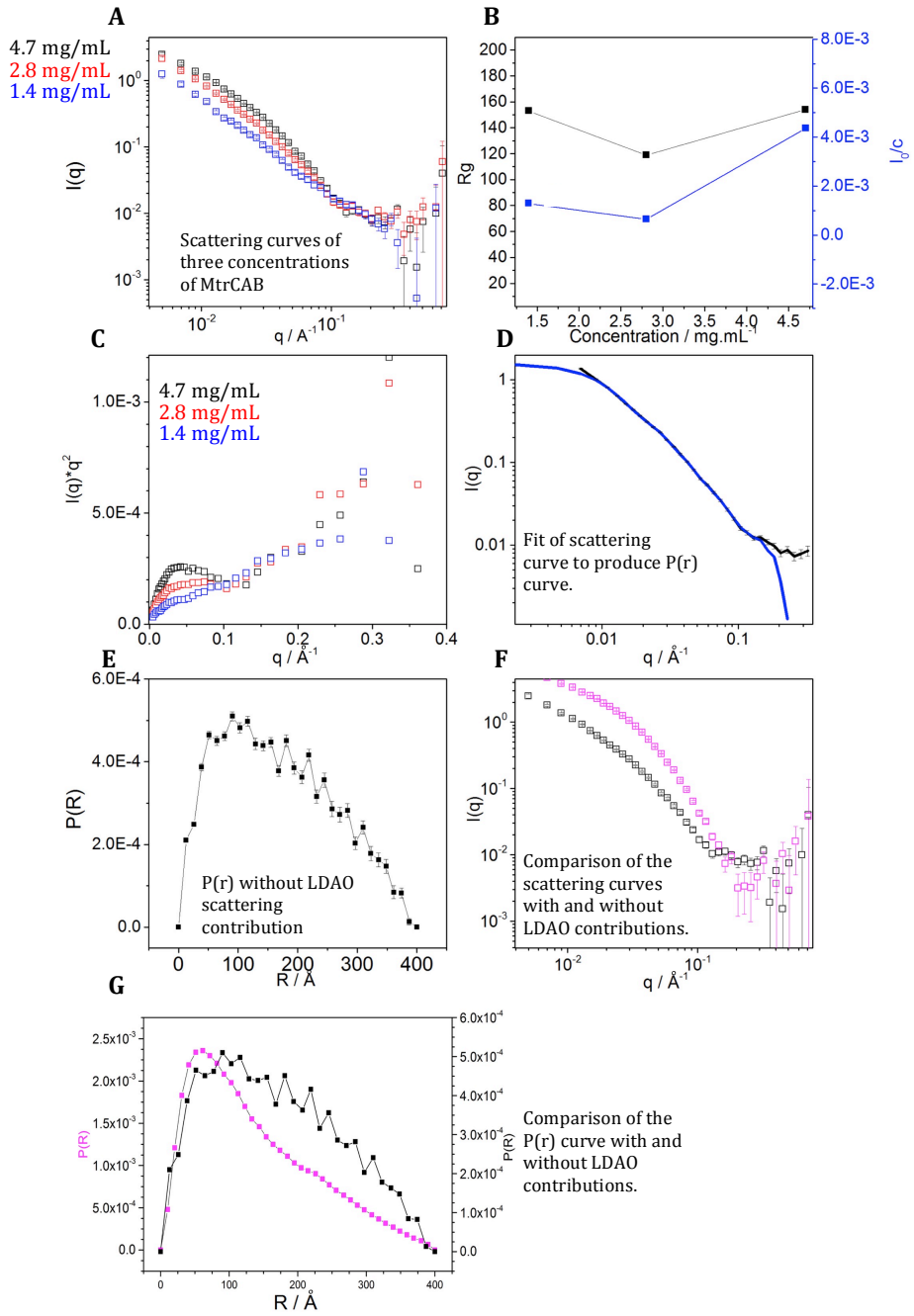

Figure 5. 12 Results from SANS experiments on MtrCAB in 20 mM HEPES pH 7.5, 5 mM LDAO 10% D_2O.

Panel A. Radially averaged scattering intesity of scattering from MtrCAB at three concentrations: 4.7 mg.mL^{-1}[Black squares], 2.8 mg.mL^{-1} [Red squares] and 1.4 mg.mL^{-1} [Blue squares].

Panel B. Radius of gyration [Black dots and lines] and theoretical I_0/c [blue dots and lines] for scattering profiles over the concentration rage of MtrCAB tested.

Panel C. Kratky plots of scattering data of MtrCAB at three concentrations: 4.7 mg.mL^{-1}[Black squares], 2.8 mg.mL^{-1} [Red squares] and 1.4 mg.mL^{-1} [Blue squares].

Panel D. Radially average scattering profile of 4.7mg.mL^{-1} MtrCAB [Black line] with fit calculated by GNOM [blue line].

Panel E. Pair distribution function, calculated by GNOM for 4.7 mg.mL^{-1} MtrCAB.

Panel F. Comparision of the radially averaged scattering profiles of MtrCAB with and without 10% D_2O [black line] scattering profile from 4.7 mg.mL^{-1} MtrCAB in 20 mM HEPES pH 7.5, 5 mM LDAO, 10% D_2O. [Purple line] scattering from 11 mg.mL^{-1} MtrCAB in 20 mM HEPES pH 7.5, 5 mM LDAO.

Panel G. Comparison of pair distrbution functions shown in Figure 5.10 Panel E and Figure 5.12 Panel E.

The p(r) curve generated from the scattering profile of 4.7 mg.mL^{-1} MtrCAB in 20 mM HEPES pH 7.5, 5 mM LDAO 10% D_2O was used to create bead model simulations. The program DAMMIF was used in interactive mode to allow an increase in the bead size range and the number of harmonics to create ten simulations of the data. These are shown in Figure 5.13 Panel A. The models are comprised of a similar number of beads as those in Figure 5.11 Panel A and are the result of the best modelling achieved using the low data density SANS profile. The beads are even further spaced out compared to the models in 5.11 Panel A, as the average length of the models has increased by 50 Å.

Using these ten models, the programs DAMAVER and DAMFILT (Volkov & Svergun 2003) were employed to create an average molecular envelope and a filtered molecular envelope comprising the components consistently present in all models. These results are presented in Figure 5.13 Panel B. In this figure the red mesh shows the average molecular envelope and the blue beads represent the filtered molecular envelope. The average molecular envelope is elongated with a globular head region, which is around 200 Å in length. The main tail extends form the globular regions is 250 Å in length. Additinally extendeding form the globular head regions are two smaller thinner tails, which are 75 Å and 25 Å in length. The filtered model is shorter (at around 400 Å) and has only a globular head region 180 Å in length and one tail roughly 220 Å long.

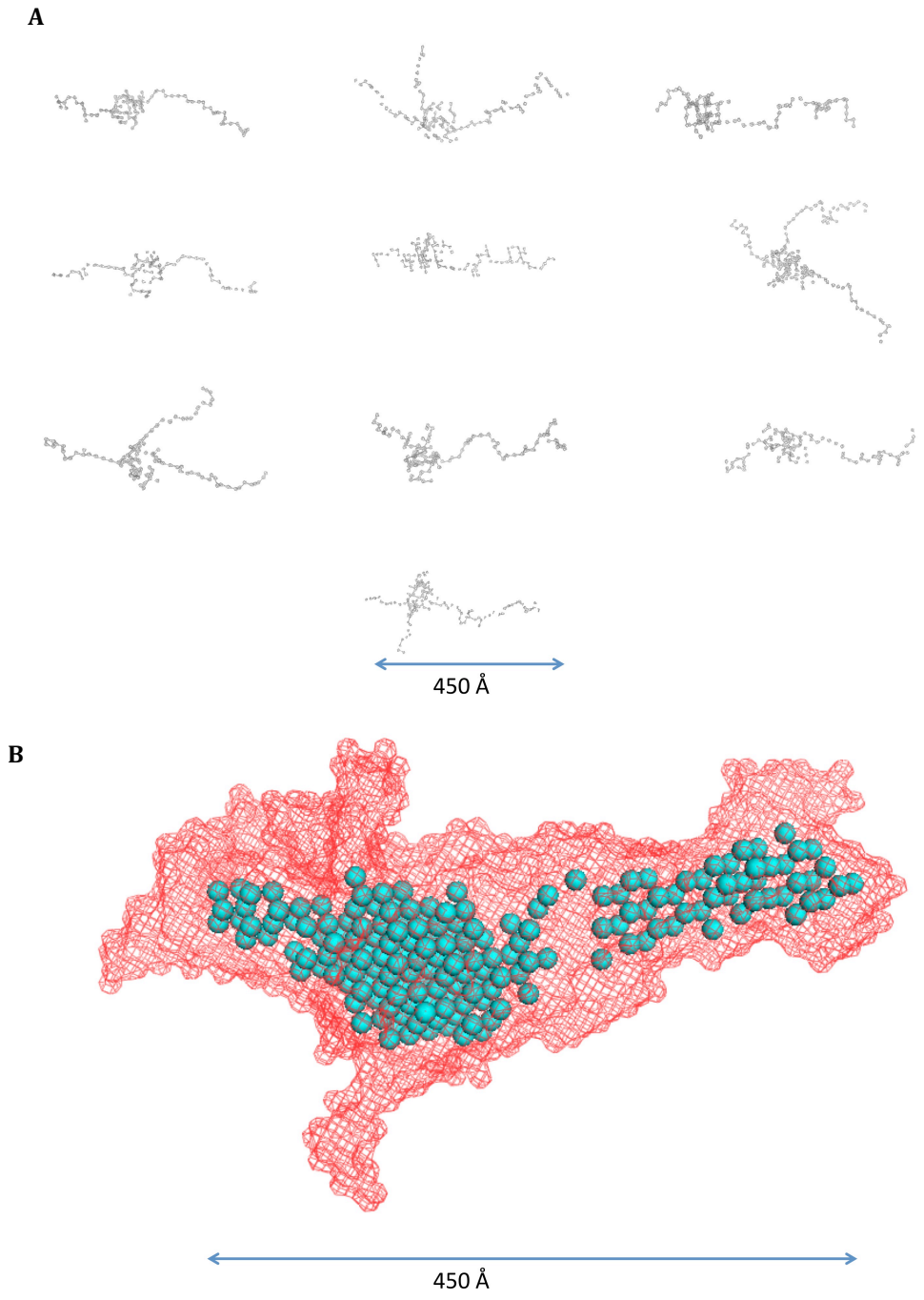

Figure 5. 13 Models of MtrCAB in 20 mM HEPES pH 7.5, 5 mM LDAO, 10 % D_2O.
Panel A. Ten simulated bead models of shapes that have p(r) functions the same as Figure 5.5 Panel E. The models were calculated by DAMMIF in interactive mode.
Panel B. [Red wire mesh] Average molecular envelope calculated from all ten DAMMIF simulations of MtrCAB, constructed using DAMAVER. [Blue spheres] molecular envelope calculated by DAMFILT of the regions consistently within all of the ten DAMMIF simulations. The two molecular envelopes were aligned using SUPCOMB.

The program SUPCOMB, (Kozin & Svergun 2001) was then used to align the H_2O and D_2O DAMAVER average molecular envelopes of MtrCAB and the DAMFILT filtered molecular envelopes. The results are shown in Figure 5.14 Panels A and B. Panel A shows the alignment between the H_2O and D_2O averaged molecular envelopes, with the H_2O molecular envelope shown as yellow spheres and the D_2O molecular envelope as a blue mesh. The two molecular envelopes have similar features, in that they both have a globular head and tail regions. The H_2O molecular envelope is shorter and smaller than the D_2O envelope and has fewer protrusions from the globular head region. This could be due to the higher concentrations of protein examined in the H_2O experiments compared to the D_2O experiments. The data quality was higher in these experiments and which led to a more defined shape.

The filtered models in Panel B also show similarities. The H_2O model is again shown as yellow spheres and the D_2O model shown as a blue mesh. Both the superposed blue wireframe and yellow bead models in Panel B are around 350 Å long, being comprised of a globular head region and a tail region. A significant single protrusion extending from the globular head region is present in both models, but is larger in the D_2O model than in the H_2O model. One possibly significant difference between the H_2O model and the D_2O model is a section in the D_2O model's tail region, just before it joins the globular head region. In this region there is a significant loss of molecular density in the D_2O models compared to the H_2O model, with only two beads joining the two sections of D_2O tail. This could be due to the phasing out of scattering from LDAO. This could indicate the presence of LDAO within the molecular envelope and thus could be used as an indication of the location of MtrB as it binds LDAO.

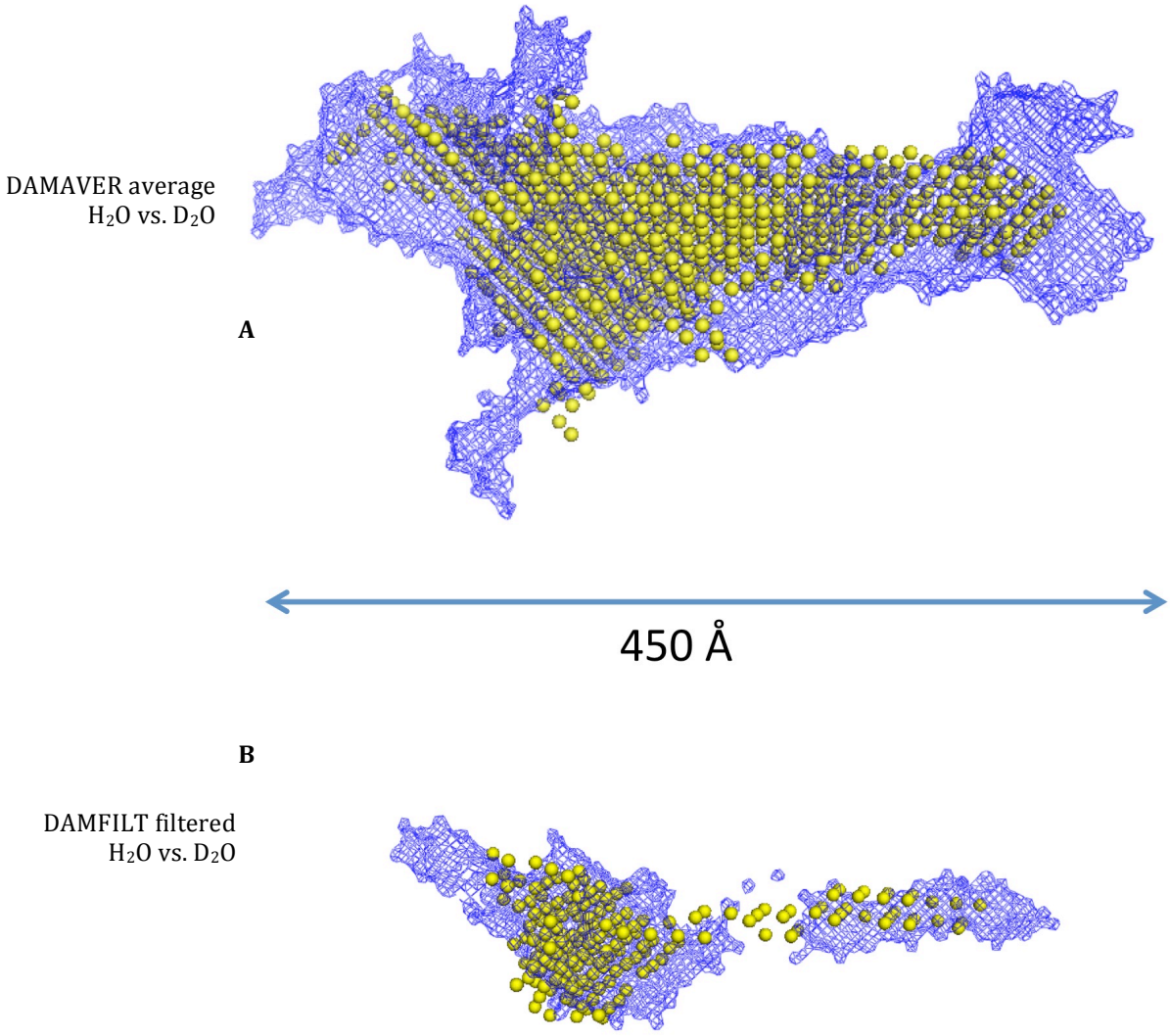

Figure 5.14 Molecular envelopes of MtrCAB calculated for SANS samples with and without the presence of D_2O, both aligned using SUPCOMB.
Panel A. Alignment of the DAMAVER average molecular envelopes of MtrCAB DAMMIF simulations [purple wire mesh] in D_2O and [yellow spheres] in H_2O.
Panel B Alignment of DAMFILT filtered molecular envelopes of MtrCAB DAMMIF simulations [purple wire mesh] in D_2O and [yellow spheres] in H_2O.

5.10 Discussion

The structure of MtrB

Currently no structures of MtrB have been published in the literature, either in isolation of as part of the MtrCAB complex. Only a handful of β-barrel pore structures have been published, such as FepA (Buchanen *et al*., 1999). Therefore *in-silico* structure prediction programs were used to generate models of the shape of MtrB both in 2D and 3D.

2D analyses by BOCTOPUS and PRED_TMBB predicted the secondary structure and location of MtrB. Both these programs found 28 β-stand intra-membrane regions predicted long loop regions in the extra cellular space. These computational predictions were proved inaccurate through digestion assays in White et al., (2013). The authors demonstrated that the supposed extracellular long regions were not accessible to extracellular protease digestion. Therefore it is likely that the programs modeled MtrB in an inverted manner, with the long loop regions being on the periplasmic face. The reasons for this discrepancy could be that the formation of MtrB is inherently different to how other related porins form in membranes. Since *in silico* predictions are based upon canonical porin formation, attempts to model MtrB would therefore result in errors. Another suggestion as to why both the programs modeled MtrB in the incorrect orientation is that MtrB's oreientation is influenced by interactions with proteins (such as MtrA, with which it is known to associate) when forming. These proteins ensure that the long loop regions remain in the periplasmic space. A previously stated hypothesis is that the C terminal section of MtrA is flexible, and requires protein:protein interactions to stabilize it. The presence of long loop regions of MtrB could provide the scaffold MtrA needs.

Attempts were made to produce an *in silico* 3D model of MtrB using the program TMB_PRO_3D. The program predicted that MtrB contained 24 trans-membrane β strand regions. This was a reduction in the number of inter membrane regions compared to the 2D models produced by BOCTOPUS and PRED_TMBB. The reduction in number of inter membrane strands was likely to be due to TMB_PRO assigning some of the sequence, that was modeled as four inter membrane β strands in the 2D models, to form a globular region, which was used to plug the β barrel pore when in 3D. Because of the rarity of the crystallization of β-stand pore proteins, structure simulations programs have a very small pool of known structural motifs can be used to predict currently un-crystalized proteins. FepA, crystalized in Buchanen *et al*. (1999) has a globular plug in its pore. Structures like

this could have been the cause of TMB_PRO_3D modeling MtrB with a globular protein plug in in its pore. This is likely to mean that the TMB_PRO_3D structural prediction of MtrB gives a pore that is smaller than in MtrB's actual structure. Truncated versions of MtrB were then created to clear the 'plug' from the barrel of MtrB so it could be more easily used when modeling MtrCAB. The TMB_PRO algorithm did not remove any more beta stands from the trans-membrane barrel in the structure predictions of truncated MtrB. This could be because the 24 beta strands it predicts are particularly well defined as transmembrane regions, compared to the additional four transmembrane regions predicted by BOCTOPUS and PRED_TMBB .

How MtrB might interact with MtrA

Figure 5.15 shows that the SAXS molecular envelope of MtrA developed in Chapter 3 has appropriate dimensions to fit fully within the *in silico* model of MtrB. The crystal structure of MtrC has a globular shape with a length of ~80 Å. Therefore, only small fractions of MtrC would be able to fit into the pore of MtrB, and only to a shallow depth. Based on this model it is likely that MtrA is the component of MtrCAB that fits inside MtrB and that MtrA spans the majority of the intermembrane space. However, as this model of MtrB is composed of 24 beta strands, and MtrB is predicted to contain up to 28 beta strands, the pore of MtrB could be in the order of a few Angstroms larger than the dimensions shown. If the pore of MtrB was actually larger, MtrC may be able to fit further in the pore than the current model suggests. This model therefore works well as a lower limit for the pore size. These alignments provide a valuable first insight into possible conformations of MtrCAB. However the quality of the SAXS MtrA model, and the *in silico* MtrB structure were not reliable enough to produce firm conclusions.

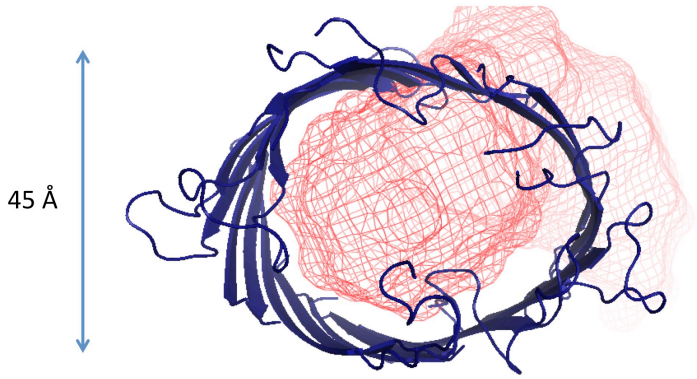

Figure 5. 15 A cartoon illustrating how MtrB could interact with MtrA and MtrC in MtrCAB, using the DAMFILT filtered moleuclar envelope of MtrA from SAXS experiments [red wire mesh] and the in-silico structure of MtrB [dark blue cartoon structure].

Using SANS to explore the structure of MtrC

Crystal structures of MtrC and its homologues do appear in the literature (Edwards et al. 2012, Edwards et al 2015 in press), however no solution based models of MtrC are available. Comparing MtrC crystal structures to SANS derived models is useful in demining how well SANS experiments produce reliable models. Only one SANS experiment was conducted on MtrC, this was primarily because there was limited beam-time available, as otherwise a range of concentrations would have assessed. The DAMMIF simulated bead models of MtrC looked very little like the globular protein predicted by the crystal structure and instead resembled a folded tubular structure. However, the SANS structure did mimic the way the four domains of MtrC linked together. Through averaging the DAMMIF simulations with DAMAVER, a globular molecular envelope was produced. This fitted well with the MtrC crystal structure. The DAMFILT filtered molecular envelope resembled the original DAMMIF simulations, and thus was not well aligned to the crystal structure. However, like the DAMMIF bead models, the filtered model did seem to follow the domain structure of MtrC. Further use of the SANS-based models of MtrC will probably concentrate on the DAMAVER molecular envelope as it appears to be more consistent with the crystal structure. As the crystal structure and the SANS model appear to be consistent with each other it can be predicted that through packing MtrC in a crystal lattice, its shape has not been significantly changed. Therefore the crystal structure of MtrC is physiologically relevant.

Predications of the molecular weight of MtrC from the SANS scattering curve using the method described in Fischer et al. (2010) gives a value of ~180 kDa. This is far heavier than the ~90 kDa molecular weight MtrC has been determined by (Hartshorne et al. 2007; Clarke et al. 2011). This inaccuracy in the predicting the molecular weight seems to have produced a value that is double the predicted mass of MtrC based on sequence composition. This highlights that the low data density for the SANS curves can lead to inaccuracies in the molecular weight prediction.

Using Analytical ultracentrifugation to investigate MtrCAB

AUC experiments were used to investigate MtrCAB and the suitability of the prepared samples of MtrCAB for SANS experimentation. The AUC results showed that light scattering from LDAO caused some features to be anomalously predicted in c(s) analysis. Using interference based methods that suit samples containing detergents (which contribute to absorbance), these features were shown to probably be artifacts and not due

to the presence of real species (or MtrCAB aggregation). The sedimentation coefficient for MtrCAB in 20 mM HEPES pH 7.5, 5 mM LDAO was determined to be 6.1 S, and when in 20 mM HEPES, 5 mM LDAO, 10% D_2O it was 5.8 S. The increase in density or the presence of D_2O could have caused a change in the binding of the complex, such as altering the amount of LDAO. The sedimentation coefficients calculated predict that MtrCAB is highly extended in one axis compared to the others. Using the axial ratio prediction tool in ULTRASCAN, the a/b major axis ratio was determined to be between 20 and 30, depending on whether MtrCAB was simulated as oblate, prolate or a long rod. The simulation predicted MtrCAB to be over 300 Å long in the longest dimension.

Using SANS to explore the structure of MtrCAB

Currently there is no published literature investigating the structure of MtrCAB as a complex. Using SANS experiments, models of MtrCAB were produced. This allowed predictions about the structure of MtrCAB to be made. SANS experiments were conducted on MtrCAB in buffers that contained and did not contain D_2O. The results indicate that MtrCAB could have a globular domain and long tail region. Bead model simulations were performed using programs from the ATSAS suite of software (Petoukhov et al. 2012), and shapes were produced with these characteristics. The flux of neutrons used for SANS experiments was much lower than the flux of X-rays used for SAXS experiments. Therefore after the data was binned, the density and scattering intensity of the data was much lower compared to SAXS experiments conducted in Chapter 3. The quality of the data was sufficient for a 'first look' at the shape of MtrCAB, and it was the intention to complete a further set of more detailed SANS experiments. In these experiments, MtrCAB would be solubilized with a deuterated detergent. This deuterated detergent would have a higher nuclear density compared to non-deuterated analogues and, most importantly, much higher than any protein. This would have enabled a better "matching out" process where D_2O in the buffer solution matches scattering from the detergent, enabling protein scattering to be isolated. Samples were prepared for these experiments but unfortunately the beam-time allocated for these experiments was postponed due to technical difficulties. The models generated from the SANS data were composed of only around 100 beads. This was a very low number compared to the numbers used to generate SAXS models. The models should therefore be considered to be of very low resolution. The settings used when running DAMMIF simulations to create these models were selected to ensure the highest possible quality of outcome, however the input data needed to be better for a more detailed model to be produced.

The SANS data collected was used to predict the molecular weight of the MtrCAB complex. Using the method in Fischer et al. (2010) the molecular weight was predicted to be ~500 kDa based on the scattering curves of both H_2O and D_2O samples. This is larger than could be expected for an accurate MtrCAB molecular weight. However, the low data density and scattering error bars would have introduced error into the scattering plot that could have caused this discrepancy. This is proportionally similar to the discrepancy in the estimation of the molecular weight of MtrC from SANS scattering profiles using the Fischer et al. (2010) method. In both cases, the estimated molecular weight was much heavier than predicted by sequence composition or AUC.

Matching the individual components of MtrCAB to the SANS molecular envelopes

The average and filtered SANS molecular envelopes developed for MtrCAB have distinct head and tail regions, and these roughly match the shapes of MtrC ,which is globular, and MtrA, which is long and thin. There were distinctive differences between the H_2O and D_2O SANS molecular envelopes. The region that connected the head and tail of the D_2O SANS molecular envelope had less nuclear density predicted than for the H_2O model. This reduction in scattering could be due to the loss of scattering by LDAO, as a result of adding D_2O to the buffer medium. The identification of the location of LDAO in the MtrCAB shape allows for the identification of the location of MtrB, as this is the MtrCAB component that it is attached to.

Using these deductions it is possible to reconstruct MtrCAB using the individual structures of MtrC, MtrA and MtrB, producing a rough alignment with the SANS MtrCAB models Figure 5.16. Positioning MtrB at the point where nuclear scattering is lost in D_2O models compared to H_2O models leaves an elongated cylindrical tail region that has roughly the same length and diameter as the MtrA SAXS model and a globular head region, in which to fit MtrC. The MtrA SAXS model has discrepancies with published SAXS models of MtrA, (Firer-Sherwood et al. 2011). It was also constructed using only one SAXS scattering profile, thus the model produced may not be a true representation of the shape of MtrA, most likely being too long. The length of both the MtrA SAXS model and the MtrCAB SANS model could be improved with experiments with greater data density and this may lead to a reduction in size of both these models. The globular head region of both the average and filtered SANS molecular envelopes of MtrCAB were observed to be bigger than the MtrC crystal structure. This was in the order of double the volume. This discrepancy could be

due to the low data density of the SANS experiment and further experiments may allow a more detailed and nuanced model to be produced.

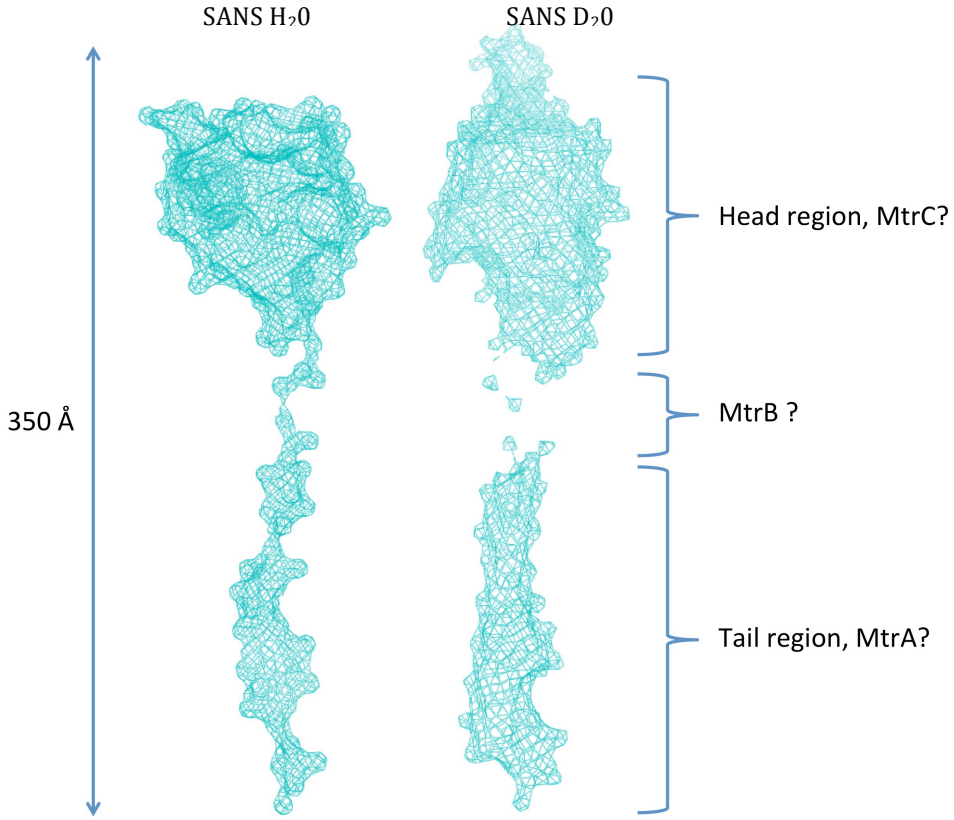

Figure 5. 16 The shapes of MtrCAB [blue wire mesh] the DAMFILT filtered molecular envelopes of MtrCAB produced from H_2O and D2O SANS experiements

Positioning MtrCAB in context of the bacterial periplasm

The overall length of MtrCAB as estimated from the SANS molecular envelope model suggests that the MtrCAB complex may be able to span the periplasm and contact the inner membrane. Dohnalkova et al. (2011) have used Cyro-EM techniques to estimate the width of the *S. oneidensis* periplasm. They found an average width of 23.5 ± 3.5 nm, which was 25% thicker than previously determined using more traditional EM techniques. (Dohnalkova et al. 2011). stated that these traditional EM techniques could potentially distort cellular features to a greater degree than their Cyro-EM techniques. CymA, a 21 kDa tetra-heme protein located on the inner membrane of *S. oneidensis*, is the likely source of electrons transported by MtCAB, (Myers & Myers 2000). If CymA is a globular protein, it likely has dimensions similar or slightly larger than STC, another tetra-heme cytochrome

which is 20 x 30 x 40 Å^3 in size. The proposed MtrA component of the MtrCAB SANS filtered model is roughly 200 Å long, when MtrCAB is positioned in the outer membrane using the proposed location of MtrB with the model. Thus MtrA would be long enough to span the periplasm and make contact with CymA if all the size estimates are correct, Figure 5.17.

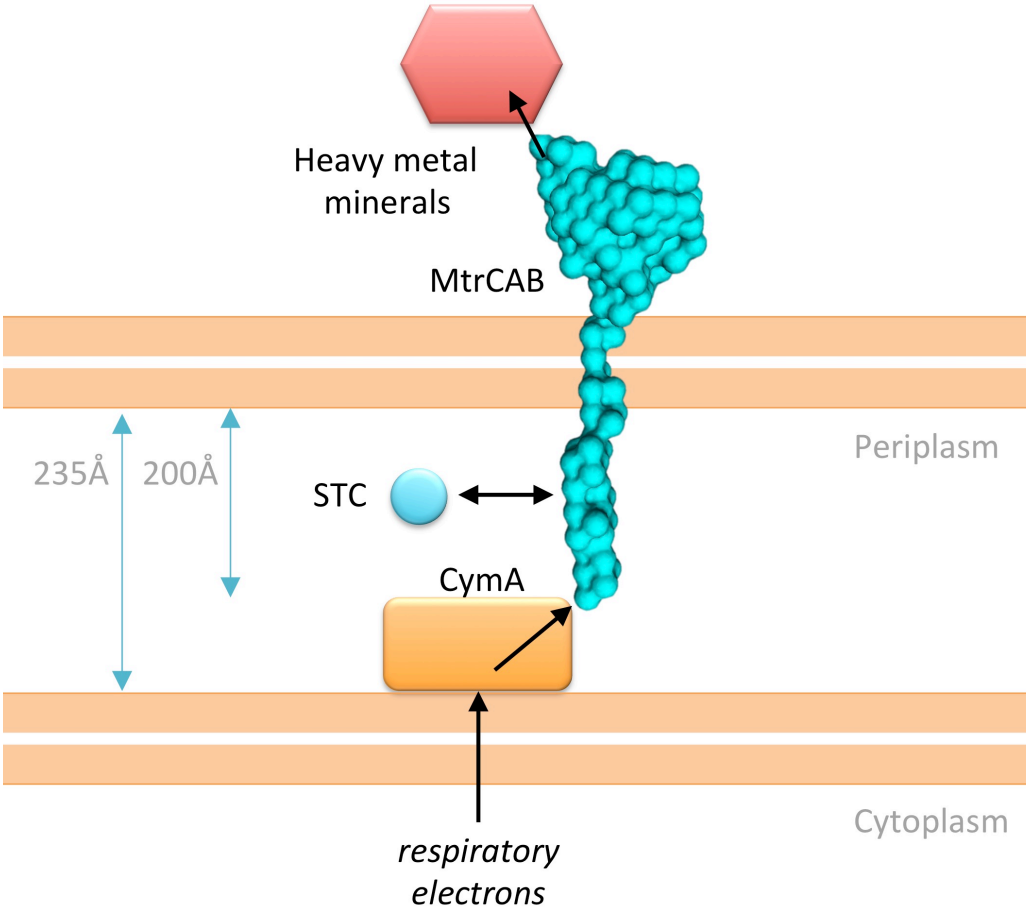

Figure 5. 17 Cartoon demonstrating the potential ability of MtrCAB to span the periplamic space based on the dimensions predicted by Dohnalkova et al. (2011) and the SANS derived MtrCAB DAMFILT model.

This model suggests that a direct contact DMR electron transport chain could start at the inner membrane of *S. oneidensis* and cross the periplasm and the outer membrane, all in one go. This hypothesis would negate the need for soluble redox shuttles such as STC to feed electrons to MtrCAB for DMR.

5.11 Bibliography

Altschul, S.F. et al., 1990. Basic local alignment search tool. *Journal of molecular biology*, 215(3), pp.403–410.

Bagos, P.G. et al., 2004. PRED-TMBB: a web server for predicting the topology of beta-barrel outer membrane proteins. *Nucleic acids research*, 32(Web Server issue), pp.W400–4.

Berthaud, A., Manzi, J. & Pe, J., 2012. Modeling Detergent Organization around Aquaporin-0 Using Small- Angle X-ray Scattering. *Journal of the American Chemical Society*, 134, pp. 10080-10088

Breyton, C. et al., 2013. Small angle neutron scattering for the study of solubilised membrane proteins. *The European physical journal. E, Soft matter*, 36(7), p.71.

Nuchanen et al., 1999. Crystal structure of the outer membrane active transporter FepA from *Escherichia coli*. *Nature Structural Biology*, 6, pp.56-63

Chaudhuri, B.N. et al., 2011. A combined global and local approach to elucidate spatial organization of the mycobacterial ParB-parS partition assembly. *Biochemistry*, 50(11), pp.1799–1807.

Christie, M.P. et al., 2012. Low-resolution solution structures of Munc18:Syntaxin protein complexes indicate an open binding mode driven by the Syntaxin N-peptide. *Proceedings of the National Academy of Sciences of the United States of America*, 109(25), pp.9816–21.

Clarke, T.A. et al., 2011. Structure of a bacterial cell surface decaheme electron conduit. *Proceedings of the National Academy of Sciences*, 108(23), pp.9384–9389.

Coursolle, D. & Gralnick, J. a, 2010. Modularity of the Mtr respiratory pathway of Shewanella oneidensis strain MR-1. *Molecular microbiology*, 77(July), pp.995–1008.

Dohnalkova, A.C. et al., 2011. Imaging hydrated microbial extracellular polymers: comparative analysis by electron microscopy. *Applied and environmental microbiology*, 77(4), pp.1254–62.

Edwards, M.J. et al., 2012. The crystal structure of the extracellular 11-heme cytochrome UndA reveals a conserved 10-heme motif and defined binding site for soluble iron chelates. *Structure (London, England : 1993)*, 20(7), pp.1275–84.

Edwards, M.J. et al., 2014. The X-ray crystal structure of Shewanella oneidensis OmcA reveals new insight at the microbe-mineral interface. *FEBS letters*, 588(10), pp.1886–90.

Firer-Sherwood, M.A. et al., 2011. Solution-based structural analysis of the decaheme cytochrome, MtrA, by small-angle X-ray scattering and analytical ultracentrifugation. *J Phys Chem B*, 115(38), pp.11208–11214.

Fischer, H. et al., 2010. Determination of the molecular weight of proteins in solution from a single small-angle X-ray scattering measurement on a relative scale. *Journal of Applied Crystallography*, 43, pp.101–109.

Franke, D. & Svergun, D.I., 2009. DAMMIF , a program for rapid ab-initio shape determination in small-angle scattering. *Journal of Applied Crystallography*, 42(2), pp.342–346. A

Hartshorne, R.S. et al., 2007. Characterization of Shewanella oneidensis MtrC: a cell-surface decaheme cytochrome involved in respiratory electron transport to extracellular electron acceptors. *Journal of biological inorganic chemistry*, 12(7), pp.1083–94.

Hayat, S. & Elofsson, A., 2012. BOCTOPUS: Improved topology prediction of transmembrane β barrel proteins. *Bioinformatics* .

Kozin, M.B. & Svergun, D.I., 2001. Automated matching of high- and low-resolution structural models. *Journal of Applied Crystallography*, 34(1), pp.33–41.

Li, J., Callaway, D.J.E. & Bu, Z., 2009. Ezrin induces long-range interdomain allostery in the scaffolding protein NHERF1. *Journal of molecular biology*, 392(1), pp.166–80.

Madl, T., Gabel, F. & Sattler, M., 2011. NMR and small-angle scattering-based structural analysis of protein complexes in solution. *Journal of structural biology*, 173(3), pp.472–82.

Myers, J.M. & Myers, C.R., 2000. Role of the Tetraheme Cytochrome CymA in Anaerobic Electron Transport in Cells of Shewanella putrefaciens MR-1 with Normal Levels of Menaquinone. *Journal of Bacteriology*, 182(1), pp.67–75.

Neylon, C., 2008. Small angle neutron and X-ray scattering in structural biology: recent examples from the literature. *European biophysics journal : EBJ*, 37(5), pp.531–41.

Niemann, H.H. et al., 2008. X-ray and neutron small-angle scattering analysis of the complex formed by the Met receptor and the Listeria monocytogenes invasion protein InlB. *Journal of molecular biology*, 377(2), pp.489–500.

Petoukhov, M. V & Svergun, D.I., 2007. Analysis of X-ray and neutron scattering from biomacromolecular solutions. *Current opinion in structural biology*, 17(5), pp.562–71.

Petoukhov, M. V. et al., 2012. New developments in the ATSAS program package for small-angle scattering data analysis. *Journal of Applied Crystallography*, 45(2), pp.342–350.

Randall, A. et al., 2008. TMBpro: secondary structure, beta-contact and tertiary structure prediction of transmembrane beta-barrel proteins. *Bioinformatics (Oxford, England)*, 24(4), pp.513–20.

Schicklberger, M. et al., 2011. Involvement of the Shewanella oneidensis decaheme cytochrome MtrA in the periplasmic stability of the beta-barrel protein MtrB. *Applied and environmental microbiology*, 77(4), pp.1520–3.

Schuck, P., 2003. On the analysis of protein self-association by sedimentation velocity analytical ultracentrifugation. *Analytical Biochemistry*, 320(1), pp.104–124.

Schuck, P., 2000a. Size-Distribution Analysis of Macromolecules by Sedimentation Velocity Ultracentrifugation and Lamm Equation Modeling. *Biophysical Journal*, 78(March), pp.1606–1619.

Schuck, P., 2000b. Size-Distribution Analysis of Macromolecules by Sedimentation Velocity Ultracentrifugation and Lamm Equation Modeling. *Biophysical Journal*, 78(3), pp.1606–1619.

Stafford, W.F. 3rd, 1992. Boundary analysis in sedimentation transport experiments: a procedure for obtaining sedimentation coefficient distributions using the time derivative of the concentration profile. *Analytical biochemistry*, 203(2), pp.295–301.

Stafford, W.F. & Sherwood, P.J., 2004. Analysis of heterologous interacting systems by sedimentation velocity: curve fitting algorithms for estimation of sedimentation coefficients, equilibrium and kinetic constants. *Biophysical chemistry*, 108(1-3), pp.231–43.

Svergun, D.I., 1992. Determination of the regularization parameter in indirect-transform. *Journal of Applied Crystallography*, 25, pp.495–503.

Viklund, H. & Elofsson, A., 2008. OCTOPUS: improving topology prediction by two-track ANN-based preference scores and an extended topological grammar. *Bioinformatics (Oxford, England)*, 24(15), pp.1662–1668.

Volkov, V. V & Svergun, D.I., 2003. Uniqueness of ab initio shape determination in small-angle scattering. *Journal of Applied Crystallography*, 36(3 Part 1), pp.860–864.

White, G.F. et al., 2013. Rapid electron exchange between surface-exposed bacterial cytochromes and Fe(III) minerals. *Proceedings of the National Academy of Sciences of the United States of America*, 110(16), pp.6346–51.

6 | Discussion

Questions answered in the thesis

The literature review in Chapter 1 demonstrated that there were several interesting questions that needed to be addressed concerning MtrCAB, these were: What is the structure of MtrA? What are the mid point potentials of MtrA? How does MtrCAB transport electrons? What is the structure of MtrCAB?

In Chapter 3, the structure of MtrA was investigated. AUC experiments conducted on MtrA showed that the protein was elongated in one axis compared to the other. The N and C terminal truncations of MtrA were also elongated in one axis, but to a lesser extent than the full-length MtrA. This result is consistent with the idea that MtrA serves as a biological wire, facilitating the transport of electrons. It could be presumed that the elongated axis would sit in the direction of electron transport. SAXS experiments then allowed structural modeling to be conducted for MtrA and the N terminal truncation, as well as the evolutionary related STC. Similarly to the conclusions from the AUC data, SAXS experiments modeled MtrA as a roughly prolate, highly extended tube. SAXS experiments with MtrA were complicated due to the presumably flexible and associative nature of MtrA, which gave inconsistent scattering profiles in different concentrations. Bead model reconstructions were completed using scattering curves that did not show signs of abnormalities or aggregation, and so were most likely to be representative of MtrA. These were much larger and longer than previously published SAXS structures of MtrA. This could indicate that the presented SAXS model has inaccuracies within it.

SAXS experiments on the N terminal truncation of MtrA (MtrA N) were also carried out. These produced high quality data and therefore high quality reconstructions. These models resembled an elongated prolate shape that was only just smaller than the full MtrA SAXS structure published by Firer-Sherwood *et al*., (2011). The MtrA N terminus structure appeared to fit with one end of the full length MtrA SAXS structure. Using this, the N terminus, and therefore the C terminus, of MtrA could be identified. No SAXS structures for MtrA C terminus were produced due to the heterogeneity of the protein solution. The MtrA C protein was not purified, and solutions of it always contained contaminants, with which it presumably interacted. This indicates that MtrA, particularly its C terminus, usually forms strong protein interactions, presumably with MtrB. This theory explains why purified MtrA appeared to be so flexible and was unable to be crystalized. It also raises the issue of whether structures of MtrA in free solution are representative of

functional MtrA, as its conformation in protein complexes where it is active may be dictated by its interacting partners. SAXS structures of STC revealed a close similarity to X-ray crystallography structures and both these structures seemed to fit well with the structures of MtrA N. This could indicate that STC is possibly an evolutionary ancestor of MtrA N.

The shape of the MtrCAB was investigated in Chapter 5. SANS techniques were used to develop models of MtrC and MtrCAB. These models contained a globular region and a tail region, with the section joining the tail region to the globular head region affected when detergent moieties were phased out from contributing to scattering. The globular head region was deemed most likely to be MtrC, the detergent affected region deemed likely to be MtrB (as this binds detergents and lipids) and the long tail region MtrA. The section identified as MtrA had a shape that was in agreement with structural information obtained from AUC and SAXS. Interestingly, the proposed length of MtrCAB suggests it would be long enough to span the estimated width of the periplasm. This indicates that MtrCAB could make direct contact with CymA in the DMR respiration process, rather than relying on a pool of soluble periplasmic intermediates, such as STC, for reduction. The data density of the SANS experiments was not as high as for SAXS experiments and the models produced contained more variability within them. Predictions about the models developed from SANS scattering curves suggested that the models were larger than the sum of the component MtrC, MtrA and MtrB proteins combined. This indicates that more detailed models from more dense scattering curves would produce smaller more defined structures. These experiments were planned, however they were not completed due to synchrotron technical issues.

Chapter 3 also investigated the mid-point potentials of MtrA, which assists our understanding of how MtrA, as part of MtrCAB, transports electrons. Through using two different techniques, soluble redox titrations and optically transparent electrode spectra, Nerstian derived redox curves were constructed for MtrA, MtrA N and MtrA C. These results showed that the active potential range of MtrA was from 0 V to -0.35 V and three distinct groups of hemes were identified. It was found that MtrA N contained the heme group at high potential and MtrA C contained the heme group at low potential, with both of these truncations also containing the middle group of hemes. The middle group of hemes was predicted to contain the most hemes, whereas the higher or lower heme groups contained fewer hemes than this group, in all three proteins. This suggests that

only the hemes starting and ending the electron transport chain of MtrA have mid point potentials that are unique and therefore define the potential gradient through MtrA and thus any electron transport direction biases.

To investigate the question of how MtrCAB transports electrons, MtrCAB complexes were inserted into liposomes to form proteoliposomes. These proteoliposomes contained redox indicators that exhibited measurable absorbance changes depending on redox state. The movement of electrons into and out of proteoliposomes was proved to be solely through the functioning of MtrCAB. Three different redox indicators were used for proteoliposome interiors, methyl viologen, STC and cytochrome c. These had a range of mid point potentials ranging from low to high potential respectively. The real time flow of electrons into and out of sets of proteoliposomes was measured when sodium dithionite reductant and then ferric citrate oxidant was added to the proteoliposomes in an anaerobic environment. This rate was determined to be biphasic with a fast initial rate and a slower secondary rate. Proteoliposomes, which contained methyl viologen (which has a more negative mid point potential than MtrCAB), were found to be reduced slower than they were oxidised. STC containing proteoliposomes (with a redox potential similar to MtrCAB) was reduced by sodium dithionite at a faster rate than when they were re-oxidised. Cytochrome C proteoliposomes (with a mid point potential more positive than MtrCAB) were able to be reduced in what appeared to be a monophasic process, but were not able to be re-oxidised by ferric citrate or the stronger oxidant potassium ferricyanide. Using these initial rates, an electron transport rate of between 200 and 3000 $e.s^{-1}$ for each MtrCAB was calculated. This estimate of rate was the same for the reduction of each of the three types of proteoliposome and for the oxidation of methyl viologen and STC proteoliposomes. This was consistent with results from White *et al*., (2013) and the rates are in the range that could allow fast enough respiration from DMR to sustain life. The fact that all of the STC held within proteoliposomes could be rapidly re-oxidised indicates that a periplasm filled with electron shuttles such as STC can lose all of its electrons and become oxidised.

Extending the current understanding beyond this thesis

Following on from Chapter 3, more work could be conducted on the shape of MtrA. If crystal structures of MtrCAB were completed this would give the opportunity to study MtrA in a functional shape. This shape may be different from SAXS structures developed

for MtrA. The SAXS structures in Chapter 3 could be extended and developed to give more structural detail, particularly across a broader range of protein concentrations. The size of the current SAXS structures developed may have inaccuracies within them, due to the data quality,. However, these inaccuracies may alternatively be due to the suspected inherent flexibility of MtrA. If SAXS structures of MtrA C-terminus could be developed, this, along with the already produced SAXS structures of MtrA N, would enable the re-construction of full length MtrA and an exact comparison to full length MtrA structures. In addition to improving the structural understanding of MtrA, the development of a structure of MtCAB is a vital next step. This could be achieved through X-ray crystallographic techniques if suitable crystals become available or through a more refined and detailed SANS MtrCAB model. Through using MtrCAB solubilized in deuterated detergent buffers, a more effective phase contrast between protein and lipid scattering could be achieved and thus more defined scattering curves produced and better bead models built. It was planned that these types of advanced SANS experiments would be completed, however the synchrotron developed a fault the day before the allowed experimental time and the re-scheduling of the experiments took place outside the timeframe of this thesis. It would be extremely interesting to compare MtrCAB crystal structures to MtrCAB SANS structures.

The function of MtrCAB could be explored through the continued and extended use of liposomes in electrochemical cells. This would allow for more detailed examination of the rates of electron flow through MtrCAB and the elimination of extraneous chemical reactions occurring when chemical oxidants or reductants are added to proteoliposomes suspensions. The use of STC and cytochrome c proteoliposomes in the electrochemical carbon pot set up would enable further verification of the chemical redox experiments carried out in Chapter 4. One of the biggest steps in future work concerning proteoliposomes would be the accurate measurement of the number of MtrCAB complexes facilitating electron transport within a suspension. At present only rough estimates have been made. If these could be improved by one or two orders of magnitude the rates of electron transport reported would have higher significance.